Université Paris-Sud

Ecole Doctorale Particules Noyau Cosmos
Laboratoire de structure du nucléon au CEA/Irfu/SPhN

Discipline : Physique

Thèse de doctorat

Soutenue le 25 juin 2015 par

Maxime DEFURNE

Photon and π^0 electroproduction at Jefferson Laboratory - Hall A

Directeur de thèse :	Franck Sabatié	Docteur (CEA/Irfu/SPhN/LSN)

Composition du jury :

Président du jury :	Etienne Augé	Professeur (Université Paris Sud)
Rapporteurs :	Zein-Eddine Meziani	Professeur (Temple University)
	Paul Stoler	Professeur (Rensselaer Polytechnic Institute)
Examinateurs :	Gunar Schnell	Professeur (University of the Basque Country)
	Peter Kroll	Professeur (Bergische Universität Wuppertal)
	Carlos Muñoz Camacho	Docteur (IPN Orsay)

July 1, 2015

Contents

Acknowledgements

First I would like to express my endless gratitude to my PhD supervisor Franck Sabatié for his trust, his advices and his support. I will keep working hard to become an expert as accomplished as he is, on both human and scientific aspects. Thank you also for reminding to take vacations when I needed some.

I have spent three years with the amazing people of the former group CLAS in the *Service de physique nucléaire* (SPhN) at CEA-Saclay. This work could not have been as rich as it is without all the members of the group: I am not only talking about the carbohydrate intake that represent the numerous cakes we shared, but also all the discussions about experimental and theoretical aspects. Thank you Hervé Moutarde (undoubtly the head pastry chef of the group) and Adrien Besse for the patience and the clarifications in explaining me the QCD theory in hadronic physics. Thank you Sébastien Procureur, Gabriel Charles, Simon Bouteille and Maxence Vandenbroucke for this discussions about detectors but also for some mémorable table tennis games (keep training hard Gabriel). In advance, thank you Bryan Berthou for the future advices you will provide me in structuring the analysis code of the CLAS12 DVCS experiment. Finally I want to thank Jacques Ball and Michel Garçon. I have learnt so much from them.

I acknowledge all the members of SPhN. Particularly I want to thank the always-smiling head of the division, Héloïse Goutte, for welcoming me during my PhD. I am also grateful to Danielle Coret and Isabelle Richard, making everything so much easier in the division. Finally a special thanks to my friend Eric Fuchey for all his strong help and support here at Saclay but also back at Jefferson Laboratory during my internship.

My gratitude also goes to the members of the Hall A DVCS collaboration. Special thanks to Carlos Muñoz Camacho and Charles Hyde with whom we spent hours debatting on data analysis, radiative corrections and many more analysis details. It was a great pleasure for me working with you. Finally I would have never heard about generalized parton distributions and deeply virtual Compton scattering without Alexandre Camsonne who made me discover Jefferson Laboratory, the Hall A, hadronic physics, the best restaurants in Newport News, and so on.

I would like to thank all the members of the examination committee. Special thanks to Paul Stoler and Zein-Eddine Meaziani for their careful reading of the manuscript.

On the personal side, I thank my friends Benoit Latour, Jordane Soussi and Patrick Hsia for encouraging me all along these years. I enjoyed our reflections about how to change the world. A special thanks to my friends Cédric Mezrag and Laetitia Leduc who helped me getting ready for the most important interview of my life. I have appreciated a lot watching a good old *Doctor Who* episode before this "D-Day" in order to relax. Since I was born, my family supports me and I would have never reached this far without them. I thank them for having been there at anytime. Finally I want to dedicate the last sentences to my lovely girlfriend. Although the last months were very difficult, she was there, helping me to give the best of myself. Thank you for your patience, kindness and love. We finally did it!

Introduction

The deepest desire of mankind[1] has always been to understand the universe. A significant step toward this undertanding will be achieved when the following question is answered: *What is it made of ?* Since the ancient greeks and the four elements, a lot have been learnt about the structure of matter. It appears to be built with a finite set of elementary particles, connected through four interactions which are described by the Standard Model. Whereas the Large Hadron Collider keeps challenging the predictions of the Standard Model at higher and higher energies, we are still far from completely understanding how these elementary blocks organize themselves in a proton.

Indeed, in the late 1960s, DIS measurements at SLAC confirmed that the proton is a composite object made of quarks and gluons. These particles interact through the strong interaction. At high energy, the strong interaction can be computed using perturbative quantum chromodynamics (QCD), the associated field theory. Indeed the coupling constant becomes small and quarks behave as if they were free. It is the so-called *asymptotic freedom*. Nevertheless, at long distance (typically the proton size), the coupling constant becomes large and perturbation theory cannot be applied anymore. In other words, despite the promising ways of non-perturbative calculations (Schwinger-Dyson equations, lattice QCD,...), the structure of the hadrons cannot be accessed through calculations yet.

Pieces of information about the nucleon structure have been revealed by scattering experiments. Indeed scattering processes can be split into two parts:

- A hard part/short distance part calculable perturbatively.

- A soft part describing the interaction with the nucleon medium. This part encodes the nucleon structure.

This splitting method is called *factorization*. As a consequence the scattering cross section is parametrized by functions associated to the soft part. From the cross section measurement, we derive these functions and get some insight about the structure of the hadron. For instance form factors and parton distribution functions, related to spatial and momentum distributions, have been studied using elastic and deep inelastic scattering. Unfortunately, it is not enough to explain the confinement of the quarks inside hadrons, the proton mass and spin.

In the mid 90's, new kinds of distributions called *generalized parton distributions* are defined. They represent a higher level of information than FFs and PDFs since they encapsulate both spatial and momentum information. Using the GPDs, we could derive the total orbital angular momentum of quarks thanks to Ji's sum rule. Experimentally they are related to deep exclusive processes. A worldwide experimental program has been dedicated to study such processes. This thesis deals in particular with two experiments measuring cross sections of photon and π^0 electroproduction in order to determine the GPDs. The thesis is articulated as follows:

---

[1]It is maybe more exact to say one of the deepest desires.

- Chapter 1 introduces the theoretical framework of GPDs and how they are involved in the cross sections of interest. We discuss also GPD models and the existing experimental data.

- Chapter 2 is dedicated to the description of Jefferson Lab, Hall A of Jefferson Lab and the experimental setup.

- Chapter 3 focuses on the extraction of the DIS cross section in order to perform a quality check of our data set. It allows us to develop a method for cross section extraction.

- Chapter 4 is about the data analysis of the E00-110 experiment. All the cuts and corresponding corrections are presented.

- Chapter 5 is subdivided into three parts: It presents the radiative corrections and the Monte-Carlo simulation used for acceptance computation. In the last part, we explain the fitting procedure employed to extract DVCS cross sections and effective CFFs.

- Chapter 6 summarizes the results on photon electroproduction and compares them to predictions from different GPD-based models.

- Finally Chapter 7 is a condensate of chapters 4,5 and 6 applied on the π^0 analysis. The results of the first Rosenbluth separation performed on the π^0 electroproduction cross section are commented on and compared to two GPD models. A careful study of systematic errors has been carried out.

Chapter 1

Nucleon structure through deep exclusive processes

One of the hints that the proton has an internal structure were obtained by studying elastic scattering off the proton in the late 1950's at Stanford university by Hofstadter and his team. The corresponding cross section can be parametrized using form factors (FFs), which are related to the spatial distribution of charge in the nucleon (proton and neutron). In the late 1960's at the Standford Linear Accelerator (SLAC), the study of Deep Inelastic Scattering (DIS) confirmed the existence of quarks and that the proton is a composite particle. The parton distribution functions (PDFs) parametrize the DIS cross section and are related to the longitudinal momentum distribution of partons (quark and gluon) in the nucleon. Nevertheless the correlation between both spatial and momentum information cannot be derived from FFs and PDFs. It is only in the mid-90's that was introduced the concept of Generalized Parton Distributions (GPDs) which are a generalization of the FFs and PDFs. GPDs are objects that encapsulate a higher level of information since they actually encode the correlation between momentum and spatial distributions. GPDs obey a set of properties and sum rules from which modelization is possible. These models are then tested by comparing observables measured in deep exclusive processes. In particular we will focus here on Deeply Virtual Compton Scattering (DVCS) and deep π^0 electroproduction. After explaining how GPDs are involved in these processes, we briefly present the current state of the experimental program. Finally we introduce the experiments of interest in this thesis and what new information we want to extract from the data.

1.1 Elastic scattering and form factors

A particle a scatters elastically off a particle b when the final state is only composed of particles a and b. Figure 1.1 shows a diagram of elastic scattering. We note:

- $k_i = (\mathbf{k_i}, E)$ the 4-momentum of the incident electron.

- $k_f = (\mathbf{k_f}, E')$ the 4-momentum of the scattered electron.

- θ_e the scattering angle in the lab frame.

- $q = k_i - k_f$ the 4-momentum of the virtual photon and $Q^2 = -(k_f - k_i)^2$ its virtuality.

In 1911, Rutherford studied the scattering of alpha particles off a gold foil [1]. Assuming a point-like target with no recoil and a non-relativistic scattered particle, the cross section

is given by:

$$\left(\frac{d\sigma}{d\Omega}\right)_{Rutherford} = \frac{\alpha}{16E^2 \sin^4\left(\frac{\theta_e}{2}\right)}, \tag{1.1}$$

where α is the fine-structure constant. If one uses relativistic electrons instead of α-particles, the cross section reads:

$$\left(\frac{d\sigma}{d\Omega}\right)_{Mott} = \frac{\alpha}{4E^2 \sin^4\left(\frac{\theta_e}{2}\right)} \cos^2\left(\frac{\theta_e}{2}\right), \tag{1.2}$$

but the experimental cross section deviated from this formula. If the target is an extended object, the electron cross section is modified and becomes:

$$\frac{d\sigma}{d\Omega} = \left(\frac{d\sigma}{d\Omega}\right)_{Mott} |F(\Delta)|^2, \tag{1.3}$$

with $\Delta = p - p'$ and $F(\Delta)$ the form factor. $F(\Delta)$ is the Fourier transform of the transverse spatial distribution of charge $\rho(r)$:

$$F(\Delta) = \int \rho(r)e^{i\Delta r}dr^3. \tag{1.4}$$
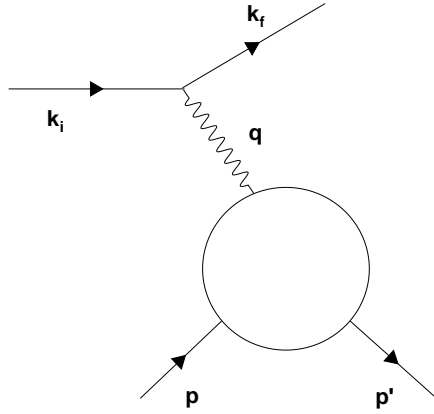
Figure 1.1: Elastic scattering diagram. Note that in the case of elastic scattering, $\Delta = -q$.

Following the steps of Rutherford, Robert Hofstadter studied the nucleon structure using elastic scattering $ep \to e'p'$ at SLAC between 1954 and 1957. His work was awarded the Nobel prize in 1961. In the nucleon case, the cross section can be parametrized by two structure functions called the Sachs form factors G_E and G_M. The cross section is written [2]:

$$\frac{d\sigma}{d\Omega} = \frac{\alpha}{4E^2 \sin^4\left(\frac{\theta_e}{2}\right)} \frac{E'}{E} \left[\frac{G_E^2(\Delta^2) + \tau G_M^2(\Delta^2)}{1+\tau} \cos^2\left(\frac{\theta_e}{2}\right) + 2\tau G_M^2(\Delta^2) \sin^2\left(\frac{\theta_e}{2}\right)\right], \tag{1.5}$$

with $\tau = \frac{-\Delta^2}{4M^2}$ and M the mass of the proton. By measuring the cross section at the same Δ^2 but two different beam energies, it is possible to extract G_E and G_M. This way of separating the two FFs using different beam energies is called a *Rosenbluth separation*. Later in this chapter, we will use the Pauli and Dirac FFs defined as:

$$F_1(Q^2) = \frac{G_E(Q^2) + \tau G_M(Q^2)}{2\tau} \tag{1.6}$$

$$F_2(Q^2) = \frac{G_M(Q^2) - G_E(Q^2)}{1+\tau} \tag{1.7}$$

In the Breit frame in which the initial and final proton momenta have the same magnitude but opposite directions, G_E and G_M are the Fourier transform of the charge and magnetic distributions of the proton. The proton charge radius can be derived from the knowledge of G_E using the formula:

$$\langle r_E^2 \rangle = -\frac{6}{G_E(0)} \frac{dG_E(Q^2)}{dQ^2}\bigg|_{Q^2=0}. \tag{1.8}$$

Applying Eq. 1.8, a charge radius of $r_p = \sqrt{\langle r_E^2 \rangle} = 0.879(8)$ fm was derived by extrapolating G_E-measurements performed at low Q^2 [3]. This result is in good agreement with the radius provided by the study of the Lamb shift and the hyperfine structure of electronic hydrogen atoms [4], giving $r_p = 0.8768(69)$ fm. Nonetheless, recent studies of muonic hydrogen's Lamb shift [5] gave $r_p = 0.84184(67)$ fm, at 7-σ from the value given by the electronic measurements. This discrepancy has not been understood yet.

1.2 Deep inelastic scattering and parton distribution functions

Let us now consider the inelastic reaction $ep \to eX$. We define two additional variables:

- The Bjorken variable $x_B = \frac{Q^2}{2M\nu}$, where $\nu = E - E'$.

- $W^2 = (p+q)^2 = M^2 + Q^2\left(\frac{1}{x_B} - 1\right)$ the invariant mass of the hadronic final state.

The deep inelastic regime is defined by $W \gg M$ and $Q^2 \gg M^2$. In this regime, the final state is composed of more particles than the initial state. Under the one-photon exchange assumption, the DIS cross section is given by the contraction of the leptonic and hadronic tensors. The information about the proton is encapsulated in the hadronic tensor. In the case of unpolarized DIS, once symmetries and invariances have been applied, the hadronic tensor can be parametrized by two dimensionless structure functions depending on Q^2 and x_B. As a consequence the cross section is related to these two functions by:

$$\frac{d\sigma}{d\Omega dE'} = \left(\frac{d\sigma}{d\Omega}\right)_{Mott} \left[\frac{F_2(x_B, Q^2)}{\nu} + \frac{2}{M} F_1(x_B, Q^2) \tan^2\left(\frac{\theta_e}{2}\right)\right], \tag{1.9}$$

In the late 1960's at SLAC, Friedman, Kendall and Taylor performed DIS cross section measurements at several Q^2 [6] [7]and were later awarded the Nobel Prize in 1990. From these measurements they noticed first that F_2 was independent of Q^2, as if the electron was scattering off point-like particles. Moreover F_1 and F_2 were related through the Callan-Gross relation, indicating that these particles were fermions:

$$F_2(x_B) = 2x_B F_1(x_B). \tag{1.10}$$

These results validated the theory of Gell-Mann [8] (Nobel Prize 1969) and Zweig [9] in 1964 that the proton was composed of quarks and gluons. Richard Feynman (Nobel Prize 1965) developed the parton model in 1969: In the limit $Q^2 \to \infty$ and $\nu \to \infty$ but fixed x_B (Bjorken limit), the virtual photon interacts with a single quark in the proton (Figure 1.2). Within this model, F_2 is related to the so-called parton distribution functions (PDFs).

$$F_2(x_B) = x_B \sum_f e_f q_f(x_B), \tag{1.11}$$

where e_f stands for the quark electric charge in units of the positron charge and q_f the PDF for a quark of flavor f.
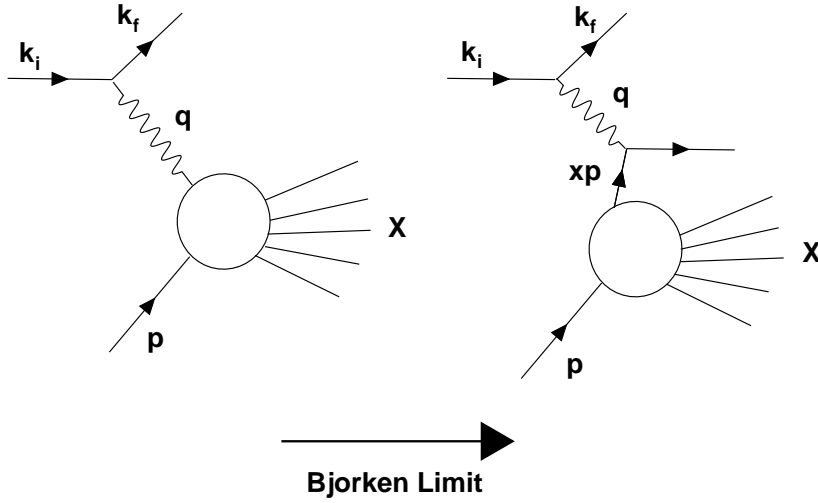
Figure 1.2: Deep inelastic scattering. In the Bjorken limit, the photon interacts with a single quark.

In the infinite momentum frame, where the proton speed is close to the speed of light along the z-axis colliding head-on with the virtual photon, x_B represents the fraction of momentum carried by the struck quark. In this frame $q_f(x_B)$ can be interpreted as the probability to find a parton with flavor f carrying a fraction x_B of the proton momentum. Since the time scale of the interaction between two partons is much greater than the one between the photon and the active quark, the DIS cross section can be rewritten as the product of the probability to find a quark and the probability to scatter off this quark:

$$\frac{d^2\sigma_{DIS}}{dx_B dQ^2} = \sum_f q_f(x_B) \times \frac{d^2\sigma_{eq \to eq}}{dx_B dQ^2}, \tag{1.12}$$

$$= \sum_f q_f(x_B) \times e_f^2 \frac{2\pi\alpha^2}{Q^4} \left[1 + \left(1 - \frac{Q^2}{x_B s} \right) \right], \tag{1.13}$$

where $s = (p + k_i)^2$. Through this factorized form, the parton model infers the notion of *asymptotic freedom*: At high Q^2 and therefore small resolved distance, the reaction occurs as if the electron scatters off a free quark.

By extracting F_2 over a larger kinematic domain, the experimentalists noticed that the scaling becomes violated when moving away from the x_B value of first SLAC measurements. The scaling violation is explained by the active quark emitting gluons (see Figure 1.3), in other words by QCD radiative corrections. The Q^2-evolution of PDFs is driven by the DGLAP (Dokshitzer, Gribov, Lipatov, Altarelli and Parisi) equations, resulting in a logarithmic Q^2-dependence of the PDFs.

1.3 Generalized parton distributions

The FFs and PDFs give information on either the position or the momentum fraction of the parton in the nucleon, but do not correlate both information. In the quest of understanding nucleon structure, theorists have been looking for distributions containing the most information and related to experimental observables. We are going to define the GPDs starting from
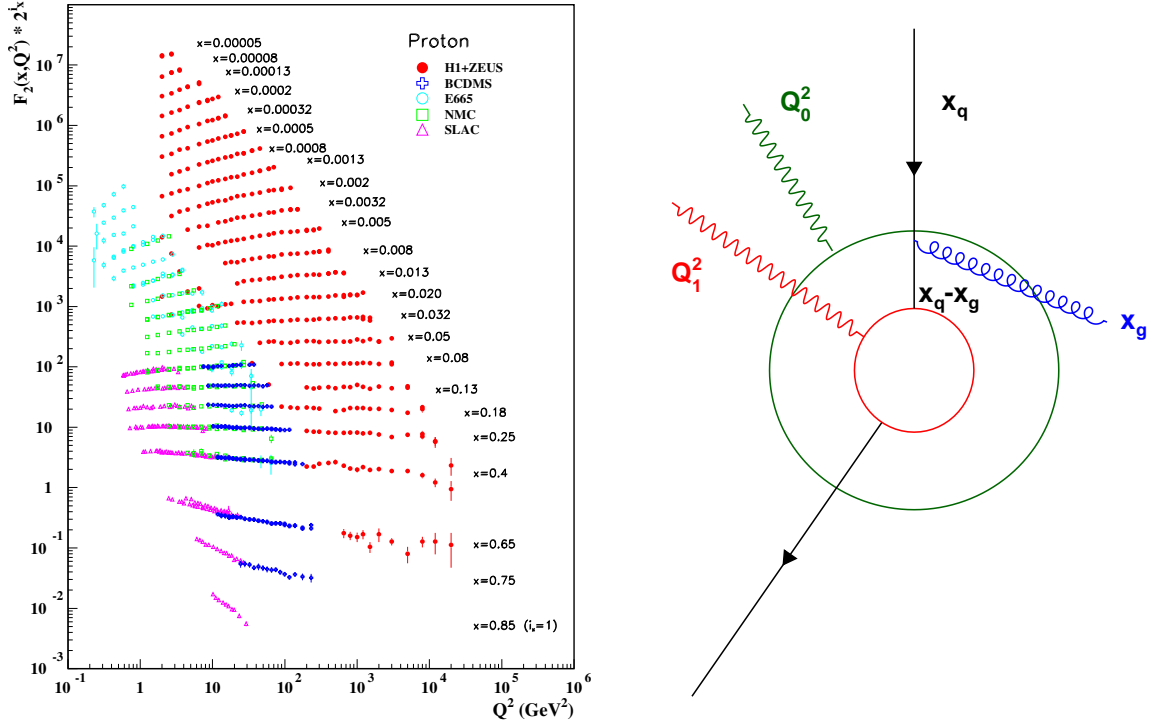
Figure 1.3: Left: F_2 measured at different x_B and Q^2. There is an apparent scaling at $x_B \sim 0.2$ where SLAC performed their first measurements. Right: The green virtual photon interacts with a quark with a momentum fraction x_q. At $Q_1^2 > Q_0^2$, the red virtual photon resolves smaller distances and interact with a quark $x_q - x_g$ which has emitted previously a gluon. As a consequence, when going at higher Q^2, the quark PDF decreases for $x_B > 0.2$ and increases below. The gluon PDFs also increases with Q^2.

the Wigner distributions. Then we will describe their support and several of their properties which may be used to constrain models. At the end of this section, we will present the double distributions which are convenient ways to build a GPD model given their properties.

1.3.1 From Wigner distributions to generalized parton distributions

In 1932, Wigner (Nobel Prize 1963) defined a new kind of distribution which is a function of both spatial and momentum coordinates. Taking a wave function $\psi(r)$, Wigner defined the following distribution:

$$P(r, k) = \int_{-\infty}^{+\infty} dz e^{ikz} \psi^*(r - z/2) \psi(r + z/2) . \tag{1.14}$$

The spatial distribution is recovered by simply integrating the Wigner distribution over the momentum variables. Inversely, we integrate over the spatial variables to recover the momentum distribution. Adapting this formalism in quantum field theory, we first define the Wigner operators:

$$\mathcal{W}_\Gamma^f(r, k) = \int d^4 z e^{ik \cdot z} \bar{\Psi}^f \left(r - \frac{z}{2} \right) \Gamma \mathcal{L} \Psi^f \left(r + \frac{z}{2} \right), \tag{1.15}$$

where r is the space-time coordinates of the quark with flavor f, k being the associated 4-momentum and Ψ its field. Γ is a Dirac operator. $\mathcal{L}$ is a Wilson line which ensures the gauge invariance.
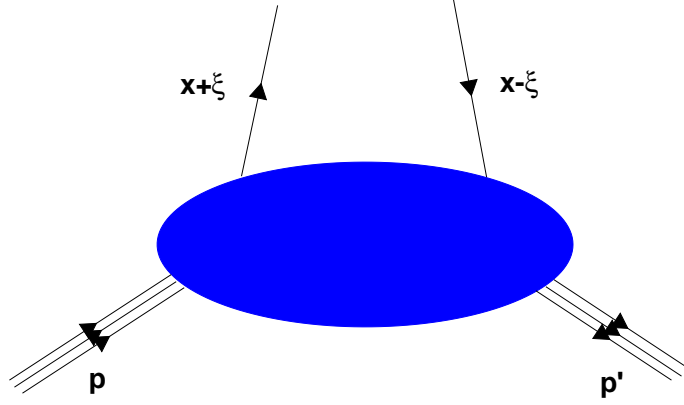
Figure 1.4: Diagram associated to the matrix element F_Γ^f.

From the Wigner operators, the Wigner distributions are given by:

$$W_\Gamma^f(r,k) = \frac{1}{2M} \int \frac{d^4q}{(2\pi)^4} \left\langle p' \left| \mathcal{W}_\Gamma^f(r,k) \right| p \right\rangle, \qquad (1.16)$$

where p and p' are the inital and final momenta of a proton, with $q = p' - p$. The Wigner distributions encapsulate all the information about the momentum and spatial distributions of partons, including their correlations. In the infinite momentum frame where the proton moves along the z-axis, the interacting parton is mainly on the light cone $+$ component (see Appendix C for definitions). Therefore the k^- and $k_\perp$ components are very small and difficult to access. By integrating over k^- and both components of $k_\perp$ and chosing a light cone gauge, we obtain the so called generalized parton distributions (GPDs):

$$F_\Gamma^f(x,\xi,t) = \frac{P^+}{4\pi} \int dz^- e^{ixP^+z^-} \langle p'|\bar{\Psi}_q\left(-\frac{z}{2}\right)\Gamma\Psi_q\left(\frac{z}{2}\right)|p\rangle|_{z^+=\vec{z}_\perp=0}. \qquad (1.17)$$

The GPDs F_Γ^f are associated to the diagram illustrated by the Figure 1.4: x is the average longitudinal momentum fraction carried by the active quark, -2ξ the longitudinal momentum transfer and P the sum $p+p'$. ξ is approximately given by $\frac{x_B}{2-x_B}$. t is the squared momentum transfer to the proton $|p - p'|^2$. Note that, in the case of GPDs and PDFs, the Wilson line reduces to unity when chosing a light-cone gauge.

Taking $\Gamma = \gamma^+$ or $\Gamma = \gamma^+\gamma_5$, we obtain the chiral-even GPDs (same helicity for the emitted and reabsorbed parton):

$$F_{\gamma^+}^f(x,\xi,t) = H^f(x,\xi,t)\bar{N}(p')\gamma^+ N(p) + E^f(x,\xi,t)\bar{N}(p')\sigma^{+\nu}\frac{\Delta_\nu}{2M}N(p), \qquad (1.18)$$

$$F_{\gamma^+\gamma_5}^f(x,\xi,t) = \tilde{H}^f(x,\xi,t)\bar{N}(p')\gamma^+\gamma_5 N(p) + \tilde{E}^f(x,\xi,t)\bar{N}(p')\gamma_5\frac{\Delta^+}{2M}N(p), \qquad (1.19)$$

The correlator with $\Gamma = \sigma^{+\perp}\gamma_5$ is parametrized by four chiral-odd GPDs called also transversity GPDs H_T, $\tilde{H}_T$, E_T and $\tilde{E}_T$. Unlike E-GPDs, H-GPDs are not sensitive to the parton helicities. When they are tilded, GPDs are involved in processes with a flip of the nucleon helicity. The variables x and ξ evolve between [-1 ; 1]. By comparing x and ξ, we may interpret the process in different ways:

- For $x < -\xi$ an antiquark exits and is reabsorbed in the nucleon. Same thing with a quark for $x > \xi$. These two regions are called the DGLAP regions since the GPDs evolve in this region like the PDFs, *i.e.* according to the DGLAP equations.

- For $-\xi < x < \xi$: the nucleon emits a quark-antiquark pair. This region is called the ERBL (Efremov, Radyushkin, Brodsky and Lepage) region.

1.3.2 Properties of GPDs

The chiral-even GPDs are generalizations of PDFs and FFs just by looking at their associated correlator. Indeed, for a flavor f, we have when the squared momentum transfer to the proton $t \to 0$:

$$H^f(x, 0, 0) = q_f(x), \tag{1.20}$$
$$\tilde{H}^f(x, 0, 0) = \Delta q_f(x) . \tag{1.21}$$

Moreover the elastic form factors are obtained from the first moment of the corresponding GPDs:

$$\int_{-1}^{1} H^f(x, \xi, t) \, dx = F_1^f(t) \qquad \forall \xi, \tag{1.22}$$

$$\int_{-1}^{1} E^f(x, \xi, t) \, dx = F_2^f(t) \qquad \forall \xi, \tag{1.23}$$

$$\int_{-1}^{1} \tilde{H}^f(x, \xi, t) \, dx = G_A^f(t) \qquad \forall \xi, \tag{1.24}$$

$$\int_{-1}^{1} \tilde{E}^f(x, \xi, t) \, dx = G_p^f(t) \qquad \forall \xi . \tag{1.25}$$

Finally the total angular momentum of quark J^f can be accessed through Ji's sum rule [10, 11]:

$$\int_{-1}^{1} x \left[H^f(x, \xi, 0) + E^f(x, \xi, 0) \right] \, dx = J^f \ \forall \xi . \tag{1.26}$$

The chiral-odd GPDs are almost unknown compared to the chiral-even GPDs from the experimental and theoretical points of view. Although the chiral-odd GPDs also describe the nucleon structure, they are more difficult to interpret. No model-independent relations with orbital angular momentum of quarks involves the transversity GPDs. The only existing constraint is the forward limit of H_T.

$$H_T^f(x, 0, 0) = \delta_T q_f(x), \tag{1.27}$$

where $\delta_T q_f(x)$ is the transversity distribution function. In a transversely polarized proton, $\delta_T q_f(x)$ represents the difference between the densities of partons with parallel and antiparallel spins with respect to the proton spin. The chiral-odd GPDs might be necessary to describe several exclusive processes, especially pseudo-scalar meson production.

We finish this exhaustive list of GPD properties with the polynomiality. This property states that the nth moment of GPDs is an even polynomial in ξ.

$$\text{if n even}: \int_{-1}^{1} dx x^n H(x, \xi, t) = a_0 + a_2 \xi^2 + a_4 \xi^4 + \cdots + a_n \xi^n , \tag{1.28}$$

$$\text{if n odd}: \int_{-1}^{1} dx x^n H(x, \xi, t) = a_0 + a_2 \xi^2 + a_4 \xi^4 + \cdots + a_{n+1} \xi^{n+1} . \tag{1.29}$$

Note that the coefficients a_i depend on t. The same property applies to E, $\tilde{H}$ and $\tilde{E}$. The coefficient a_{n+1} of E has the opposite sign of the one of H. In the case of odd n, the highest power is $n-1$ for GPDs $\tilde{H}$ and $\tilde{E}$. Polynomiality is a consequence of the Lorentz invariance.

1.3.3 GPDs and double distributions

Previous properties constrain the GPD models. The polynomiality condition is the most complicated to respect. Nevertheless A. Radyushkin [12, 13] and D. Mueller [14] noticed that the double distributions (DDs) are a convenient way to naturally obey the polynomiality. We first define two variables α and β such that:

$$(x+\xi)P^+ = \beta P^+ - \frac{1}{2}(1+\alpha)\Delta^+, \tag{1.30}$$

where Δ^+ is the longitudinal component of the transferred momentum Δ. α plays the same role as ξ, except that it is not relative to P^+. As $-2\xi = \frac{\Delta^+}{P^+}$, we have $x = \beta + \alpha\xi$. The GPDs is then constructed from the DDs by:

$$GPD^f(x,\xi) = \int_{-1}^{1} d\beta \int_{-1+|\beta|}^{1-|\beta|} d\alpha\, \delta(x-\beta-\xi\alpha)DD^f(\alpha,\beta), \tag{1.31}$$

The integration boundaries are constrained by x between [-1;1] and ξ between [0;1].

When the momentum transfer $\Delta = 0$, we recover the usual PDF. In the limit $P = 0$ and $\Delta \neq 0$, the matrix element becomes:

$$\langle P+\Delta|\bar{\Psi}_q\left(-\frac{z}{2}\right)\Gamma\Psi_q\left(\frac{z}{2}\right)|P\rangle\big|_{z^+=\vec{z}_\perp=0} \rightarrow \langle\Delta|\bar{\Psi}_q\left(-\frac{z}{2}\right)\Gamma\Psi_q\left(\frac{z}{2}\right)|0\rangle\big|_{z^+=\vec{z}_\perp=0}, \tag{1.32}$$

which is a distribution amplitude (DA) representing the probability to produce a meson from a quark-antiquark pair carrying respectively a longitudinal momentum fraction $1+\alpha$ and $1-\alpha$. A. Radyushkin [12, 13] found a profile which respects these two limits:

$$DD(\beta,\alpha) = h(\beta,\alpha)q(\beta), \tag{1.33}$$

$$h(\beta,\alpha) = \frac{\Gamma(2b+2)}{2^{2b+1}\Gamma^2(2b+1)}\frac{[(1-|\beta|)^2-\alpha^2]^b}{(1-|\beta|)^{2b+1}}, \tag{1.34}$$

where $q(\beta)$ is a PDF and $h(\beta,\alpha)$ a profile function allowing to recover a DA when $\alpha \to 0$. The parameter b is a free parameter which tunes the ξ-dependence: when $b \to \infty$, the DD looks like a PDF.

Concerning the t-dependence, it was first included in a factorized manner, *i.e.* such as $H(x,\xi,t) = H_{DD}(x,\xi)F_1(t)$ where $F_1(t)$ is the form factor and $H_{DD}(x,\xi)$ computed with Equation 1.31. Nowadays it is incorporated in the double distribution such as:

$$DD(\beta,\alpha,t) = h(\beta,\alpha)q(\beta) \times \exp\left(p(\beta)t\right), \tag{1.35}$$

where $p(\beta)$ is a profile function. A usual choice is $p(\beta) = a\ln\beta + c$ with a and c parameters but more complex forms exist [15]. Later we will compare our results with several GPD models based on double distributions.

1.4   Deep exclusive processes to access GPDs

GPDs are accessible through the study of deep exclusive processes: they are a rare subset of deep inelastic processes where all particles in the final state are detected as shown in Fig. 1.5.
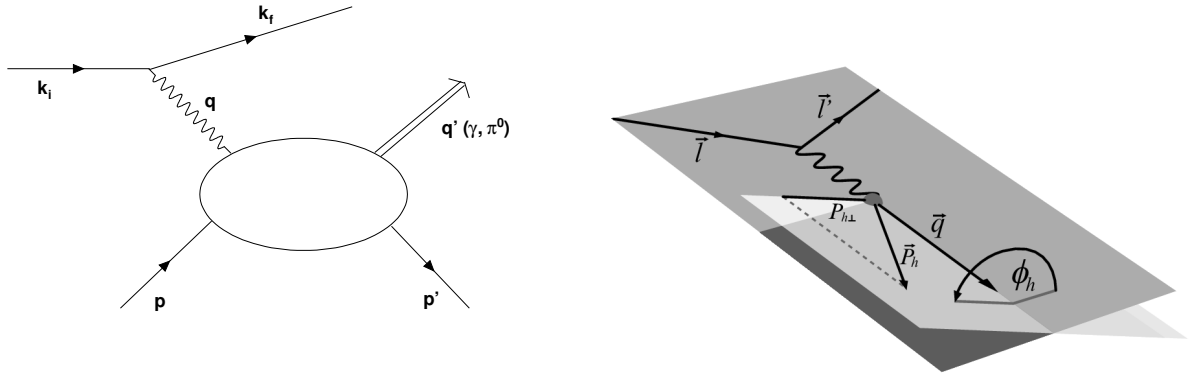
Figure 1.5: Left: Diagram of electroproduction off a proton. Right: Definition of ϕ, the angle between the leptonic and the hadronic plane. On this figure, $P_h = q'$, $l = k_i$ and $l' = k_f$.

We focus on the photon and π^0 electroproduction for which the final state is composed of the scattered electron, the recoil proton and a photon or a π^0.

We define ϕ the angle between the leptonic plane, formed by the scattered electron and the virtual photon, and the hadronic plane defined by the virtual photon and the recoiled proton (Fig. 1.5). We follow the Trento convention [16] defined such as:

$$\cos\phi = \frac{(\mathbf{q} \times \mathbf{k_i})}{|\mathbf{q} \times \mathbf{k_i}|} \cdot \frac{(\mathbf{q} \times \mathbf{q'})}{|\mathbf{q} \times \mathbf{q'}|} \ , \tag{1.36}$$

$$\sin\phi = \frac{(\mathbf{k_i} \times \mathbf{q'}) \cdot \mathbf{q}}{|\mathbf{q} \times \mathbf{k_i}||\mathbf{q} \times \mathbf{q'}|} \ , \tag{1.37}$$

The GPDs parametrize the cross sections of deep exclusive processes but in a more involved way than PDFs for DIS. Indeed we have seen that the DIS cross section factorizes into two parts: a term describing the electron-quark scattering and the PDF related to the quark content in the nucleon. GPDs are related to deep exclusive processes based also on the concept of *factorization*. We will sketch the principle of factorization and derive another essential property of the GPDs. Finally we will describe how GPDs enter the photon and π^0 electroproduction cross sections.

1.4.1 Light cone dominance

When computing the amplitude for DVCS (but also DVMP or DIS), we obtain a δ function for momentum conservation involving the 4-momentum of the virtual photon.

$$\delta^4(q) = \frac{1}{(2\pi)^4} \int d^4z e^{iqz} \ . \tag{1.38}$$

Applying the equality 1.38 to this δ function, the amplitude is given as an integral of e^{iqz}. In the proton rest frame, with the z-axis going in the opposite direction with respect to the virtual photon, we have:

$$q = \left(\frac{Q^2}{2Mx_B}, 0, 0, -\frac{Q^2}{2Mx_B}\sqrt{1 + 4Mx_B/Q^2} \right) \ . \tag{1.39}$$

In the Bjorken limit, Eq. 1.38 gives a non-vanishing result only when:

$$z^- \quad \sim 1/Mx_B \ , \tag{1.40}$$

$$z^+ \quad \sim Mx_B/Q^2 \ . \tag{1.41}$$

As causality ensures that $z^2 > 0$, we have $z_\perp < z^- z^+ \sim \frac{1}{Q^2}$. Therefore, in the Bjorken limit, only the space-time regions close to the light cone contribute to the amplitude.

1.4.2 Factorization and twist

The factorization has been proven rigorously at leading-twist for DVCS. In the case of deep virtual meson production, only with longitudinally polarized photon. The following short explanation of factorization is based on DVCS which is the simplest process.

The DVCS amplitude is given by:

$$\mathcal{T}_{DVCS} = i \int d^4 z e^{iqz} \langle p' | T\{j_\mu(z) j_\nu(0)\} | p \rangle, \tag{1.42}$$

with $j_\mu(z)$ the electromagnetic current of quarks defined such as:

$$j_\mu(z) = \sum_f e_f \bar{\Psi}_f(z) \gamma_\mu \Psi_f(z), \tag{1.43}$$

In the Bjorken limit, $z^2 \to 0$ and the correlator of the electromagnetic currents becomes singular. To describe the singularity of the product of operators, Wilson derived the operator product expansion (OPE). It is a Taylor expansion of the product of currents using local operators. Therefore we can write the correlator:

$$T\{j_\mu(z) j_\nu(0)\} \overset{z^2 \to 0}{\sim} \sum_{\tau=2}^{\infty} \sum_{n=0}^{\infty} C_{\tau,n}(z^2) z^{\mu_1} z^{\mu_2} ... z^{\mu_n} \hat{\mathcal{O}}^\tau_{\mu_1...\mu_n}(0), \tag{1.44}$$

$\hat{\mathcal{O}}^\tau_{\mu_1...\mu_n}(0)$ are a basis of local operators, $z^{(\mu_1} z^{\mu_2} ... z^{\mu_n)}$ traceless homogeneous polynomials. $C_{\tau,n}(z^2)$ are coefficients carrying the singularity. They evolve as:

$$C_{\tau,n}(z^2) \overset{z^2 \to 0}{\sim} \left(\frac{1}{z^2} \right)^{(n - d_{\mathcal{O}} - 2d_j)/2} \tag{1.45}$$

with $d_{\mathcal{O}}$ the mass dimension of the operator $\hat{\mathcal{O}}^\tau_{\mu_1...\mu_n}$, and n its spin. $\tau = d_{\mathcal{O}} - n$ is called *twist* and the most important singularities are carried by operators with the minimal twist $\tau=2$. The GPDs introduced in the previous section are associated with the lowest twist operators. The soft part, or the nucleon medium, is described by the operators. The hard/high energy part is given by the coefficients $C_{\tau,n}(z^2)$ which are calculated perturbatively in powers of α_s (Figure 1.7).

To separate the soft part from the hard part, a factorization scale μ_F is introduced. The GPDs and the coefficient describing the hard part depends on it such that the observable is μ_F-independent.

Therefore, the difference between all the exclusive reactions such as DVCS or DVMP lies in the hard scattering kernel, the GPDs being factorized in the soft part. The GPDs are therefore considered *universal*. As a consequence, we can combine the different reactions to get a unified picture of the nucleon.

When $Q^2 \to \infty$, the leading-twist contribution dominates and higher-twist contributions can be safely neglected. In practice, the experiments run at Q^2-values of a few GeV^2 and higher-twist contributions might appear with increasing ratios $\frac{M^2}{Q^2}$ and $\frac{-t}{Q^2}$.
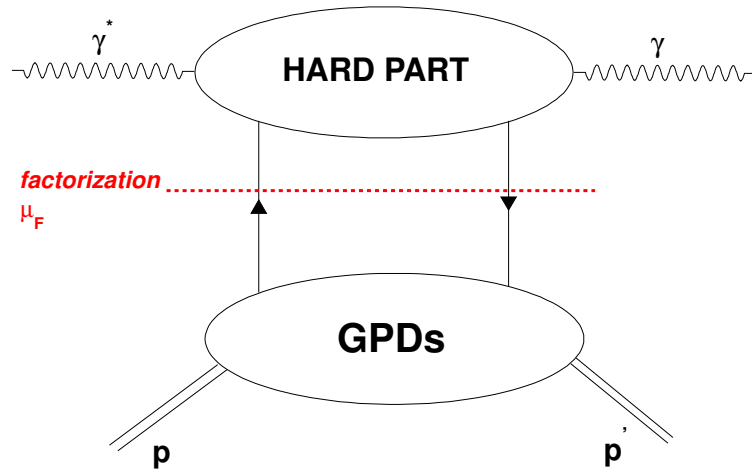
Figure 1.6: The factorization separates a hard scattering kernel computable perturbatively from a low energy part described by the GPDs with respect to a factorization scale μ_F.
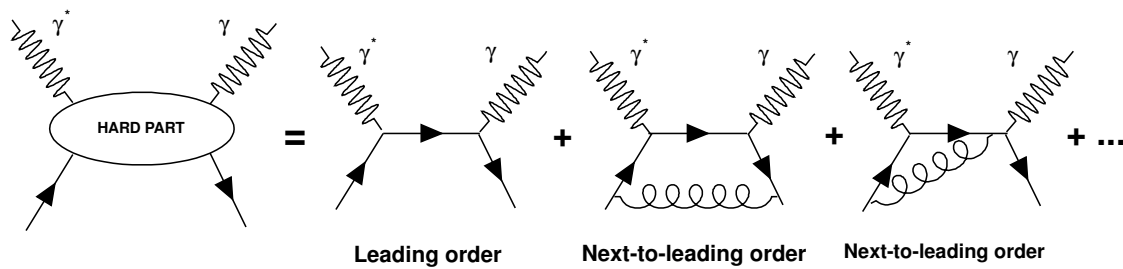
Figure 1.7: The hard scattering kernel is computed perturbatively in α_s.

1.4.3 Deeply virtual Compton scattering

Photon electroproduction arises from the interference of two processes:

- The Bethe-Heitler (BH) process where the photon is emitted by either the incoming or outgoing electrons. In this well-known process, the structure of the nucleon is encoded by the FFs.

- The DVCS process where the photon is emitted by the nucleon. At leading-twist and leading-order, it is described by the handbag diagram (Fig 1.8).

As a consequence, the photon electroproduction cross section reads:

$$\frac{d^5\sigma(\lambda, \pm e)}{dQ^2 dx_B dt d\phi d\phi_e} = \frac{d\sigma_0}{dQ^2 dx_B} \frac{1}{e^6} \times \left[\left| \mathcal{T}^{BH} \right|^2 + \left| \mathcal{T}^{DVCS} \right|^2 \mp \mathcal{I} \right] , \qquad (1.46)$$

where $\mathcal{T}_{DVCS}$ is the DVCS amplitude, $\mathcal{T}_{BH}$ the BH amplitude and $\mathcal{I}$ the interference term between the two processes. e is the electron charge, λ the beam helicity. Then we have:

$$\frac{d\sigma_0}{dQ^2 dx_B} = \frac{\alpha^3}{16\pi^2 (s - M^2)^2 x_B} \frac{1}{\sqrt{1 + \epsilon^2}} , \qquad (1.47)$$

$$\epsilon^2 = 4M^2 x_B^2 / Q^2 , \qquad (1.48)$$

$$s = 2ME + M^2 . \qquad (1.49)$$
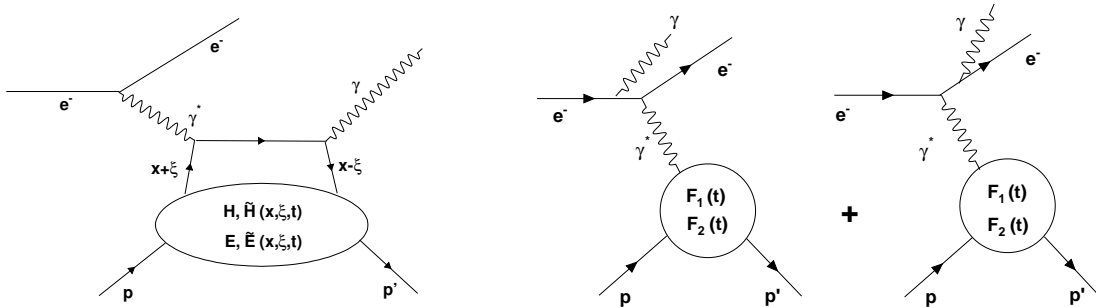
Figure 1.8: On the left, diagram of DVCS at leading-twist, traditionally called handbag diagram. The virtual photon interacts with a single quark inside the nucleon, which then emits a real photon. All vertices in the short distance part are electromagnetic, making the DVCS the golden channel to extract information about GPDs. The two diagrams on the right represents the Bethe-Heitler process with the photon emitted by the electron.

1.4.3.1 Compton Form Factors

The GPDs parametrize the DVCS amplitude but are not directly accessible through the cross section. Indeed, whereas ξ and t are kinematic variables defined by the scattered electron and photon, x is integrated over. The DVCS amplitude is given, at leading-order, by integrals of the form:

$$\int_{-1}^{1} \frac{H(x, \xi, t)}{x - \xi + i\epsilon} dx = \mathcal{P} \int_{-1}^{1} \frac{H(x, \xi, t)}{x - \xi} dx - i\pi H(\xi, \xi, t) , \qquad (1.50)$$

where $\frac{1}{x-\xi+i\epsilon}$ is the bare quark propagator. By taking into account the crossed diagram, we define the Compton Form Factors such as:

$$\mathcal{H} = \int_{-1}^{1} H(x,\xi,t) \left(\frac{1}{\xi - x - i\epsilon} - \frac{1}{\xi + x - i\epsilon} \right) dx \ . \tag{1.51}$$

By reducing the integration range from [-1,1] to [0,1] and gathering imaginary and real parts, we define 8 GPD-related quantities directly connected to the DVCS amplitude (same sign conventions for E and $\tilde{E}$):

$$\Re e \mathcal{H}(\xi,t) = \mathcal{P} \int_{0}^{1} \left[H(x,\xi,t) - H(-x,\xi,t) \right] C^{+}(x,\xi) dx, \tag{1.52}$$

$$\Im m \mathcal{H}(\xi,t) = \pi \left(H(\xi,\xi,t) - H(-\xi,\xi,t) \right), \tag{1.53}$$

$$\Re e \tilde{\mathcal{H}}(\xi,t) = \mathcal{P} \int_{0}^{1} \left[\tilde{H}(x,\xi,t) + \tilde{H}(-x,\xi,t) \right] C^{-}(x,\xi) dx, \tag{1.54}$$

$$\Im m \tilde{\mathcal{H}}(\xi,t) = \pi \left(\tilde{H}(\xi,\xi,t) + \tilde{H}(-\xi,\xi,t) \right), \tag{1.55}$$

$$\tag{1.56}$$

where $C^{\pm}$ is :

$$C^{\pm}(x,\xi) = \frac{1}{x - \xi} \pm \frac{1}{x + \xi} \ . \tag{1.57}$$

1.4.3.2 Higher twists and CFF extraction from DVCS

The photon electroproduction cross section depends on the angle ϕ. Mueller and Belitsky performed an harmonic expansion of $|\mathcal{T}_{DVCS}|^2$, $|\mathcal{T}_{BH}|^2$ and $\mathcal{I}$ as a function of ϕ up to twist-3. Since it is central to our analysis, we are going to review this expansion for the unpolarized and beam helicity dependent cross sections. Further details can be found in [17].

1.4.3.2.1 The squared Bethe-Heitler amplitude The Bethe-Heitler process is a pure QED process. Its cross section has been calculated and expressed as a harmonic expansion as a function of ϕ [18]:

$$|\mathcal{T}_{BH}|^2 = \frac{e^6}{y^2 x_B^2 [1 + 4x_B^2 M^2/Q^2]^2 t P_1(\phi) P_2(\phi)} \left\{ c_0^{BH} + \sum_{n=1}^{2} c_n^{BH} cos(n\phi) + s_1^{BH} sin(\phi) \right\}, \tag{1.58}$$

with

$$J = \left(1 - y - \frac{y\epsilon^2}{2} \right) \left(1 + \frac{t}{Q^2} \right) - (1 - x_B)(2 - y)\frac{t}{Q^2}, \tag{1.59}$$

$$P_1(\phi) = -\frac{1}{y(1 + \epsilon^2)} \{ J + 2K \cos(\phi) \}, \tag{1.60}$$

$$P_2(\phi) = 1 + \frac{t}{Q^2} + \frac{1}{y(1 + \epsilon^2)} \{ J + 2K \cos(\phi) \}, \tag{1.61}$$

where $y = \frac{\nu}{E}$ and $\epsilon = \frac{2Mx_B}{Q}$. The kinematic coefficients can be found in [18].

1.4.3.2.2 The squared DVCS amplitude The squared DVCS amplitude contribution has been calculated up to twist-3. When performing the harmonic expansion as a function of ϕ, it reads:

$$|\mathcal{T}_{DVCS}|^2 = \frac{e^6}{y^2 Q^2} \left\{ c_0^{DVCS} + \sum_{n=1}^{2} c_n^{DVCS} cos(n\phi) + \lambda s_n^{DVCS} sin(n\phi) \right\} \tag{1.62}$$

where λ refers to the beam helicity. The c_i^{DVCS} and s_i^{DVCS} coefficients are given by bilinear combinations of CFFs. For example we have:

$$c_0^{DVCS} = 2\frac{2 - 2y + y^2 + \frac{\epsilon^2}{2}y^2}{1 + \epsilon^2}\mathcal{C}_{unp}^{DVCS}(\mathcal{F}, \mathcal{F}^*),$$ (1.63)

$$\mathcal{C}_{unp}^{DVCS}(\mathcal{F}, \mathcal{F}^*) = 4(1 - x_B)\mathcal{H}\mathcal{H}^* + 4\left(1 - x_B + \frac{2Q^2 + t}{Q^2 + x_B t}\frac{\epsilon^2}{4}\right)\tilde{\mathcal{H}}\tilde{\mathcal{H}}^* + \cdots$$ (1.64)

The different functions contributing to the squared DVCS amplitude for an unpolarized target are listed in the table 1.1.

	Order	ϕ-**dependence**
$\mathcal{C}_{unp}^{DVCS}(\mathcal{F}, \mathcal{F}^*)$	twist-2	constant
$\mathcal{C}_{unp}^{DVCS}(\mathcal{F}_{eff}, \mathcal{F}_{eff}^*)$	twist-3	constant
$\Re e[\mathcal{C}_{unp}^{DVCS}(\mathcal{F}_{eff}, \mathcal{F}^*)]$	twist-3/twist-2	$\cos\phi$
$\Im m[\mathcal{C}_{unp}^{DVCS}(\mathcal{F}_{eff}, \mathcal{F}^*)]$	twist-3/twist-2	$\sin\phi$

Table 1.1: GPD content of the DVCS^2 term up to twist-3.

1.4.3.2.3 The interference between the Bethe-Heitler and the DVCS processes

The DVCS squared amplitude is given by bilinear combinations of CFFs. In other words we mainly get information about the modulus of the CFFs. We need information about the phase to extract the CFFs and it cannot be provided by the squared DVCS amplitude. The Bethe-Heitler/DVCS interference term makes the photon electroproduction unique because it is parametrized by the real and imaginary parts of the CFFs. For instance, the unpolarized cross section is sensitive to the real part of $\mathcal{H}$ whereas we extract its imaginary part from the difference of cross sections for opposite beam helicities.

Using the same method as for the squared amplitude of DVCS and BH, we write:

$$I = \frac{\pm e^6}{x_B y^3 t P_1(\phi) P_2(\phi)}\left\{c_0^I + \sum_{n=1}^{3} c_n^I \cos(n\phi) + \lambda s_n^I \sin(n\phi)\right\}.$$ (1.65)

The Fourier coefficient are then given by:

$$c_n^I = C_{++}(n)\ \Re e\mathcal{C}_{++}^I(n|\mathcal{F}) + C_{0+}(n)\ \Re e\mathcal{C}_{0+}^I(n|\mathcal{F}_{eff}),$$ (1.66)

$$s_n^I = S_{++}(n)\ \Im m\mathcal{S}_{++}^I(n|\mathcal{F}) + S_{0+}(n)\ \Im m\mathcal{S}_{0+}^I(n|\mathcal{F}_{eff}).$$ (1.67)

The $C_{++}(n)$, $S_{++}(n)$, $C_{0+}(n)$ and $S_{0+}(n)$ are only kinematical factors depending on Q^2, t, x_B, ϕ. And $\mathcal{C}_{0+}^I(n|\mathcal{F}_{eff})$ and $\mathcal{C}_{++}^I(n|\mathcal{F})$ are defined such as:

$$\mathcal{C}_{++}^I(n|\mathcal{F}) = \mathcal{C}^I(\mathcal{F}) + \frac{C_{++}^V(n)}{C_{++}(n)}\mathcal{C}^{I,V}(\mathcal{F}) + \frac{C_{++}^A(n)}{C_{++}(n)}\mathcal{C}^{I,A}(\mathcal{F}),$$ (1.68)

$$\mathcal{C}_{0+}^I(n|\mathcal{F}_{eff}) = \frac{\sqrt{2}}{2 - x_B}\frac{\widetilde{K}}{Q}\left[\mathcal{C}^I(\mathcal{F}_{eff}) + \frac{C_{0+}^V(n)}{C_{0+}(n)}\mathcal{C}^{I,V}(\mathcal{F}_{eff}) + \frac{C_{0+}^A(n)}{C_{0+}(n)}\mathcal{C}^{I,A}(\mathcal{F}_{eff})\right],$$ (1.69)

Finally, the CFFs are encapsulated in $\mathcal{C}^I$, $\mathcal{C}^{I,V}$, $\mathcal{C}^{I,A}$:

$$\mathcal{C}^I_{unp}(\mathcal{F}) = F_1\mathcal{H} - \frac{t}{4M^2}F_2\mathcal{E} + \frac{x_B}{2 - x_B + x_B\frac{t}{Q^2}}(F_1 + F_2)\widetilde{\mathcal{H}}, \tag{1.70}$$

$$\mathcal{C}^{I,V}_{unp}(\mathcal{F}) = \frac{x_B}{2 - x_B + x_B\frac{t}{Q^2}}(F_1 + F_2)(\mathcal{H} + \mathcal{E}), \tag{1.71}$$

$$\mathcal{C}^{I,A}_{unp}(\mathcal{F}) = \frac{x_B}{2 - x_B + x_B\frac{t}{Q^2}}(F_1 + F_2)\widetilde{\mathcal{H}}. \tag{1.72}$$

We notice that the form factors F_1 and F_2 are associated with the CFFs because they parametrize the Bethe-Heitler process.

	Order	ϕ-**dependence**
$\Re e\ \mathcal{C}^I_{unp}(\mathcal{F})$	twist-2	$\cos\phi$
$\Re e\ \mathcal{C}^{I,V}_{unp}(\mathcal{F})$	"twist-3"	constant
$\Re e\ \mathcal{C}^{I,A}_{unp}(\mathcal{F})$	"twist-3"	$\cos\phi$
$\Re e\ \mathcal{C}^I_{unp}(\mathcal{F}_{eff})$	twist-3	$\cos 2\phi$
$\Im m\ \mathcal{C}^I_{unp}(\mathcal{F})$	twist-2	$\sin\phi$
$\Im m\ \mathcal{C}^{I,V}_{unp}(\mathcal{F})$	"twist-3"	$\sin\phi$
$\Im m\ \mathcal{C}^{I,A}_{unp}(\mathcal{F})$	"twist-3"	$\sin\phi$
$\Im m\ \mathcal{C}^I_{unp}(\mathcal{F}_{eff})$	twist-3	$\sin 2\phi$

Table 1.2: GPD content of the interference term up to twist-3. "twist-3" means *kinematically suppressed like a twist-3*.

1.4.4   Deep π^0 electroproduction

1.4.4.1   Deeply virtual meson production

Deeply virtual meson production is also a key process to study the nucleon. The DVMP cross section can be decomposed into responses according to the polarization states of the virtual photon and their interferences.

$$\frac{d^4\sigma}{dtd\phi dQ^2 dx_B} = \frac{1}{2\pi}\Gamma_{\gamma^*}(Q^2, x_B, E_e)\left[\frac{d\sigma_T}{dt} + \epsilon^*\frac{d\sigma_L}{dt} + \sqrt{2\epsilon^*(1 + \epsilon^*)}\frac{d\sigma_{TL}}{dt}cos(\phi) + \epsilon^*\frac{d\sigma_{TT}}{dt}cos(2\phi)\right], \tag{1.73}$$

$$\Gamma_{\gamma^*}(Q^2, x_B, E_e) = \frac{\alpha}{8\pi}\frac{Q^2}{M^2E_e^2}\frac{1 - x_B}{x_B^3}\frac{1}{1 - \epsilon^*}, \tag{1.74}$$

$$\epsilon^* = \frac{1 - y - \frac{Q^2}{4E_e^2}}{1 - y + \frac{y^2}{2} + \frac{Q^2}{4E_e^2}}, \tag{1.75}$$

where $\Gamma_{\gamma^*}(Q^2, x_B, E_e)$ represents the flux of virtual photons, and ϵ^* its degree of polarization. σ_L and σ_T are the responses to a photon with longitudinal and tranverse polarizations. σ_{TL} is the interference between the longitudinal and the transverse responses, σ_{TT} the interference between the two transverse polarizations.

Unlike DVCS, the hard part involves strong vertices and an additional non-perturbative object, the distribution amplitude, to describe the structure of the produced meson.

$$\Phi_\pi(x) = \int\frac{dz^-}{2\pi}e^{i(2x-1)P^+\frac{z^-}{2}}\langle\pi, P|\bar{\Psi}\left(-\frac{z}{2}\right)\gamma\cdot n\gamma_5\Psi\left(\frac{z}{2}\right)|0\rangle\big|_{z^+=\vec{z}_\perp=0}. \tag{1.76}$$
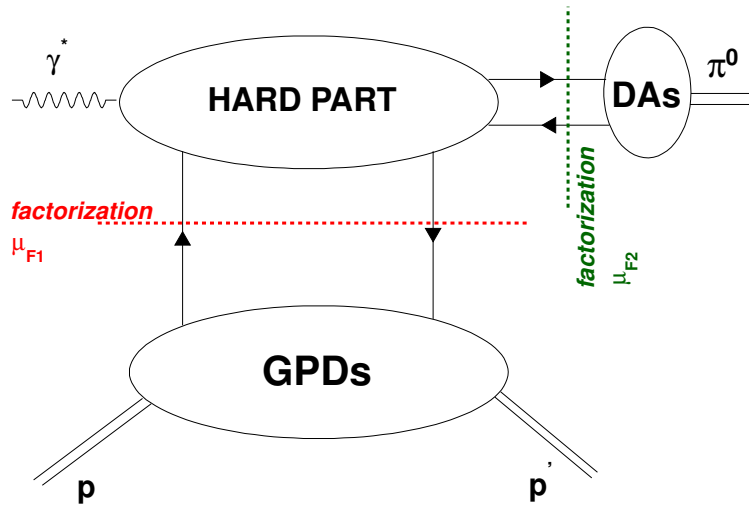
Figure 1.9: Two factorizations are needed to describe π^0 electroproduction with GPDs. The factorization scales μ_{F1} and μ_{F2} are not necessarily equal.
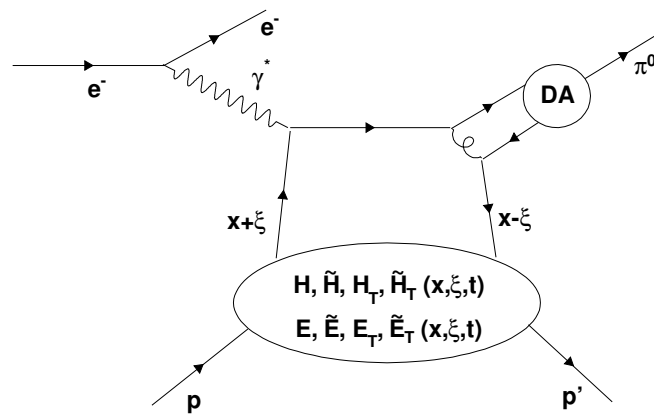
Figure 1.10: One of the diagrams for π^0 electroproduction at leading-twist, leading-order. Unlike DVCS, there are strong vertices in the hard part and one needs to introduce another non-perturbative object called distribution amplitude (DA), which describes the structure of the meson. Note that factorization has been proven only for longitudinally polarized photons.

Because of this additional subtlety, the factorization theorem has been proven only for longitudinally polarized virtual photons. At leading-twist, the longitudinal amplitude involves the unpolarized GPDs H and E for vector mesons, $\tilde{H}$ and $\tilde{E}$ for pseudoscalar mesons. For π^0 at leading-twist and leading-order, the longitudinal amplitude reads:

$$\mathcal{M}_{\pi^0}^L = -ie\frac{4}{9}\frac{1}{\sqrt{Q^2}}4\pi\alpha_S \left[\int_0^1 dz\frac{\Phi_{\pi^0}(z)}{z}\right] \times \frac{1}{2}\int_{-1}^1 dx\left[\frac{1}{x-\xi+i\epsilon}+\frac{1}{x+\xi+i\epsilon}\right]$$
$$\left\{\tilde{H}_{\pi^0}^p(x,\xi,t)\bar{N}(p')\slashed{n}\gamma^5 N(p) + \frac{\xi}{2M}\tilde{E}_{\pi^0}^p(x,\xi,t)\bar{N}(p')\gamma^5 N(p)\right\}, \quad (1.77)$$

where Φ_{π^0} is the neutral pion twist-2 asymptotic distribution amplitude, $(\tilde{H}_{\pi^0}^p, \tilde{E}_{\pi^0}^p)$ linear combinations of u/d-GPDs in proton defined such as:

$$\Phi_{\pi^0}(z) = \sqrt{2}f_\pi 6z(1-z), \quad (1.78)$$

$$\tilde{H}_{\pi^0}^p(x,\xi,t) = \frac{1}{\sqrt{2}}\left\{\frac{2}{3}\tilde{H}_{\pi^0}^{u/p} - \left(-\frac{1}{3}\right)\tilde{H}_{\pi^0}^{d/p}\right\}, \quad (1.79)$$

$$\tilde{E}_{\pi^0}^p(x,\xi,t) = \frac{1}{\sqrt{2}}\left\{\frac{2}{3}\tilde{E}_{\pi^0}^{u/p} - \left(-\frac{1}{3}\right)\tilde{E}_{\pi^0}^{d/p}\right\}, \quad (1.80)$$

with $f_\pi=0.0924$ GeV and $z = (p\cdot q')/(p\cdot q)$.

Using models of $\tilde{H}$ and $\tilde{E}$ adjusted on DVCS data, the longitudinal response for π^0 electroproduction is expected to be small.

1.4.4.2   Beyond leading-twist: Twist-3 DA and transversity GPDs

Although factorization has not yet been proven for transverse virtual photons in DVMP, Goloskokov *et al.* have elaborated a model [19][20] involving the transversity GPDs. As the transversity GPDs are chiral-odd, they cannot couple to the twist-2 DA of the pion which is chiral-even. Chiral-odd DAs appear at twist-3 when considering the transverse momentum of the quark entering the meson, with respect to the meson momentum. Although the twist-3 contributions are kinematically suppressed with respect to twist-2 ones, the twist-3 DAs include a factor $\mu_\pi = \frac{m_\pi^2}{m_u+m_d}$ (with m_u and m_d are the bare quark masses) which does not appear in the twist-2 DA. As a consequence, this factor boosts the transverse response and significantly increases the π^0 electroproduction cross section. It is interesting to note that, within this model, we can directly access the information on H_T, $\tilde{H}_T$ and E_T by measuring σ_T and σ_{TT}.

$$\frac{d\sigma_T}{dt} = \frac{4\pi\alpha}{2k'}\frac{\mu_\pi^2}{Q^8}\left[(1-\xi^2)|\langle H_T\rangle|^2 - \frac{t'}{8m^2}|\langle 2\tilde{H}_T+E_T\rangle|^2\right], \quad (1.81)$$

$$\frac{d\sigma_{TT}}{dt} = \frac{4\pi\alpha}{2k'}\frac{\mu_\pi^2}{Q^8}\frac{t'}{16m^2}|\langle 2\tilde{H}_T+E_T\rangle|^2, \quad (1.82)$$

where k' is a phase space factor given by:

$$k' = \frac{16\pi}{Q^2}\left(\frac{1}{x_B}-1\right)\sqrt{(W^2-m^2)^2+Q^4+2W^2Q^2+2Q^2m^2}. \quad (1.83)$$

Finally $\langle F\rangle$ stands for the following convolution of a GPD F with the hard scattering kernel $\mathcal{D}_{\mu'\lambda'\mu\lambda}$ summed over the incoming quark helicity λ.

$$\langle F\rangle = \sum_\lambda \int_{-1}^1 dx\mathcal{D}_{\mu'\lambda'\mu\lambda}F, \quad (1.84)$$

λ, λ' are the helicity of the incoming and outgoing quarks, μ the helicity of the incident electron. μ' is the helicity of the produced meson which is 0 for pseudo-scalar mesons.

1.5 Experimental status

1.5.1 DVCS results

A worldwide experimental program has been developed in order to measure DVCS observables in different kinematical regions (Figure 1.11). In this review, we are not going to talk about the Jefferson Lab-Hall A experiments since they are the topic of this thesis.
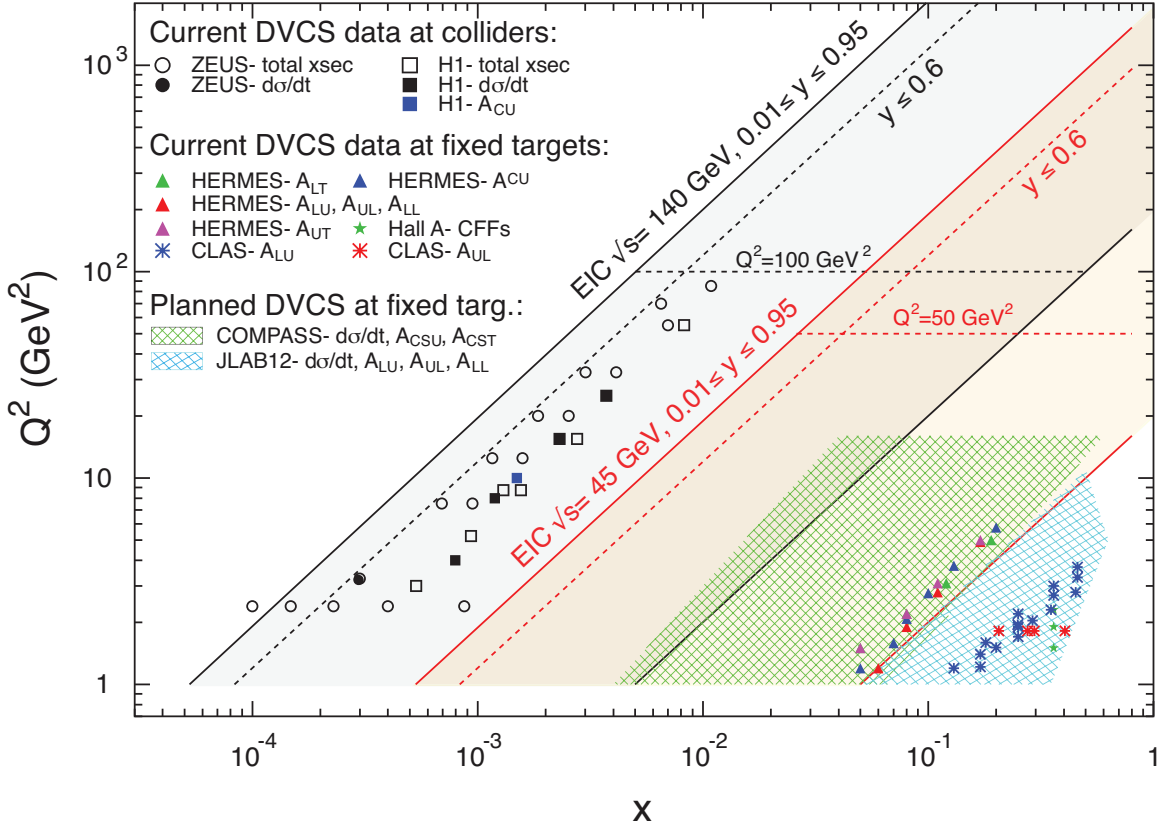
Figure 1.11: Q^2 versus x_B for the past and future experiments [21]. Unpolarized and beam-helicity dependent cross sections have recently published by the CLAS [22] and Hall A [23] collaborations.

1.5.1.1 H1 and ZEUS

The H1 and ZEUS experiments were located at DESY laboratory in Hamburg, Germany and ran until 2007. They were collider experiments between an electron/positron beam and a proton beam provided by the HERA (Hadron-Elektron-Ring-Anlage) accelerator. H1 and ZEUS measured total ([24][25]) and t-differential ([26][27]) cross sections for Q^2 up to 25 GeV^2 and W up to 100 GeV. Thanks to the ability to use both electrons and positrons, the H1 collaboration also extracted beam charge asymmetries [28].

The factorization of the cross section and the dominance of gluon GPDs at low x_B were demonstrated with these data.

1.5.1.2 HERMES

The HERMES spectrometer also installed on the HERA accelerator was a fixed target experiment using an internal gaseous target. The HERMES collaboration measured DVCS

observables in the Q^2 range from 1 to $\sim$6 GeV^2 and x_B from 0.04 to 0.2. For the first measurements, exclusivity was ensured by a missing-mass cut $M^2_{ep \to e\gamma X}$. For the last run period until June 2007, a recoil detector was added to the spectrometer in order to reduce systematic errors related to exclusivity [29].

The target could be polarized both longitudinally and transversely. Combining the target and beam polarizations, using electron and positrons, HERMES measured an almost complete set of asymmetries, but no cross sections. This very complete set of observables is a convenient way to unfold the different CFF contributions [30][31][32] (see section 1.4.3.2).

1.5.1.3 JLab-CLAS results

CLAS (*CEBAF large acceptance spectrometer*) is installed in the Hall B of Jefferson Laboratory in Virginia, USA. As its name indicates, CLAS covers a large solid angle, compared to Hall A for instance, albeit at a reduced luminosity. The CLAS collaboration measured DVCS observables over a wide range in Q^2 (between 1 and $\sim$4.8 GeV^2) and x_B (between 0.1 to almost 0.6). The longitudinally polarized electron beam from the accelerator interacts with a liquid hydrogen target to study beam spin asymmetries [33]. Later, data on longitudinally polarized NH$_3$ target were taken to extract target spin [34] and double spin asymmetries [35]. Very recently, the CLAS collaboration released unpolarized and beam-helicity-dependent cross sections [22].

Within their statistical accuracy, HERMES and CLAS data are well described by leading-twist predictions. Note that there is a disagreement between CLAS and HERMES data concerning the $\sin 2\phi$ harmonic of the asymmetry unpolarized beam on a longitudinally polarized target (A_{UL}): whereas CLAS find a result compatible with 0, HERMES finds a sizeable $\sin 2\phi$ harmonics which cannot be reproduced by only considering the leading-twist contribution [36].

1.5.1.4 Future experiments

As seen on figure 1.11, available data are spread over a large kinematic area but there are some domain with no data:

- A large area between $x_B=10^{-3}$ and $x_B=10^{-2}$ where no data are available yet. But in 2016, the Common Muon and Proton Apparatus for Structure and Spectroscopy (COMPASS) experiment will measure DVCS cross sections in this region, connecting the fixed target domain to the high energy collider one. A 160 GeV muon beam interacts with a 2 m-long liquid hydrogen target. A recoil detector, CAMERA, detects the proton. The photon will be detected in a set of three calorimeters. The scattered muon will be detected in the standard COMPASS spectrometer.

- The high x$_B$-region suffers from a lack of statistically significant data. Nevertheless the upgrade of CEBAF to 12 GeV allows for high accuracy experiments in this kinematical region. In particular, a dedicated experiment started in Hall A at the end of 2014. After the CLAS spectrometer is upgraded with a new detector package and new magnets, a number of experiments will also take data in this enlarged kinematical domain. Finally, Hall C of Jefferson Laboratory will perform the Rosenbltuh separation of photon and π^0 electroproduction cross sections around 2020, accessing higher Q^2 and x_B values thanks to the High Momentum Spectrometer.

- Last but not least, it is the strong desire of the hadronic physics community worldwide to build the ultimate accelerator in order to study nucleon structure: The Electron-Ion Collider (EIC) will use intense and polarized beams of electrons and ions in order
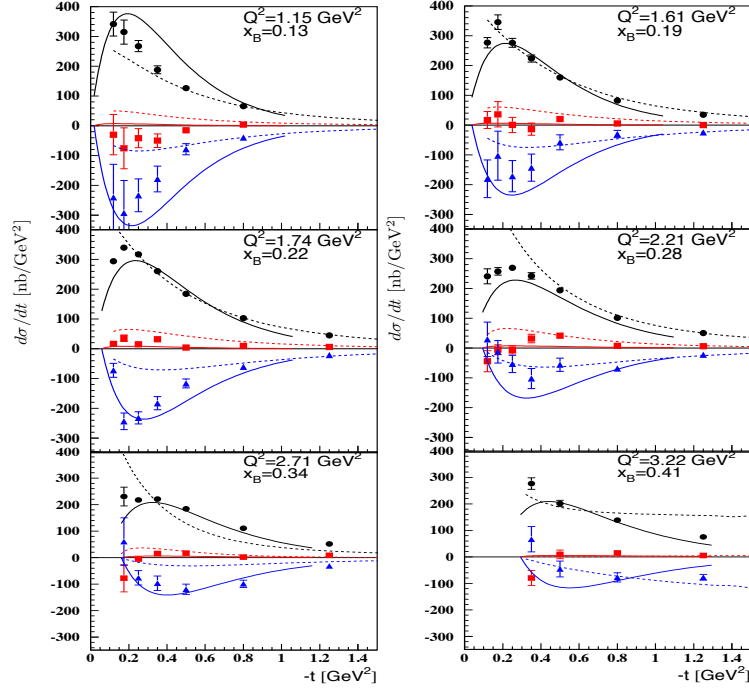
Figure 1.12: $\sigma_T + \epsilon^*\sigma_L$ (back points), σ_{TT} (blue points) and σ_{TL} (red points) extracted by the CLAS collaboration [38]. The solid curves represent Goloskokov and Kroll's model [20], able to reproduce the behaviour of the cross sections. The dashed lines represent prediction of the model developed by Goldstein and Liuti [39].

to study gluon-dominated matter. In particular, the ability to transversally polarize protons will help tremendously to pinpoint the elusive GPD E.

1.5.2 Pion electroproduction data

Measurements of pion electroproduction cross sections have been carried out in the different JLab experimental hall. We focus on the unpolarized cross section results of π^0. We also dedicate a section to the Rosenbluth separation performed on the π^+ electroproduction.

1.5.2.1 π^0 electroproduction data

Two experiments have measured π^0 electroproduction cross sections in the valence region. First results were published by the Hall A collaboration [37]. These measurements have then been extended in a wider kinematical range by the CLAS collaboration [38] (Figure 1.12). Whereas σ_L is expected small by twist-2 GPD models, both experiments measured high unpolarized cross sections potentially indicating a large transverse contribution.

The large transverse-transverse interference term σ_{TT} also supports the assumption of a large σ_T-contribution.

1.5.2.2 Rosenbluth separation on π^+ electroproduction cross section

A L/T separation has been performed on $ep \rightarrow en\pi^+$ in the Hall C of Jefferson Lab [40]. The longitudinal and transverse contributions have both been found significant (Figure 1.13), even at high Q^2, whereas the transverse response is supposed to be suppressed by $1/Q^2$ with respect to the longitudinal one. Although σ_L is expected to be small for π^0, it is enhanced in the case of π^+ by an additional channel. This channel consists of an exchange of a virtual
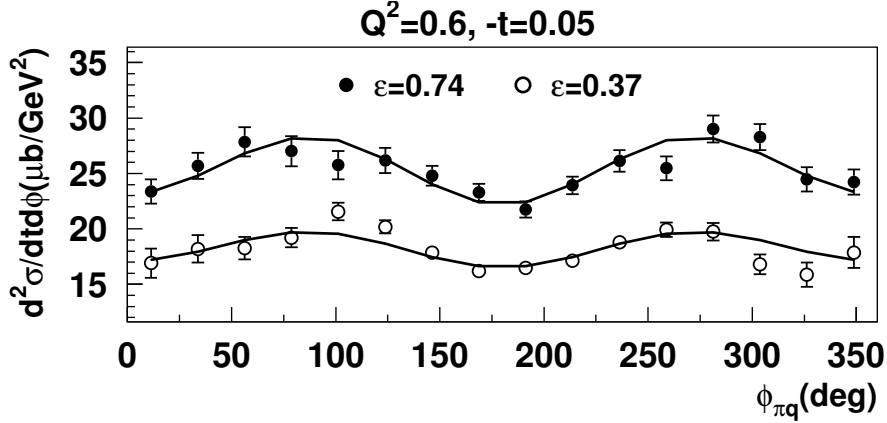
Figure 1.13: $\gamma^* p \to n\pi^+$ extracted at two ϵ^*'s values [41]. Because σ_L and $\Delta\epsilon$ are important, the cross section has increased significantly.

π^+ between the virtual photon and the nucleon. It can be seen as virtual photon scattering off the pion cloud in the proton. As a consequence, the associated amplitude has $(t - m_\pi)$ in its denominator, coming from the pion propagator, enhancing the longitudinal response. Finally, the Q^2-dependence of σ_L was in agreement with the model whereas σ_T was found to scale down much slower than the expected $\frac{1}{Q^8}$.

1.6 The E00-110 and E07-007 experiments

In this thesis, we will describe and analyze two experiments which ran in the Hall A of Jefferson Lab. We may consider them as two run periods of a same experiment. They both studied photon and π^0 electroproduction. We first introduce the 2004 [42] and then the 2010 [43] run periods.

1.6.1 The E00-110 experiment: the 2004 run period

The first run period was in 2004. Its purpose was to perform a Q^2-scan at fixed x_B of the beam helicity dependent DVCS cross section to test the scaling of DVCS [44]. The kinematical settings are listed in Table 1.3. In addition, an extra set of unpolarized cross sections for the kinematics with the highest value of Q^2 was extracted. Indeed it was possible to evaluate the π^0 contamination (explained later in the thesis) for the highest Q^2 setting, hinting that π^0 electroproduction could be extracted.

Setting	k' (GeV/c)	θ_e (°)	Q^2 (GeV^2)	x_B	θ_q (°)	W (GeV)	E_γ (GeV)
2004-Kin1	3.53	15.6	1.5	0.36	−22.3	1.9	2.14
2004-Kin2	2.94	19.3	1.9	0.36	−18.3	2.0	2.73
2004-Kin3	2.34	23.8	2.3	0.36	−14.8	2.2	3.32

Table 1.3: Experimental $ep \to ep\gamma$ kinematics, for incident beam energy $E_b = 5.7572$ GeV. θ_q is the central value of the **q**-vector direction. E_γ is the photon energy for $t = t_{\min}$. Note that only the average kinematic values for each setting are listed in this table : in order to minimize systematic bin centering effects, we actually used the kinematic of each bin in x_B, Q^2 and t according to their average value in the bin.

A CFF extraction was performed on the polarized and unpolarized results. From the polarized cross section, hints of scaling was found since the extracted combinations of CFFs

showed no Q^2-dependence (Figure 1.14). Assuming a negligible contribution of $|\mathcal{T}_{DVCS}|^2$, the three lowest twist CFFs parametrizing the interference contribution have been extracted using the unpolarized data. However, the large size of the extracted interference terms raised doubts concerning the hypothesis of a negligible $|\mathcal{T}_{DVCS}|^2$.
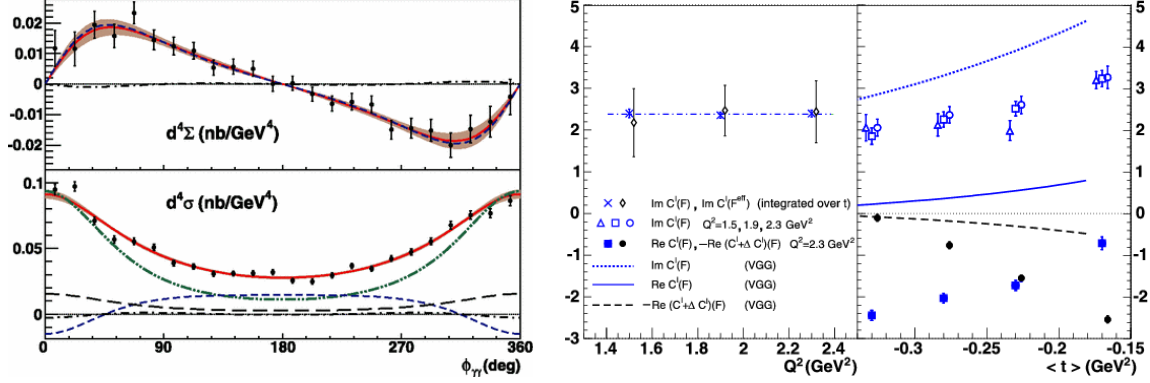
Figure 1.14: Left: Beam helicity dependent and unpolarized photon electroproduction cross sections at $t = -0.28$ GeV^2, $Q^2 = 2.3$ GeV^2 and $x_B = 0.36$ from [44]. Right: Compton form factors extracted from the 2004 experiment, assuming a negligible $DVCS^2$ contribution.

From the same run period, π^0 electroproduction cross sections have been extracted [37]. Almost instantly, π^0's decay into two photons with a branching ratio of 98.8%. As this experiment was suited to detect the photon in the DVCS process, it was sensitive to π^0's through the decay photons. However the threshold set on the energy of the photon at ~ 1 GeV reduced the phase space of the π^0 detection, possible only with 2-photon detection. As the π^0 energy decreases with decreasing Q^2, this phase space was too small for 2004-Kin1 to extract π^0 electroproduction cross section. However it was large enough for 2004-Kin3 and 2004-Kin2 [37]. They also studied the x_B-dependence by defining new kinematics from the 2004-Kin2 and 2004-Kin3 data set.

An interesting point is that π^0 electroproduction cross sections have been extracted for 2004-Kin2. It implies that the π^0 contamination can be estimated for 2004-Kin2 data. A chapter of this thesis is dedicated to the full reanalysis of DVCS data from the E00-110 experiment.

1.6.2 The E07-007 experiment: the 2010 run period

The conclusion of the 2004 run period was that both photon and π^0 electroproduction unpolarized cross sections were higher than predicted. But we did not know the size of the different contributions, nor did we understand the discrepancy with the predictions. It was the goal of the 2010 experiment to perform a complete separation of photon and π^0 electroproductions. Similarly to 2004, the goal of the 2010 run period was to extract DVCS and π^0 electroproduction cross section but at two different beam energies E for each kinematical setting (Table 1.4). The idea is to combine the dependences in ϕ and E to disentangle all contributions. Indeed the kinematical factors in front of the dominant terms of interference and $DVCS^2$ do not depend on ϕ but have different beam energy dependences (see the tables 1.1 and 1.2). For π^0, as shown explicitly in Eq 1.73, we have to measure the cross section at two different values of ϵ^* in order to disentangle the transverse and the longitudinal responses.

The experiment ran from October to December 2010, at the same time as the Q-weak experiment in Hall C. Because of constraints on the beam energy due to Q-weak, kinematics were slightly different compared to the E00-110 experiment.
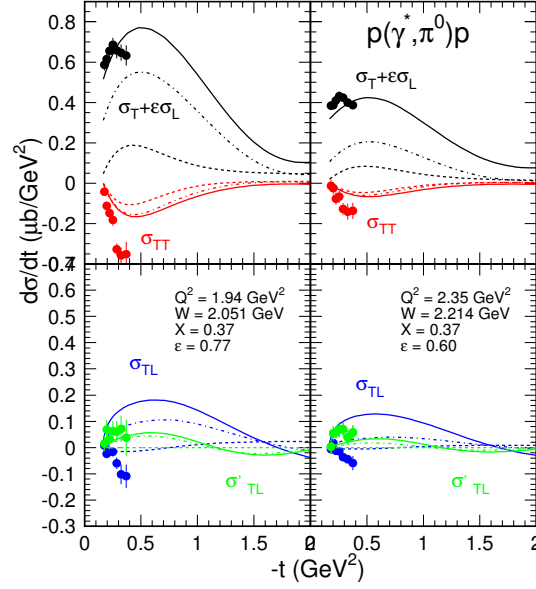
Figure 1.15: Results of π^0 electroproduction from Hall A [37]. The lines represent predictions based on t-channel meson exchange [45].

Name	Q^2 (GeV^2)	x_B	W^2 (GeV^2)	E (GeV)	ϵ^*
2010-Kin1	1.5	0.36	3.55	(3.355 ; 5.55)	(0.52 ; 0.84)
2010-Kin2	1.75	0.36	3.99	(4.455 ; 5.55)	(0.65 ; 0.79)
2010-Kin3	2	0.36	4.44	(4.455 ; 5.55)	(0.53 ; 0.72)

Table 1.4: Table of kinematics for the 2010 experiment.

As explained in section 1.4.4, σ_L is expected to be very small and the lever arm in ϵ^* is rather small. It makes this measurement a technical challenge, with a dire need to reduce as much as possible the systematic uncertainties.

Chapter 2

The experimental setup

Jefferson laboratory is located in Newport News (Virginia, USA) and was founded in 1985. Its primary mission is to investigate the structure of nuclei and nucleons. To accomplish this mission, a continuous electron beam accelerator facility (CEBAF) has been built and has provided a longitudinally polarized electron beam to three experimental halls since 1995. Both experiments of interest in this thesis took place in the Hall A of Jefferson laboratory, dedicated to high luminosity and high precision experiments. Except for a few details which will be presented in their dedicated chapters, the E07-007 and E00-110 experiments are identical.

First, we are going to introduce CEBAF and then the Hall A of Jefferson Lab. We will then describe the experimental setup of both experiments.

2.1 Continuous electron beam accelerator facility

The electron source is a stressed gallium arsenide crystal, placed in an ultra-vacuum chamber. Using optical pumping, the conduction band of the crystal is filled with electrons from the valence band [46]. By choosing the polarization of the pumping laser, we can choose the polarization state of the electrons in the conduction band. To increase the probability for the electron to go in the vacuum, a layer of cesium fluoride is deposited at the interface to lower the potential barrier between the vacuum and the conduction band. Once the electron escapes from the crystal, a difference of potential extracts it. Instead of a unique laser illuminating the GaAs cathode, there are three lasers functionning at 499 Mhz each. Each experimental hall is synchronized with its own laser.

Until 2014, CEBAF was composed of two superconducting linacs made of 20 cryomodules, each cryomodule composed of 8 radio-frequency cavities in pure Niobium (see Figure 2.1). The electromagnetic magnetic field in the cavities is a stationary sinusoidal field synchronized with the injector (1497 MHz). The resulting increase for each cavity in energy is $\sim$7 MeV/m. The two linacs were connected by recirculating arcs allowing to reinject the beam 5 times in each linac for a maximal beam energy of $\sim$6 GeV. To avoid the spatial spread of the electron bunches, the electrons from the source have to be accelerated by a first set of cavities up to 45 MeV before entering the linacs. Using RF separators and magnets, the beam is then sent in the 3 experimental Halls. Hall A and C could receive up to 150 μA of beam current, whereas Hall B was limited to 200 nA.
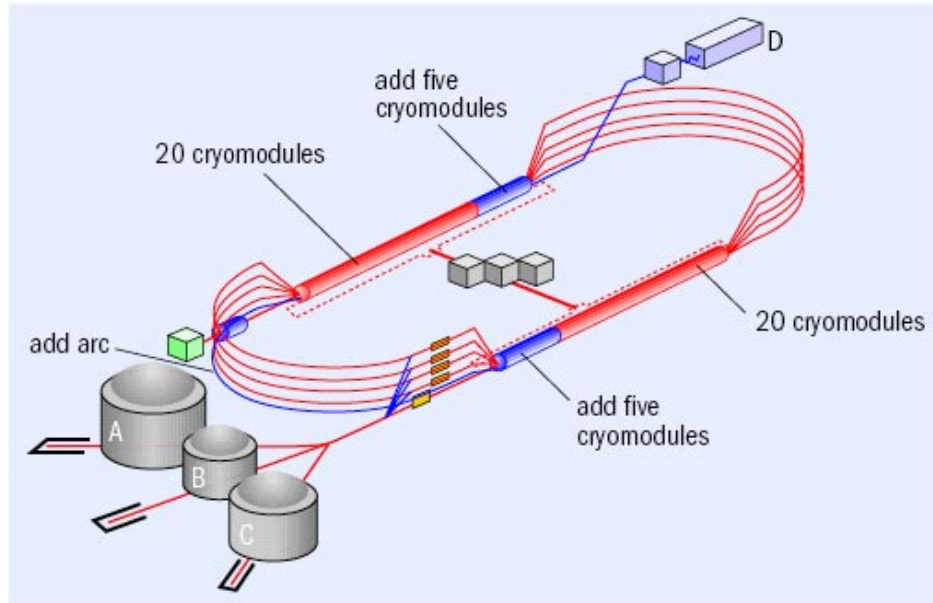
Figure 2.1: Jefferson Lab has been upgraded to 12 GeV since late 2014. 10 cryomodules have been added. An additional arc has been built in order to recirculate into the linac the beam before ending in the brand new Hall D.

2.2 Hall A instrumentation

In the Hall, the beam goes through several diagnostic apparatus before hitting the target. The basic Hall A detectors include two High Resolution Spectrometers (HRS). Extensive details about the standard Hall A equipment can be found in [47].

2.2.1 The beamline

For the measurements of photon and π^0 electroproduction cross sections, it is essential to determine accurately the beam energy, position, current and polarization. A set of dedicated apparatus are placed along the beamline.

2.2.1.1 Polarimeters

Two polarimeters are placed along the beamline. The first one is the Compton polarimeter. As its name indicates, it is based on the Compton scattering process. At the Hall entrance, the beam is deviated through a chicane (=magnets). In the middle of the chicane there is a Fabry-Pérot cavity in which the electron beam crosses a circularly polarized photon beam. As it is a pure QED process, the dependences of the cross section with respect to the scattering angles and the polarization of the beams are known. Measuring the asymmetry and knowing the photon beam polarization, we derive directly the polarization of the electron beam. This measurement is non-invasive: The vast majority of electrons does not interact with the laser, and continues to the target.

A second polarimeter uses the Møller scattering process. Electrons from the beam will scatter off polarized atomic electrons in a ferromagnetic foil. This foil is placed within a 24 mT magnetic field. The scattering cross section depends on the beam polarization. A dedicated spectrometer then detects the Møller events. This method is invasive: The foil is directly inserted in the beamline before the target. Moreover the Møller method can only

be performed at a low beam current ∼0.5 μA. But the polarization of the beam may vary with the beam current.

Because the Møller polarimeter method is invasive, the polarization was measured with the Compton polarimeter for both experiments. A comparison between the two methods was performed for the 2004 run period: they were in good agreement within their systematic and statistical uncertainties.
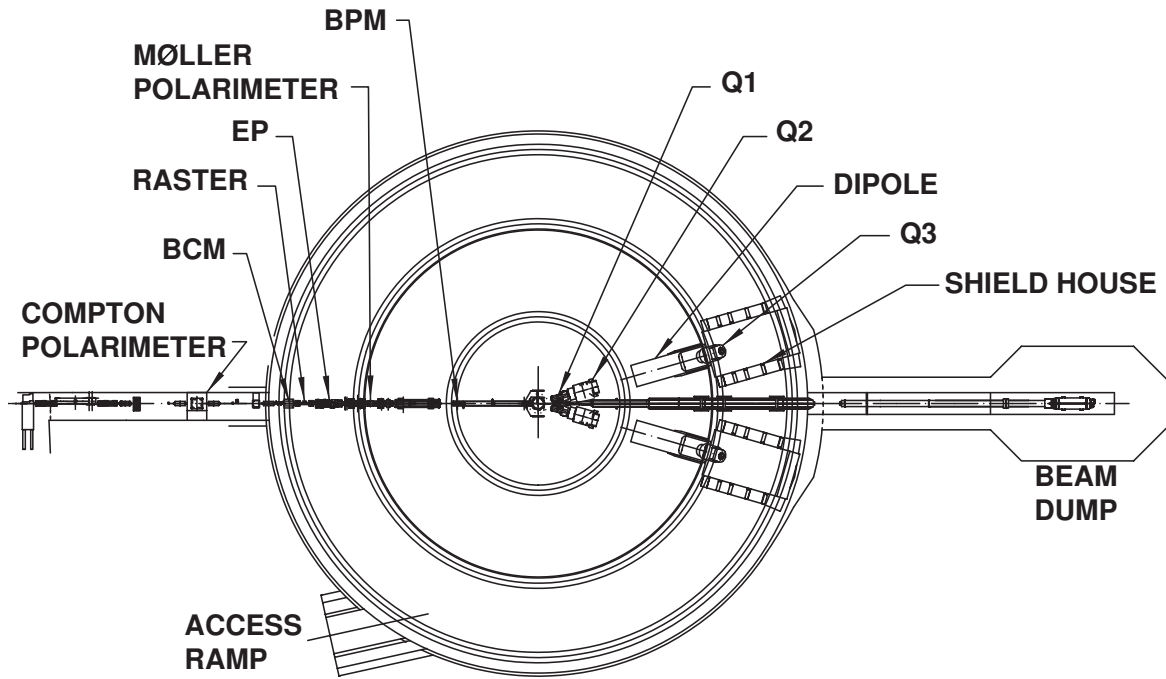
Figure 2.2: Schematic view of the Hall A experimental setup. [47]

2.2.1.2 Beam Cavity Monitors

Two RF cavities are located in the beamline at the entrance of the Hall. They are stainless steel cylindrical waveguides amplifying the magnetic field created by the beam passing through. This magnetic field induces a voltage which is proportionnal to the beam current in the cavities. In order to extend the precision measurement to low currents, two amplifiers with gains 3 and 10 are used.

2.2.1.3 Beam Position Monitors

Two beam position monitors are located 7.524 m and 1.286 m upstream of the target and determine the position and direction of the beam. Each BPM consists of a set of four antennas displayed around the beam. The beam induces a current in each of them. The relative position of the beam with respect to the antennas is determined by comparing the intensity in each antenna. For beam currents above 1 μA, the resolution is about 100 μm. The BPMs are calibrated using wire scanners, whose positions are surveyed regularly and known within 200 μm.

2.2.1.4 Beam energy measurements

The beam energy is measured by two methods. The first consists in studying electron-proton elastic scattering. A polyethylene foil is placed on the beam path, 17 m upstream of the target. Silicon strips detectors, a Čerenkov gas chamber and scintillator paddles detect the scattered electron and the recoil proton. With the scattering angles θ_p and θ_e, the beam energy is given by:

$$E = M \frac{\cos\theta_e + \sin\theta_e / \tan\theta_p - 1}{1 - \cos\theta_p} + \mathcal{O}\left(\frac{m_e^2}{E^2}\right) \ . \tag{2.1}$$

The second is the ARC method. Between the accelerator and the Hall A, there is a 40 m arc section. Tuned in dispersive mode, the beam is deflected using eight dipoles located in the arc section. The bend angle is measured using wire scanners at the entrance and exit of the arc. Because the eight dipoles are under vacuum, the field integral of the dipoles is measured using a ninth dipole in a separate room. It is identical to the eight others and powered in series with them.

Both methods are invasive.

2.2.2 The target system

The original plan of the E00-110 experiment was to detect all the particles in the final state. Typical recoil proton momenta for DVCS events are about a few hundreds of MeV. Whereas the usual scattering chambers in the Hall are 1-inch-thick stainless-steel cylinders, the custom DVCS scattering chamber was a 1-cm-thick spherical chamber made of aluminium. Thanks to the spherical shape, energy losses become independent of the scattering angle. This chamber was also used for the E07-007 experiment.

The scattering chamber encloses several targets under vacuum. Liquid hydrogen (LH_2) and deuterium (LD_2) targets were used to study DVCS and π^0 electroproduction on protons and neutrons for the 2004 and 2010 experiment. The target itself is an empty aluminium cylinder mounted on a ladder, and is part of a loop in which the LH_2 (or LD_2) is circulating. This ladder is remotely controlled to place the selected target on the beam path. At 130 μA, the beam heating is about 700 W. To keep the temperature stabilized during beam operation, the flow of hydrogen (or deuterium) has to go through a heat exchanger with liquid helium at 15 K. The flow of helium can be adjusted by valves controlled from the counting house. The temperature and pressure during beam operation were 17 K and 0.17 MPa for LH2, 22 K and 0.15 MPa for LD_2. Because LH_2 and LD_2 are highly flammable, their temperature, density and pressure are monitored accurately at several locations of the loop. Finally E07-007 and E00-110 ran at low current (between 1 and 5 μA), so that the boiling effect (local phase change along the beam path in the target) could be neglected.

Besides the cryotargets, the target ladder includes several solid targets used for different purposes:

- Two dummy targets are empty replicas of the LH_2 targets to study target wall effects.

- An empty target is used to reduce radiation for detectors during invasive beam studies such as wire scanners.

- A BeO target which glows where the beam hits the target. Therefore we could visualize the beam position with a camera installed in the scattering chamber.

- A C target which is a 1-mm-thick carbon foil used as a point-like target.
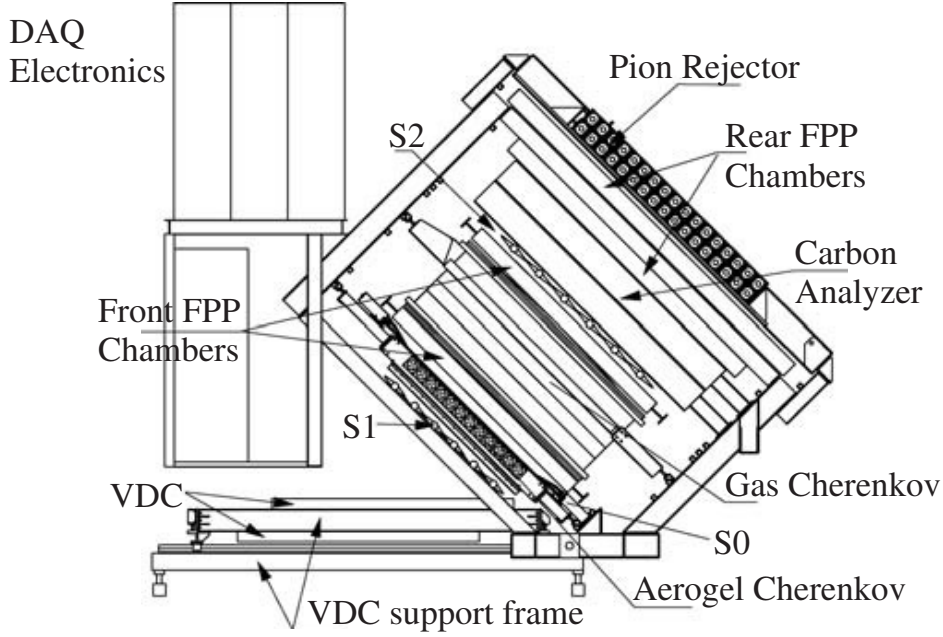
Figure 2.3: Detector package of the left HRS which detects and characterizes the electron. First the electron goes throught the VDCs, then scintillators and Čerenkov detector before the pion rejector.

- An optics target consisting of seven 1-mm-thick carbon foils, used to determine the optical matrix of the spectrometer.

2.2.3 The high resolution spectrometer

Hall A is permanently equipped with two HRSs. They are designed following a QQDQ scheme: 2 quadrupoles focus the particles into a dipole. The dipole selects particles according to their momentum and sends them to a detector package. At the exit of the dipole, a last quadrupole focuses the interesting particles in the detector hut. Both HRS have a momentum acceptance of 4.5% with respect to the central momentum set in the HRS[1]. The angular acceptance is ±30 mrad horizontally and ± 60 mrad vertically.

Both spectrometer detector packages are quite similar. As the right HRS (with respect to the beamline in the beam direction) was not used for our experiments, we only describe the left HRS detector package. First the particles go through two sets of vertical drift chambers (VDCs) placed in the focal plane of the spectrometer. These VDCs provide information about the position of the particles in the focal plane and the angle of the track with respect to the focal plane. With an optical matrix determined with dedicated runs using the optics target, we are able to derive the track at the vertex from the focal plane variables. Two scintillators S_1 and S_2 have been included for trigger purposes. Between the two scintillators, a gas Čerenkov detector ensures the π/e discrimination. It is filled with carbon dioxide at atmospheric pressure. The threshold for pions is 4.8 GeV/c whereas it is 17 MeV/c for electrons.

Finally the last detector dedicated to particle identification is the Pion Rejector (PR). It is an electromagnetic calorimeter made of two layers of lead glass blocks. Electrons deposit almost all of their energy whereas hadrons deposit a few percent of its energy in most cases.

---

[1]The left HRS momentum range is 0.3-4 GeV/c, For the right HRS it is 0.3-3 GeV/c.

2.3 The DVCS/π^0 experiment design

The goal of both E00-110 and E07-007 experiments was to extract 4-fold differential cross sections in Q^2, x_B, t and ϕ for DVCS and π^0 electroproduction. Q^2 and x_B are determined using only the scattered electron four momentum. For t and ϕ, we only need the four momenta of the scattered electron and of the photon/π^0. As a consequence, the left HRS is dedicated to the scattered electron detection. In order to detect the photon(s), an electromagnetic calorimeter of lead fluoride and a dedicated DAQ system have been designed. To ensure the exclusivity with a triple coincidence, a recoil proton detector was installed for the E00-110 experiment. But, we are going to show that a cut on the missing mass[2] $M^2_{ep\to e\gamma X}$ is enough to validate the exclusivity, justifying the absence of a recoil detector for the E07-007 experiment.

2.3.1 The proton array

For the first experiment in 2004, a circular array of scintillators was installed in order to detect the recoil proton. This detector was called the proton array (PA) and made of 20 columns, each column composed of 5 plastic scintillator blocks. As the DVCS final state presents an azimuthal symmetry with respect to the virtual photon, the PA was placed around the calorimeter as seen on Figure 2.4.

It subtended a solid angle (relative to the nominal direction of the virtual photon) of $18° < \theta_{\gamma^*p} < 38°$ and $45° < \phi_{\gamma^*p} < 315°$. The 90° cut-out in ϕ_{γ^*p} allows for the exit-beam pipe in the kinematic setting where the detector stack is the closest to the beamline. Therefore the triple coincidence analysis suffered from the absence of acceptance at $\phi = 180°$.
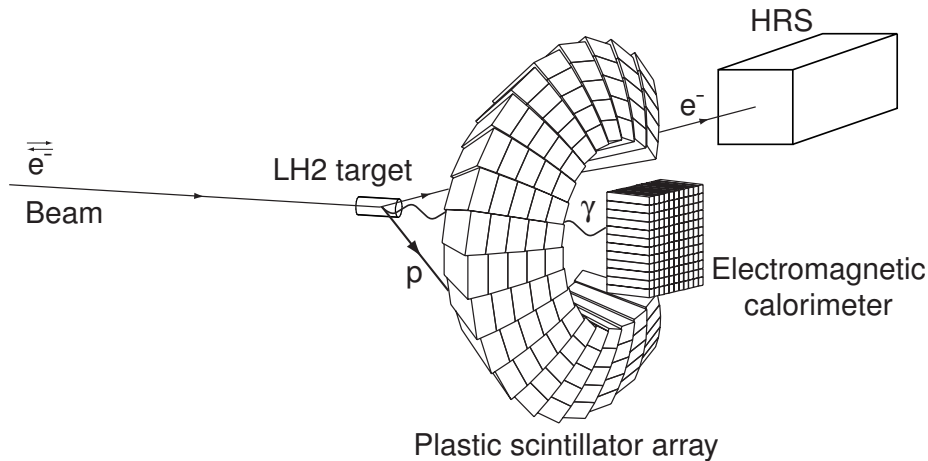
Figure 2.4: The DVCS experimental setup for the 2004 experiment. The electron was detected in the HRS and the photon in the calorimeter. The recoil proton was detected in a plastic scintillator array called Proton Array.

---

[2]Here and in all the following chapters, *missing mass* refers to *the missing-mass squared*.

2.3.2 The PbF$_2$ calorimeter

Because of a possible high hadronic background, the calorimeter has been made of lead fluoride, a Čerenkov medium. As a Čerenkov medium, there is a momentum threshold according to the particle for emission of Čerenkov light. Moreover, since the Čerenkov light pulse is short, lead fluoride is convenient to avoid pile-up events. However its energy resolution is about three times lower than for scintillator media such as PbWO$_4$. A Monte-Carlo simulation estimated a number of 1000 photoelectrons per GeV.

The calorimeter is an array of PbF$_2$ blocks whose dimensions are $3 \times 3 \times 18.6$ cm^3 . It corresponds to 20 radiation lengths. The Molière radius of lead fluoride is 2.2 cm. A typical electromagnetic shower is contained in 9 adjacent blocks and 90% of the energy is deposited in the central block. Each block was first wrapped in Tyvek and then in Tedlar paper in order to avoid light loss and leakage between the blocks. Behind each block was attached a PMT (Hamamatsu R7700).
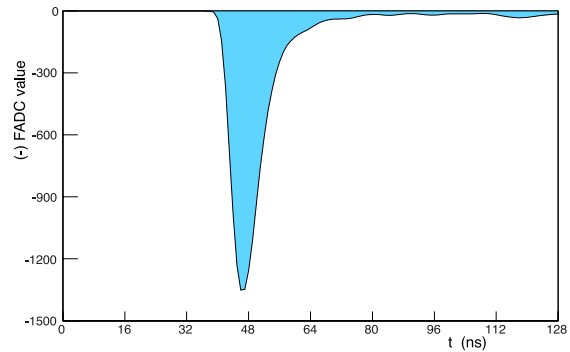
Figure 2.5: Left: Principle of the ARS system. Each of the 128 capacitors stores 1 ns of a PMT signal. Right: Flash ADC value as a function of time recorded by the ARS system for a typical calorimeter pulse.

For the E00-110 experiment in 2004, the calorimeter was composed of 132 blocks distributed in 12 rows and 11 columns. For the 2010 experiment, it was larger with 16 rows and 12 columns, for a total of 208 PbF$_2$ blocks.

2.3.3 The analog ring sampler

Due to the high luminosity and the proximity of the PA and PbF$_2$ calorimeter to the beamline, singles rates up to 10 MHz were expected in both detectors and measured in a test run during the design phase. To cope with the resulting pile-up events from this high background environment, all electronic channels of the PA and the calorimeter were digitized by the analog ring sampler (ARS) CMOS ASIC, developed at CEA Saclay [48][49].

The ARS uses the concept of analog memories to sample data at a clock rate of 1 GHz: each channel contains a circular array of 128 capacitors: every 1 ns, the ARS points the signal to the next capacitor, eventually overwriting itself after 128 ns. When a trigger is issued, the capacitor array is isolated and the previous 128 samples are stored. In case of pile-up events, the ARS is able to differentiate two photons if they are separarated by more than 4 ns.

2.3.4   Data acquisition

The DAQ is run by the software CODA (CEBAF online data acquisition). Each detector in Hall is connected to analog digital converters (ADCs), time-to-digital converters (TDCs) and scalers. They are gathered on VME crates, one crate per detector. Each crate is controlled by a read-out controller (ROC). The ROCs are connected to the trigger supervisor (TS), a multifunction VME board. Combining the different ROC data, the trigger supervisor tests different triggers. If the test is positive for a specific trigger, the trigger supervisor orders the read out of the VME crates. Data are then recorded and sent to a mass storage tape silo for long-term storage. As long as one ROC is processing and sending data, the trigger supervisor is inhibited and no trigger is accepted, resulting in acquisition deadtime. It is only when all ROCs are available that the trigger supervisor can accept triggers again.

The calorimeter and the proton array are specific detectors for the DVCS experiment, requiring the installation of two additional ROCs. A specific calorimeter trigger module has been designed in order to synchronize the trigger supervisor with the calorimeter and the proton array. The event builders, recorders and transfers were customized to include the calorimeter and proton array data in the usual Hall A data package.

2.3.5   Trigger logic

The first level trigger is a coincidence between the scintillator S2 and the Čerenkov detector in the HRS. A threshold is set on the Čerenkov detector, high enough to remove most of the π^- triggering the scintillator and low enough to keep most of the electrons. When a coincidence between the two detectors occurs, the trigger supervisor issues a STOP signal to the ARS system.

The signal of each block is integrated over 128 ns by 12-bit-flash ADCs reading the ARS. Then the calorimeter trigger module computes the sum of the integrated ARS signals for all 2×2 neighboring blocks combinations in 340 ns. If a sum is above the hardware threshold, the calorimeter trigger module sends a VALID signal to the trigger supervisor. Then the data from HRS, calorimeter and proton array are transfered and recorded on disks while triggers and ARS are reset. Only data of neighboring blocks above the threshold are transferred. It takes 128 μs to digitize and transfer the ARS data for each 2×2 block combination.
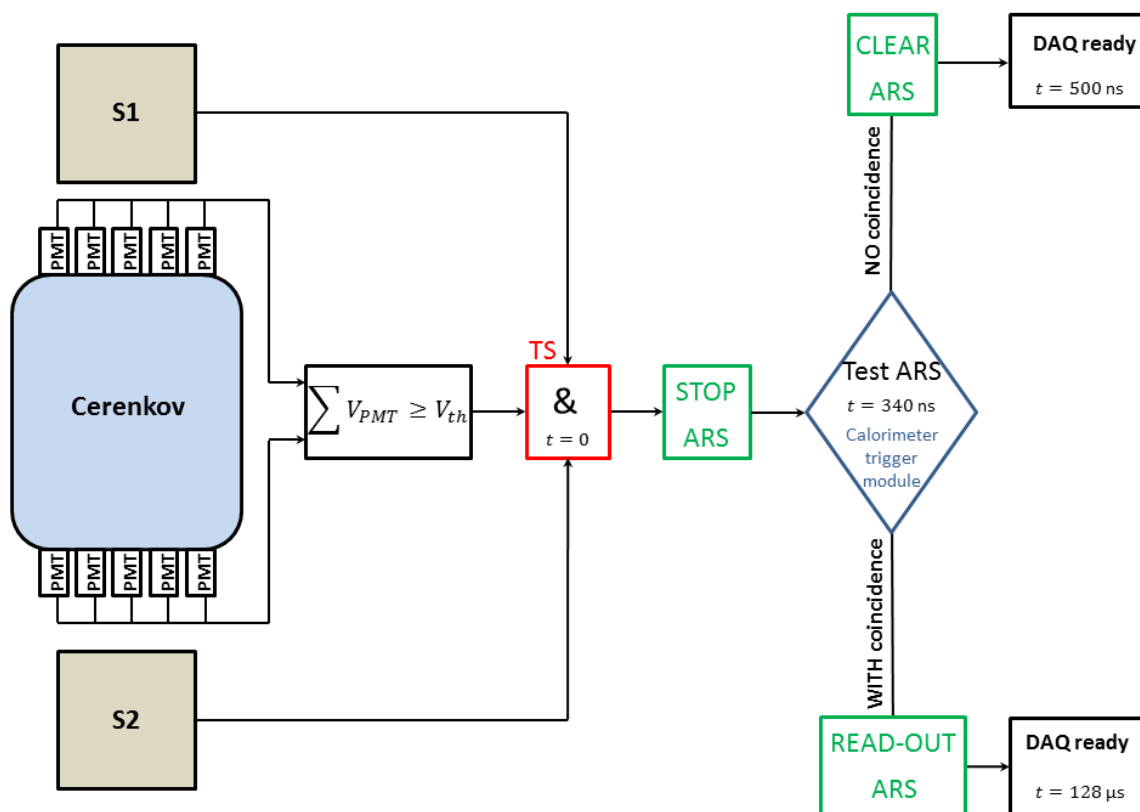
Figure 2.6: Diagram of the trigger logic used for the 2004 run period. In 2010, S1 was not in the trigger.

Chapter 3

Normalization studies using deep inelastic scattering

For five of the six kinematical settings of the E07-007 experiment, the trigger was formed by the Čerenkov detector and the S2 scintillator only. In other words, it was an inclusive electron trigger. It was therefore possible to extract the deep inelastic scattering cross section. A high accuracy extraction of the DIS cross section allows us to test each run's quality, evaluate systematic errors and most importantly, check the quality of the normalization.

For the 6th kinematic settings, approximately 75% of the runs were taken with the calorimeter in the trigger. The DIS cross section had been extracted for the remaining 25% of runs, with the inclusive electron trigger. A comparison based on the DVCS cross sections between the two periods is described in appendix A.

3.1   Principle of the extraction

A cross section is a physical quantity associated with the probability for a process to happen. In the case of DIS, it is the probability for an electron to interact with a proton at high Q^2 and W. As a cross section is a universal quantity, it is not simply given by the ratio between the number of detected electrons and the total number of electrons sent on the target. We have to remove all dependences on the characteristics of the experimental setup: the so-called normalization of the cross section. To extract the DIS cross section from the data, we apply the following formula:

$$\frac{d\sigma}{d\Omega dE} = \frac{N_{\mathcal{C}}}{\mathcal{L}} \times \frac{1}{\eta_{virt} \times \eta_{exp} \times \Gamma_{DIS}}, \tag{3.1}$$

with:

- $N_{\mathcal{C}}$: the number of events passing all the analysis cuts.

- η_{exp}: a factor correcting for event losses induced by deadtime, trigger inefficiency and analysis cuts.

- Γ_{DIS}: the phase space from which the $N_{\mathcal{C}}$ events are coming. This is estimated by Monte-Carlo.

- η_{virt}: a term correcting for first order QED diagram interfering with the Born process.

- $\mathcal{L}$: the integrated luminosity.

The integrated luminosity is given by:

$$\mathcal{L} = \int \frac{d\mathcal{L}}{dt}\,dt = \frac{Q}{e}\frac{N_A \rho l}{A_H}\,, \qquad (3.2)$$

where $e = 1.602 \cdot 10^{-19}\,\mathrm{C}$ is the electron charge, $A_H = 1.0079\,\mathrm{g/mol}$ is the atomic mass of H, and $N_A = 6.022 \cdot 10^{23}\,\mathrm{mol^{-1}}$ is Avogadro's number. The $\mathrm{LH_2}$ target length was $l = 15$ cm and was operated at $17\,\mathrm{K}$ and pressure of $25\,\mathrm{psi}$, which gives a density of $\rho = 0.07229\,\mathrm{g/cm^3}$.

We are going to first describe the set of cuts $\mathcal{C}$ applied to the data to select the events. Then we focus on the computation of η_{exp}, η_{DT} and the integrated luminosity. Before presenting the results and conclusions of this normalization study, we describe the Monte-Carlo simulation developed to compute Γ_{DIS}.

3.2 Event selection

The events selected by the inclusive electron trigger does not constitute a pure electron sample scattered off the $\mathrm{LH_2}$ target. A set of cuts have to be applied in order to ensure the reliability of the track reconstruction, as well as the particle and process identifications.

3.2.1 Acceptance cuts

In order to get a reliable kinematics reconstruction, one needs to select events which went through a well known part of the HRS acceptance. Indeed our ability to properly reconstruct the event depends on our knowledge of the magnetic field in the HRS, which is limited on its edges. However the HRS acceptance is a complicated region depending on 5 correlated variables (see Figure 3.1): x_{tg} and θ_{tg} (the position of the particle and the tangent of the angle made by its trajectory along the dispersive direction), y_{tg} and ϕ_{tg} (the position and the tangent of the angle perpendicular to the dispersive direction), and δ_{tg} (the fractional deviation of the particle momentum with respect to the central momentum of the HRS). Trajectories of higher momentum particles have lower curvature in the dipole, and in order for them to fit into the spectrometer they need to have lower θ_{tg}. The dipole magnet has trapezoidal cross section and higher momentum particles tend to fly closer to its shorter base (high magnetic field) side, and this makes the accepted range of ϕ_{tg} smaller for higher δ_{tg}. Finally, increasing y_{tg} requires decreasing ϕ_{tg} in order for the particle to get into the spectrometer entrance window. Making cuts independently in each of the variables to limit events to flat acceptance regions in each of them is thus very inefficient. Instead, we used the R-function, an acceptance function [50], which allows to place a 4-dimensional cut ($x_{tg} = 0$ is assumed). This procedure is almost twice more efficient than the traditional sequential acceptance cuts. This function takes the arguments y_{tg}, θ_{tg}, ϕ_{tg} and δ_{tg} and returns a so-called R-value which is the minimum distance (in radians) to the (θ_{tg}, ϕ_{tg}) solid angle acceptance region appropriate for a given value of y_{tg} and δ_{tg}. A value of 5 mr was used in order to constrain a well-defined region of the HRS acceptance.

During the E07-007 experiment, five of the six kinematics were run with a collimator in front of the HRS entrance in order to better define our acceptance. This collimator consists of a 8 cm thick tungsten block. Its entrance (target side) is 12.18 cm-vertical and 6.29 cm-horizontal. It gets larger at the exit (HRS side) with a 12.97 cm-vertical and 6.68 cm-horizontal opening. As the R-function was developed for the HRS without collimator, we perform an additional set of cuts on the position of the particle at the collimator entrance to select events.

Finally, more than one particle sometimes reach the VDCs. The VDC system of the HRS has unfortunately not been designed to handle multiple tracks. For such events, the tracking
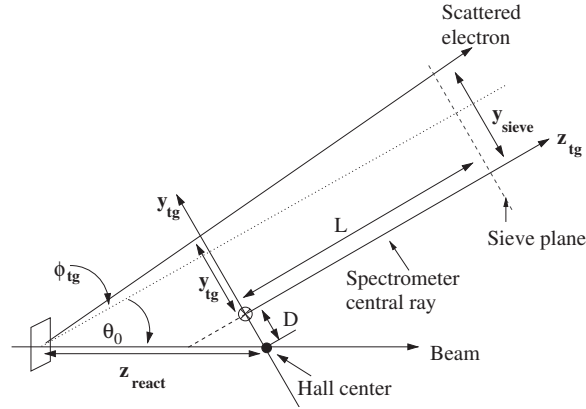
Figure 3.1: HRS variables used to define its acceptance.

algorithm sometimes fail to reconstruct the tracks. As we cannot perform any acceptance cut on these events, we remove them from the analysis and consider only events with one track.

3.2.2 Cut on the vertex position

The target cell windows are made of $\sim$0.14 mm-thick aluminium and some electrons are scattered by them into the spectrometer (Figure 3.2). In order to remove these events, we cut on the position of the vertex. The spectrometer has a resolution on the position of the vertex given by:

$$\sigma_{vertex} = \frac{1.2 \ mm}{\sin \theta_{HRS}} \ , \tag{3.3}$$

where Θ_{HRS} is the angle between the beam axis and the HRS central axis.

For the kinematical setting with the smallest HRS angle, the resolution is 4.3 mm. Moreover the center of the target is shifted by +5mm. So for all kinematics we decided to apply a conservative cut and require the vertex to be in the interval [-6 cm ; 7.5 cm].
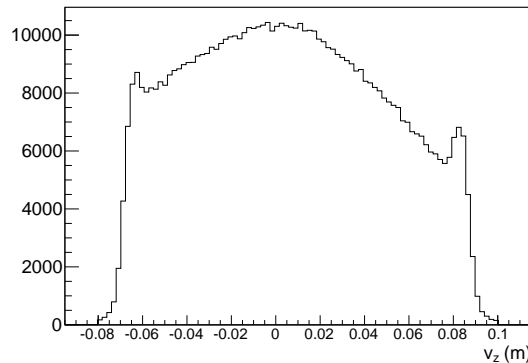
Figure 3.2: Z-coordinate of the vertex. The left and right peaks correspond to the target aluminium windows at -7.5 and 8 cm.

3.2.3 Particle identification

3.2.3.1 Čerenkov cut

In order to remove π^- contamination, a threshold was set on the output voltage summed over the ten PMTs of the Čerenkov detector. In order to simplify the evaluation of the Čerenkov efficiency, we applied a software cut slightly higher than the hardware cut. As the
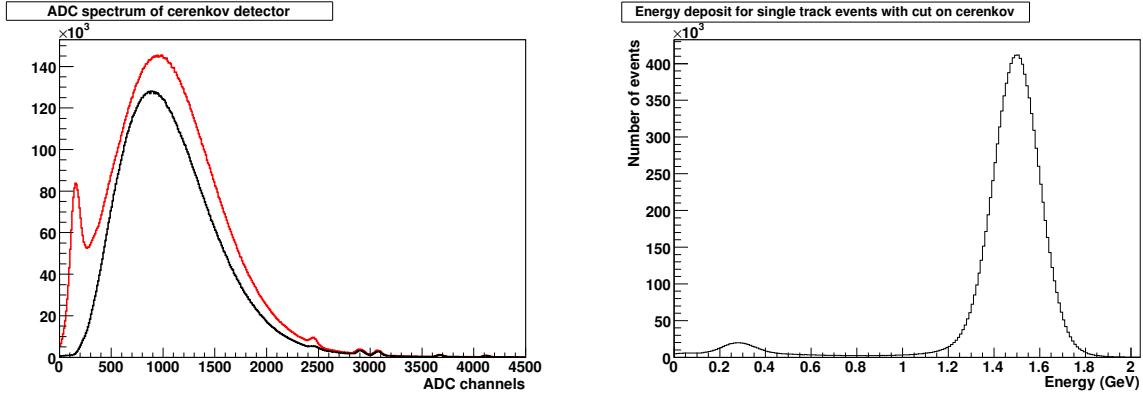
Figure 3.3: Left: Čerenkov ADC spectrum for kin3low, the first kinematics which was run. For the first two weeks, the threshold set on the Čerenkov was at 200 mV (black spectrum) corresponding to about 200 ADC channels. Then it was lowered at 50 mV corresponding to 50 channels for the rest of the experiment (red spectrum). The single photo-electron peak stands at 150 ADC channels. The average number of photo-electrons is 7. Right: Energy spectrum in the pion rejector for events after Čerenkov and acceptance cuts.

threshold on the Čerenkov changed once during the experiment, there are two values for the corresponding software cut: 250 ADC channels for the first two weeks and 80 ADC channels for the rest of the experiment (see figure 3.3).

3.2.3.2 Pion rejector cut

Since the Čerenkov detector is in the trigger, we may think that all events are electrons. But as seen on Fig 3.3, there is a peak corresponding to a single photo-electron emission at 150 ADC channels. This peak coresponds to δ-rays. δ-rays are secondary electrons, from pions which ionize the matter before the Čerenkov detector, and which may trigger the DAQ. This contamination represents up to 10% of the events, depending on the kinematics.

We can improve the particle identification by using the pion rejector (PR). Electrons will deposit all their energy into the PR, whereas pions will most of the time deposit a small amount. By applying a cut on the energy deposit, we are able to discriminate pions from electrons.

In order to be able to apply a cut on the energy deposit in the PR, it needs to be calibrated using a sample of electrons from a production run. This sample is created with a high cut on the Čerenkov signal to maximize the fraction of electrons. The energy of the electrons is determined by the tracking algorithm. If E^n is the energy of the electron from the nth event, we have:

$$E^n = \sum_i G_i \times A_i^n$$

with A_i^n the amplitude of the signal for the nth event and G_i the gain coefficient associated

with the ith block. In order to determine the G_i coefficients, we minimize the following χ^2:

$$\chi^2 = \sum_n \left(E^n - \sum_i G_i \times A_i^n \right)^2 , \qquad (3.4)$$

$$\frac{\partial \chi^2}{\partial G_{i_0}} = 0 \implies \sum_i G_i \left(\sum_n A_{i_0}^n A_i^n \right) = \sum_n E^n A_{i_0}^n \qquad \forall i_0 , \qquad (3.5)$$

The gain coefficient are then obtained by solving the system $AG = B$, with $A_{ij} = \sum_n A_i^n A_j^n$ and $B_i = \sum_n E^n A_i^n$. We use the production run in the middle of each kinematics with high statistics to perform the calibration.

As seen on figure 3.3 representing the PR spectrum for kin3low, we can discriminate δ-rays from electrons by cutting on the energy deposit. This cut depends on the kinematic settings. For kin3low, we set the cut at 0.8 GeV.

3.3 Efficiencies

A significant fraction of good events may be lost and need to be corrected for. There are two main ways to lose good events: the inefficiency of the experimental setup (trigger efficiency, deadtime, VDCs,...) and the cuts applied in the analysis. We are going to review the corrections due to the trigger as well as the detector and analysis cuts. For each of them, we evaluate the fraction of good events which are lost to estimate the correction factor η_{exp} of Eq 3.1

3.3.1 Tracking efficiency

As mentionned in the previous section, we removed $\sim 10\%$ of events with more than one track. We have to estimate the fraction of good events that were lost by this cut. Historically the correction factor η_{Trk}^{old} was defined by:

$$\eta_{Trk}^{old} = 1 + \frac{\sum_{k \geq 2} N_k}{N_1}, \qquad (3.6)$$

where N_k is the number of events with k tracks.

This correction factor assumes that there is the same probability to find an electron in our acceptance cuts in multitrack events as in single track events. The usual assumption was that these events were a scattered electron with another particle in coincidence. In that case, one would expect the number of n-track events to follow the distribution r^{n-1} with r the probability of a 2-track event. But there are far too many 3-track and 4-track events compared to the number of 2-track events (Figure 3.4).

The PR energy deposit for these events allows us to get some information about their content. First, they are mainly low energy events: it indicates that they are most likely pions creating secondary particles in the VDC. Only 2-track events exhibit a signal in the PR corresponding to electrons. However there is also a large contribution of pions. we correct the multitrack events with the following factor:

$$\eta_{Trk} = 1 + \frac{N_{2T}^c}{N_{1T}^c} , \qquad (3.7)$$

where N_{2T}^c and N_{1T}^c are the number of 2-track and 1-track events with a minimum energy deposit in the PR. This minimum is the same as the one we require for the 1-track event analysis in subsection 3.2.3.2. Table 3.1 summarizes the corrections we applied to all E07-007-kinematic setting.
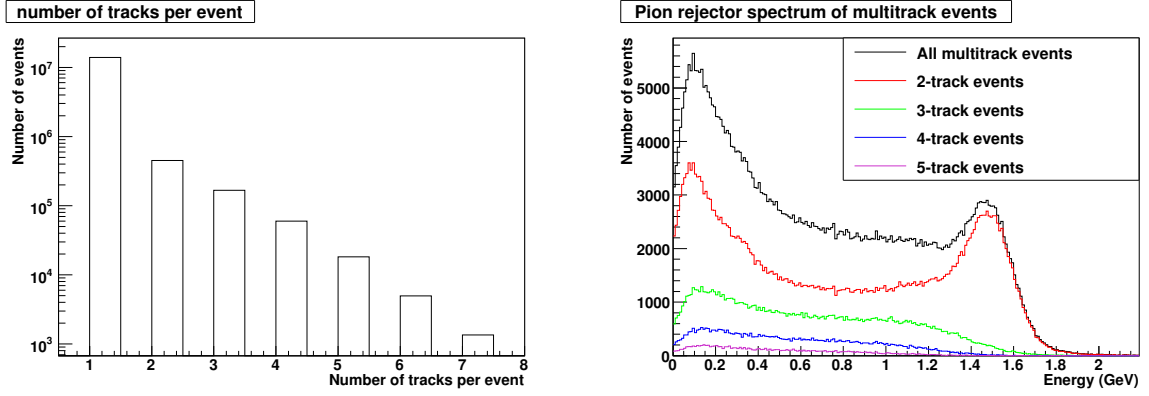
Figure 3.4: Left: Distribution of events according to the number of tracks. Right: Energy deposit in the PR according to the number of tracks for kin3low. Only 2-track events show a clear electron peak like 1-track events in Figure 3.3.

Kinematics	η_{Trk}
Kin1low	1.01
Kin1high	1.021
Kin2low	1.018
Kin2high	1.02
Kin3low	1.016
Kin3high	1.019

Table 3.1: η_{Trk} for each E07-007-kinematics. The former correction η_{Trk}^{old} was therefore inducing an error of $\sim 8\%$.

3.3.2 Deadtime

The trigger supervisor is connected to a set of scalers. One scaler counts the total number of coincidences between the Čerenkov and S2, even when the DAQ is busy. It is then the total number of electrons N_{HRS} detected by the HRS. Another scaler counts the number of ARS STOP signals sent to the ARS when the DAQ is available. As a consequence the ARS STOP scaler gives N_{STOP} the number of analyzed events. Thus the deadtime correction η_{DT} is given by:

$$\eta_{DT} = \frac{N_{STOP}}{N_{HRS}}, \tag{3.8}$$

This correction is applied run-by-run and independently from the calorimeter being or not in the trigger. The deadtime is correlated to the trigger rate in a non-trivial way. As explained in section 2.3.5, the deadtime is mainly due to transfer of the ARS data. When the calorimeter is not in the trigger, all ARS STOP signals give an ARS VALID. As a consequence all ARS data are digitalized and transfered for all events. Including the calorimeter in the trigger is equivalent to pre-analyzing the events, usually called a level-2 trigger. The goal is to determine if it is worth transfering the data to increase the fraction of $ep \to e\gamma X$ events in the transfered data. As seen in table 3.2, even though the beam current has been multiplied by 2.2 for kin2high, the deadtime with the calorimeter in the trigger remains smaller than without the calorimeter in the trigger. Scalers are also subject to deadtime but it is negligible with respect to the averaged time between two events.

Kinematics	Beam current (μA)	Trigger rate (Hz)	Deadtime (%)
kin1low	2.97	79	6.5
kin1high	1.1	297	35
kin2low	3	165	8.5
kin2high	1.5/3.3	240/552	19.7/18
kin3low	3.45	118	7.7
kin3high	2.77	222	17.7

Table 3.2: Trigger rate and deadtime according to kinematics at a given beam current. For Kin2high, black is used for trigger without calorimeter, red for trigger with calorimeter.

3.3.3 Efficiency of S2 scintillator

In order to evaluate the efficiencies of the Čerenkov detector and S2, we took dedicated runs with different triggers. For Čerenkov and scintillator efficiency runs, the triggers are listed in the table 3.3.

Trigger	Logic	Measured efficiency
T3	$S1 \cap S2$	Čerenkov / Scintillators
T4	$\overline{T3} \cap \text{Cer} \cap (S1 \cup S2)$	Scintillators

Table 3.3: Table summarizing the two triggers for efficiency. For each event of an efficiency run, we know the trigger which fired the DAQ. $\overline{T3}$ is the boolean complementation of $T3$.

To compute the efficiency of the scintillators, we need first to create a sample of particles detected by the Čerenkov. Therefore we only keep events with a number of Čerenkov ADC channels above 500. Thus the efficiency of S2 (η_{S2}) can be defined as:

$$\eta_{S2} = \frac{N_{SSC}}{N_{S1C}}, \tag{3.9}$$

where N_{S1C} is the number of events detected only by S1 and the Čerenkov detector, whereas N_{SSC} is the number of events detected by both scintillators and the Čerenkov detector. N_{SSC} is simply given by the number of T3 events passing the cut on the Čerenkov. Since we have:

$$S1 \cap Cer = (S2 \cap S1 \cap Cer) \cup (\overline{S2} \cap S1 \cap Cer), \tag{3.10}$$

N_{S1C} is given by the sum $N_{SSC} + N_{S1C\overline{S2}}$ and we obtain:

$$\eta_{S2} = \frac{N_{SSC}}{N_{SSC} + N_{S1C\overline{S2}}}. \tag{3.11}$$

$N_{S1C\overline{S2}}$ is the number of T4 events with no hit in S2, passing the Čerenkov cut. The efficiency of S2 was found to be around 99.9% during all the experiment.

3.3.4 Efficiency of the Čerenkov detector

To compute the Čerenkov detector's efficiency, we use the T3 trigger introduced in table 3.3. It corresponds to a particle, an electron or a pion, detected by both S1 and S2. We want to evaluate the fraction of electrons passing the analysis cut applied in section 3.2.3.1.

We create an electron sample by applying a cut on the energy deposit in the PR. We note N_{PR} the number of electrons selected by this cut. N_{Cer} is the number of electrons in the sample passing the software cut. Thus the Čerenkov efficiency is given by the following ratio:

$$\eta_{Cer} = \frac{N_{Cer}}{N_{PR}} \tag{3.12}$$

Applying this method, the Čerenkov efficiency was found to depend on the central momentum of the HRS.

Kinematics	Momentum in HRS (GeV/c)	η_{Cer}	η_{Cer}^{cor}
kin1low	1.136	95%	98.5%
kin3low	1.494	94%/97%	95%/98.5%
kin2low	1.864	98%	98.5%
kin3high	2.59	98.5%	98.5%
kin2high	2.96	98.5%	98.5%
kin1high	3.332	98.6%	98.6%

Table 3.4: Čerenkov Efficiency according to the different kinematics. The kinematics are presented with increasing HRS central momentum. The red numbers are results for the runs with high threshold for the Čerenkov detector.

However a cut on the energy in the PR is not enough to get a pure sample of electrons, especially at low HRS central momentum. Indeed pions have a small probability to create hadronic showers and thus lose all of their energy in the PR. We have to evaluate this contamination in order to correct for this bias. The PR spectrum of our sample was fitted with the sum of a skewed gaussian distribution S(E) for the electrons and a second order polynomial P(E) for the pions (Figure 3.5).

$$S(E) = C \left[\frac{p}{\sqrt{2\pi}\sigma} e^{\frac{-(E-\mu)^2}{2\sigma^2}} + (1-p)\frac{\alpha}{2\sigma} e^{\frac{-\alpha^2}{4}} e^{\alpha\frac{E-\mu}{\sigma}} \left\{ 1 + erf\left(\frac{-(E-\mu)}{\sigma} \right) \right\} \right] \tag{3.13}$$

where μ and σ represent the position and the width of the electron peak. p and α stand for the height and the length of the tail [51]. We define the efficiency for the PR η_{PR}
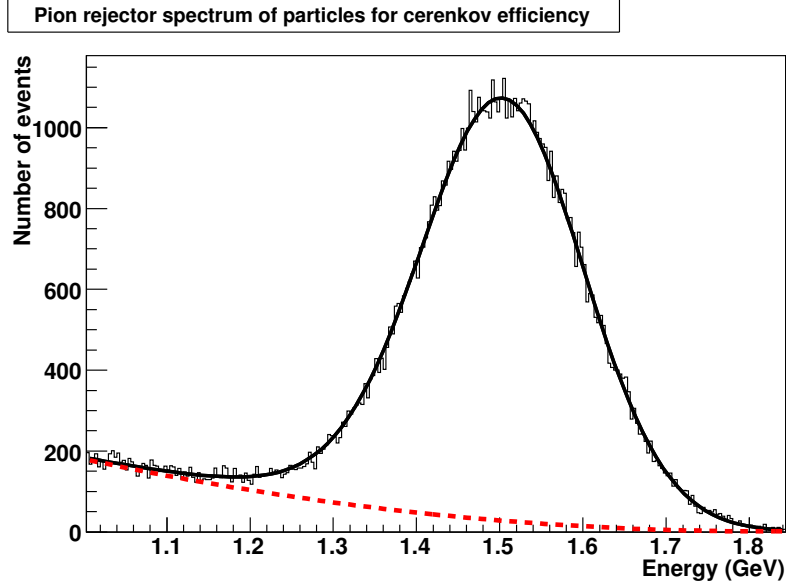
Figure 3.5: PR spectrum for kin3low. The result of a fit using the sum of an asymmetric gaussian (electrons) and a 2nd-order polynomial (pions) is also shown.

corresponding to the purity of the sample. η_{PR} is estimated by applying a cut E_s on the energy deposit E in the PR:

$$\eta_{PR}(E_s) = 1 - \frac{\int_{E_s}^{E^{kin}} P(E)dE}{\int_{E_s}^{E^{kin}} P(E) + S(E)dE} \ , \tag{3.14}$$

where E^{kin} represents the root of the polynomial corresponding to the maximum value of the energy deposit. Figure 3.5 represents the spectrum for kin3low, and $E^{kin} \sim 1.84$ GeV for kin3low. The actual number of electrons N_{e^-} in the sample is given by the product $N_{PR} \times \eta_{PR}$. Correcting η_{Cer} with η_{PR} gives an efficiency of 95% for the first two weeks of experiment and then a stable value of 98.5%.
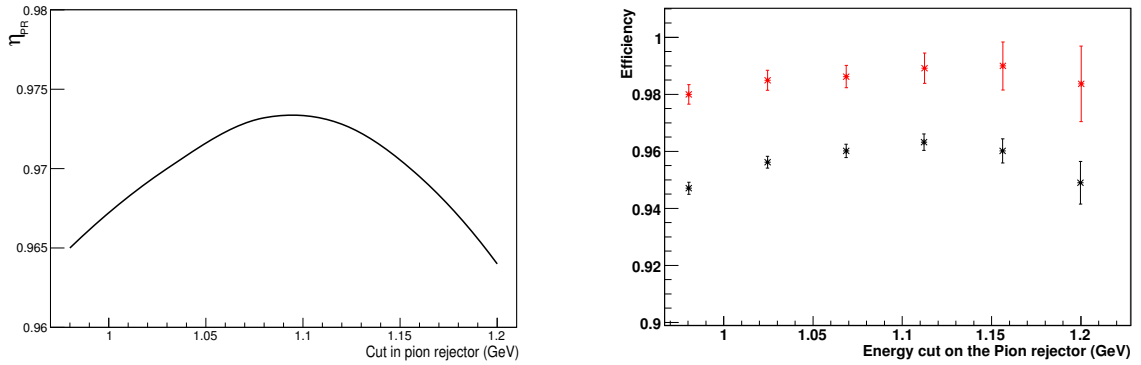
Figure 3.6: Left, η_{PR} for setting kin1low as a function of the cut applied on the PR energy deposit. Right, the black points represent η_{Cer} and the red points $\eta_{Cer}^{cor} = \frac{\eta_{Cer}}{\eta_{PR}}$. The corrected efficiency η_{Cer}^{cor} is more stable than η_{Cer} with respect to the cut on the PR. Finally we associate a 0.5% systematic error on the Čerenkov efficiency, coming from the dependence on the energy deposit cut of η_{Cer}^{cor}.

3.4 Monte-Carlo simulation

The last term of the equation 3.1 to be evaluated is Γ_{DIS}. It represents the phase space covered by the HRS. Γ_{DIS} depends on the HRS acceptance but also on any cut we perform to select events. To determine it, we use a Monte-Carlo simulation consisting in generating events in a phase space Γ_{MC} whose volume is known. Γ_{DIS} is then simply given by:

$$\Gamma_{DIS} = \Gamma_{MC} \times \frac{N_{acc}}{N_{gen}} \qquad (3.15)$$

where N_{gen} is the number of generated events and N_{acc} the number of events detected by the HRS according to the simulation. Because of the energy losses by radiative effects and the detector resolutions, Γ_{DIS} is vast. Consequently Γ_{MC} has to be taken large enough and the simulation has to consider radiative effects and detector resolutions in order to correct for them.

This Monte-Carlo simulation is based on a C++ code written for the E97-110 experiment analysis [52]. In this code, most of the Hall A experimental setup was included. It has been adapted to our experimental setup and our kinematics. An event generator for inclusive DIS events has been implemented, including radiative corrections. For clarity, I am going to introduce first the radiative effects before the Monte-Carlo simulation.

3.4.1 QED radiative effects

Dealing with an electron beam has a lot of advantages such as the ability to reach high luminosity. However, because of its very light mass, an electron easily radiates photons. This emission of photons occurs when the electron goes trough matter: in that case, they are said *external*. But this emission of photons also happens at the vertex, they are said *internal*. We will first explain how the external photon emission is implemented. Then we will describe the internal radiative effects and how they are corrected.

3.4.2 External radiative corrections

The external radiative effects are radiation of a real photon by the electron when it goes through matter. This effect is also known as Bremsstrahlung. The energy loss by an electron of energy E_0, through a material thickness t_{mat} given in units of radiation length, will follow the distribution [53] ($b \simeq 4/3$):

$$I(E_0, \Delta E, t_{mat}) = \frac{bt_{mat}}{\Delta E} \left[\frac{\Delta E}{E_0} \right]^{bt_{mat}}, \qquad (3.16)$$

Inverting the previous relation, we get an energy loss ΔE to simulate event-by-event, material by material, with the following relation:

$$\frac{\Delta E}{E_0} = r^{1/bt_{mat}}, \qquad (3.17)$$

with r generated uniformly in $[0; 1]$. We apply the energy loss within the peaking approximation: the radiated photon is emitted along the electron direction.

3.4.3 Internal radiative corrections

Photons emitted at the vertex may be real (bremsstrahlung) or virtual. We present here the radiative corrections for *ep* elastic scattering. It represents a good approximation for
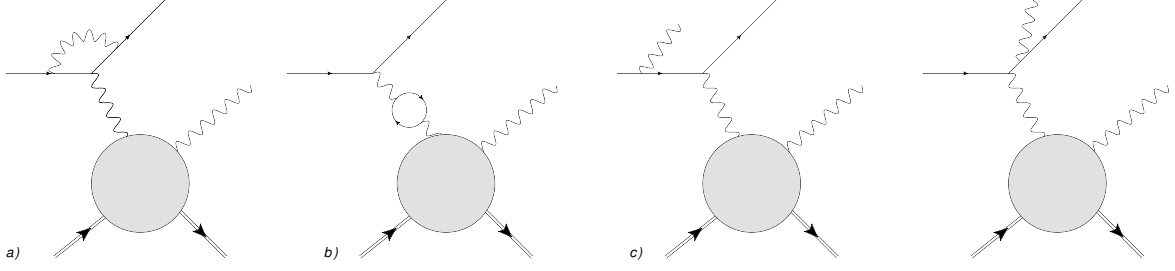
Figure 3.7: First order internal radiative corrections illustrated in the case of DVCS.

DIS, DVCS or DVMP since all these corrections are taking place on the leptonic part of the diagram which is the same for elastic scattering.

At first order in QED, there are three radiative processes:

- The vertex correction (Figure 3.7 (a)): the electron emits a photon before scattering, which will change its momentum. Then this photon will be reabsorbed by the scattered electron.

- The vacuum polarization (Figure 3.7 (b)): the virtual photon turns into a electron-positron pair.

- The internal bremsstrahlung (Figure 3.7 (c)): A real photon is emitted by either the incoming or outgoing electron.

As a consequence, the measured cross section is an interference of the Born process with diagrams (a,b) in addition to a contribution from the internal bremsstrahlung diagram. Each diagram iterated to all orders, we obtain the following relation between the measured and the Born cross sections [54]:

$$\sigma_{exp} = \sigma_{Born} \frac{e^{\delta_R + \delta_{ver}}}{(1 - \delta_{vac})^2}, \tag{3.18}$$

with:

$$\delta_{vac} = \frac{\alpha}{3\pi} \left[\ln\left(\frac{Q^2}{m_e^2}\right) - \frac{5}{3} \right], \tag{3.19}$$

$$\delta_{ver} = \frac{\alpha}{\pi} \left[\frac{3}{2} \ln\left(\frac{Q^2}{m_e^2}\right) - 2 + \frac{\pi^2}{6} - \frac{1}{2} \ln^2\left(\frac{Q^2}{m_e^2}\right) \right], \tag{3.20}$$

$$\delta_R = \frac{\alpha}{\pi} \left[Sp\left(\cos\frac{\theta_e}{2}\right) - \frac{\pi^2}{3} + \frac{1}{2} \ln^2\left(\frac{Q^2}{m_e^2}\right) \right] + \frac{\alpha}{\pi} \ln\left(\frac{(\Delta E)^2}{EE'}\right) \left[\ln\left(\frac{Q^2}{m_e^2}\right) - 1 \right], \tag{3.21}$$

Looking at Eq 3.21, we can separate a term dependent on the energy loss ΔE and another which depends only on Q^2. We can then rewrite the exponential of the internal bremsstrahlung term:

$$e^{-\delta_R} \sim e^{-\delta_R^{(0)}} \times \left(\frac{\Delta E}{E}\right)^{\delta_R^{(1)}} \left(\frac{\Delta E'}{E'}\right)^{\delta_R^{(1)}}, \tag{3.22}$$

with the definitions:

$$\delta_R^{(0)} = \frac{\alpha}{\pi} \left[Sp\left(\cos\frac{\theta_e}{2}\right) - \frac{\pi^2}{3} + \frac{1}{2} \ln^2\left(\frac{Q^2}{m_e^2}\right) \right], \tag{3.23}$$

$$\delta_R^{(1)} = \frac{\alpha}{\pi} \left[\ln\left(\frac{Q^2}{m_e^2}\right) - 1 \right] \tag{3.24}$$

The term $\left(\frac{\Delta E}{E}\right)^a$ can be interpreted as the fraction of incoming electrons losing an amount of energy ΔE. We can derive a distribution I_{int} such that:

$$\int_0^{\Delta E} I_{int}(E, X, \delta_R^{(1)}) dX = \left(\frac{\Delta E}{E}\right)^{\delta_R^{(1)}}, \tag{3.25}$$

$$I_{int}(E, \Delta E, \delta_R^{(1)}) = \frac{\delta_R^{(1)}}{\Delta E}\left(\frac{\Delta E}{E}\right)^{\delta_R^{(1)}}, \tag{3.26}$$

We recognize the equation 3.16 in 3.26 with an equivalent radiator thickness $\delta_R^{(1)}$. Thus, to reproduce the energy loss by internal bremsstrahlung, we are going to apply the same method as for the external case, presented in subsection 3.4.2. It will be applied two times: once for the incoming and another time for the outgoing electron.

One can notice that we need to know Q^2 to compute $\delta_R^{(1)}$. But Q^2 can only be computed after having lost the energy by internal Bremsstrahlung. A method to resolve this ambiguity is presented later in the section dedicated to the event generator.

Finally, the value of the logarithm in Eqs (3.19)(3.20)(3.23) is almost constant from $Q^2 = 1.5$ GeV^2 to $Q^2 = 2.3$ GeV^2. For all the kinematics we take:

$$\eta_{virt} = \frac{e^{\delta_R^{(0)} + \delta_{ver}}}{(1 - \delta_{vac})^2} = 1.072. \tag{3.27}$$

3.4.4 Computation of Γ_{DIS} using Monte-Carlo

The Monte-Carlo simulation for the computation of Γ_{DIS} can be split into two parts:

- The event generator, responsible for generating all kinematic configurations compatible with the acceptance of our experiment. In addition radiative effects need to be taken into account. Energy losses and the kinematics of the scattering events have to be compatible. Therefore there is a list of steps that have to be executed in a specific order.

- The transport of the electron from the vertex to the HRS entrance. We have to include all materials between the vertex and the HRS to simulate all the energy losses. Inside the HRS, the electron is in vacuum until it reaches the focal plane.

3.4.4.1 Event generator

As we mentioned before, Γ_{DIS} depends on the acceptance of the spectrometer, a complicated hypervolume of four variables. In order to compute it, we generate events in the full target length and in a solid angle $\Delta\Omega$ larger than the solid angle covered by the HRS.

We first generate the vertex v_z. It determines the thickness of target material before the scattering process. We then use the procedure described in 3.4.2 to compute the energy loss by going through the upstream aluminum cell window and liquid hydrogen. We obtain the electron energy E_v^{ext} which can be much lower than E the beam energy. Then we generate $\cos\theta_e$ and ϕ_e in ranges large enough to cover the full geometrical acceptance of the spectrometer.

Once the direction of the scattered electron is determined, we generate the energy after scattering. However, because of the energy losses, the kinematics of the scattering process can be far different from the central HRS kinematics. The phase space at the vertex of the detected events is vast, including elastic scattering associated with an important energy loss. Therefore we consider a large range for the scattered electron energy, going from the lowest
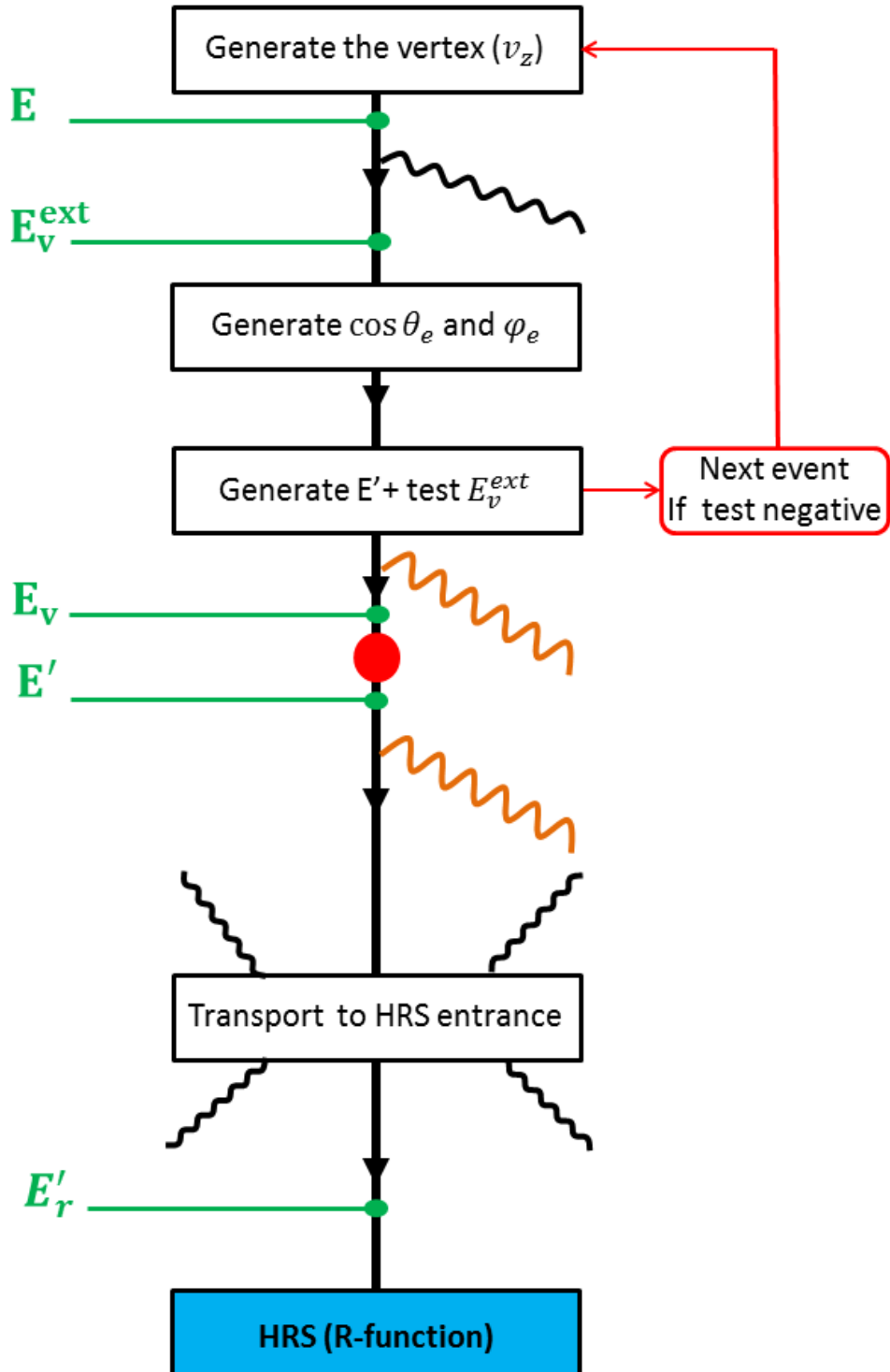
Figure 3.8: Diagram representing the main steps of the Monte-Carlo simulation. Escaping photons represents energy losses either by external (black) or internal (orange) bremsstrahlung. We specifiy the energy of the electron in green.

detectable energy to the highest possible energy given by elastic scattering. The range $\Delta E'$ is thus defined as follows:

$$\Delta E' = [\, 0.94\, p_{HRS};\ E_{el}(E_v^{ext}, \theta_e)\,]\,, \tag{3.28}$$

$$E_{el}(E_v^{ext}, \theta_e) = \frac{E_v^{ext}}{1 + 2\frac{E_v^{ext}}{M}\sin^2(\theta_e/2)}\,, \tag{3.29}$$

where p_{HRS} and E_{el} respectively stand for the HRS central momentum and the energy of an elastically scattered electron. For a small fraction of events, E_{el} is smaller than $0.94\, p_{HRS}$ because of a very low E_v^{ext}. In that case, the event is considered as lost.

Once E' and the scattering angle are generated, we simulate the internal bremmstrahlung as presented in 3.4.2. However generating r in $[0;1]$ may lead to an energy loss before scattering which is incompatible with the generated scattering angle and E'. The idea is to consider that internal bremsstrahlung occurs only if the scattering process occurs. Therefore, to avoid this situation of impossible events, r is no longer generated in $[0;1]$ but $[0; r_{lim}]$ with r_{lim} defined as:

$$r_{lim} = \left(1 - \frac{E_{lim}}{E_v^{ext}}\right)^{\delta_R^{(1)}}. \tag{3.30}$$

E_{lim} is the lowest energy of the incoming electron allowing to get the generated scattered electron. It is given by $E' = E_{el}(E_{lim}, \theta_e)$. As we do not know the Q^2-value of the event yet, we evaluate $\delta_R^{(1)}$ at our nominal kinematics. After the first energy loss by internal bremsstrahlung, the incoming electron is left with an energy E_v for the scattering process. For the internal post-scattering bremsstrahlung, we generate r in $[0;1]$ that we apply to E'. Finally, the radiation lengths of the various materials crossing the path of the electron between the vertex and the HRS entrance are evaluated using the setup geometry. We then apply the method in subsection 3.4.2 to estimate the resulting energy losses.

Once the electron reaches the spectrometer, we smear the position of the vertex to simulate the resolution of the spectrometer. All the analysis cuts are then applied on the "reconstructed" kinematic variables at the entrance of the HRS to compute the phase space volume Γ_{DIS}. Since the phase space factor $\Gamma_{MC} = \Delta\cos\theta_e \Delta\phi_e \Delta E'$ depends on the energy E_v^{ext}, Γ_{DIS} is defined such that:

$$\Gamma_{DIS} = \frac{1}{N_{gen}} \sum_{i \in \mathcal{C}} \Gamma_{MC}^i \tag{3.31}$$

where the sum is over the events passing the set of analysis cuts $\mathcal{C}$ and N_{gen} is the total number of generated events.

3.4.5 Unfolding acceptance and radiative effects

We are interested in extracting deep inelastic cross section at our nominal kinematics. However, even if the acceptance of the spectrometer is small, events are spread over a large range of Q^2 and x_B. Moreover radiative effects may move events which are outside the HRS acceptance into it.

In conclusion, we do not control the kinematics at which the cross section is extracted. To recover the cross section at the nominal values, we compute a coefficient α to correct for the kinematic deviation and defined such as:

$$\int_{\Gamma_{DIS}} \frac{d\sigma}{d\Omega dE}(Kin_v)d\Omega dE = \alpha \times \frac{d\sigma}{d\Omega dE}(Kin_{HRS}) \times \Gamma_{DIS}\,, \tag{3.32}$$
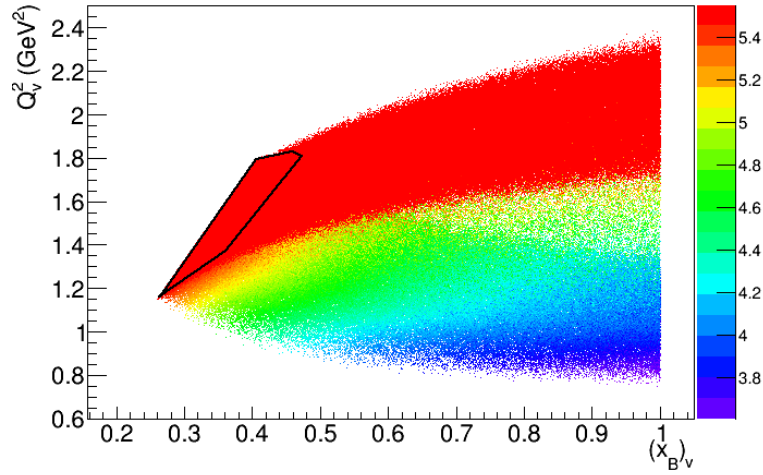
Figure 3.9: Distribution of vertex Q_v^2 and $(x_B)_v$ for events detected in the HRS. The color scale represents the energy just before scattering, after external and internal bremsstrahlung. The black contour represents the acceptance of the HRS: all events have been reconstructed at kinematic values inside the HRS acceptance. The migration exhibits two branches corresponding to two important energy losses: the low and high-energy incoming electron events. The two branches are the result of the peaking approximation and the two-step internal bremsstrahlung.

with Kin_v stands for the vector $(E_v, Q_v^2, (x_B)_v)$ and Kin_{HRS} for the nominal kinematics vector $(E, Q_{HRS}^2, (x_B)_{HRS})$. Then one straightforwardly gets:

$$\alpha = \frac{1}{\Gamma_{DIS} \times \frac{d\sigma}{d\Omega dE}(Kin_{HRS})} \sum_{i \in \mathcal{C}} \frac{d\sigma}{d\Omega dE}(Kin_v^i)\Gamma_{MC}^i \tag{3.33}$$

It is striking from eq. 3.33 that we need a parametrization of the cross section in order to disentangle acceptance and radiative effects.

3.4.6 Parametrization of DIS cross section

The DIS cross section has been measured for a large set of kinematics over the past fifty years. These data have been used by various groups to parametrize the structure functions F_1 and F_2, allowing us to compute the DIS cross section for our kinematics. But most of these data are at much higher Q^2 and lower x_B where higher twist contributions are suppressed. As seen on Figure 3.9, scattering events occuring at low Q^2 values of about ~1 GeV^2 might be detected. To correct for these events in the HRS, the cross section parametrization must include these higher twist contributions no longer suppressed at 1 GeV^2.

Table 3.5 shows the predictions for the DIS cross section for two different structure function parametrizations. To unfold radiative effects and as reference, we use the parametrizations of F_1 and F_2 taking into account target-mass corrections [56], adapted for JLab kinematics.

3.5 Results

The extraction of the DIS cross section allows us to conclude on two different aspects of data quality. The first one is to get a stable cross section over the runs of the same kinematic

x_B	Q^2 (GeV²)	E^{beam} (GeV)	Name	$\frac{d\sigma^{NMC}}{d\Omega dE}$ (nb/GeV/sr)	$\frac{d\sigma^{TMC}}{d\Omega dE}$ (nb/GeV/sr)
0.36	1.5	3.355	Kin1low	9.16	9.0
		5.55	Kin1high	56.1	55.2
	1.75	4.455	Kin2low	13.4	13.14
		5.55	Kin2high	29.4	28.93
	2	4.455	Kin3low	6.7	6.6
		5.55	Kin3high	16.1	15.93

Table 3.5: Comparison of the DIS cross sections for the NMC [55] and TMC parametrizations [56].

setting. This gives us information about some systematic errors. The other one is the quality of the normalization by comparing our theoretical and experimental results averaged over all runs of a setting. This comparison revealed many problems needing a particular solution and helped in elaborating a good run list. After fixing them, the extracted cross section agrees with the theoretical prediction within 5%.

3.5.1 Stability and systematic errors

Except for the first kinematic setting kin3low, the run-by-run DIS cross section is stable and stays between ± 2.2% of the global value extracted from all runs (Figure 3.10). A few runs have been removed from the data analysis for two main reasons:

- the scalers counting the number of triggers for the deadtime were not read correctly or encountered a problem. Therefore the deadtime was miscalculated for isolated runs which were removed from the final analysis.

- the BCMs were experiencing electronic problems due to radiation damages. Indeed the PRex experiment ran just before our experiment, using the electron beam on a lead target. The induced radiations damaged the electronics of the BCMs. As a consequence their gain was drifting or suddenly jumping, as seen on Figure 3.10 for kin2low around run 8660. Problematic runs were removed from the analysis. However, the different BCMs sometimes disagreed by 2%. Consequently we have decided to average the measurement of both BCMs and to attribute a 2% systematic uncertainty on the charge.

Concerning the kin3low setting, the threshold on the Čerenkov detector to trigger the DAQ was lowered starting from run 8202. Despite the efficiency correction, the extracted DIS cross section changes by 4% and no clear reason was found. Several factors may explain this: the BCMs should have been regulated in temperature, but they were not at this time of the experiment. Their gain are known to change by +1.3% with a 1F temperature increase. Since the experiment stopped for several hours between runs 8202 and 8215, the temperature may have decreased slightly in the hall. A 1.5°C-variation would induce a 4% change in the cross section. As no thermal regulation were applied for this specific kinematic setting, a 4%-systematic error on the charge must be apply on the kin3low set.

Concerning the HRS acceptance, the DIS cross section does not change by more than 1% when increasing the cut on the R-value from 5 msr to 20 msr. As a consequence we assign a systematic error of 1% to the HRS acceptance.

In conclusion, the charge and the radiative corrections represent the most significant contributions to the total systematic error. All these errors need to be taken into account in the π^0/DVCS data analysis.
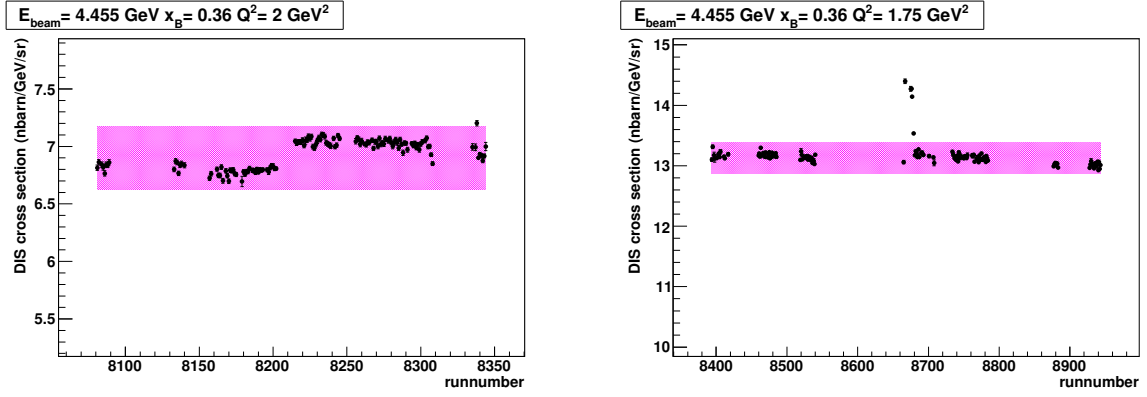
Figure 3.10: DIS cross sections calculated run by run for kin3low (left) and kin2low (right). The magenta band represents the stability of the extracted value given in table 3.7.

	Systematic errors
Charge	2%
Deadtime	1%
Detector efficiency	1%
Multitrack events	0.5%
HRS acceptance	1%
Radiative corrections	2%
Quadratic total	4.5%

Table 3.6: Table of systematic errors for the DIS cross section.

3.5.2 Quality of the normalization factor

The difference between the theoretical prediction and the extracted cross section remains below 5%. However it appears that the cross section tends to be overestimated for low beam energy settings, whereas it is underestimated for high beam energy ones. After having carefully studied all cuts applied for the analysis and found no explanation for this fact, we conclude that it must be a systematic effect arising from global normalization parameters such as the deadtime correction and/or the charge measurement.

Kinematics	$\frac{d\sigma^{TMC}}{d\Omega dE}$	$\frac{d\sigma^{TMC}_{exp}}{d\Omega dE}$	Relative difference (%)	Stability (%)
Kin1low	9.0	9.26	+2.8	1.6
Kin1high	55.2	53.3	-3.4	1.3
Kin2low	13.14	13.14	0	2
Kin2high	28.93	27.9	-3.4	1.3
Kin3low	6.6	6.9	+4.5	4
Kin3high	15.93	15.26	-4	2.2

Table 3.7: Table summarizing the theoretical and the extracted values of the DIS cross sections for both parametrizations.

Although the total systematic error is higher than the discrepancy between theory and experiment, this systematic effect between low/high energy kinematics may have significant consequences on the Rosenbluth separation.

Chapter 4

DVCS data analysis

Whereas the previous chapter focused on the 2010 run period, this chapter is dedicated to the 2004 experiment. The HRS did not change between the two run periods, except for the collimator which was not used in 2004. To extract the photon electroproduction cross section, we follow the same procedure as for the DIS process. In this chapter, we first develop the calorimeter analysis and the characterization of the photons. Then we describe the set of cuts applied to select exclusive photon events. We also discuss the corrections and the calculation of the luminosity. Concerning the Monte-Carlo simulation, it will be described in length in Chapter 5.

4.1 Calorimeter analysis

The calorimeter analysis is done in two steps: first, the recorded ARS waveforms are analyzed in order to extract the time and energy information. Then, an algorithm is used to aggregate the block information into photon clusters with a measured position, time and total energy.

4.1.1 Waveform analysis

All the detector channels of the electromagnetic calorimeter were equipped with ARS electronics, which allowed us to save the full waveform of blocks that were recorded during a trigger, in a manner similar to a digital oscilloscope. In order to extract time and amplitude information from the ARS, a waveform analysis is needed and performed offline.

The waveform fit algorithm is based on the assumption that the signal *shape* is independent of its amplitude. For an ideal event without noise, the amplitude of the pulse and its arrival time are free parameters. For any given arrival time t, the amplitude $a(t)$ which best fits the signal $\{x_i\}$ is simply given by the one which minimizes:

$$\chi^2(t) = \sum_{i_{min}}^{i_{max}} (x_i - a(t)h_{i-t} - b(t))^2 \,, \tag{4.1}$$

where $\{h_i\}$ is the reference shape. Notice that we also fit a flat baseline $b(t)$. Reference shapes for each individual PMT are determined experimentally from data, using elastic calibration runs, where the probability of pile-up is very small. In order to reduce the impact of accidental events, only $i_{max} - i_{min} = 80$ ARS samples were used in the calorimeter analysis. These 80 ns are around the expected arrival time of DVCS events, which because of cable lengths, varies slightly from one channel to another. The partial derivatives of $\chi^2(t)$ with respect to $a(t)$ and $b(t)$ yield a linear set of equations in order to obtain the best amplitude for any given arrival time t. If the minimum value of $\chi^2(t)$ found for all the possible t is

above a given analysis threshold χ_1^2, the algorithm will fit a second pulse to the waveform by minimizing:

$$\chi^2(t_1, t_2) = \sum_{i_{min}}^{i_{max}} (x_i - a_1(t_1, t_2)h_{i-t_1} - a_2(t_1, t_2)h_{i-t_2} - b(t_1, t_2))^2 \,, \tag{4.2}$$

for every combination of t_1 and t_2. For every pair of t_1 and t_2 and the corresponding fitted amplitudes and baseline, a reduced χ^2 is also computed in a time window of $\pm 20\,\text{ns}$ around the minimum of the pulse. The minimum reduced χ^2 found determines the amplitudes and arrival times of the pulses. Pulses were searched in a $[-20, 25]\,\text{ns}$ interval around the expectation arrival time of events, by steps of $1\,\text{ns}$. Increased time resolution is obtained by interpolating around the time that minimizes the χ^2 for any time $t = t_1, t_2$:

$$t = t(\chi_{min}^2) + \frac{\chi_{t-1}^2 - \chi_{t+1}^2}{2(\chi_{t+1}^2 + \chi_{t-1}^2 - 2\chi_{min}^2)} \,. \tag{4.3}$$

The threshold value χ_1^2 used for the analysis corresponded to an effective missed pulse of around $280\,\text{MeV}$ for each particular calorimeter block (which translates to slightly different ARS channel thresholds due to the different calibration of each block). Also, if the χ^2 of a fit by a flat-line b was below an equivalent energy of about $\chi_0^2 \sim 40\,\text{MeV}$, no pulse was fitted and the signal was discarded. Finally, if 2 pulses were found with a relative arrival time smaller than $4\,\text{ns}$, the algorithm returns the best single pulse fit since results proved to be unstable in those cases.

4.1.2   Calorimeter calibration

The crystal-by-crystal calibration coefficients were obtained from kinematically over-constrained elastic scattering: $\text{H}(e, e'_{\text{Calo}} p_{\text{HRS}})$ in which the electron is detected in the calorimeter and the proton is detected in the HRS. The calibration procedure is explained in subsection 3.2.3.2, except that the energy of the electron is given indirectly by the momentum of the recoil proton. In order to illuminate the full acceptance of the calorimeter with elastic electrons, it was necessary to move the calorimeter back to a distance of 5.5 m from the target center during these runs. However, data at 1 m, covering only the center part of the calorimeter were taken nonetheless as a consistency check. Fig. 4.1 shows the energy resolution of the calorimeter as measured during the elastic calibration runs. Two elastic calibrations were made, one a few weeks after the start of the experiment and another one a few weeks before it finished. Calibration coefficients changed by a considerable amount for some blocks, but the energy resolution did not degrade during the almost 3 months of data taking: a value of 2.4% at 4.2 GeV was measured during both calibrations. Since calibration coefficients changed with time, in order to keep a good energy resolution all along the experiment, we interpolated these coefficients between the two calibrations runs, together with an extrapolation before and after them. This was done based on the radiation dose accumulated by each block. This dose is proportional to the beam current and depends on the block polar angle with respect to the beam line and also on the target type (LH_2 or LD_2). An estimate of relative dose accumulation for each block was made using the anode current monitoring for each crystal PMT [57].

4.1.3   Clustering algorithm

The algorithm used to separate clusters in the electromagnetic calorimeter is based on a cellular automata, as described in [58], and uses only pulses arriving within a [-3,3] ns
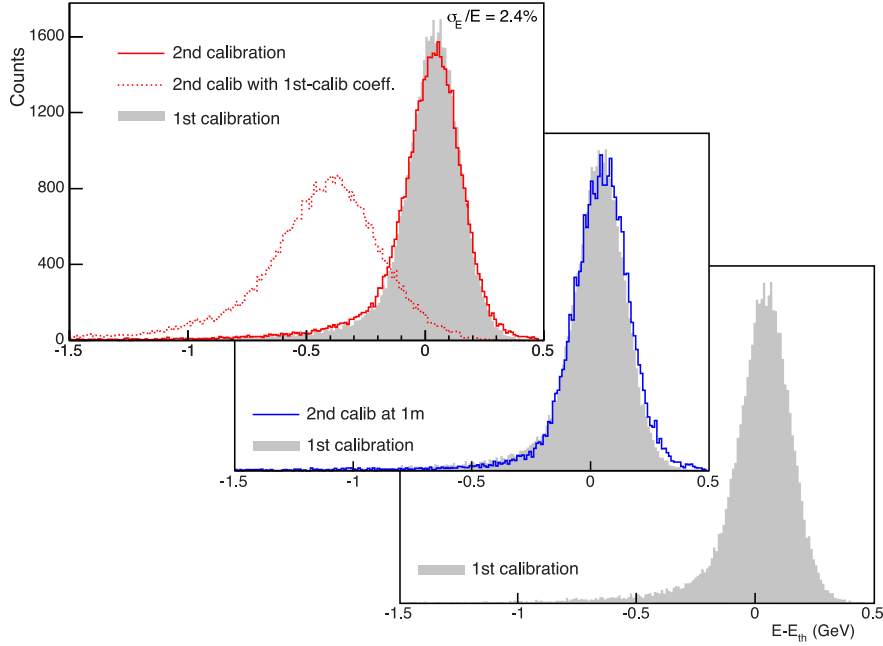
Figure 4.1: Energy measured in the calorimeter minus energy expected from elastic kinematics during elastic calibrations runs. In both elastic calibrations periods, we obtained 2.4% energy resolution at elastic energy 4.2 GeV. The results of the second calibration when first calibration coefficients are used are also plotted to show the necessity of a careful monitoring of the coefficients in between these two calibration points.

interval. This coincidence time window is more than 3 times the time resolution of the detector (~0.8 ns). For each cluster found, the photon total energy E is taken to be the sum over the deposited energy E_i in each of the cluster blocks:

$$E = \sum_i E_i \qquad E_i = C_i A_i \,, \qquad (4.4)$$

where A_i is the signal amplitude collected in block i and C_i its calibration coefficient. The impact position x_{clus} is calculated as the sum of blocks positions x_i weighted logarithmically by the relative energy deposition in each of them:

$$x_{clus} = \frac{\sum_i w_i \, x_i}{\sum_i w_i} \quad w_i = \max\left\{0, W_0 + \ln(E_i/E)\right\}. \qquad (4.5)$$

The parameter W_0 allows a further tuning of the relative weight between blocks: as $W_0 \to \infty$ the weighting becomes uniform regardless of the energy deposited in each block, whereas small values of W_0 give a larger relative weight to blocks with large energy deposition. The value of W_0 fixes the energy threshold for blocks to be taken into account in the position determination: blocks with a relative energy deposition less than e^{-W_0} are neglected in the calculation.

The calorimeter was placed at 110 cm from the 15-cm-long target. The incidence angle of particles on the front face of the calorimeter could therefore vary by significant amounts: corrections due to the vertex position in the target needed to be applied. Furthermore, the electromagnetic shower does not begin at the surface of the calorimeter, but at a certain depth. This depth is, in first approximation, independent of the incident particle energy. Taking these two effects into account, the position x_{clus} given by equation (4.5) is corrected
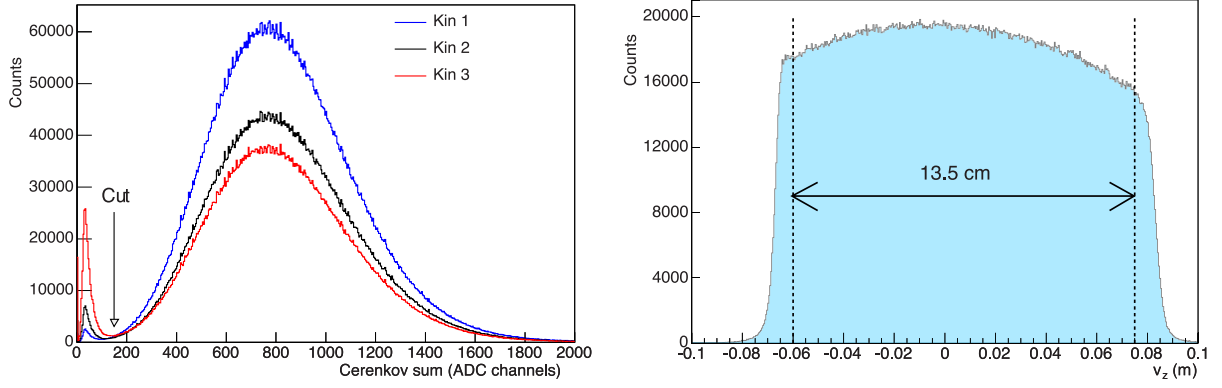
Figure 4.2: Left: Distribution of the sum of all 10 Čerenkov PMT ADC values, for each kinematic setting. The cut applied to remove the 1-photoelectron signal from data is also shown. Right: Reaction point along the beam reconstructed by the HRS. The cut on the target length applied is shown by the vertical lines. The figure shows the 7.8 mm downstream shift of the target during the experiment.

by:

$$x_{corr} = x_{clus}\left(1 - \frac{a}{\sqrt{L_{vc}^2 + x^2}}\right) \qquad (4.6)$$

where L_{vc} is the distance from the vertex to the calorimeter and a is the distance of the electromagnetic shower centroid to the calorimeter front face, taken along the direction of its propagation. The algorithm depends on two parameters W_0 and a, which have been optimized to $W_0 = 4.3$ and $a = 7$ cm by Monte-Carlo simulation and real data from the elastic runs, where a 2 mm position resolution (σ) at 1.1 m and 4.2 GeV was measured, compatible with the one obtained from Monte-Carlo simulations (3 mm at ∼3 GeV). Position resolution when two partially overlapping clusters are present is slightly worse than in the case of a single cluster: simulated data show in this case a 4 mm spatial resolution.

4.2 Selection of exclusive $ep \to ep\gamma$ events

Before computing any missing mass value, we apply a set of cuts on the HRS and the calorimeter to ensure a reliable reconstruction of the electron and photon momenta.

4.2.1 Electron selection

The HRS analysis is identical to the one performed for the DIS cross section. We require first single track events and apply a R-function cut at 5 mrad. The HRS Čerenkov detector was used for the electron identification. The number of photoelectrons detected is 7 on average, therefore the distribution is Poissonian. Fig. 4.2 shows the distribution of the sum of all 10 PMTs (in ADC channels). The first 'peak' in the spectrum is the tail of the electronic noise in the pedestal. We remove 1-photoelectron events (either thermal emission in the PMT or δ-rays from pions) by applying a cut at 150 ADC channels. The 1-photoelectron peak is only visible if the Čerenkov signal is removed from the trigger, and a cut is made on the Pion Rejector to select minimum ionizing particles (*i.e.* pions).

Fig. 4.2 shows the distribution of the reaction point along the beam v_z reconstructed by the HRS. The overall location of the target relative to the Hall center is 7.8 mm downstream. A cut in order to avoid the contribution from the target cell wall was applied to the data: -6.00 cm $< v_z < 7.50$ cm.

4.2.2   Photon selection

The $ep \to ep\gamma$ events are selected among the calorimeter 1-cluster events. The cluster has to be in coincidence with the HRS within 3 ns. A software threshold on the energy of the photon at $\sim$1.1 GeV enforces the hardware threshold which was equivalent to 1 GeV. Finally, since a typical shower develops in 9 adjacent blocks, only events whose cluster centroid resides in one of the inner blocks of the calorimeter are kept.

4.2.3   Exclusivity of the reaction

When the experiment was designed, the exclusivity was thought to be ensured by the detection of all particles in the final state. However, the constraints on the PA geometry (cutoff, surrounding the calorimeter) was greatly affecting the acceptance at small $|t|$ and ϕ=180°. As the resolution on the photon and electron are both fair, one could wonder if, depending on the background level (unknown at the time of the experiment), a cut on the missing mass $M^2_{ep \to e\gamma X}$ could be enough to select exclusive events.

To check this idea, the missing mass $M^2_{ep \to e\gamma X}$ has been computed for triple and double-coincidence events. After subtracting the π^0 contamination (explained later in subsection 4.3.2), the double-coincidence spectrum presented a fair agreement with the triple-coincidence spectrum (once rescaled) up to $\sim$1.1 GeV^2. It was the proof that a double coincidence electron/photon associated with a cut on $M^2_{ep \to e\gamma X}$ is sufficient to ensure the exclusivity. By removing the PA from the analysis, the acceptance was fuly recovered for small $|t|$-values and at ϕ=180° within the limit of the calorimeter geometry.
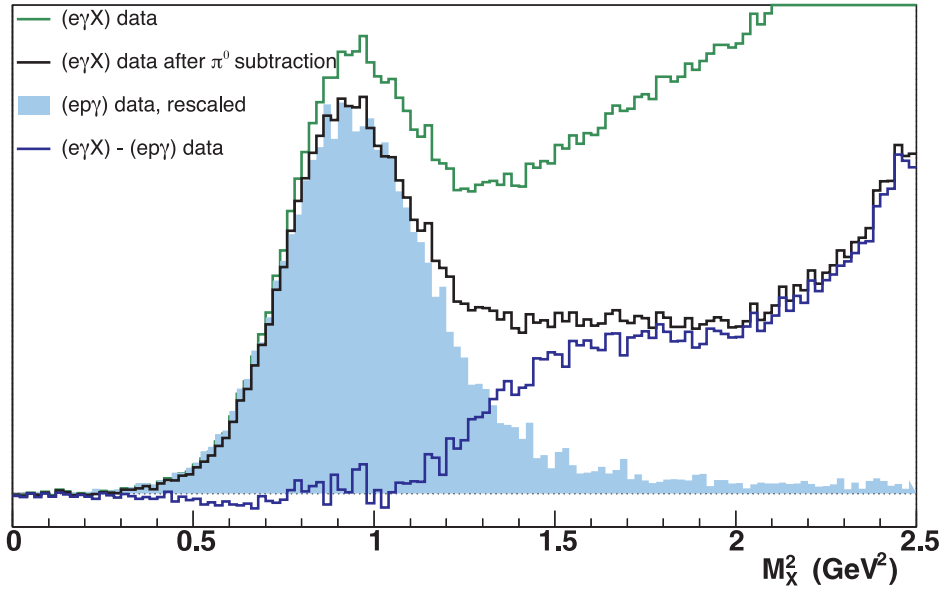
Figure 4.3: In green, missing mass spectrum $M^2_{ep \to e\gamma X}$ of $e\gamma$-coincidence events for 2004-Kin3. Once the π^0 contamination is subtracted from the green distribution, we obtain the black histogram. The blue shaded histogram represents $M^2_{ep \to e\gamma p}$ for triple coincidence events. The $M^2_{ep \to e\gamma p}$ distribution and the π^0-subtracted $M^2_{ep \to e\gamma X}$ distribution are in agreement up to $\sim$1.1 GeV^2. For missing-mass values higher than 1.1 GeV^2, the π^0-subtracted $M^2_{ep \to e\gamma X}$ includes some SIDIS events (blue histogram) such as $ep \to ep\gamma\pi$ events for which we missed the pion.

In the rest of this manuscript, the exclusivity will be ensured by applying a cut on the missing mass $M^2_{ep \to e\gamma X}$. Nevertheless some contamination remains in our event sample,

which needs to be subtracted

4.3 Contamination subtraction

The number of events below the cut can be written as the sum of three contributions:

$$N_{M_X^2 < M_{cut}^2} = N_{ep->ep\gamma} + N_{acc} + N_{\pi^0-1\gamma} + N_{SIDIS} \ , \tag{4.7}$$

with:

- $N_{ep\to ep\gamma}$ number of events from DVCS+BH, the one we want to evaluate.

- N_{acc} number of events in which the photon is coming from the background and is not related to the scattering process.

- $N_{\pi^0-1\gamma}$ number of events in which the detected photon is coming from a π^0 decay.

- N_{SIDIS} number of semi-inclusive events. Among these events, we have for instance $ep \to ep\gamma\pi$ events for which we missed the pion (see Figure 4.3).

4.3.1 Accidental subtraction

Although in coincidence, the photon in the calorimeter and the electron in the HRS are not necessarily related to each other. To estimate the contribution of these accidental events, we perform the clustering in the time window [-11;-5] ns, where all events are accidental. As the probability for accidental events does not depend on the time, the number of events in [-11;-5] ns is equal to the number of accidental events in [-3;3]. In order to reduce the statistical uncertainty on the number of accidentals, we average the number of events in [-11;-5] ns and [5;11] ns, as shown on Fig. 4.4.
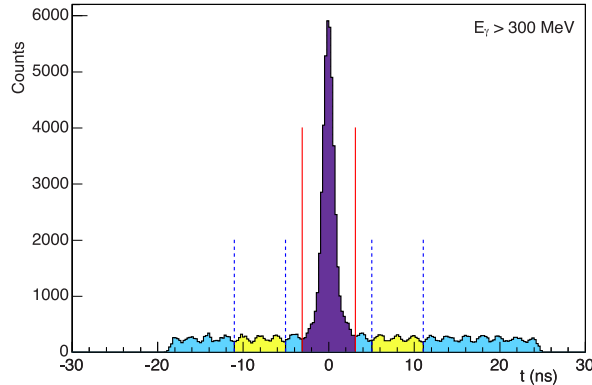
Figure 4.4: Time spectrum of blocks with $E > 300$ MeV in kinematic 3. It shows the 45 ns time window of waveform analysis. The 2 ns CEBAF beam structure can be seen. The coincidence [-3,3] ns window used for clustering is shown by the solid line. Dashed lines show windows used for HRS–calorimeter accidental subtraction. Right: Missing mass spectrum of events in [-3;3] (black) and accidental (red) events for kin3.

On the missing mass spectrum in Fig. 4.5, we notice that accidental events are responsible of the low missing mass tail. To increase the signal-over-background ratio and therefore reduce the uncertainty from the accidental subtraction, we require a missing mass value higher than 0.5 GeV^2 for the data. The accidental events mostly affect the bins around $\phi=0°$ or $\phi=360°$ as seen on Fig. 4.5, located on the beam side where the singles rate is the highest.
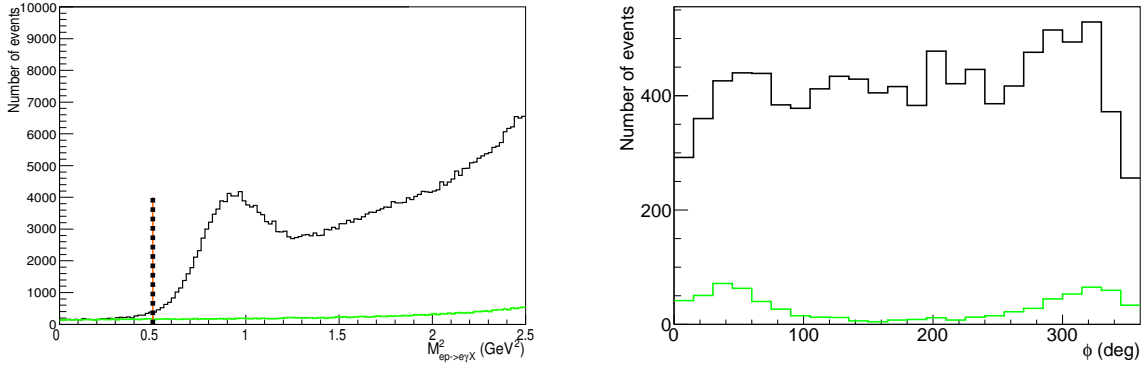
Figure 4.5: Left: Missing mass spectrum of events in [-3;3] (black) and accidental (green) events for kin3. Right: In black, the total number of events in [-3;3] ns remaining after all the analysis cuts and in green the number of accidental events for Q^2=2.36 GeV^2, t=-0.325 GeV^2 and x_B=0.37. Without the cut at 0.5 GeV^2 on the missing mass, the number of accidental events can easily be multiplied by a factor 2 at large t and ϕ=0°.

4.3.2 π^0 subtraction

Neutral pions decay into two photons with a probability of ∼99%. In their rest frame, the two photons are emitted back-to-back with equal energy $\frac{m_\pi}{2}$. In the lab frame, π^0's have a speed close to c and the two photons from the decay undergo a Lorentz boost. We have to distinguish two cases:

- If the two photons are emitted symmetrically with respect to the π^0 momentum in the lab frame, then its kinetic energy will be shared equally between the two photons. Except if the π^0 is pointing to an edge of the calorimeter, we detect the two photons.

- If the decay is asymmetrical, then one photon will get almost all the energy of the pion whereas the other one almost nothing. With the threshold of ∼1 GeV, we only detect the high energy photon.
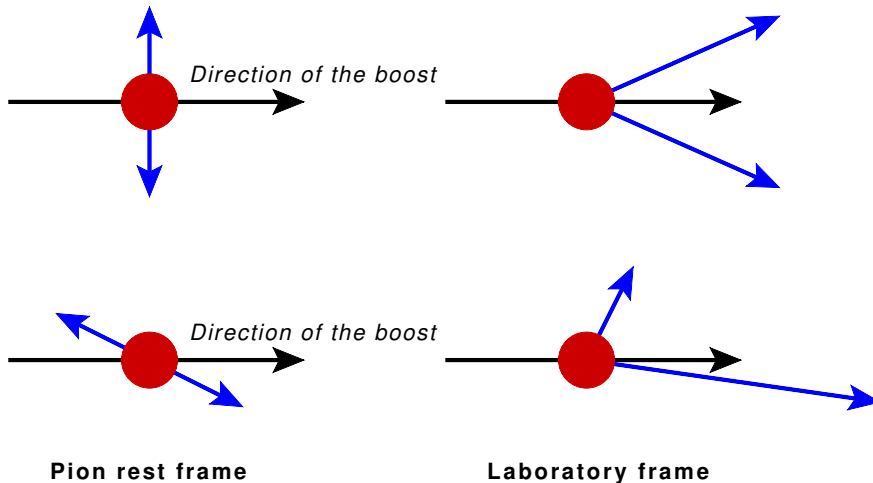
Figure 4.6: The energy of the photons depends on the symmetry of the decay with respect to the pion momentum.

In the case of an asymmetrical decays, since exclusive π^0's have an energy close to a DVCS photon, the energy of the detected photon may be compatible with a DVCS photon.

However, the contamination is only a geometrical problem. Indeed we have to evaluate the phase space of the decay leading to the contamination. Using a Monte-Carlo simulation, we generate π^0 decays using the sample of π^0 detected during the experiment. Each detected π^0 is isotropically decayed N_{dec}=5000. We have then:

$$N_{dec} = n_0 + n_1 + n_2 \tag{4.8}$$

with n_0 number of decays with no detected photon, n_1 with one detected photon and n_2 with two detected photons. In the case of one detected photon, we can compute the missing mass $M^2_{ep \to e\gamma X}$: If the missing mass is compatible with a DVCS event, we compute all kinematical variables as if it was an exclusive photon event. Then we add this event in the corresponding experimental bin with a weight $\frac{1}{n_2}$ since we use the π^0's detected thanks to the two photons. Finally we obtain the π^0 contamination as illustrated on Figure 4.7.
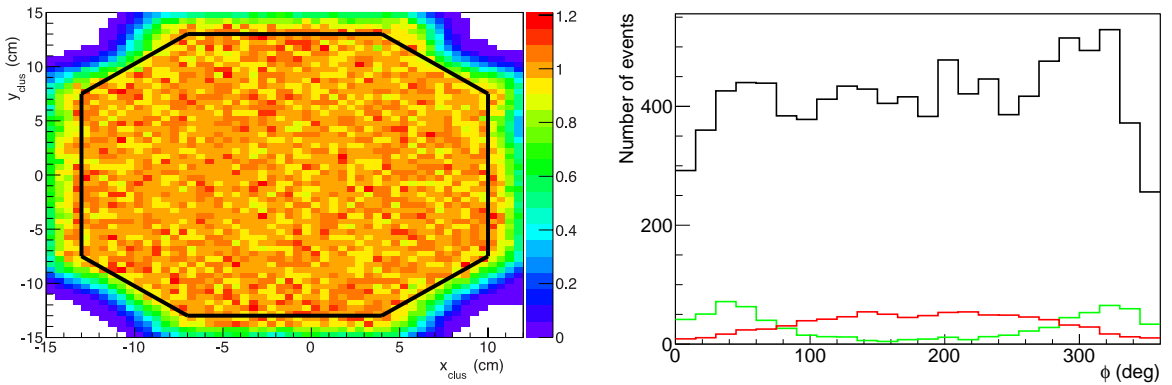
Figure 4.7: Left: Efficiency of the π^0 subtraction method estimated by Monte-Carlo. The black line corresponds to the geometrical cut to ensure an efficient subtraction. Right: On top of the Figure 4.5, we have added the estimated π^0 contamination in red. The π^0 contamination is maximal at ϕ=180° whereas the photon electroproduction signal is minimal.

The advantage of this method is that all π^0 production channels are included and properly normalized. The only drawback is that it relies on our ability to detect the two photons from a π^0 decay. A self-consistency check was performed using a Monte-Carlo simulation. π^0's are generated over our acceptance and classified into two categories: the one-photon-detected and the two-photon-detected events. After applying our π^0-subtraction method to the two-photon category, we obtain the number of one-photon events and compare it to the one-photon-detected category. This efficiency ratio is close to 1 except in the corners or close to the edges as seen on Figure 4.7. Therefore we apply a geometrical cut to both data and MC to ensure the efficiency of the π^0 subtraction.

The 2004-Kin1 had a threshold on the energy deposit in the calorimeter too high for detecting π^0's. As a consequence, π^0 subtraction cannot be performed and we cannot extract unpolarized cross sections at Q^2=1.5 GeV^2. Nevertheless we have compared for all bins of 2004-Kin2 and 2004-Kin3 the extraction of the beam helicity dependent cross section with and without π^0 subtraction. For all bins, π^0's subtract themselves when comparing the different helicities, confirming a small beam helicity dependence of π^0 electroproduction [37] [59]. Therefore, the beam helicity dependent cross sections have been extracted without π^0 subtraction for all kinematics, including 2004-Kin1.
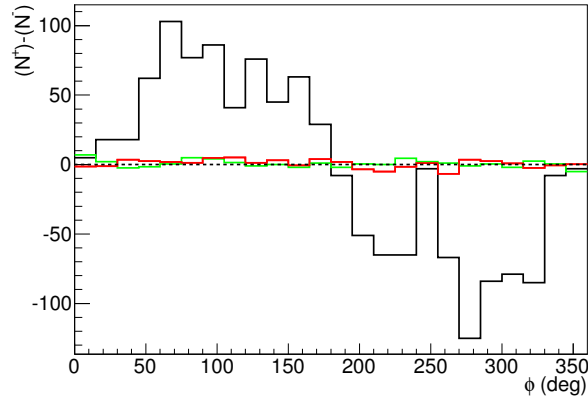
Figure 4.8: For the same bin presented in Figure 4.7, $N^+ - N^-$ according to ϕ. In black are represented all events, in red π^0s and in green accidental events.

4.4 Corrections

After all the analysis cuts and contamination subtractions, we obtain a clean exclusivity peak on the missing mass spectrum at the squared proton mass. For all events with a missing mass between 0.5 GeV^2 and a value ensuring exclusivity but determined later, we compute ϕ and t to estimate the number of count in the experimental bins. Like in Chapter 3, we
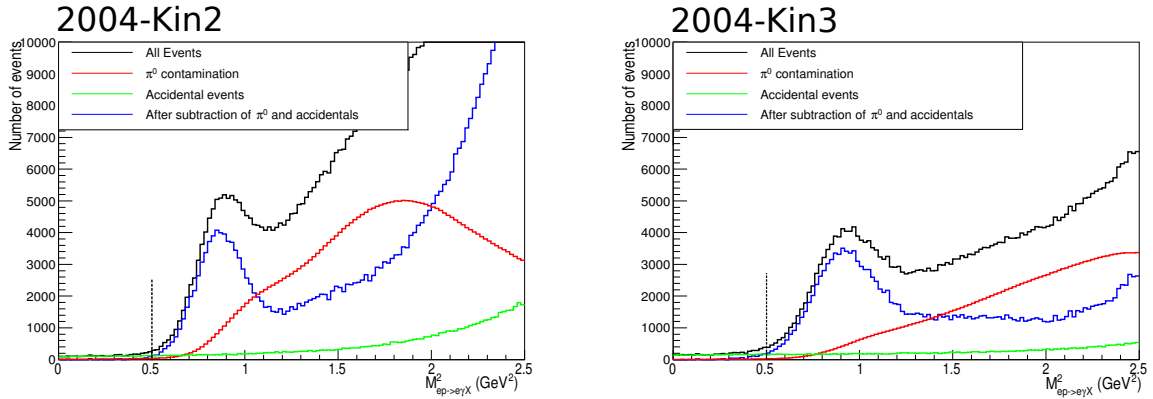
Figure 4.9: Missing mass spectra of 2004-Kin2 and 2004-Kin3 settings.

have to evaluate the efficiencies of the detectors and the impact of the cuts to correct for the good events lost in the analysis and data taking.

4.4.1 Trigger efficiency

The efficiency of the scintillators that were used for the electron trigger was monitored during dedicated runs along the experiment as explained in subsections 3.3.3 and 3.3.4. An efficiency of 99.95% was measured over the duration of the experiment. The efficiency of the Čerenkov counter used to discriminate electrons from negative pions was measured to be 99%. The purity of the electron sample was estimated at 98.8%. However, the H$(e, e'\gamma)X$ missing mass cut increases the purity. We consider that a maximum of 0.5% of electrons may still be misidentified and consider this value as the systematic uncertainty on the electron identification.

4.4.2 Multitrack events correction

Even if the electromagnetic calorimeter is in the trigger, the fraction of multitrack events still represents ∼9% of the total number of events for the three kinematic settings. After having calibrated the pion rejector for the 2004 run period, we have studied the energy deposit in the PR of the multitrack events as in subsection 3.3.1. The PR spectra look exactly the same
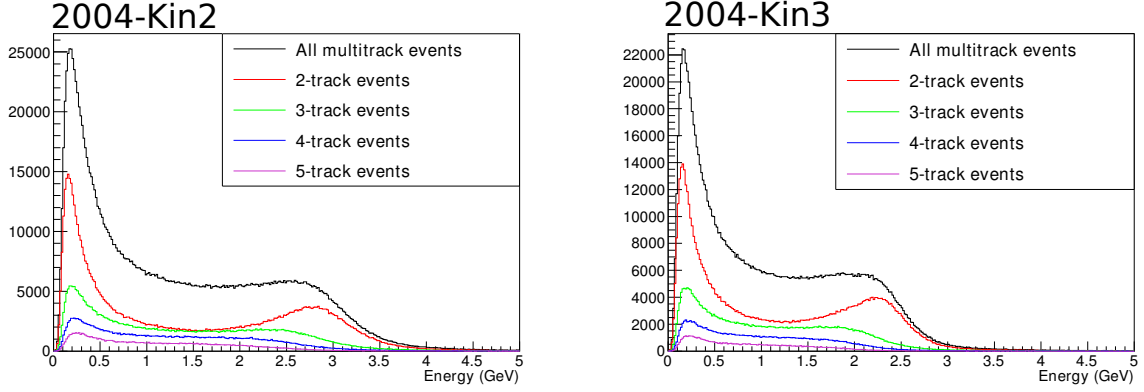
Figure 4.10: Energy deposit of multitrack events for 2004-Kin2 and 2004-Kin3.

as the spectra obtained during the 2010 run period. As a conclusion, the correction factor has the same definition as in subsection 3.3.1. It results in a 2%-correction for 2004-Kin1, Kin2 and Kin3. A systematic error of 0.5% is associated to this correction, estimated by changing the cut on the PR energy deposit.

4.4.3 Multicluster correction

The events with more than one cluster in the calorimeter are removed from the analysis. It is a fair assumption that 3-cluster (or even more) events are not related to an electroproduction of photon. Yet, considering the rate of accidental events, we might have in 2-cluster events one accidental photon with an interesting photon from an $ep \rightarrow ep\gamma$ reaction.

As a consequence, we have to analyze the 2-cluster events. We compute separately the kinematics of each photon as if they were single photon events. If γ_1 and γ_2 are the two photons, we compute t_1, t_2, ϕ_1, ϕ_2 and the squared missing masses $M^2_{ep \rightarrow e\gamma_1 X}, M^2_{ep \rightarrow e\gamma_2 X}$. We have to consider three possibilities by looking at $M^2_{ep \rightarrow e\gamma_1 X}$ and $M^2_{ep \rightarrow e\gamma_2 X}$:

- Both values are rejected by the cuts on the missing mass. In that case, none of the photons are from an electroproduction.

- Only one value is compatible with the cuts (γ_1 for example). Then we consider that we have a DVCS[1] event and put it in the experimental bin associated to $(t_1; \phi_1)$.

- Finally, if both photons are kept by the cuts on the missing mass, they are both potentially a DVCS event. We know for sure that only one of them is related to the scattered electron and the other one just accidental. By comparing the accidental rates in the experimental bins $(t_1; \phi_1)$ and $(t_2; \phi_2)$, we can determine the likelihood of each photon to be the interesting one. The probability $\mathcal{P}_1$ of γ_1 being the exclusive photon with respect to γ_2 is given by:

$$P_1 = \frac{N_2^{acc}}{N_2^{acc} + N_1^{acc}} \qquad P_2 = \frac{N_1^{acc}}{N_2^{acc} + N_1^{acc}} \tag{4.9}$$

---

[1]Here, we use DVCS in the loose sense, photon electroproduction.

with N_1^{acc}/N_2^{acc} the number of substracted accidentals in the bin $(t_1; \phi_1)/(t_2; \phi_2)$. Then we simply add P_1 to $(t_1; \phi_1)$, and P_2 to $(t_2; \phi_2)$. Please note that we just add one event to the total number of events.

To select "good" 2 clusters DVCS events, we remove the 2-cluster events with an invariant mass between 0.1 and 0.17 GeV because we used them in the π^0 substraction. The multi-cluster correction is around 1%, depending on the experimental bin. The cut $M_{ep \to e\gamma X}^2 > 0.5$ GeV^2 removes a lot of ambiguous cases.

4.5 Luminosity and beam polarization

The beam is longitudinally polarized. The beam charges according to the beam helicity must be evaluated in order to extract beam helicity dependent cross sections but also correct for any asymmetries that would affect the unpolarized results. In the case of polarized cross section, we also have to evaluate the polarization of the beam.

4.5.1 Beam polarization

The beam polarization was measured during the whole experiment concurrently with regular data taking using the Compton polarimeter introduced in section 2.2.1.1.

Figure 4.11 shows a typical Compton run ($\sim$ 3h). The beam polarization is then extracted from the asymmetry and was measured at 75.3%$\pm$0.1$_{\text{stat}}$. Because of the resolution on the position of the Compton electron, an additional 2%-systematic error must be associated to the beam polarization.

4.5.2 Luminosity

The charge is computed using the BCMs. For the 2004 experiment, the BCMs were perfectly operationnal and the uncertainty on the charge is $\sim$1%. In order to evaluate positive and negative-helicity charge, the BCM readout was synchronized with the helicity signal provided by the injector. The deadtime was measured using two 62.5 MHz clocks: One is always running whereas the other one is stopped when the DAQ is busy. Comparing them, we get η_{DT} the fraction of time the DAQ was not available. The charge has already been corrected by the deadtime in Table 4.1.

Kinematic settings	η_{DT}	Q_{+1} (C)	Q_{-1} (C)	$Q_{+1,-1}$ (C)	Q_{asy} (10^{-3})	$\mathcal{L}$ (fb^{-1})
1	0.404	0.3732	0.3733	0.7464	-0.1	3059
2	0.277	0.4057	0.4064	0.8121	-0.7	3328
3	0.143	0.6913	0.6937	1.385	-2.4	5676

Table 4.1: Deadtime, charge and luminosity for the three kinematics settings. Charge and luminosity have already been corrected by the deadtime. $\mathcal{L}$ includes the small fraction of charge with undetermined helicity.
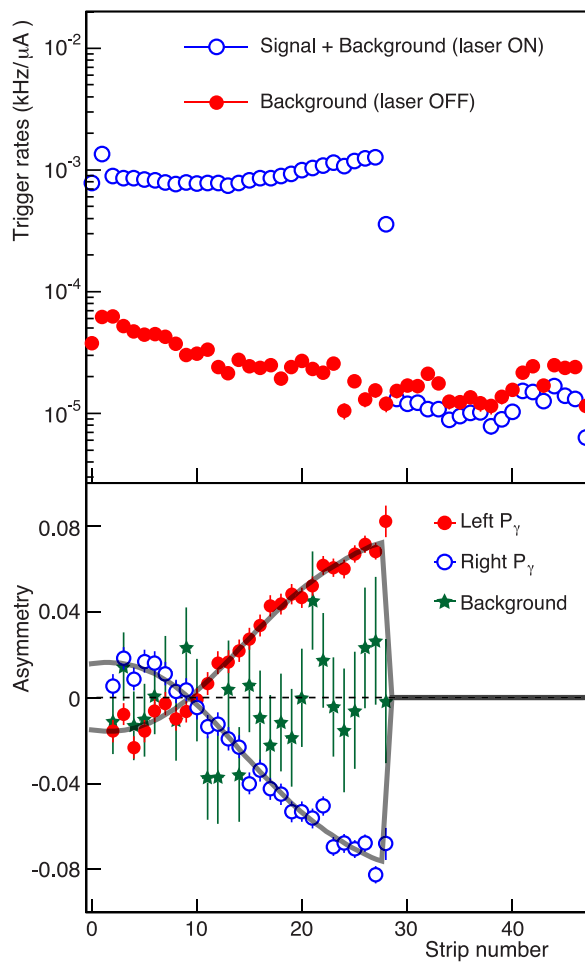
Figure 4.11: Top: Trigger rates normalized to the beam current as a function of the strip. Bottom: Corresponding asymmetries according to the strip number, measured for each of the laser polarization.

Chapter 5

Monte-Carlo simulation and cross section extraction

By applying the set of cuts and corrections described in the two previous chapters, we are able to evaluate a number of exclusive photon events. As explained in Chapter 3, the next step to extract a cross section is to evaluate the phase space that our experimental setup and the analysis cuts cover. However we are not only interested in extracting the cross section, but also in performing a separation of different contributions. This separation is realized by a fitting procedure, involving the Monte-Carlo to take into account all the known kinematical dependences. As we will also study π^0 electroproduction further in this thesis and be confronted to the same challenges, this chapter deals with both photon and π^0 electroproduction. In some cases we will compare both processes in order to shine light on some subtleties of the analysis.

Before introducing the Monte-Carlo simulation, we discuss specifics about the radiative corrections for photon and π^0 electroproduction. The last section of this chapter is dedicated to the fitting procedure: how to reduce errors such as bin migration, how to build the covariance matrix and extract the cross section.

5.1   QED radiative corrections for exclusive processes

In this section dedicated to radiative corrections, we use the term *DVCS* within its exact definition which is the emission of the photon by the nucleon. The term *photon electroproduction* must be associated to the coherent sum of DVCS and Bethe-Heitler processes.

As explained in Chapter 3, the same QED radiative corrections can be applied to DVCS, π^0 electroproduction and to DIS. However, some effects still depend on the studied process.

5.1.1   Process dependence of the radiative tail

As seen before, the energy of the incoming electron can be affected by external and internal bremsstrahlung. It induces a radiative tail in the missing mass spectrum, which does not have the same shape for photon or π^0 electroproduction (see Figure 5.1). Indeed the dependence of the cross section on the incoming electron energy is different between the two processes.

In order to convolute the value of the cross section into the evaluation of the radiative tail, the very same cross section we plan to measure needs to be known. We achieve this by using a parametrization of the cross section and evaluate it for each event in the Monte-Carlo simulation. In the case of π^0 electroproduction, we have used the parametrization extracted by the CLAS collaboration [38] to reshape the raw radiative tail given by the equivalent
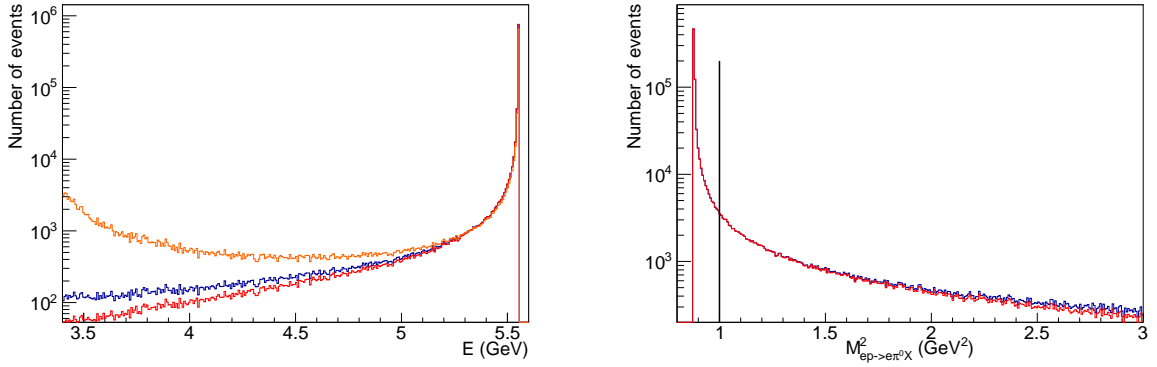
Figure 5.1: Left: Distribution of the incoming electron energy at the vertex with only internal bremsstrahlung energy loss for $Q^2 = 2$ GeV^2, x_B=0.36 and t=-0.25 GeV^2. In blue uncorrected energy distribution using the equivalent radiator method. In red, corrected energy distribution for π^0 events using a parametrization of the cross section. In orange, energy distribution for the Bethe-Heitler process. Orange and red distributions have been normalized to the blue one. Right: Missing mass spectrum for uncorrected and corrected π^0 events.

radiator method alone. We therefore multiply our acceptance by a factor η^{XS}:

$$\eta^{XS} = \frac{\sum_i \sigma_i \Theta(M_{cut}^2 - M_i^2)}{\sum_i \sigma_i} \times \frac{\sum_i 1}{\sum_i \Theta(M_{cut}^2 - M_i^2)} \qquad (5.1)$$

where the sum runs over the detected exclusive events, M_i^2 the missing mass $ep \to e'(\gamma \text{ or } \pi^0)X$ and σ_i the cross section of the ith event. The function $\Theta(x)$ returns 1 if $x > 0$, otherwise 0.

By applying a cut at 1 GeV^2 on the missing mass, the fraction of events below the missing mass cut would be 0.757 with the raw distribution whereas it is 0.768 with the cross section behaviour. Therefore we have η^{XS}=1.015 for a cut at 1 GeV^2.

For photon electroproduction, the beam energy dependence is known for all terms (interference, squared BH and DVCS amplitudes) but we do not know the decomposition of the cross section between these terms. As the Bethe-Heitler process is mostly dominantin the kinematics of our experiments, it is a fair assumption to reduce the photon electroproduction cross section to the Bethe-Heitler cross section for this purpose.

5.1.2 Internal QED radiative corrections to the Bethe-Heitler process

The case of photon electroproduction is more involved because it is given by the interference of the Bethe-Heitler and DVCS processes. Whereas the elastic approximation works fine for DVCS and π^0 electroproduction, the internal radiative corrections for Bethe-Heitler are more sophisticated. It implies more diagrams at first order because of the real hard photon which is emitted by the electron (as seen on figure 5.2).

The amplitude $\mathcal{M}$ for photon electroproduction including the virtual corrections can be written as:

$$i\mathcal{M} = \mathcal{T}_{BH}\frac{1}{1 - \delta_{vac}(-t)} + \mathcal{T}_{BH}\delta_{ver,BH} + \mathcal{T}_{BH,s.e.} + \mathcal{T}_{DVCS}\frac{1}{1 - \delta_{vac}(Q^2)} + \mathcal{T}_{DVCS}\delta_{ver,DVCS} .$$
$$(5.2)$$

By squaring it, it becomes obvious that the radiative correction factor will be different between Bethe-Heitler, DVCS and interference terms. The direct consequence is that the correction factors of different observables will be different. D. Lhuillier *et al.* [54] have
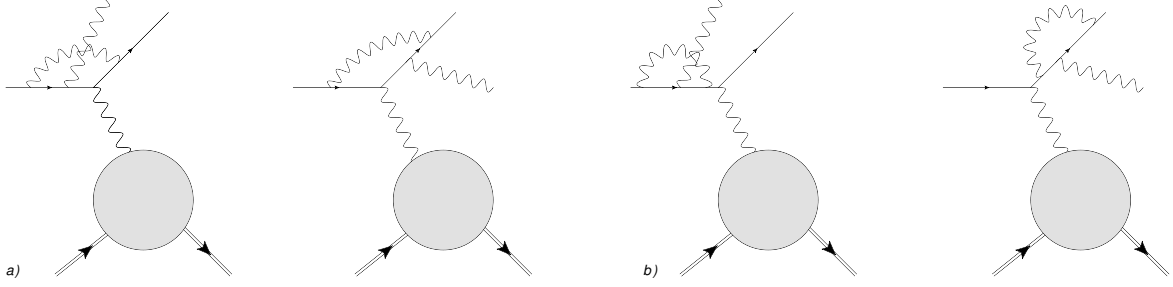
Figure 5.2: Example of diagrams including vertex and self-energy radiative effects to Bethe-Heitler process. Self-energy gives a vanishing contribution when the lepton is on-shell, therefore it does not participate in DVCS and π^0 electroproduction.

Q^2	x_B	$\frac{d\sigma^{Born}}{d\sigma^{Exp}}$	$\frac{\Delta\sigma^{Born}}{\Delta\sigma^{Exp}}$
1.5	0.36	0.9511	0.9671
1.9	0.36	0.9484	0.9724
2.3	0.36	0.9455	0.9790
2.06	0.39	0.9470	0.9755
2.17	0.34	0.9460	0.9766

Table 5.1: Radiative correction factors for polarized and unpolarized cross sections for the E00-110 kinematic settings.

developed a code to compute this virtual correction for the unpolarized and polarized photon electroproduction cross sections. This code uses a factorized GPD ansatz [60] consisting in the product of a form factor and a PDF, neglecting the ξ-dependence.

It would be more rigorous to compute a correction factor for each contribution and apply it separately. This could be perfectly incorporated in our cross section extraction as we will discover later. Nevertheless such a procedure would induce a ϕ-dependence of the correction and be model-dependent. Consequently, for the sake of simplicity and in prevision of more suitable radiative corrections in the future, we have decided to apply a unique correction factor to the entire observable (presented in table 5.1) and assign a 2% systematic error to the combined real- and virtual-radiative corrections.

5.2 Monte-Carlo simulation

In a manner similar to the case of DIS we treated before, we use a Monte-Carlo simulation to compute the phase spaces Γ_{DVCS} and Γ_{π^0} covered by the experimental setup. however, this particular simulation is based on the GEANT4 toolkit for particle transport. GEANT4 handles the interaction of the final state particles with matter between the vertex and the detectors. Interaction of the incident electron with matter before the vertex and internal radiative effects are included in the event generator.

5.2.1 Implementation of the experimental setup

We use the GEANT4 simulation package to implement the experimental setup. It has been designed in such a way that all interactions with matter from the vertex to the detector in the experiment are taken into account for the detected particles of the final state.

Therefore the target cell has the exact same dimensions in the simulation as in the real world. On figure 5.3, the scattering chamber in the simulation is an exact replica of the real

one, including the kapton window. For the HRS, only its entrance is implemented. Once the electron reaches it, we use an acceptance function (described in chapter 3) to determine if the electron is detected or not in the focal plane.
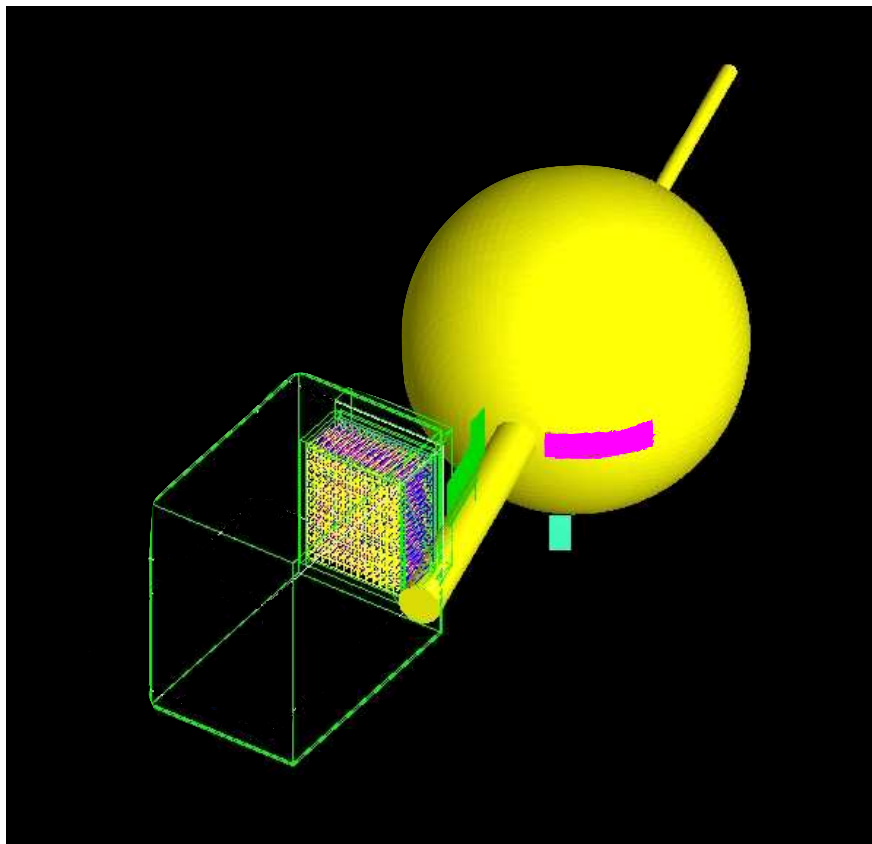
Figure 5.3: Experimental setup as implemented in Geant4. In yellow, there are the beam pipes and the scattering chamber. The kapton widow in the scattering chamber is represented in magenta. The HRS entrance is the small cyan window. On the calorimeter side, we have in green the shielding for stopping electromagnetic background from the beam pipe. The calorimeter is enclosed in a box whose only edges are represented in green.

Unlike the HRS, the calorimeter has been fully implemented. For the 2010 run period, the blocks have even been placed following a block-by-block survey performed in the Hall. The full block package (screws, PM support, Tedlar and Tyvek paper,...) is included in the simulation. Only the energy deposit of particles in the calorimeter is digitized in our simulation, as the generation and tracking of Čerenkov photons requires unrealistic simulation times and proves to be unreliable due to the difficulty to define optical surfaces in an accurate manner with GEANT4.

5.2.2 Calorimeter resolution

Because of Bremsstrahlung energy losses and resolution effects, the missing mass cut removes a significant fraction of exclusive events. This is corrected through the Monte-Carlo (MC) simulation by applying the same cut in simulated data as in the analysis. But this correction is properly computed only if the MC and the experimental exclusivity peak are at the same position and have the same shape. If there is a slight mismatch on the position or shape of the missing mass between the simulation and the experimental distributions, the resulting uncertainty may easily reach 5% or more.

However the MC exclusivity peak provided by the simulation is very different from the experimental peak:

- Its width is smaller due to a better energy resolution in the MC than in the experiment. For instance, there is no darkening of the blocks in the simulation. Moreover energy losses in the blocks are not computed using Čerenkov effect.

- The position is not centered at the squared mass of the proton whereas it is in the experiment. Again the Čerenkov effect which is not implemented can be part of the explanation. But there might be also systematic energy losses in the experimental data that are corrected through the calibration procedure of the calorimeter.

As a consequence we calibrate the MC calorimeter data against the experimental data to match the missing mass distributions in the exclusivity part. At the same time, we smear the photon energy in the simulation to match the experimental resolution on the missing mass. We call this method *the smearing procedure*, although there is also a calibration.

5.2.2.1 Necessity of a local smearing procedure

By showing how sensitive we are to a mismatch between MC and experiment about the exclusivity peak, we also prove the necessity to reproduce locally the resolution of the calorimeter.
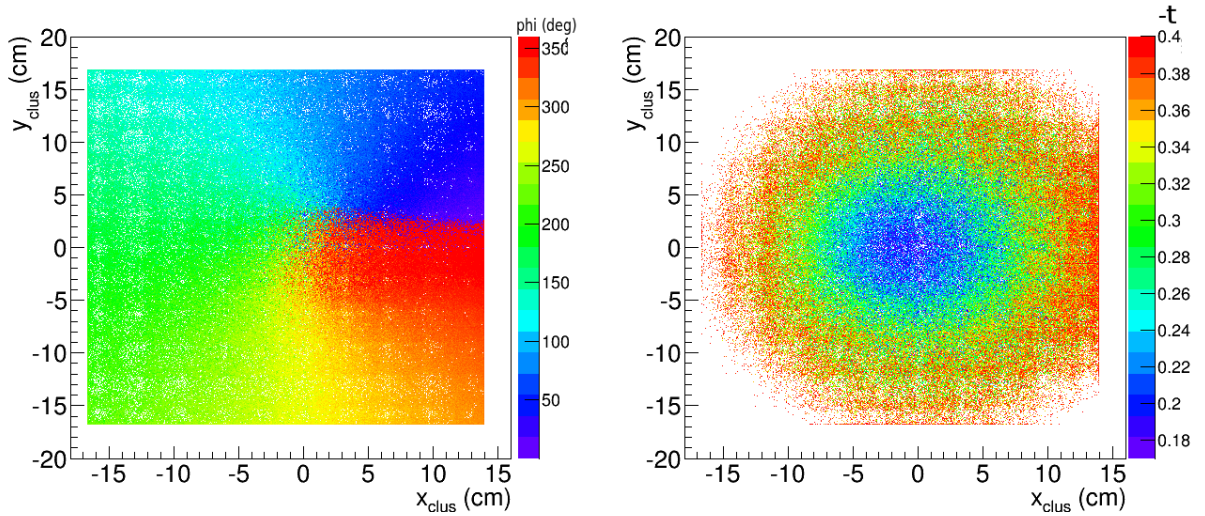
Figure 5.4: t and ϕ-distributions according to the position of the exclusive photon in the calorimeter for 2004-Kin3. The farther the photon is from the center of the calorimeter, the larger is t. ϕ is increasing by going counter-clockwise when looking the calorimeter from behind.

The events of a (t,ϕ)-bin are located in a specific area of the calorimeter, as illustrated on Figure 5.4. Drawing the missing mass spectrum for each (t,ϕ)-bin, the exclusivity peak does not have the same width or position (Figure 5.5). Radiation damage, the quality of crystals and imperfections of the calibration can explain this phenomenon.

Let us estimate the error induced by a uniform smearing procedure over the entire calorimeter surface. We take as reference shape the missing mass distribution of all events once all contamination sources are subtracted. In Figure 5.5 are summarized the mean and the standard deviation of a gaussian fitted on two "local" missing mass spectra from a same kinematical setting. We have also fitted with a gaussian distribution the sum of these two
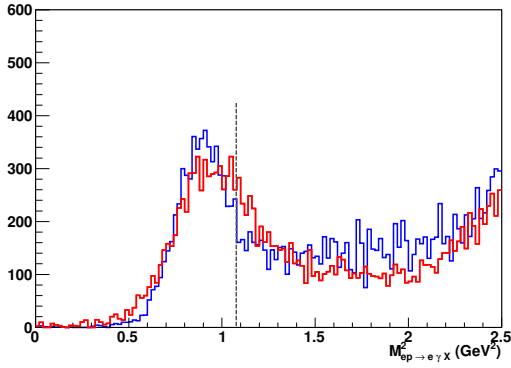
	μ (GeV^2)	σ (GeV^2)
Beam-side (red)	0.964	0.213
180°-side (blue)	0.902	0.144
sum (red+blue)	0.914	0.167

Figure 5.5: Comparison of the missing mass peaks of the beam-side edge and its opposite edge for E00-110-Kin3. The dashed gray line corresponds to the cut applied to select exclusive events. The table summarizes the parameters of a gaussian fitted on the left-side of each spectrum and to the sum of both spectra.

distributions. Approximating the missing mass spectrum of exclusive events by a gaussian, the induced error is derived by comparing the fraction of events below the exclusivity cut in the experiment with the fraction estimated using the MC distribution:

$$\delta = \frac{\int_{0.5}^{cut} M_{exp}^2(\mu_{exp}, \sigma_{exp})dM^2}{\int_{-\infty}^{+\infty} M_{exp}^2(\mu_{exp}, \sigma_{exp})dM^2} \times \frac{\int_{-\infty}^{+\infty} M_{MC}^2(\mu_{MC}, \sigma_{MC})dM^2}{\int_{0.5}^{cut} M_{MC}^2(\mu_{MC}, \sigma_{MC})dM^2}, \quad (5.3)$$

where M_{exp}^2 and M_{MC}^2 stand for the experimental and MC smeared missing mass spectra. δ should be equal to 1 as long as all the contamination is subtracted. In the case of a uniform smearing procedure, we have $\mu_{MC} = \mu_{sum}$ and $\sigma_{MC} = \sigma_{sum}$. Figure 5.6 shows δ as a function of the exclusivity cut.
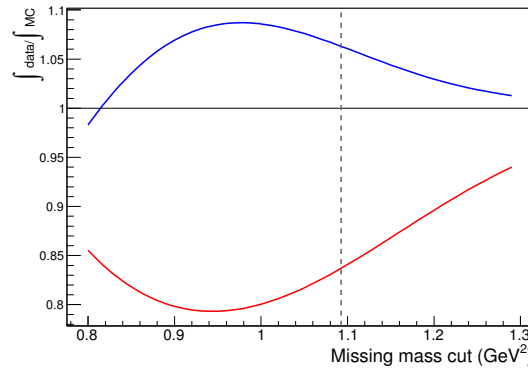
Figure 5.6: Estimated bias due to the exclusivity cut when the Monte-Carlo is smeared using the parameters μ_{sum} and σ_{sum} of the bottom row in Figure 5.5.

If we applied the analysis missing-mass cut after a uniform smearing, the cross section would be underestimated by 15% at $\phi=0°$ and overestimated by 5% at $\phi=180°$ for the corresponding (t, ϕ)-bins. The resolution study and the smearing have to be performed locally to avoid introducing a large uncertainty.

5.2.2.2 Smearing/calibration procedure of the Monte-Carlo calorimeter

We study and perform the smearing procedure of the Monte-Carlo simulation in the same time. In order to achieve this, the detector is divided into 49 partially overlapping areas. From the photon four-momentum in the Monte-Carlo simulation, the following smearing transformation is applied:

$$\begin{pmatrix} q_x \\ q_y \\ q_z \\ E \end{pmatrix} \longmapsto gaus(\mu, \sigma) \times \begin{pmatrix} q_x \\ q_y \\ q_z \\ E \end{pmatrix}, \tag{5.4}$$

where μ is the calibration coefficient and σ the smearing coefficient. In each area, the parameters μ and σ are fitted in order to best match the M_X^2 spectra of the simulated and the experimental data in the exclusive region after subtraction of accidentals and π^0's. The final values of μ and σ used to smear the simulated events are interpolated event-by-event according to the impact point of the photon in the calorimeter. Fig. 5.8 shows the resulting values of μ and σ for Kin3, interpolated across the calorimeter surface, and within the fiducial region defined by the octogonal cut shown in Fig. 4.7. The parameter μ corrects imperfections in the estimation of the energy in the Monte-Carlo simulation compared to the data. The parameter σ accounts for different resolutions on different areas of the calorimeter. The latter can be due to both different levels of background or the different quality of crystals.
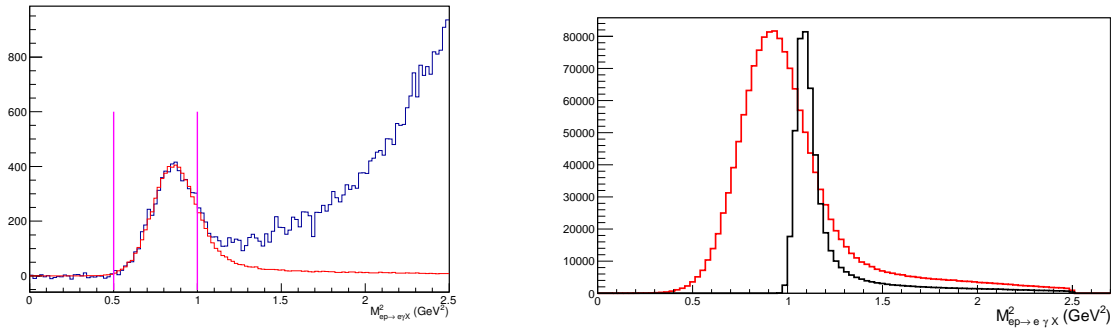
Figure 5.7: Left: Fit of the Monte-Carlo spectrum on an experimental local one. The fitting range (between pink lines) has to be chosen such that the maximum of the peak is included but the contamination is limited. Right: Comparison of Monte-Carlo spectra before (black and scaled down with a factor 0.325) and after (red) smearing.

The missing mass cut which ensures the exclusivity, is chosen at the value where the Monte-Carlo and the data spectra start to diverge, due to contamination by non exclusive events (Fig. 6.2). This leads to two different values of missing mass cut: 0.95 GeV^2 for Kin 1 and Kin 2, 1.1 GeV^2 for Kin 3.

5.2.3 Event generator

The exclusive process $ep \to e'X_1X_2$ can be decomposed in a leptonic reaction $e \to e'\gamma^*$ and a hadronic reaction $\gamma^*p \to X_1X_2$, with (X_1, X_2) the particles in the final state with masses m_1 and m_2. For the $e \to e'\gamma^*$ stage, the philosophy is inspired from the DIS event generator explained in subsection 3.4.4.1. But instead of generating the scattering angle θ_e and the energy of the scattered electron E', we generate x_B and Q^2 within the constraints of an
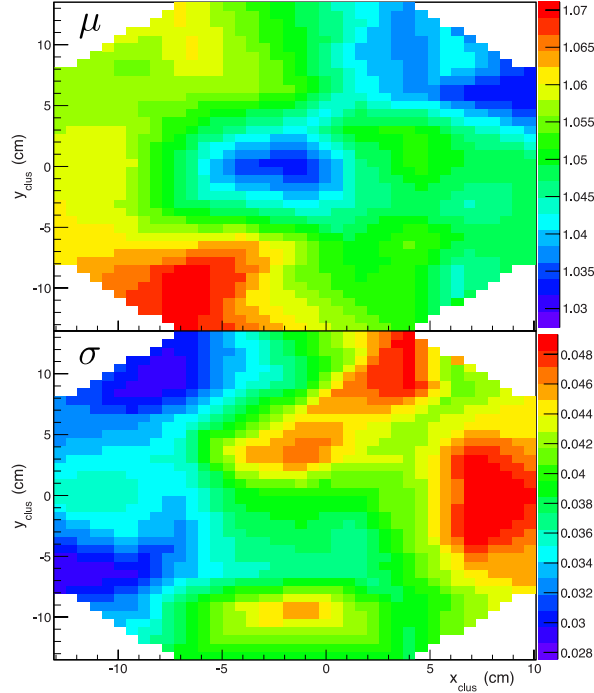
Figure 5.8: Mean μ (top) and standard deviation σ (bottom) of the gaussian distribution used to smear the simulated photon data of Kin3 viewed on the calorimeter surface y_{clus} vs. x_{clus} (beam on the right side). A worse energy resolution is observed at small angles with respect to the electron beam (positive x_{clus}). We also notice areas of fluctuating resolution corresponding to varying quality of the PbF$_2$ crystals.

exclusive reaction. Concerning the hadronic stage, it consists in generating the variables t and ϕ.

First we start with the process $e \to e'\gamma^*$. Like in the DIS case, the first variable to be generated is the vertex position v_z. We apply the corresponding external radiative corrections to infer the energy of the incoming electron E_v^{ext}. The second generated variable is Q^2, uniformly in the following range:

$$Q^2 \in \left[4 \times E_v^{ext} \times p_{min} \times sin^2(\theta_{min}/2); 4 \times E_v^{ext} \times p_{max} \times sin^2(\theta_{max}/2) \right], \qquad (5.5)$$

where (p_{min}, p_{max}) are the lower and upper momenta for the scattered electron, and $(\theta_{min}, \theta_{max})$ the lower and upper bounds for the scattering angle. Note that the Q^2-range depends on E_v^{ext}. Now, depending on the process of interest, the x_B-range will be different. If there are X_1 and X_2 in the final state, W^2 has to be greater than $(m_1 + m_2)^2$. For a given Q^2, the maximal value of x_B is given by:

$$x_B^{lim} = \frac{Q^2}{(m_1 + m_2)^2 - M^2 + Q^2} \qquad (5.6)$$

Table 5.2 lists x_B^{lim} for different exclusive processes.

	$\gamma^* p \to p\gamma$	$\gamma^* p \to p\pi^0$	$\gamma^* p \to \Delta\gamma$	$\gamma^* p \to \Delta\pi^0$
x_B^{lim}	1	0.88	0.77	0.68

Table 5.2: x_B^{lim} for different exclusive processes at Q^2=2 GeV^2.

Then x_B is generated uniformly between x_B^{min} and x_B^{max} defined as:

$$x_B^{min} = Max\left(\frac{Q^2}{2M_p(E_v^{ext} - p_{min})}, 0.05\right) \tag{5.7}$$

$$x_B^{max} = Min\left(\frac{Q^2}{2M_p(E_v^{ext} - p_{max})}, x_B^{lim}\right) \qquad \text{if } E_v^{ext} > p_{max} \tag{5.8}$$

$$= x_B^{lim} \qquad \text{if } E_v^{ext} \le p_{max} \tag{5.9}$$

The previous definitions are valid only if $E_v^{ext} > p_{min}$ and $x_B^{min} < x_B^{max}$. If it is not the case, it means that E_v^{ext} is not high enough to generate a physical event. It is considered as lost.

Once x_B and Q^2 are generated, we simulate the internal bremmstrahlung as explained in section 3.4.2. The internal bremsstrahlung is simulated exactly in the same way as for a DIS event, *i.e.* always compatible with the generated kinematics. The lowest energy E_{lim} to realize the generated kinematics is derived when we compute the scattering angle. Indeed it is given by an arcsin-function whose argument has to be in [-1;1].

$$E_{lim} = \frac{4\nu + 4\sqrt{\nu^2 + Q^2}}{8} , \tag{5.10}$$

$$\nu = \frac{Q^2}{2Mx_B} , \tag{5.11}$$

We remind that r_{lim} is the upper bound (Eq. 3.30) for r in order to generate a pre-scattering internal energy loss compatible with the generated kinematical variables. We evaluate $\delta_R^{(1)}$ with the generated Q^2. For instance, for the kinematic setting Q^2=1.75 GeV^2 and x_B=0.36, r_{lim} is listed in Table 5.3 for different incoming electron energy:

E_v (GeV)	3.355	4.455	5.55
r_{lim}	0.943	0.968	0.977

Table 5.3: r_{lim} as a function of the incoming electron energy at the vertex.

After the first energy loss by internal bremsstrahlung, the incoming electron is left with an energy E_v for the scattering process. For the internal bremsstrahlung post-scattering, we generate r in $[0; 1]$. Finally we rotate around the beam axis the scattered electron by generating ϕ_e uniformly in a range large enough to cover the full geometrical acceptance of the HRS. After all this procedure, GEANT4 handles the transport of the scattered electron to the HRS.

The second step involves the reduced reaction $\gamma^* p \to X_1 X_2$. The four-momentum of the virtual photon is computed from the four-momentum of the incident electron after internal bremsstrahlung. But we use the outgoing electron momentum before internal bremsstrahlung to ensure the momentum conservation. We place ourselves in the center-of-mass frame of the system $\gamma^* p$. The squared momentum transfer t is uniformly generated between t_{min} and t_{max}, both functions of x_B, Q^2, m_1 and m_2. Once the four-momenta of X_1 and X_2 are computed, they are boosted in the lab frame. Finally we rotate their momenta around the virtual photon by ϕ, generated according to a uniform distribution in $[0; 2\pi]$.

For the decay of the final state particle, π^0 in our case, we isotropically generate the decay in the rest frame of the particle. The decay products are then boosted in the lab frame.

It is important to note that the phase space $\Gamma_{MC} = \Delta Q^2(E_v^{ext})\Delta x_B(Q^2)\Delta t(Q^2, x_B)\Delta\phi$ is different for each event, as it is function of E_v^{ext}.
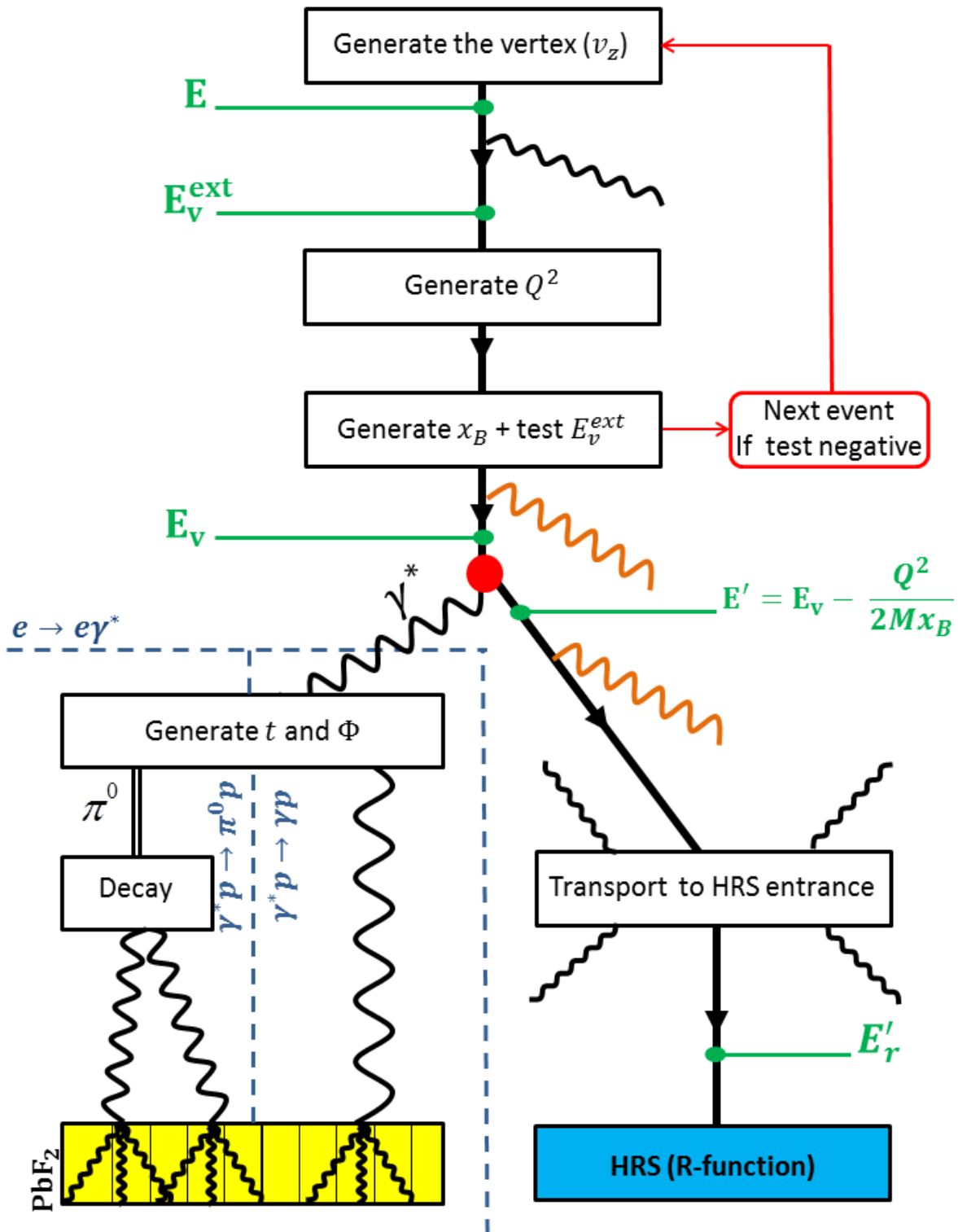
Figure 5.9: Diagram representing the main steps in the Monte-Carlo simulation. Escaping photons represents energy losses either by external (black) or internal (orange) bremsstrahlung. We specify the energy of the electron in green.

5.3 Cross section extraction and fitting procedure

The principle of the extraction is to compare an experimental number of events to a prediction from our Monte-Carlo simulation bin-by-bin. We use a parametrization of the cross section with the Monte-Carlo simulation to extract structure functions or CFFs. Once they are extracted, we reconstruct the cross section. This method presents a lot of advantages, especially in the case of the Rosenbluth separation:

- It corrects for bin migration which is the association of events to wrong bins. The bin migration may be as large as 10%, depending on the bin.

- It integrates the kinematical dependences over the entire acceptance of the experimental setup. As an example, the polarization state of the virtual photon is critical for the Rosenbluth separation. Our method ensures a tight control of its value.

5.3.1 Vertex and experimental binnings

In data analysis, we reconstruct the kinematics of an event based on the information provided by the detectors. Because of radiative effects and detector resolutions, the reconstructed kinematics might be different from the vertex kinematics. We define two binnings. One binning uses the kinematics seen by the detectors and we call the corresponding bins *reconstructed bins*. The second binning uses the kinematics at the vertex and we call the corresponding bins *vertex bins*. If we note N_r the number of events in the rth reconstructed bin and N_{rv} the number of events in the rth reconstructed bin coming from the vth vertex bin, we can write the following relation:

$$\forall r, \ N_r = \sum_{v=0}^{\mathcal{V}} N_{rv} \ , \tag{5.12}$$

where $\mathcal{V}$ is the total number of vertex bins. Reciprocally, we define $\mathcal{R}$ the total number of reconstructed bins and N_v the number of events in vertex bin v can be written as:

$$\forall v, \ N_v = \sum_{r=0}^{\mathcal{R}} N_{rv} \ . \tag{5.13}$$

Using experimental data only, there is unfortunately no way to access N_v (or N_{rv}) whereas it is needed for the cross section extraction. As we know both reconstructed and vertex kinematics in the Monte-Carlo simulation, we can derive a migration matrix K whose coefficients K_{rv} are the probabilities for an event to belong to the vertex bin v and the reconstructed bin r:

$$\forall r, \ N_r = \sum_{v=0}^{\mathcal{V}} K_{rv} N_v \ , \tag{5.14}$$

In practice, we are not interested in N_v but in $d^4\sigma_v$. It is related to N_v by:

$$N_v = \mathcal{L} \int_{\Phi_v} \frac{d^4\sigma_v}{d\Phi} d\Phi, \tag{5.15}$$

where $d\Phi = dQ^2 dx_B dt d\phi$ and Φ_v is the phase space at the vertex. We can write Eq. 5.14 using the previous relation:

$$N_r = \mathcal{L} \sum_{v=0}^{\mathcal{V}} \int_{\Phi_v^r} \frac{d^4\sigma_v}{d\Phi} d\Phi, \tag{5.16}$$

where Φ_v^r stands for the subvolume of vertex phase space contributing in N_r. Assuming a cross section constant over Φ_v, we have:

$$N_r = \sum_{v=0}^{\mathcal{V}} \left(\mathcal{L} \int_{\Phi_v^r} d\Phi \right) \times \frac{d^4\sigma_v}{d\Phi} , \tag{5.17}$$

We recover a matrix expression such as in equation 5.14, which associates the number of counts N_r and $\frac{d^4\sigma_v}{d\Phi}$. We define a new matrix $\mathcal{K}$ which convolutes migration, acceptance and phase space effects. The integration in the previous equation is performed using the Monte-Carlo simulation and gives the following result for $\mathcal{K}$:

$$\mathcal{K}_{rv} = \eta_{rv}^{XS} \sum_{i \in r \bigcap v} \frac{\Gamma_{MC}^i}{N_{gen}} , \tag{5.18}$$

where i is an event in the reconstructed bin r and the vertex bin v passing all the cuts applied in the data analysis and Γ_{MC}^i is the associated phase space factor. We have added the correction factor η_{rv}^{XS} from Eq. 5.1, computed with only the events in the reconstructed bin r and the vertex bin v. Using the matrix $\mathcal{K}$, we are now able to correct for bin migration and we have a better control on the kinematics at which the cross section is extracted.

5.3.2 Fitting procedure

As seen in Chapter 1, the π^0 or photon electroproduction cross section can be written as the sum of several contributions. Let us give the following general expression of the cross section:

$$\frac{d^4\sigma}{dQ^2 dx_B dt d\phi} = \sum_{n=0}^{N} F_n(E, Q^2, x_B, t, \phi) X^n , \tag{5.19}$$

where F_n is a known function, depending only on kinematical variables, and X^n a parameter we want to extract. N is the total number of parameters. In the case of the unpolarized cross section for DVMP, we would have $N = 4$ and $X^n = \{\sigma_T, \sigma_L, \sigma_{TT}, \sigma_{TL}\}$. The F_n-functions are the virtual photon flux multiplied by the corresponding ϵ^*-dependence associated to X^n (see Chapter 1). Using Eq 5.16 and Eq. 5.19, we recover a relation between the number of events in the reconstructed bin and the parameters of the cross section:

$$N_r = \sum_{v=0}^{\mathcal{V}} \sum_{n=0}^{N} \mathcal{K}_{rv}^n X_v^n . \tag{5.20}$$

By assuming that these parameters do not vary over the phase space Φ_v, the set of matrices $\mathcal{K}^n$ is defined as follows:

$$\mathcal{K}_{rv}^n = \int_{\Phi_v^r} F_n(E, Q^2, x_B, t, \phi) d\Phi , \tag{5.21}$$

$$= \sum_{i \in r \bigcap v} F_n(E_v^i, (Q_v^2)^i, (x_B)_v^i, t_v^i, \phi_v^i) \frac{\Gamma_{MC}^i}{N_{gen}} . \tag{5.22}$$

$(E_v^i, (Q_v^2)^i, (x_B)_v^i, t_v^i, \phi_v^i)$ represents the kinematics of event i at the vertex. The matrices $\mathcal{K}^n$ integrates the kinematical dependences over all the acceptance, still taking into account bin migration[1].

---

[1] It is possible to include in these matrices a correction factor for virtual radiative effects as discussed in subsection 5.1.2.

Using the equation 5.20 we extract the parameters by minimizing the following χ^2 (Figure 5.10):

$$\chi^2 = \sum_{r=0}^{\mathcal{R}} \left(\frac{N_r^{exp} - N_r^{MC}}{\sigma_r^{exp}} \right)^2 , \qquad (5.23)$$

where $\mathcal{R}$ represents the number of experimental bins, N_r^{exp} the number of events in the reconstructed bin r from experimental data and σ_r^{exp} the associated error. N_r^{MC} is the number of events in reconstructed bin r expected using Monte-Carlo simulation. By replacing N_r^{MC} with the expression from equation 5.20 and requiring the values $\overline{X}_v^n$ to minimize the χ^2, we have for all n and v :

$$0 = -\frac{1}{2} \frac{\partial \chi^2}{\partial X_v^n} \bigg|_{\overline{X}} , \qquad (5.24)$$

$$0 = \sum_{v'=0}^{\mathcal{V}} \sum_{n'=0}^{N} A_{v,v'}^{n,n'} \overline{X}_{v'}^{n'} - B_v^n \qquad \forall v, n . \qquad (5.25)$$

To find the solutions, we have to solve the matrix system $AX = B$ with A a matrix whose dimensions are $(N \times \mathcal{V}) \times (N \times \mathcal{V})$ and B a column vector with $N \times \mathcal{V}$ rows. Their coefficients are defined such as:

$$A_{v,v'}^{n,n'} = \sum_{r=0}^{\mathcal{R}} \mathcal{L}^2 \frac{\mathcal{K}_{r,v}^n \mathcal{K}_{r,v'}^{n'}}{[\sigma_r^{exp}]^2}, \qquad (5.26)$$

$$B_v^n = \sum_{r=0}^{\mathcal{R}} \mathcal{L} \frac{\mathcal{K}_{r,v}^n N_r^{exp}}{[\sigma_r^{exp}]^2}. \qquad (5.27)$$

We obtain the value of the parameters by inverting A:

$$\overline{X}_v^n = \sum_{v'=0}^{\mathcal{V}} \sum_{n'=0}^{N} [A^{-1}]_{v,v'}^{n,n'} B_{v'}^{n'}, \qquad (5.28)$$

A^{-1} is the covariance matrix and the associated error on $\overline{X}_v^n$ is given by $[A^{-1}]_{v,v}^{n,n}$. From the covariance matrix, we can derive the correlation matrix C:

$$C = Diag(A) \times A \times Diag(A), \qquad (5.29)$$

where $Diag(A)$ is a diagonal matrix defined by $[Diag(A)]_{ii} = A_{ii}$. The correlation between the coefficients is an additionnal source of error on the extracted parameter.

Finally the experimental cross section is given by:

$$\frac{d^4 \sigma_r^{exp}}{dQ^2 dx_B dt d\phi} = \frac{N_{rv}^{exp}}{N_{rv}^{MC}} \sum_{n=0}^{N} \mathcal{F}_n(E, \overline{Q_v^2}, \overline{(x_B)_v}, \overline{t_v}, \phi_r) \overline{X}_v^n, \qquad (5.30)$$

where all overlined kinematical variables are averaged values from the corresponding experimental bin. An additional check of our procedure is the equality between these experimental averaged values and the ones predicted by the Monte-Carlo simulation. Concerning E and ϕ_r, they are purely kinematical, *i.e.* the extracted parameters are independent of them. As a consequence we choose them freely. We used logically the beam energy and the ϕ-bin center. The value N_{rv}^{exp} represents the number of events whose experimental bin is the same as the vertex bin. Using equations 5.14 and 5.20 , it is given by:

$$N_{rv}^{exp} = N_r^{exp} - \mathcal{L} \sum_{n=0}^{N} \sum_{v' \neq v} \mathcal{K}_{rv'}^n \overline{X}_{v'}^n. \qquad (5.31)$$
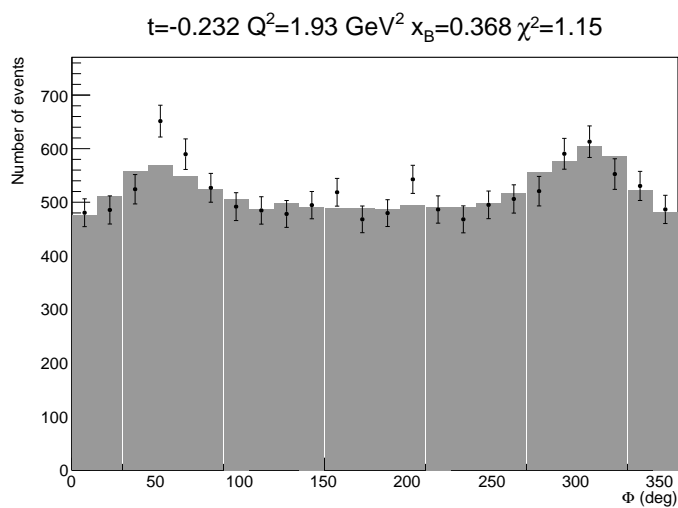
Figure 5.10: The number of events in a typical *t*-bin of Kin2 is represented by the black points with their statistical errors. We extract the parameters by minimizing the difference between the experimental number of counts and the estimate of the Monte-Carlo simulation (grey histogram).

Chapter 6

Photon electroproduction results and discussion

Using the formalism developed in Chapter 1, we derive a parameterization of the photon electroproduction to use in the fitting procedure presented in the previous chapter. After summarizing all sources of systematic uncertainties, we present cross section results associated with an extraction of Compton Form Factors. Results are compared to GPD-based models and a discussion is developed about specific kinematical higher-twist effects, also known as target-mass and finite-t corrections.

6.1 Choice of parameterization

We study the harmonic coefficients introduced in subsection 1.4.3.2 which are the sum of $(c, s)_n^{\mathcal{I}}$ and $(c, s)_n^{DVCS}$, themselves involving several combinations of twist-2 and twist-3 CFFs. The ϕ-dependence is therefore not enough to separate all linear/bilinear combinations of CFFs. The ϕ-dependence of the cross section can thus be properly described by different choices of free parameters.

In this analysis, we chose to parametrize the DVCS helicity-independent cross section by the three following combinations of effective CFFs: $\mathcal{C}^{DVCS}(\mathcal{F}, \mathcal{F}^*)$ (Eq. 1.63), $\Re e[\mathcal{C}^{\mathcal{I}}(\mathcal{F})]$ (Eq. 1.68) and $\Re e[\mathcal{C}^{\mathcal{I}}(\mathcal{F}_{eff})]$ (Eq. 1.69). The helicity-dependent cross section is fitted using the $\Im m[\mathcal{C}^{\mathcal{I}}(\mathcal{F})]$ and $\Im m[\mathcal{C}^{\mathcal{I}}(\mathcal{F}_{eff})]$. Three reasons have lead to this choice:

- The contributions to the cross section associated with each of these parameters have a distinct ϕ-dependence, minimizing the correlations among them,

- We keep the dominant twist DVCS^2 contribution,

- Higher twist contributions are kinematically suppressed.

While this is the most physical choice of parameters, any other choice that provides a good fit ($\chi^2/dof \sim 1$) to the ϕ-dependence of the number of counts, is an equally valid choice as far as the cross section extraction is concerned. The fitted parameters, though, would have a less straightforward physics interpretation in that case. We have tested the stability of our cross section results against a different choice of free parameters and results are discussed in section 6.2.2.

The cross section extraction procedure described in section 5.3 was applied to all data sets, for both the unpolarized and the helicity-dependent cases. In addition to the Q^2-dependence of the helicity-dependent cross sections, we were able to measure the Q^2-dependence of the unpolarized cross section, at two values of Q^2=1.9 and 2.3 GeV^2. Moreover, the x_B

Settings	χ^2_{pol}/dof	χ^2_{unp}/dof
Kin1	0.88	-
Kin2	1.00	1.16
KinX2	0.96	0.82
Kin3	1.15	0.99
KinX3	1.08	1.28

Table 6.1: χ^2/dof resulting from the extraction method for all kinematics settings. The subscript "pol" stands for polarized cross sections, "unp" for unpolarized cross sections.

dependence of helicity dependent and independent cross sections were studied using the KinX2 and KinX3 settings.

An example of the cross section extraction is presented on Fig. 6.1 for $x_B = 0.37$, $Q^2 = 2.36$ GeV^2 and $-t = 0.32$ GeV^2, along with the different contributions resulting from the fit, which gave an overall χ^2/dof of 1.1. For the unpolarized cross section, one observes a significant contribution from the term associated with $\left|\mathcal{T}^{DVCS}\right|^2$ in our fit, in addition to a large contribution from the interference term: the Bethe-Heitler is large, but the precision of the data is such that other contributions are obviously necessary to explain the observed cross section. The helicity-dependent cross section is dominated by the twist-2 interference term, as noticed before [44] [32, 33]. These conclusions extend to all bins in our analysis, whose results are shown in Appendix B. Table 6.1 lists the χ^2/dof resulting from the extraction method for all kinematics settings.

6.2 Systematic errors

Systematic uncertainties are divided into uncorrelated (or point-to-point) and correlated (or normalization) uncertainties. The largest source of uncorrelated error in this experiment was associated with the missing mass cut. The correlated uncertainties have been described before, a summary table is shown in this section.

6.2.1 Missing Mass Cut

Two systematic effects are associated with the missing-mass-squared cut. The first comes from semi-inclusive events contaminating our sample. These events have larger missing-mass-squared values induced by extra missing particles. Indeed, even if the cut is supposed to keep this contamination minimal, a small fraction of such events may remain below the missing-mass-squared cut. In order to evaluate an upper value for this systematic error, we examined the ratio of the integrals of the experimental and Monte-Carlo missing-mass-squared spectra. As seen in Fig. 6.2, this ratio increases significantly with the missing-mass-squared cut, which is expected since the Monte-Carlo only contains exclusive events. By varying the cut from the nominal value 0.95 GeV^2/c^4 up to 1 GeV^2/c^4, the observed contamination remains smaller than 1%, which we took as the systematic uncertainty on the cross section. The second effect induced by the missing-mass-squared cut arises from a mismatch on the position and shape of the missing-mass-squared peaks between data and Monte-Carlo. This is due to our limited ability to reproduce perfectly the response of our calorimeter. This mismatch increases as the missing-mass-squared cut decreases and is maximal around the maximum of the distribution. We estimate the corresponding error by looking at the variation of the cross section between the nominal cut and a lower cut value. This lower bound is chosen such that the loss of statistics is 15%, ensuring that the observed variations are not statistical in nature. The systematic error is evaluated for each (t, ϕ) bins of each kinematic setting and

Figure 6.1: Unpolarized (top) and helicity-dependent (bottom) cross section extraction for the typical Kin3 bin $x_B = 0.37$, $Q^2 = 2.36$ GeV^2 and $-t = 0.32$ GeV^2. The shaded areas represent the statistical uncertainty for each contribution. The different contributions are computed using the extracted parameter of the corresponding bin multiplied by the associated kinematical factor evaluated at the kinematical center of the bin. For instance the DVCS squared amplitude contribution is

$$|DVCS|^2 = F_{DVCS}\left(E = 5.7572, Q^2 = 2.36, x_B = 0.37, t = -0.32, \phi\right) \times \mathcal{C}^{DVCS}(\mathcal{F}, \mathcal{F}^*).$$
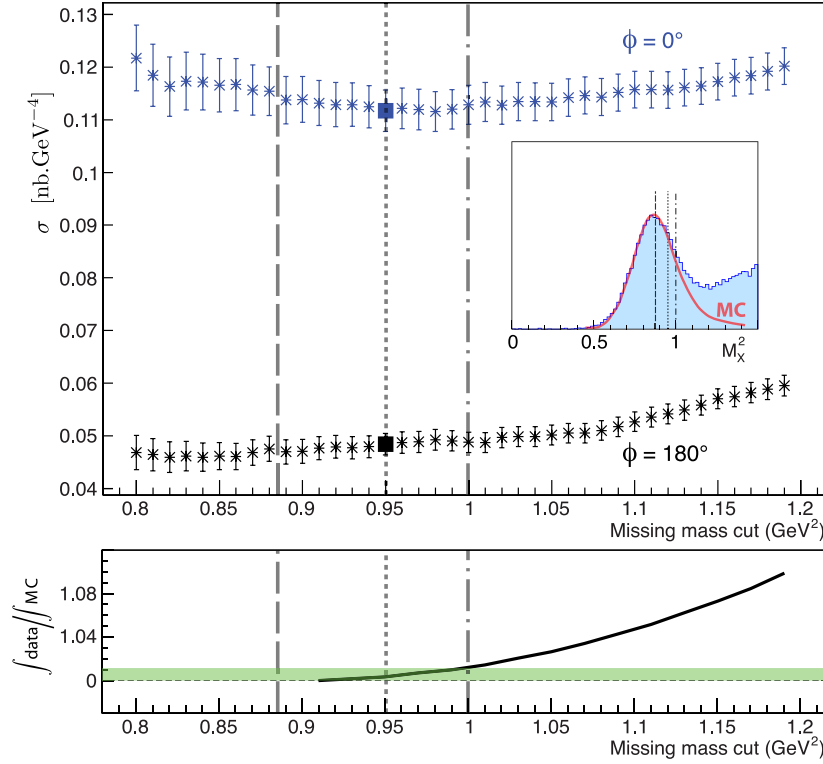
Figure 6.2: Top: Variation of the $ep \to ep\gamma$ cross section for Kin2, $-t = 0.17$ GeV^2, as a function of the missing-mass-squared cut, for $\phi = 0°$ (upper blue points) and $\phi = 180°$ (lower black points). The dotted vertical line corresponds to the nominal cut. The systematic errors are evaluated bin by bin in ϕ and t for each kinematic setting by studying the variation of the cross section between the nominal and the lower missing-mass-squared cut (dashed line). The insert represents the same cuts on the missing-mass plot. Bottom: Ratio of the integrals of the experimental and Monte-Carlo missing-mass spectra, as a function of the missing-mass-squared cut. By varying the cut up to 1 GeV^2/c^4 , represented by the dotted-dash line, the observed contamination remains smaller than 1% (green band).

may reach up to a few percent. These point -to-point uncertainties are included in the data tables of Appendix B.

6.2.2 Cross Section Parameterization

As mentioned in section 6.1, the cross section results should be independent of our choice of parameterization in the extraction method. To evaluate the impact of this choice, we used a different parameter set by replacing the squared DVCS amplitude term by the interference term $\Re\, \mathcal{C}^{\mathcal{I},V}$, which yields an equally good fit to the data. A difference in the cross section up to 1% appears locally depending on the kinematic bin, as shown on Fig 6.3. As a consequence, we estimated the systematic error from the parameter choice to be 1%.
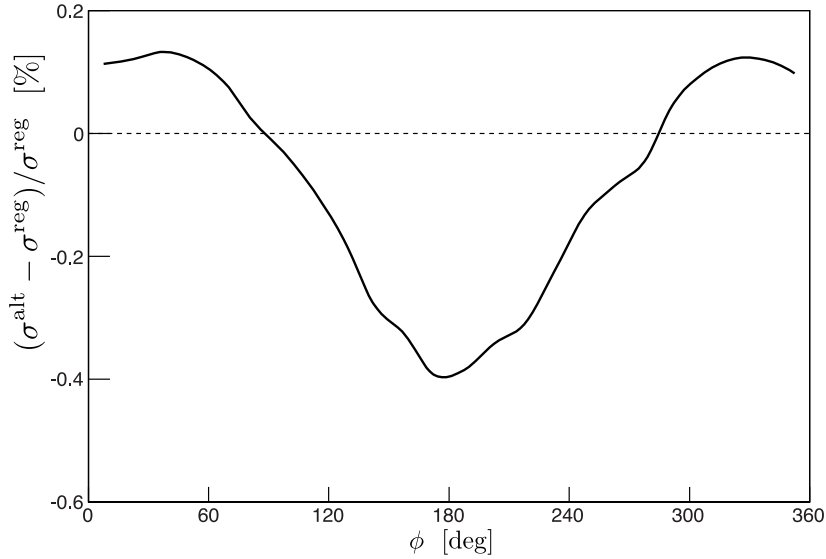
Figure 6.3: Difference in % between the cross section extracted with the squared DVCS amplitude term and with the $\Re\, \mathcal{C}^{\mathcal{I},V}$ term for $x_B = 0.37$, $Q^2 = 2.36$ GeV^2 and $-t = 0.33$ GeV^2. The ϕ-profile of the difference is a consequence of the small $\cos\phi$ and $\cos 2\phi$ dependences of $\Re\, \mathcal{C}^{\mathcal{I},V}$ kinematic coefficient. Naturally, the two different extractions give almost the same reduced χ^2/dof=0.94 (nominal) and 0.93 (alternate) for the entire Kin2 setting.

6.2.3 Correlated Uncertainties

Table 6.2 presents the systematic uncertainties on the cross section stemming from normalization effects, which are considered 100% correlated bin-by-bin. Note that the helicity-dependent cross sections have an extra uncertainty coming from the beam polarization measurement. The determination of these uncertainties are discussed in the associated section listed in the table.

6.3 Photon electroproduction results

Before comparing our data to existing models, we will try to interpret the extracted effective CFFs within the assumptions stated in section 6.1. Systematic uncertainties represented on the figures are the point-to-point exclusivity uncertainties added linearly to the normalization uncertainty.

Systematic uncertainty	Value	Section
HRS acceptance cut	1%	3.5.1
Electron ID	0.5%	3.3.4
HRS multitrack	0.5%	4.4.2
Corrected luminosity	1%	4.5.2
Fit parameters	1%	6.2.2
Radiative corrections	2%	5.1.2
Beam polarization	2%	4.5.1
Total (helicity-independent)	2.7%	
Total (helicity-dependent)	3.4%	

Table 6.2: Normalization systematic uncertainties on the extracted photon electroproduction cross sections. The systematic error coming from the fit parameter choice is not a normalization error per se, but we consider that 1% is an upper limit for this error on all kinematic bins. The helicity-dependent cross sections have an extra uncertainty stemming from the beam polarization measurement. The last column gives the section in which each systematic effect is discussed.

6.3.1 Scan in Q^2

The different combinations of effective CFFs which have been extracted from our fits to Kin1–3 using the formalism developed in [17] are shown integrated over t, on Fig. 6.4. With the choice of parameters used to describe the kinematical dependence of the cross sections (introduced in section 6.1), the contribution associated with the $\left|\mathcal{T}^{DVCS}\right|^2$ term is large for the unpolarized case. The twist-2 interference term is significant and the contribution of the twist-3 interference term is often found to be small, with large systematic errors. For the polarized case, the twist-2 interference term is dominant, the twist-3 contribution is small, again with large systematic errors. Note that the errors on the effective CFFs represented in this plot correspond to the diagonal of the error matrix.

Overall, the extracted parameters show no Q^2–dependence for neither the helicity-dependent or helicity-independent cases over our Q^2–range. Note that the logarithmic Q^2–evolution can safely be neglected within this Q^2 lever arm at this x_B.

The full set of results for settings Kin1–3 are presented in Fig. B.1–B.7 in Appendix B.

6.3.2 Scan in x_B

The results from KinX2 and KinX3 showing the x_B-dependence of cross sections are presented in Fig. B.3–B.9 in Appendix B. KinX3 has a limited acceptance close to $0°$, which increases the correlation between the different fit parameters describing the azimuthal dependence of the cross section (Figure 6.5). Indeed, the separation of the real part of the twist-2 interference and $\left|\mathcal{T}^{DVCS}\right|^2$ contributions in the fit is particularly sensitive to the relative value of the cross section measured around both 0 and $180°$. These difficulties have basically no impact on the determination of the cross sections themselves. The measured x_B-dependence will set interesting constraints on GPD models and parametrizations, especially thanks to the relatively high accuracy of our data.

6.3.3 Comparison with models

In Fig. 6.6, we compare our results with various models and previous fits to data. We have chosen to use two different kinds of double-distribution GPD models, namely the VGG [61] and KMS12 [36] models. Note that in contrast to VGG, the KMS12 model was tuned using
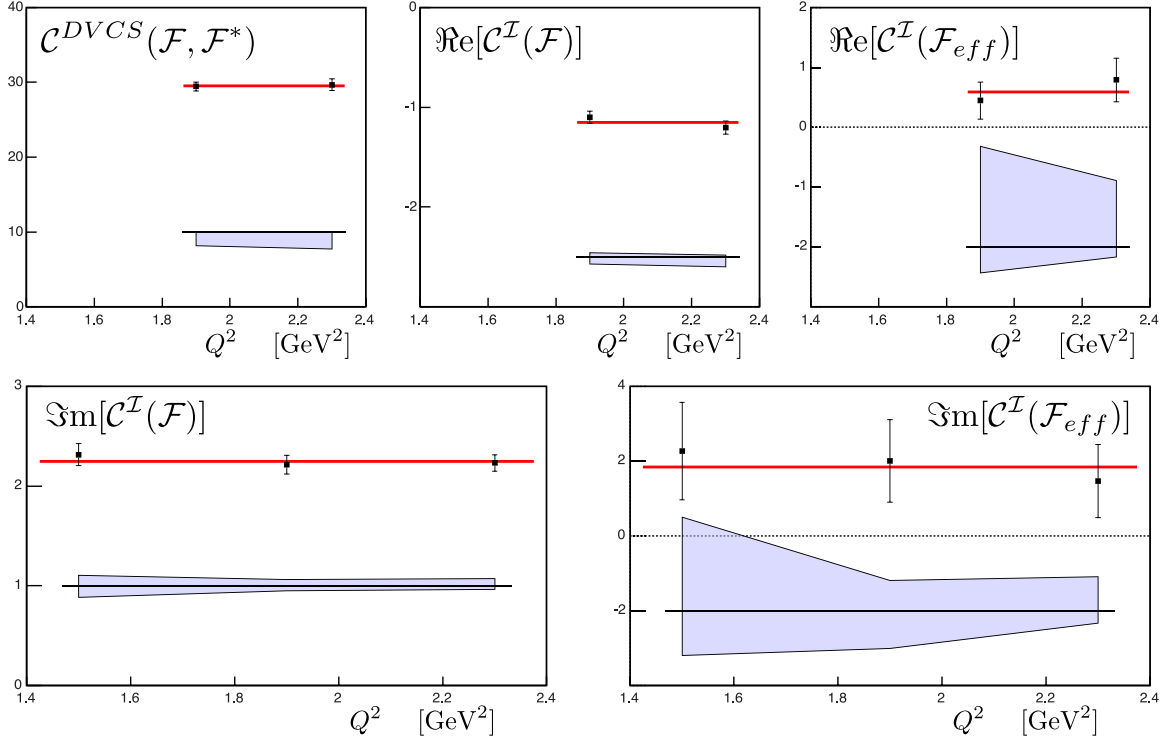
Figure 6.4: Different combinations of effective CFFs extracted from our fits using the formalism developed in [17], integrated over t and plotted as a function of Q^2. The top three plots show the effective CFFs resulting from the unpolarized cross section fit (Kin2 and Kin3), whereas the bottom plots show the effective CFFs resulting from the helicity-dependent cross section fit (Kin1–3). The shaded areas represent only the systematic error due to the exclusivity cut. No significant Q^2–dependence is observed on the full set of parameters.
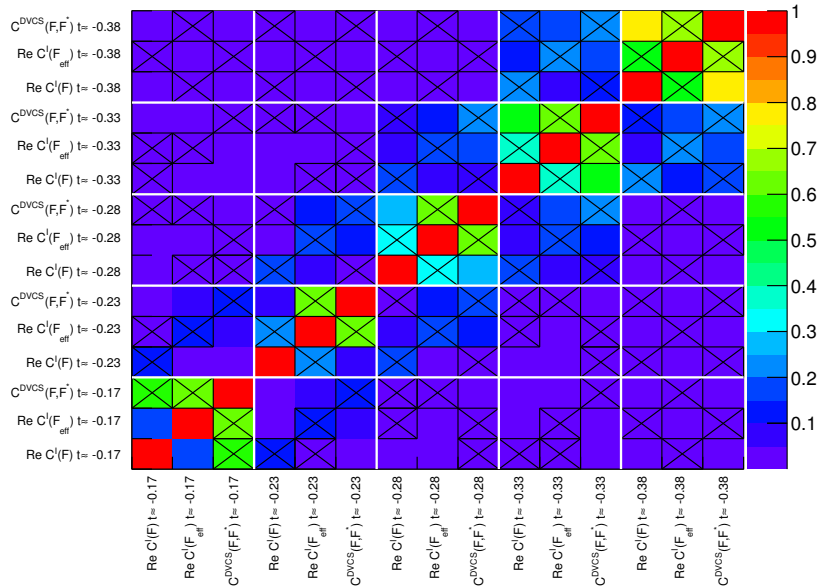
Figure 6.5: Correlation matrix for KinX3. The crosses represent negative correlation coefficients. The correlation between $\Re[\mathcal{C}^{\mathcal{I}}(\mathcal{F})]$ and $\mathcal{C}^{DVCS}(\mathcal{F}, \mathcal{F}^*)$ is getting important since they are both ϕ-independent around 180° and there is no data at 0° to disentangle them. The correlation matrices are shown in Appendix B.

vector meson data at low to very-low x_B, and is not adapted yet to the valence quark region. In any case, one observes that both models overshoot the helicity-dependent cross section data in this Kin2 bin, whereas VGG is more adequate for the unpolarized data.

In addition, we have compared our data with the KM10a model [62], which fits some of its parameters to all DVCS data available worldwide except for the previously published results from a subset of the present experiment. The consequence is that no absolute DVCS cross-section data in the valence region were used for this fit. The KM10a model is clearly very close to the helicity-dependent data, which is not a surprise considering that the CLAS asymmetry data in the same kinematic region were used to constrain this model. However, this same model significantly underestimates the DVCS unpolarized cross section around $\phi = 180°$ (Figure 6.6).

Recently, kinematic twist-4 target-mass and finite-t corrections (TMC) have been calculated for DVCS on the proton and estimated for the KMS12 model [63, 64] (shown in Fig. 6.6). Since this model is not adapted to the valence quark region, we have extracted the correction factor and applied it to the KM10a parametrization [1]. This allows us to gauge the effect of such corrections in the most realistic model available to us. It is striking that the lack of strength observed at $\phi = 180°$ for the KM10a model is largely compensated by the TMC, giving a surprisingly good agreement between this modified KM10a model and our data.

An update of the KMS12 model, taking into account the DVCS data in the valence region, would allow for a much stronger statement about the necessity of target-mass and finite-t corrections at these moderate Q^2. At any rate, we emphasize that the high accuracy of the present data is crucial to disentangle the different contributions at play in this critical area around 180°. There is no doubt that the addition of our new data set to the KM fit will be most interesting, especially in the light of these new higher-twist calculations.

All the features we have described remain true for most of our data bins, which are shown in Appendix B. It is interesting to note that for the highest bins in t, especially for Kin2 and KinX2 (Figure B.1 and B.3), the TMC to the unpolarized cross section is of the same order as the cross section itself around $\phi = 180°$. This corresponds to values of $(-t/Q^2) \sim 0.15$ or larger. It is not unreasonable to expect that higher-order corrections in $(-t/Q^2)^2$ start to be important at these values, and may compensate the peculiar behavior of the TMC around $\phi = 180°$, which is not visible in data. Efforts to achieve a resummation of the $(-t/Q^2)^k$ series to all orders are currently undertaken [66].

6.4   Conclusion about photon electroproduction

The E00-110 experiment [42] ran in Hall A at Jefferson Lab in the fall of 2004. Its goal was to measure the Q^2−dependence of the DVCS helicity-dependent cross sections at fixed value of x_B. A first analysis [44] extracted $\Im m\ \mathcal{C}^I_{unp}(\mathcal{F})$ and $\Im m\ \mathcal{C}^I_{unp}(\mathcal{F}_{eff})$ [18] which were not showing any Q^2-dependence, hinting the handbag diagram dominance. A set of unpolarized cross section at Q^2=2.3 GeV^2 was also published. In the previous chapters of this thesis, we have detailed a reanalysis of the E00-110 results.

Several improvements have been performed compared to the 2006-analysis:

- The DIS study of the 2010 run period performed in Chapter 3 brought new elements

---

[1]In principle, the full calculation of TMC can only be evaluated knowing the GPDs in the entire region $x > \xi$. KM10a however uses a dispersion relation fit for the valence region by parametrizing the GPD H on the cross-over $x = \xi$ line and a subtraction constant. Moreover, even if the main part of the TMC for unpolarized observables could in principle be evaluated by a change of conventions to CFFs and the ξ variable [65], the KM10a parametrization is currently only available as a binary package giving directly the photon electroproduction cross section.

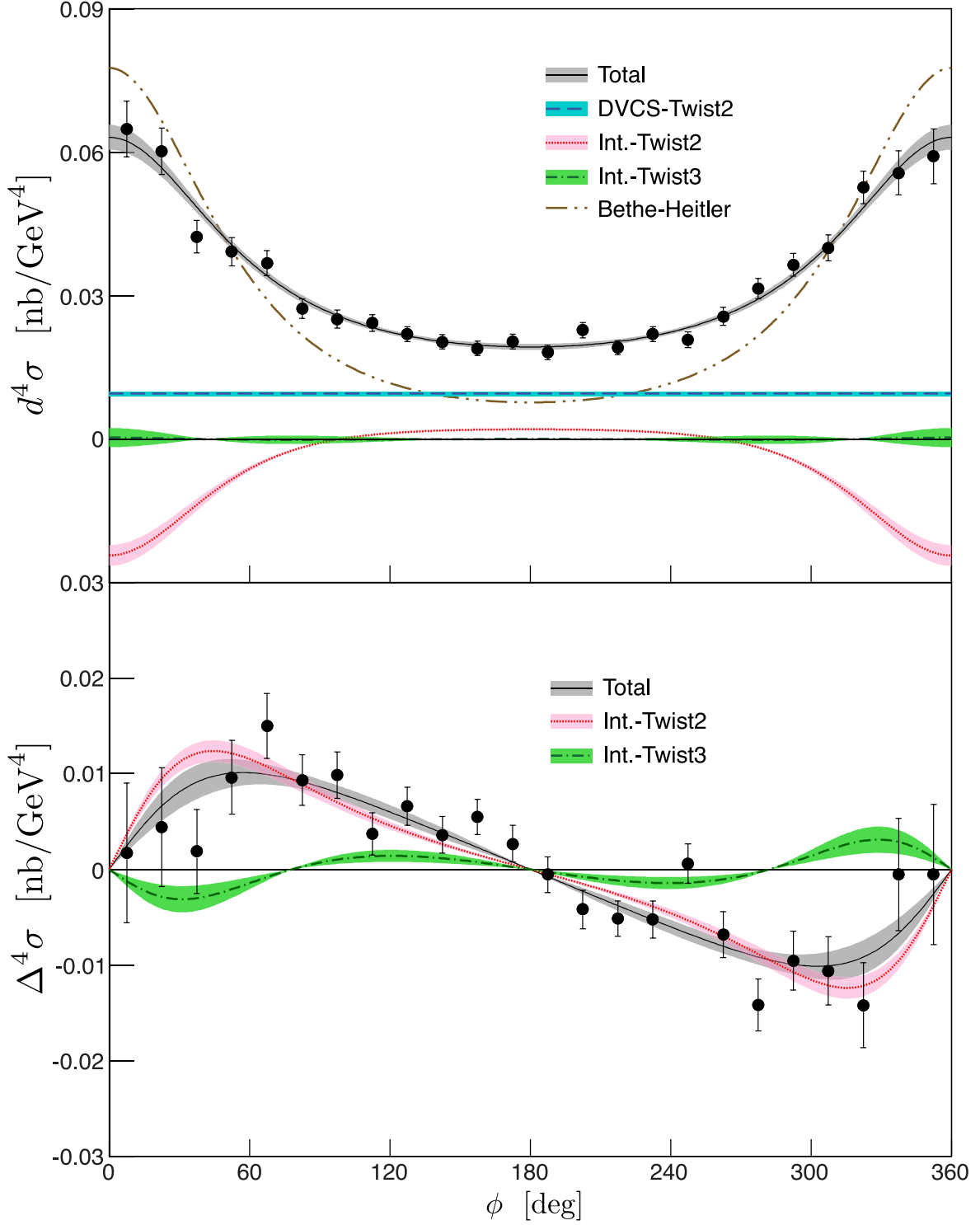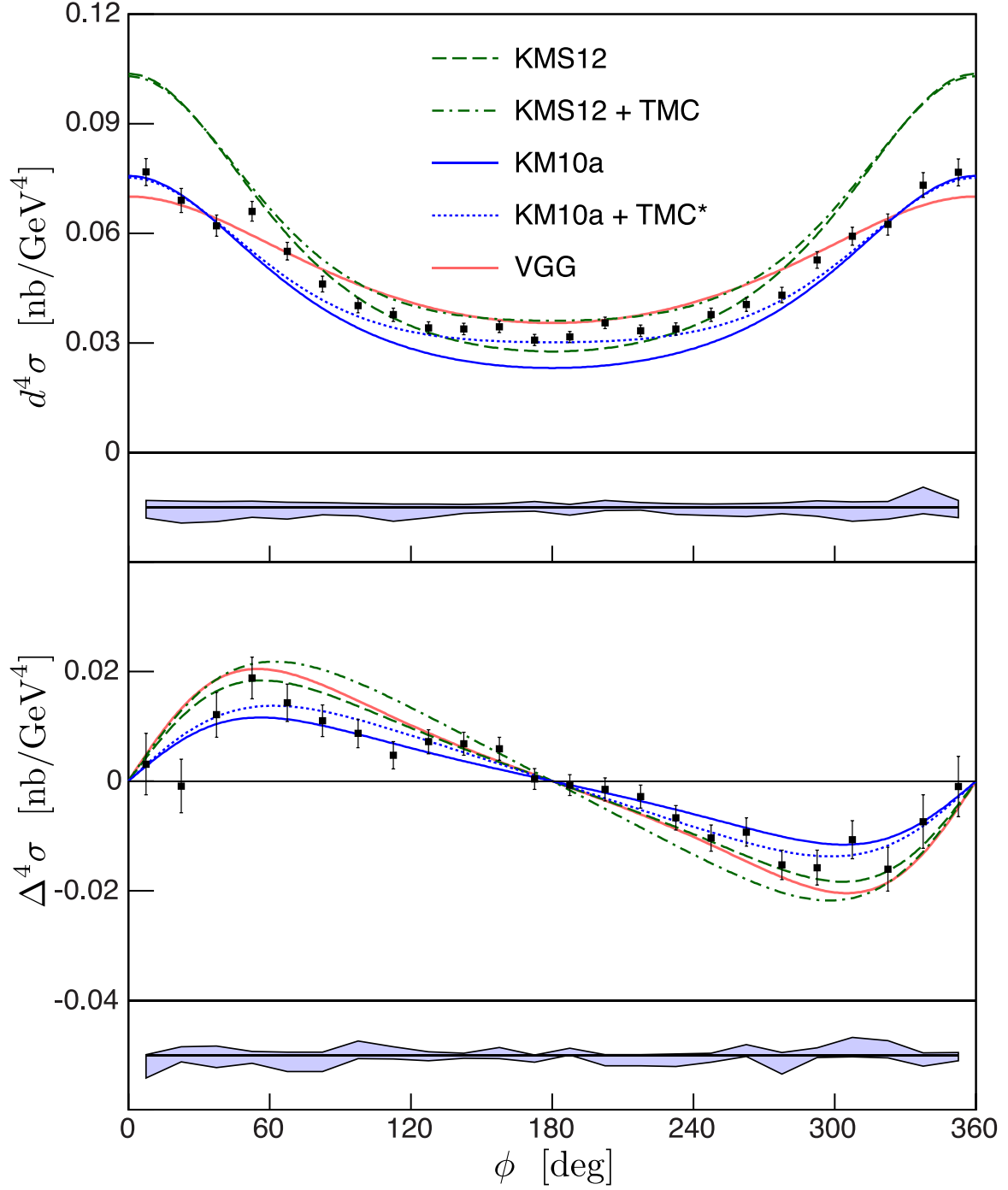Figure 6.6: Unpolarized (top) and helicity-dependent (bottom) cross sections for the typical Kin2 bin $x_B = 0.37$, $Q^2 = 1.93$ GeV^2 and $-t = 0.23$ GeV^2. The light blue area represents the point-to-point systematic uncertainties added linearly to the normalization error. The predictions from the distribution-based models KMS12 and VGG are shown respectively as dashed green and solid red curves. The KM10 fit is represented as the solid blue line. The target-mass and finite-t corrections are included in the KMS12 model and shown as the dotted-dash curve. The correction is then applied to the KM10a model shown as the dotted blue line.

about the normalization of the cross sections. The main change concerns the multitrack correction which drops from 10% to 2% (see section 3.3.1).

- The π^0-subtraction method has been tested and validated for 2004-Kin3. Nevertheless the full efficiency is reached for 2004-Kin2 as long as the edges and corners are removed.

- We have shown that the cut on the missing mass distribution could easily induce a systematic error of 10%. Consequently a calibration/fitting/smearing procedure has been developed in order to reproduce as much as possible the resolution of the calorimeter and reduce the corresponding systematic error.

- A careful study of the systematic uncertainties has been done.

- The radiative corrections have been improved by using a dedicated code [54] for photon electroproduction.

- The formalism introduced in [18] neglects several kinematical terms by assuming $Q^2 \rightarrow \infty$. Since most of the published data are at Q^2 of a few GeV^2, an updated version including these neglected terms was published in 2010 [17]. Considering the moderate Q^2 of the present measurements, this analysis uses the 2010 formalism.

Whereas the same set of parameters as for 2006-analysis was applied to extract the beam-helicity dependent cross sections, we used a different set for the unpolarized cross sections. Indeed, in 2006, only effective CFFs involved in the interference term were used and the squared DVCS contribution was assumed negligible. Here we have replaced an interference term by the twist-2 term of the DVCS amplitude. Thanks to the π^0 results [37], we have extracted another unpolarized data set at Q^2=1.9 GeV^2, making the scaling test possible for unpolarized data. Although both parametrizations give the same result, it is interesting to only recover the scaling with the set including the $|DVCS|^2$ contribution. It seems to confirm the handbag diagram dominance observed on polarized data . Moreover it is possible that we performed a clean separation of the interference and $|DVCS|^2$ contributions. Since the interference and $|DVCS|^2$ contributions have not the same beam-energy dependence, a full separation will be possible using the data of the 2010 run period and confirm (or not) the previous statement.

In addition to the Q^2−dependence at fixed x_B, we present here new results on the x_B-dependence of the DVCS cross section at fixed Q^2 by using a subset of the data from the Kin2 and Kin3 settings with $1.95 < Q^2 < 2.30$ GeV^2.

The only unpolarized data in the valence region for comparison have been recently published by the CLAS collaboration [22]. Unfortunately their small acceptance at our kinematical values induce large statistical uncertainty and jeopardize a strong consistency check between both sets of results.

For all the data sets, the excellent accuracy in the 120-240° region allows for precise comparison with models in this critical region where the Bethe-Heitler process is not the dominating contribution. The era of 20%-accuracy measurements is over, where you can fit any pure leading-twist parametrization with no correction. Moreover it was shown that Next-To-Leading order corrections are significant with respect to the statistical accuracy of these results and of the future experiments [67]. The extraction of GPDs is more challenging and exciting than ever: it requires the theoreticians to work on their extraction codes and models until they match the experimental data within its higher and higher accuracy .

Chapter 7

Rosenbluth separation of π^0 electroproduction

Whereas we analyzed in the previous chapter the 2004 run period, the π^0 analysis described in this chapter was performed on the 2010 run period. The kinematical settings in 2010 (Table 7.1) are close from those of 2004. Since we want to perform a Rosenbluth separation of the π^0 electroproduction cross section, two beam energies are used for each Q^2-value. The detector package was the same as for the 2004 experiment, except for the calorimeter which was larger for a total of 208 PbF$_2$ blocks. As pointed out before, the trigger for the 2010 run period was simply an inclusive electron trigger for most of the experiment, with no hardware threshold on the energy deposit in the calorimeter.

Name	Q^2 (GeV^2)	x_B	W^2 (GeV^2)	E (GeV)	ϵ^*
2010-Kin1	1.5	0.36	3.55	(3.355 ; 5.55)	(0.52 ; 0.84)
2010-Kin2	1.75	0.36	3.99	(4.455 ; 5.55)	(0.65 ; 0.79)
2010-Kin3	2	0.36	4.44	(4.455 ; 5.55)	(0.53 ; 0.72)

Table 7.1: Table of kinematics for the 2010 experiment. Sometimes we will refer to the high beam energy kinematical settings by adding a suffix *high*, and similarly for the low beam energy with the suffix *low*. As an example, the 2010-Kin1 with the beam energy at 3.355 GeV is called 2010-Kin1low and 2010-Kin1high refers to 2010-Kin1 with the beam energy at 5.55 GeV.

The calorimeter analysis is the same as for the 2004 run period, except for a new calibration method introduced in the first section. Note that the HRS analysis is common with the DIS analysis described in Chapter 3. Then we present the set of cuts used to select exclusive π^0 events. Before applying the fitting procedure introduced in Chapter 5, we perform the fitting/calbration/smearing procedure of the Monte-Carlo simulation to minimize the systematic uncertainty associated with the exclusivity cuts.

7.1 Calorimeter calibration

The same waveform analysis and clustering algorithm explained for the DVCS analysis in Chapter 4, have been used for the 2010 analysis. However the calibration of the calorimeter differs slightly. The first step is nonetheless the same: dedicated elastic scattering runs with the proton detected by the HRS and the scattered electron in the calorimeter were used to extract first order calibration coefficients. The drawback of this calibration is that it

cannot take into account changes in gain between two elastic runs. A complementary method using π^0's has been elaborated, allowing us to monitor the gain and adapt the calibration coefficients on a daily basis [68]. The principle of this method is to select exclusive π^0 events and derive the energy of each photon knowing the invariant mass and the squared missing mass.

Indeed the energies of the decay photons in the reaction $\pi^0 \to \gamma_1 \gamma_2$ are the solutions of the following system of equations:

$$E_{\pi^0} = E_1 + E_2 \ , \tag{7.1}$$

$$m^2_{\gamma_1 \gamma_2} = 2 E_1 E_2 \left(1 - \cos \theta_{\gamma_1 \gamma_2}\right) \ , \tag{7.2}$$

where E_1 and E_2 represent the energies of γ_1 and γ_2. E_{π^0} is the energy of the π^0. The cosine of the angle between the two photons is related to their 4-momenta by:

$$\cos \theta_{\gamma_1 \gamma_2} = \frac{\mathbf{q}_1 \cdot \mathbf{q}_2}{E_1 E_2} \ . \tag{7.3}$$

Thanks to the gain coefficients extracted from elastic scattering calibration, we have an experimental measurement of $\cos \theta_{\gamma_1 \gamma_2}$. In order to determine E_{π^0}, we compute the missing mass $M^2_{ep \to \gamma_1 \gamma_2 X}$:

$$M^2_{ep \to \gamma_1 \gamma_2 X} = W^2 + m^2_{\gamma_1 \gamma_2} - 2 \left(\nu + M\right) E_{\pi^0} + 2 ||\mathbf{q}|| \sqrt{E^2_{\pi^0} - m^2_{\gamma_1 \gamma_2}} \cos \theta \ , \tag{7.4}$$

where $\cos \theta$ stands for the angle between the momenta of the virtual photon and of the π^0. Therefore $\cos \theta$ is also measured experimentally. In the case of events associated with exclusive π^0 electroproduction, we have $M^2_{ep \to e' \gamma_1 \gamma_2 X} = M$ and $m_{\gamma_1 \gamma_2} = m_\pi$. We therefore derive E_{π^0} and solve the system 7.1. Once E_1 and E_2 are known, we write the usual relations:

$$E_1 = \sum_{i=0}^{207} G_i A_i \ , \qquad E_2 = \sum_{i=0}^{207} G_i A_i \ , \tag{7.5}$$

where A_i is the amplitude of the ith block and G_i its calibration coefficient. To determine G_i we apply the same method as in subsection 3.2.3.2. The change of calibration coefficients may affect the position of the photons in the calorimeter, and consequently $\cos \theta_{\gamma_1 \gamma_2}$ and $\cos \theta$. This calibration is then iteratively performed, looping between calibration and clustering with the new coefficients.

We need about one day worth of statistics to carry out an accurate π^0 calibration. As a consequence, the variations of the gain can be monitored and corrected on a daily basis (Figure 7.1).

7.2 Event selection

A Rosenbluth separation requires a tight control of the kinematics at which the cross sections are extracted. In particular, previous results from Hall A [37] and CLAS [38] show a large Q^2- and x_B-dependence of $\sigma_T + \epsilon^* \sigma_L$. To reduce the systematic uncertainty caused by a slightly different bin center between low and high beam energy kinematical settings, we need to select events with specific Q^2 and x_B values.

7.2.1 HRS acceptance cut

We select electrons going through a well-known part of the HRS acceptance, similarly to the DIS analysis of Chapter 3. All the cuts detailed in this chapter are used here, except
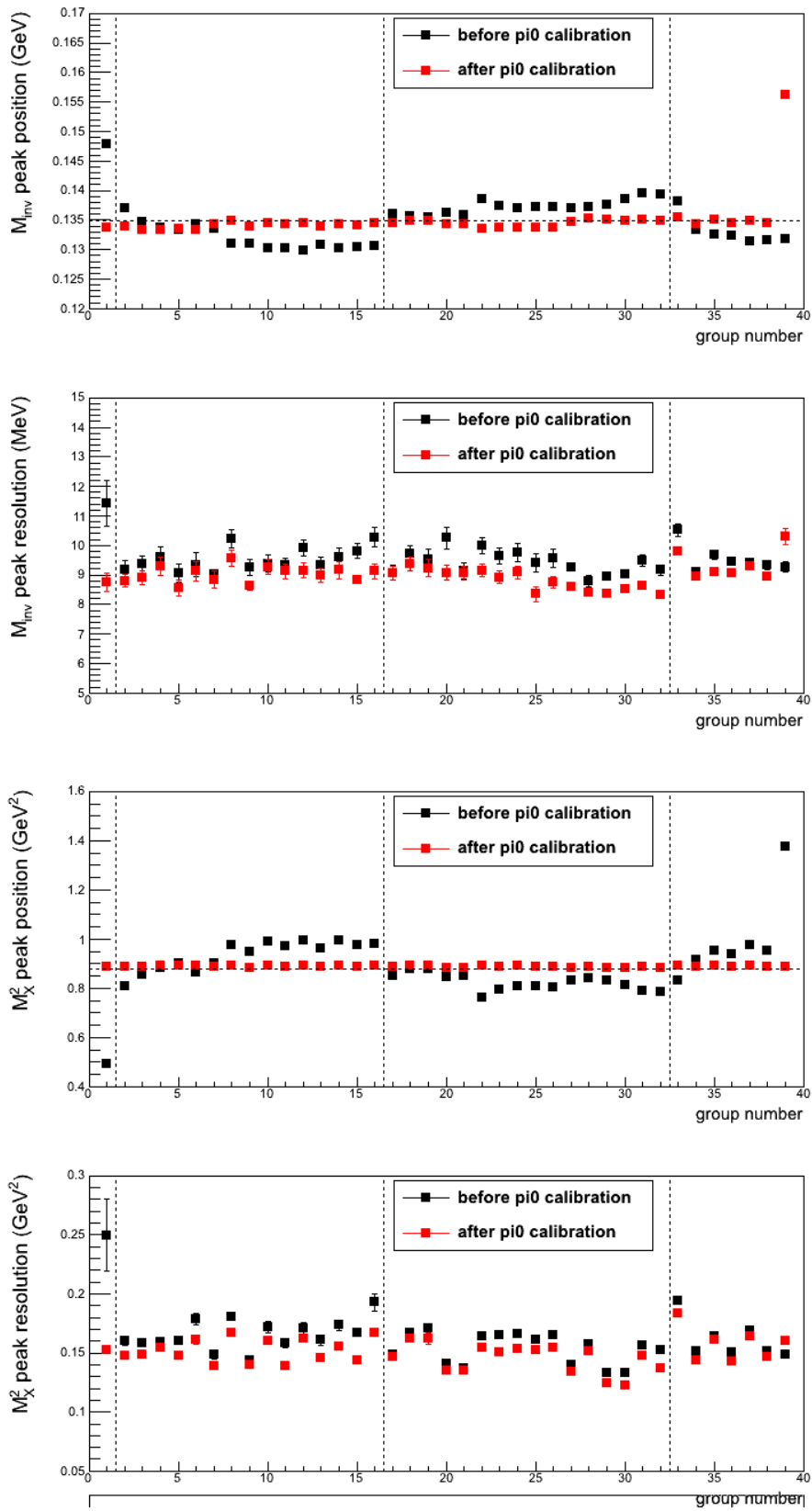
Figure 7.1: Comparison of the mean and standard deviation of the invariant-mass and the missing-mass peaks for exclusive π^0 events, before (black) and after (red) π^0 calibration. The dashed-lines represent elastic calibration runs. Using the π^0 calibration, the resolution on both peaks is slightly improved and their positions are much more stable.
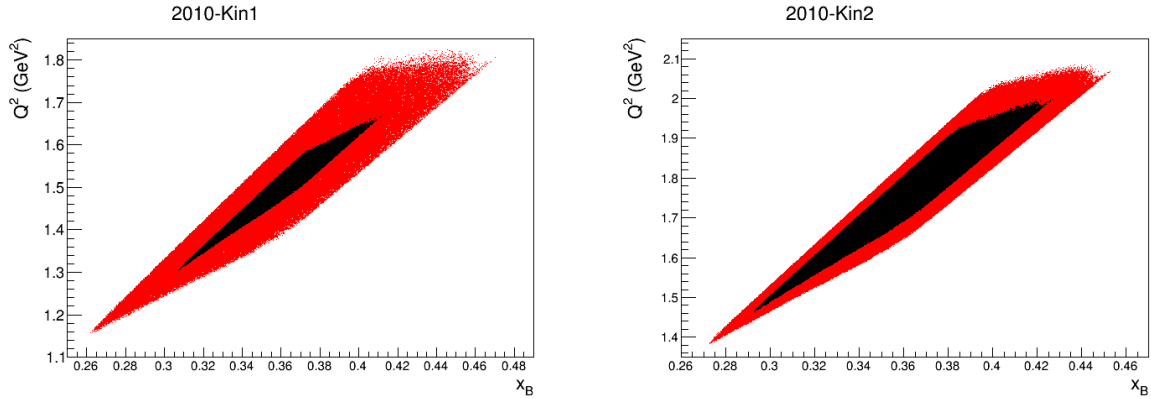
Figure 7.2: Left: Comparison of (Q^2,x_B) phase speaces between kin1low (black) and kin1high (red). Right: Comparison of (Q^2,x_B) phase spaces between kin2low (black) and kin2high (red).

for the cut on the energy deposit in the Pion Rejector. Indeed, the exclusivity cuts on the two-gamma invariant mass and the missing mass are enough to clean the electron sample without requiring a PR cut.

The phase space in (Q^2, x_B) selected by the HRS at high beam energy (HBE) is much larger than at low beam energy (LBE) (Figure 7.2). Because of the uncertainty and size of the kinematical dependences, we chose to apply a 2D-cut in the (Q^2,x_B) acceptance, limiting the HBE phase space to match the LBE one. The induced uncertainty on the kinematics of the extraction is therefore reduced and becomes similar for the two beam energy settings.

7.2.2 Selection of photons

The identification of π^0's is ensured by the invariant mass of the two photons from their decay (Figure **??**). Unlike the 2004 experiment, there was no hardware threshold on the energy deposit in the calorimeter for most of the 2010 run period. A software threshold needs to be applied in order to increase the signal-over-background ratio:

- An excessively low threshold would increase the multiplicity of detected photons, some of them being uncorrelated background or noise.

- An excessively high threshold would reduce the number of accepted π^0 events. We recall that it was the reason why no unpolarized photon electroproduction cross section were extracted from 2004-Kin1 since there were not enough detected π^0's to apply our subtraction method.

For the π^0 data analysis, we apply a software threshold at 500 MeV, filling the two conditions above. We select only 2-cluster events. Finally we also applied a geometrical cut on the two cluster positions in order to remove photons that hit the calorimeter less than 1.5 blocks away from the calorimeter edge. This limits the electromagnetic shower leakage and ensures a full reconstruction of the photon energy.

7.2.3 Process identification

In order to evaluate the number of exclusive π^0 events, we check the invariant mass of the two photons for particle identification and the missing mass associated with the $ep \rightarrow e\gamma\gamma X$ reaction. Because of the correlation between the invariant mass and the associated missing

mass stemming from imperfections in the calorimeter calibration, a 2-dimensional cut on these variables is applied (Figure 7.3).
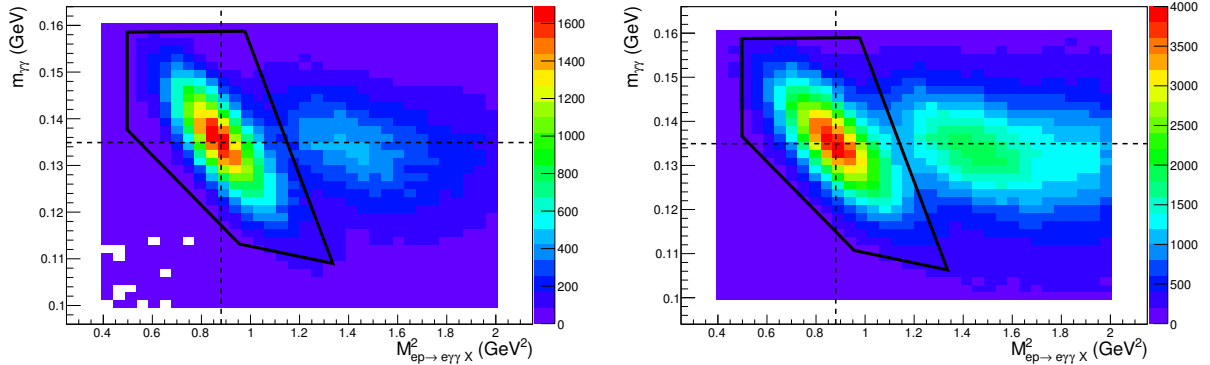
Figure 7.3: Invariant mass of photon pairs ($m_{\gamma\gamma}$) versus missing-mass squared of the $ep \rightarrow \gamma\gamma X$ system ($M^2_{ep\rightarrow\gamma\gamma X}$) for 2010-Kin1high (left) and 2010-Kin2high (right). The two dimensional exclusivity peak is clearly spotted at $M^2_{ep\rightarrow\gamma_1\gamma_2 X} = M^2$ and $m_{\gamma_1\gamma_2} = m_\pi$ (Intersection of the dashed lines). The π^0-identification/exclusivity cut is shown in black and is the same for all kinematical settings.

7.3 Accidental subtraction

Most of the contamination comes from accidental photons detected in the calorimeter. The number of accidental events can be decomposed into three terms:

$$N^{\pi^0}_{acc} = N_{a-aa} + N_{c-ac} + N_{a-cc} \,, \tag{7.6}$$

where:

- N_{a-aa} is the number of events for which all three particles are accidental with each other.

- N_{c-ac} is the number of events for which one of the photon and the scattered electron are in coincidence and we detect an accidental photon. For instance, such events can result from an exclusive photon event with an accidental photon detected in the calorimeter.

- N_{a-cc} is the number of events for which both photons are related to each other but accidental with respect to the scattered electron. Accidental π^0's create such events.

To estimate each term, we study the different cases looking at events in the coincidence time window [-11;-5], [-3;3] and [5;11] ns (Figure 7.4).

1. We apply all analysis cuts to two-photon events in the time range [-11,-5] ns. The total number of events passing the cuts is $N_{c-cc} + N_{a-aa}$.

2. When an event presents one photon detected in [-3;3] ns and one photon in [-11;-5], we combine the two photons and apply all analysis cuts to this event. The number of events estimated with this study is $N_{c-ac} + N_{a-aa}$.

3. Finally we study events with one photon in [-11;-5] ns and one photon in [5;11] ns, combine the two photons and apply the analysis cuts. We obtain N_{a-aa}. We get $N^{\pi^0}_{acc}$ by simply adding the two first terms and subtracting this last term.
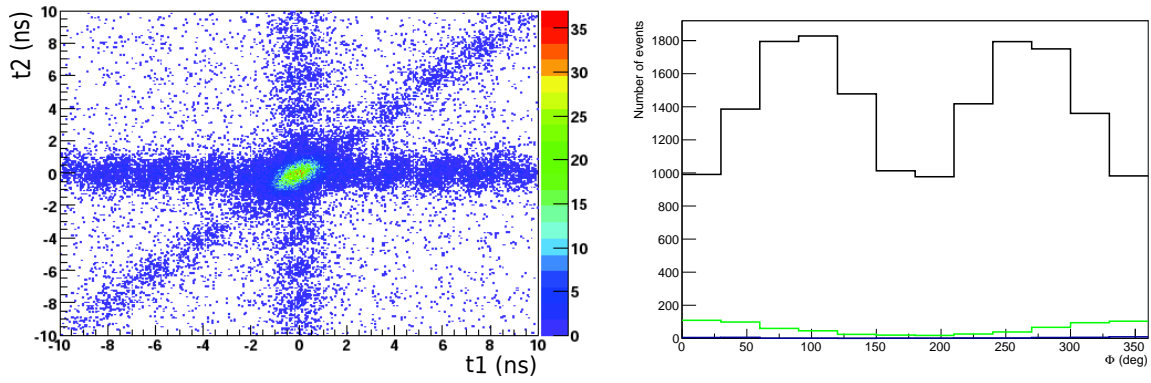
Figure 7.4: Left: Time distribution of 2-photon events. The horizontal and vertical bands correspond to N_{c-ac}. The diagonal is related to N_{a-cc}. Finally the random points give N_{a-aa} [69]. Right: Distribution of events in a typical bin. The total number of events in [-3;3] ns after analysis cut is represented in black. We have represented in green 2 N_{a-aa} + $N_{c-ac} + N_{a-cc}$ given by steps 1 and 2. N_{a-aa} is represented in blue (close to 0).

In order to reduce the statistical uncertainty on $N_{acc}^{\pi^0}$, we also use the window [5;11] ns for steps 1 and 2 and divide the corresponding results by 2.

7.4 Corrections

The corrections associated with the spectrometer for the 2010 run period have been developed in Chapter 3. We still need to apply the multicluster correction.

We use a method similar to the multicluster correction developed in section 4.4.3, but applied to π^0 events with two clusters in the calorimeter: For each 3-cluster events, photons are paired two-by-two. For each of the three pairs, we apply the analysis cuts. If a pair passes the cuts, we compute the corresponding kinematical variables and consider it as an exclusive π^0 to reintegrate in the corresponding experimental bins.

In the case of several pairs passing the analysis cuts, we cannot apply the trick used for DVCS which consists in evaluating the probability for each photon to be the exclusive one by looking at the accidental rates. Indeed for a few bins with small acceptance, we have no accidental event. Nevertheless we assume that the pairs have the same possibility to be the exclusive π^0's. As a consequence, we add in the experimental bin a fraction of event equal to $\frac{1}{N_{pair}}$, with N_{pair} the number of pairs passing the analysis cuts.

7.5 Luminosity

Since the analysis of the Compton polarimeter is still in progress, we only show the integrated luminosity in Table 7.2.

7.6 Monte-Carlo calorimeter calibration and resolution effects

In the case of the exclusive π^0 analysis, we have to reproduce the main features of the two-dimensional plot representing the invariant mass $m_{\gamma\gamma}$ versus the missing mass $M_{ep \rightarrow e\pi^0 X}^2$. Whereas the missing mass is essentially sensitive to the energy resolution, the invariant mass is mostly sensitive to the resolution on the angle between the two photons.

Setting	Luminosity (fb^{-1})
2010-Kin1low	3164
2010-Kin1high	522
2010-Kin2low	4415
2010-Kin2high	3102
2010-Kin3low	6095
2010-Kin3high	2233

Table 7.2: Integrated luminosity corrected for deadtime for the 2010 experimental settings. The deadtime can be found in Table 3.2 in Chapter 3.

The two photons are separated on average by ~ 13 cm, depending on the kinematics. Although the resolution of the calorimeter changes less from a bin to another in the case of π^0 than in the case of γ electroproduction, it may still induce some systematic effects. The accuracy of the local study is limited by the distance between the two photons and the available statistics. For this reason, the detector is divided into only 9 partially overlapping areas. The π^0's are associated with the area in which they would have hit the calorimeter.

Because we cannot disentangle the resolution effects on each photon separately, we work with the π^0 energy and 4-momentum. Indeed we apply the same transformation as in Eq. 5.4, except that we apply it to the 4-momentum of the π^0 instead of the photons. Concerning the angular resolution, we smear isotropically the directions of the photons with an angle θ_s generated according to a gaussian distribution.

Once the fitting/calibration/smearing procedure is performed, we have a map of the calibration coefficient, the energy and angular resolutions. The resolutions are worse when close to the beam side, as expected due to the high radiation background (Figure 7.5).
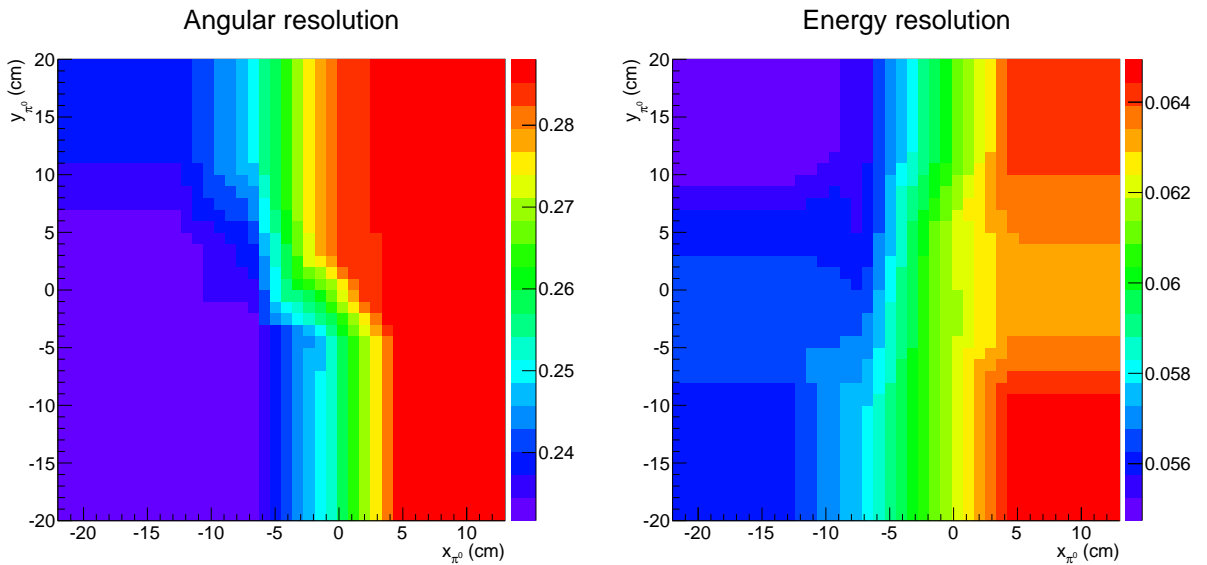
Figure 7.5: Left: θ_s for 2010-Kin3high as a function of the x_{π^0} and y_{π^0}, coordinates of the points where the π^0 would have hit the calorimeter. θ_s is given in degrees and corresponds to a resolution on the cluster position of ~ 4 mm. Right: Resolution on the π^0 energy (parameter σ) for 2010-Kin3high as a function of the x_{π^0} and y_{π^0}, coordinates of the points where the π^0 would have hit the calorimeter. The beam is located on the positive-x side.

7.7 Cross section extraction and full separation

We adapt the method introduced in Chapter 5 to extract the different terms of the cross section. Nevertheless the natural parametrization of the DVMP cross section (Eq 1.73) does not include the kinematical dependences of σ_T, σ_L, σ_{TL} and σ_{TT}[1]. We add a functionnal form to take into account these dependences.

7.7.1 Principle of the extraction

In the Chapter 5, we introduced a method to extract a cross section based on the minimization of a χ^2. This χ^2 compares the number of experimental events with the number of events estimated with a Monte-Carlo simulation and a parametrization of the cross section. In the case of a linear parametrization, the minimization of the χ^2 is equivalent to solving a matrix system:

$$A\overline{X} = B \ , \tag{7.7}$$

where A is the covariance matrix and B a vector, both defined in Eq. 5.26. $\overline{X}$ is a vector encapsulating the parameters of the cross section we want to extract, *i.e.* σ_T, σ_L, σ_{TL} and σ_{TT} for all vertex bins. Since we integrate some kinematical dependences over the acceptance automatically with the Monte-Carlo, this method is very efficient to reduce the error from a miscalculation of the bin kinematical center.

We apply the first steps of the fitting procedure on each beam energy setting separately. We compute the matrices (A_{low}, B_{low}) for low energy and (A_{high}, B_{high}) for high energy kinematics. Since we are looking for a vector $\overline{X}$ solution of both systems (Figure 7.6), we can write:

$$\left.\begin{array}{l} A_{low}\overline{X} = B_{low} \\ A_{high}\overline{X} = B_{high} \end{array}\right\} \Rightarrow (A_{low} + A_{high})\,\overline{X} = B_{low} + B_{high}, \tag{7.8}$$

We have a new matrix system combining the two kinematics together, with $[A_{low} + A_{high}]^{-1}$ as covariance matrix and $B_{low} + B_{high}$ as column vector.
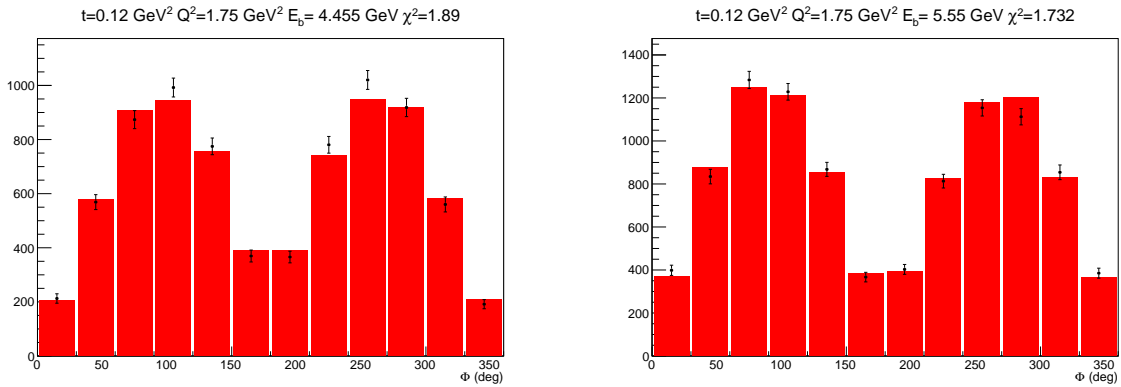
Figure 7.6: Left: The black points represent the number of events in a t'-bin for 2010-Kin2low. The red histogram represents the number of counts estimated by the Monte-Carlo simulation once the fit has been performed. On the right: Same t'-bin for 2010-Kin2high with the experimental number of counts represented by the black points and the Monte-Carlo estimation by the red histogram. χ^2/dof are close to 1 whereas we require the same quadruplet (σ_T, σ_L, σ_{TL}, σ_{TT}) for both bins.

---

[1] In order to simplify the notations, $\sigma_i \equiv \frac{d\sigma_i}{dt}$.

Then, with Eq. 5.30, we extract the experimental cross sections for both beam energies. Figure 7.7 shows the experimental virtual photon cross section $\frac{d^2\sigma}{dtd\phi}$ for both beam energies corresponding to the bin in Figure 7.6.
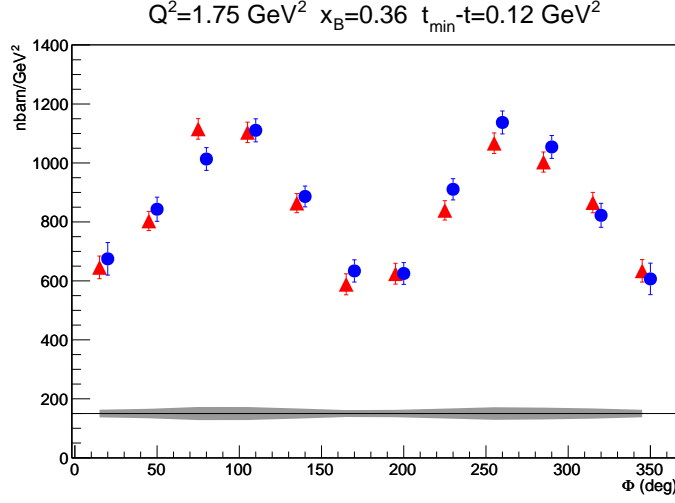
Figure 7.7: In red experimental $\frac{d^2\sigma}{dtd\phi}$ for 2010-Kin2high at t'=0.12 GeV^2, corresponding to $\epsilon^* = 0.79$. In blue $\frac{d^2\sigma}{dtd\phi}$ for 2010-Kin2low at t'=0.12 GeV^2, corresponding to $\epsilon^* = 0.65$. The shaded area represents the 2%-systematic error on the normalization.

7.7.2 Kinematical dependences

The terms σ_T and σ_{TT} depends strongly on Q^2 and for only σ_{TT} on $t' = t_{min}(x_B, Q^2) - t$. Because of this dependence, a slight error on the central value of the bin can induce a few percent error on $\sigma_T + \epsilon^*\sigma_L$. As the final goal is to compare $\sigma_T + \epsilon^*\sigma_L$ at two different beam energies, you must either compute exactly Q^2 and t' for the two beam energies or integrate these kinematical dependence in the fitting procedure to correct naturally for them. We choose the latter. We rewrite σ_T such as:

$$\frac{d\sigma_T}{dt} = \Lambda_T(t, Q, x_B) \times r_T , \tag{7.9}$$

$$\Lambda(t, Q, x_B) = \frac{(t_{min}(x_B, Q^2) - t)^{a_T}}{Q^{b_T}} , \tag{7.10}$$

where a_T and b_T are parameters to fit on data. Similarly we have $\frac{d\sigma_{TT}}{dt} = \Lambda_{TT}(t, Q, x_B) \times r_{TT}$ with the parameters a_{TT} and b_{TT}. $|t_{min}|$ is the minimal squared momentum transfer to the proton given by:

$$t_{min} = \frac{(Q^2 + m_\pi^2)^2}{4W^2} - \left[\sqrt{\frac{W^2 + Q^2 + M^2}{4W^2} - M^2} - \sqrt{\frac{W^2 - m_\pi^2 + M^2}{4W^2} - M^2}\right]^2 . \tag{7.11}$$

Such a functional form is only used for σ_T and σ_{TT} which are the cleanest signals. Then, the parametrization used for the extraction reads:

$$\frac{d^4\sigma}{dtd\phi dQ^2 dx_B} = \frac{1}{2\pi}\Gamma_{\gamma^*}(Q^2, x_B, E_e)\left[\Lambda_T(t, Q, x_B)r_T + \epsilon^*\frac{d\sigma_L}{dt}\right.$$
$$\left. + \sqrt{2\epsilon^*(1 + \epsilon^*)}\frac{d\sigma_{TL}}{dt}cos(\phi) + \epsilon^*\Lambda_{TT}(t, Q, x_B)r_{TT}cos(2\phi)\right] , \tag{7.12}$$

where r_T and r_{TT} are supposed to be independent of Q^2 and t'. To determine a_T, b_T, a_{TT} and b_{TT}, we have to iterate between the extraction and the fit. Then we follow the steps:

1. For the first extraction, we set $a_T = b_T = a_{TT} = b_{TT} = 0$. Therefore we have $\Lambda_T = \Lambda_{TT} = 1$ for all t' and Q^2 values.

2. We extract σ_T, σ_L, σ_{TT} and σ_{TL}. From this first extraction, σ_T shows a strong dependence on Q^2 and σ_{TT} on Q^2 and t'.

3. Therefore we fit a_T and b_T with the extracted σ_T over all the bins. a_{TT} and b_{TT} are obtained by fitting σ_{TT}.

4. Then we go back to step 1 and use the fitted values of a_T, b_T, a_{TT} and b_{TT}. As a consequence, we extract no longer σ_T and σ_{TT} in step 2, but r_T and r_{TT}.

The results do not change anymore after three iterations. We reconstruct then σ_T and σ_{TT} with Equation 7.9 at the mean kinematical value of the experimental data.

7.8   L/T separation of the π^0 electroproduction

The results presented in this section are still preliminary results. Although all sources of systematic errors have been identified, their propagation to the final results is still in progress.

7.8.1   Systematic uncertainties

7.8.1.1   Normalization

The normalization has been tested by extracting the DIS cross sections. Although the results were found within 4% of the theoretical DIS prediction, there is a systematic underestimation for high-beam-energy kinematics and an overestimation for low-beam-energy kinematics. We have decided to normalize our result to the DIS prediction which allows reducing the normalization systematic uncertainty from 4.5% to 2%.

To propagate this uncertainty, we extract 4 combinations for each response:

- σ_T^{++}, σ_L^{++}, σ_{TL}^{++} and σ_{TT}^{++} corresponding to an increase of 2% the normalization factor for both beam energies.

- σ_T^{--}, σ_L^{--}, σ_{TL}^{--} and σ_{TT}^{--} corresponding to a decrease of 2% the normalization factor for both beam energies.

- σ_T^{+-}, σ_L^{+-}, σ_{TL}^{+-} and σ_{TT}^{+-} corresponding to a decrease of 2% the normalization factor for the low beam energy and an increase of 2% for the high beam energy, and vice versa (σ_T^{-+}, σ_L^{-+}, σ_{TL}^{-+} and σ_{TT}^{-+}).

We then define the lower and upper uncertainty for σ_T such as:

$$\delta_T^+ = Max(\sigma_T^{++}, \sigma_T^{--}, \sigma_T^{-+}, \sigma_T^{+-}) - \sigma_T , \tag{7.13}$$

$$\delta_T^- = \sigma_T - Min(\sigma_T^{++}, \sigma_T^{--}, \sigma_T^{-+}, \sigma_T^{+-}) . \tag{7.14}$$

The normalization uncertainties for σ_L, σ_{TL} and σ_{TT} are defined similarly as for σ_T.

7.8.1.2   Exclusivity cut

To evaluate the systematic error on the extraction induced by the exclusivity cut, we extract the four terms using three different cuts. On Figure 7.8, we show the three cuts and the corresponding σ_T and σ_L extracted for Q^2=2 GeV^2. The resulting variation is small for σ_T and σ_L and it appears that we are dominated by the normalization uncertainty.
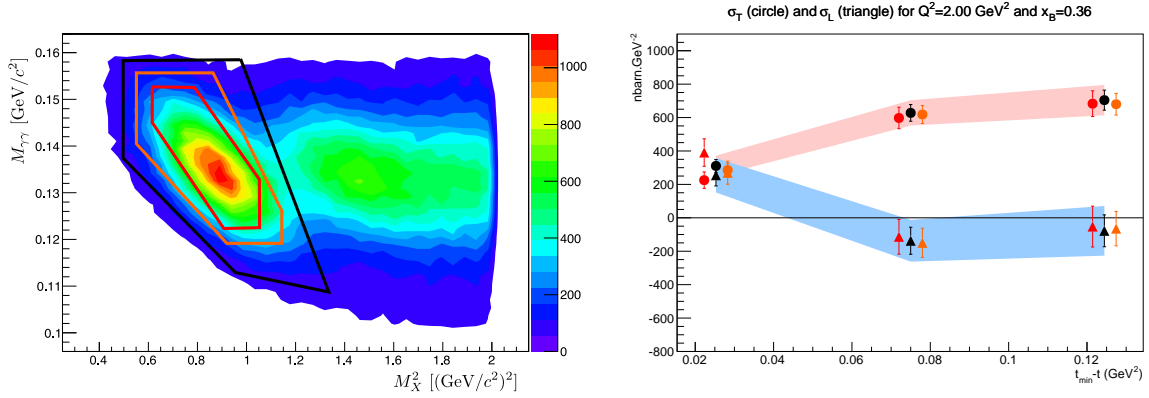
Figure 7.8: Left: Invariant mass of photon pairs versus missing-mass squared of the $ep \rightarrow \gamma\gamma X$ system for 2010-Kin3high. The black, orange and red lines represents the different cuts used to evaluate the systematic uncertainty. Right: σ_L and σ_T in nbarn.GeV^{-2} as a function of $t_{min} - t$ extracted with the three different cuts. The error bands represent a 2% normalization uncertainty.

Concerning σ_{TT} and σ_{TL}, the systematic uncertainty due to the exclusivity cut is larger than the normalization uncertainty, as illustrated on Figure 7.9. Their extraction is based on the ϕ-dependence of the cross sections, and therefore much more sensitive to local resolution effects.
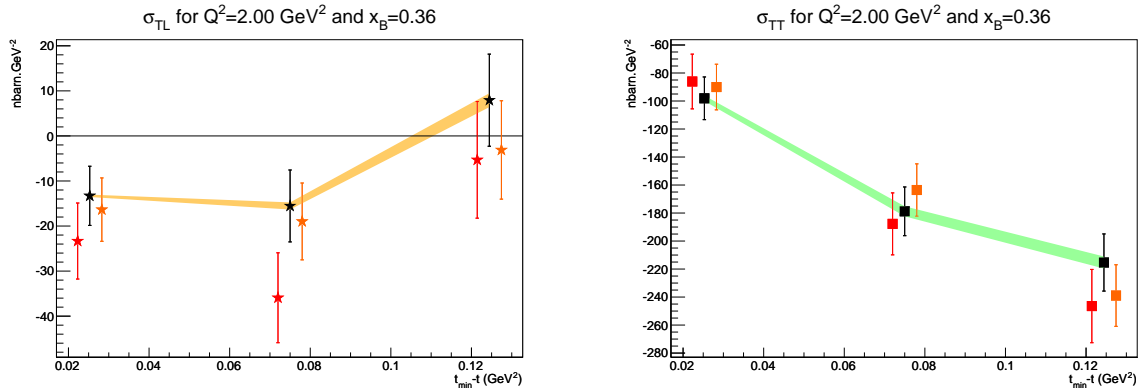
Figure 7.9: Left: σ_{TL} in nbarn.GeV^{-2} as a function of $t_{min} - t$ extracted with the three different cuts on $(m_{\gamma\gamma}; M^2_{ep \rightarrow e\pi^0 X})$ for Q^2=2 GeV^2. Right: σ_{TT} in nbarn.GeV^{-2} as a function of $t_{min} - t$ extracted with the three different cuts on $(m_{\gamma\gamma}; M^2_{ep \rightarrow e\pi^0 X})$ for Q^2=2 GeV^2. The error bands represent a 2% normalization uncertainty.

Indeed the value of the differential cross sections in $t' = (t_{min} - t)$ and ϕ changes locally when changing the 2D-cut on $(m_{\gamma\gamma}; M^2_{ep \rightarrow e\pi^0 X})$, as seen on Figure 7.10. Such point-to-point uncorrelated errors must be included in our extraction to properly propagate the exclusivity systematic uncertainty. This work is still in progress.

7.8.2 Results

We have used three bins in t' for the kinematics at Q^2=1.5 and Q^2=2 GeV^2. The high statistics of the kinematical setting at Q^2=1.75 GeV^2 and the large t'-acceptance have allowed us to extract a fourth bin for this intermediate setting. For most of the bins, σ_L is found to be compatible with 0 and consequently σ_T represents almost all the ϕ-independent term.
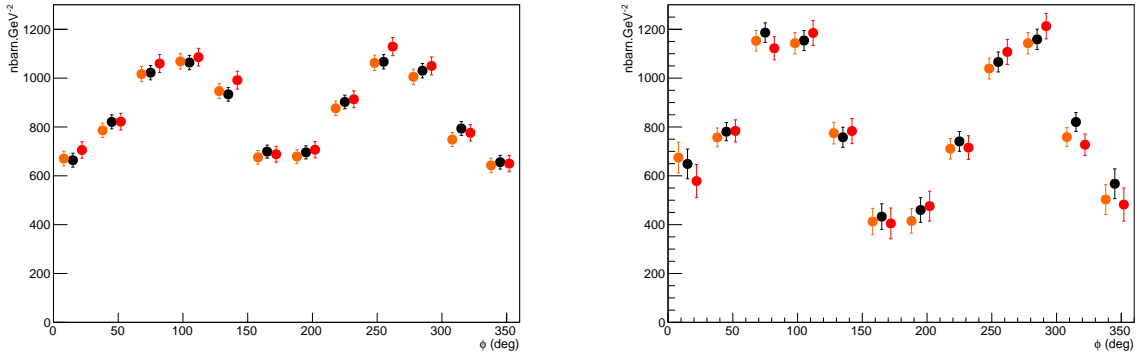
Figure 7.10: $\frac{d^2\sigma}{dt d\phi}$ in nbarn.GeV^{-2} as a function of ϕ for two bins of 2010-Kin2 with different exclusivity cuts. We apply the same color code as in Figure 7.8.

On Figure 7.11, we have a non-zero σ_L contribution at Q^2=2 GeV^2 and $t' = 0.02$ GeV^2. It is at this kinematical values that the Goloskokov-Kroll (GK) model [20] predicts the largest longitudinal contribution. Figure 7.11 shows also predictions from Liuti-Goldstein (LG) [39] models involving also transversity GPDs. The GK model is in fair agreement, although it overestimates slightly σ_T. The LG model is only shown for Q^2=2 GeV^2 on a limited range in t' and underestimate the transverse contribution. In addition, we have studied the Q^2-dependence of σ_T. We have fitted a function $\frac{A}{Q^n}$ on the average value of σ_T extracted at each Q^2. Since $n \sim 8$, it seems to indicate that the handbag diagram dominates even though our study is performed at moderate Q^2.

Concerning σ_{TT}, its amplitude increases as Q^2 decreases. Again the GK model over-estimates this term (Figure 7.12), which tends to indicate that the $\bar{E}_T$ contribution in the GK model is larger than what it is in the experiment. We have studied the Q^2-dependence, using again a functional form $\frac{A}{Q^n}$; we find $n \sim 6$ whereas it should be 8 in the hypothesis of the handbag diagram dominance. However the error on n does not include the systematic uncertainty from the exclusivity cut whereas it is the major source of uncertainty for σ_{TT}. Although rather small, σ_{LT} is not compatible with zero and found negative whereas both theoretical predictions give a positive value. But there is no theoretical constraint on the sign of σ_{TL}. However it seems that the GK model succeeds to predict its amplitude for the two highest Q^2-values and underestimate it at Q^2=1.5 GeV^2. Because σ_{TL} is small and the systematic uncertainty from exclusivity is large, no conclusion can be drawn from its Q^2-dependence.

The GK model reproduces the main features of the π^0 electroproduction cross section. Indeed its fair agreement with the results strongly suggests that there is a coupling between the transversity GPDs and the twist-3 DAs of the pion. It makes π^0 electroproduction an interesting channel to study these GPDs, under the assumptions of a fairly good knowledge of the DAs and that the factorization for transversely polarized photons is valid.

Concerning longitudinally polarized photons, the theoretical framework is well established. The longitudinal contribution involving the GPDs $\tilde{H}$ and $\tilde{E}$ is small, compatible with 0 for most of the bins. At Q^2=2 GeV^2 and the smallest t' value, *i.e.* the bin with the highest expected ratio $R = \frac{\sigma_L}{\sigma_T}$, σ_L is not compatible with 0. Therefore, at slightly higher Q^2, it should be possible to study $\tilde{H}$ and $\tilde{E}$ using π^0 electroproduction.
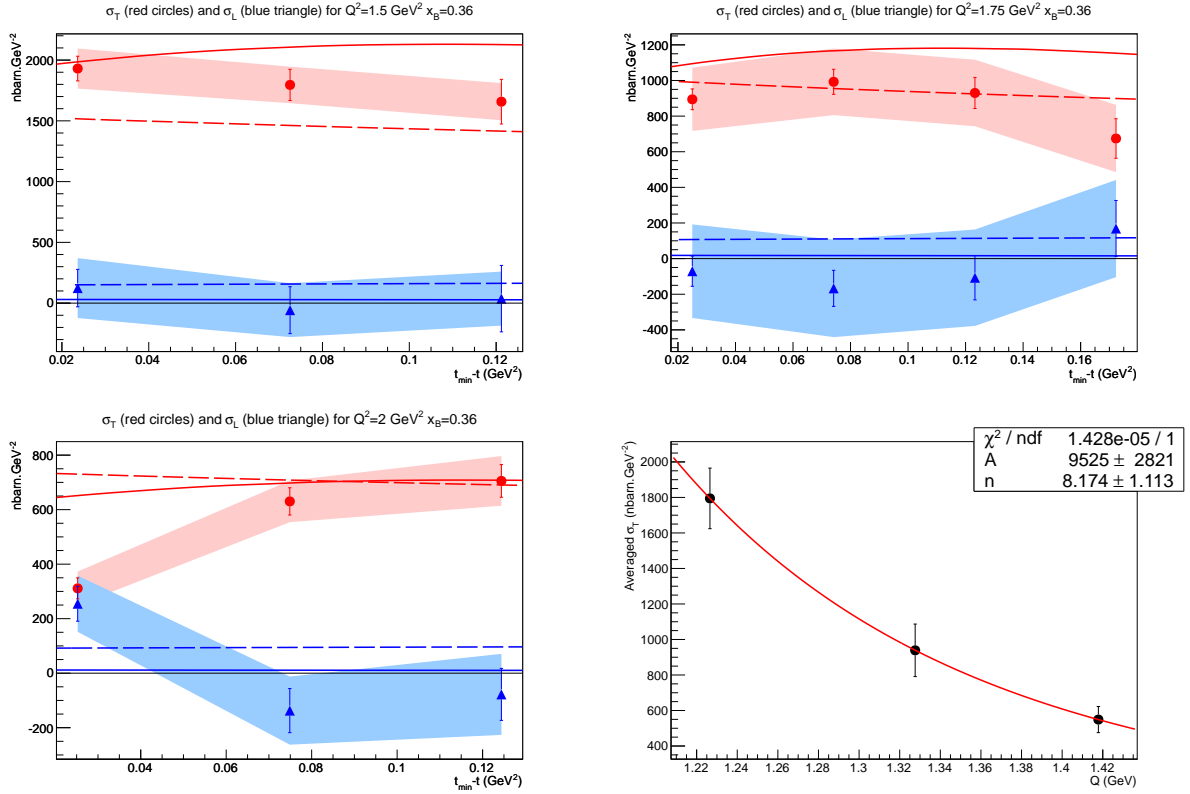
Figure 7.11: Longitudinal and transverse π^0 electroproduction cross sections, σ_T (red) and σ_L (blue) in nbarn.GeV^{-2} as a function of $t_{min} - t$ in GeV^2. The shaded area represents the systematic normalization uncertainty. The solid lines in the corresponding colors represent predictions by GK [20], the dashed lines in corresponding colors represent predictions by LG [39]. Bottom right: Fit Q^2-dependence of σ_T when averaged over t'. The error bars are the linear sum of the statistical uncertainty with the systematic uncertainty of normalization.
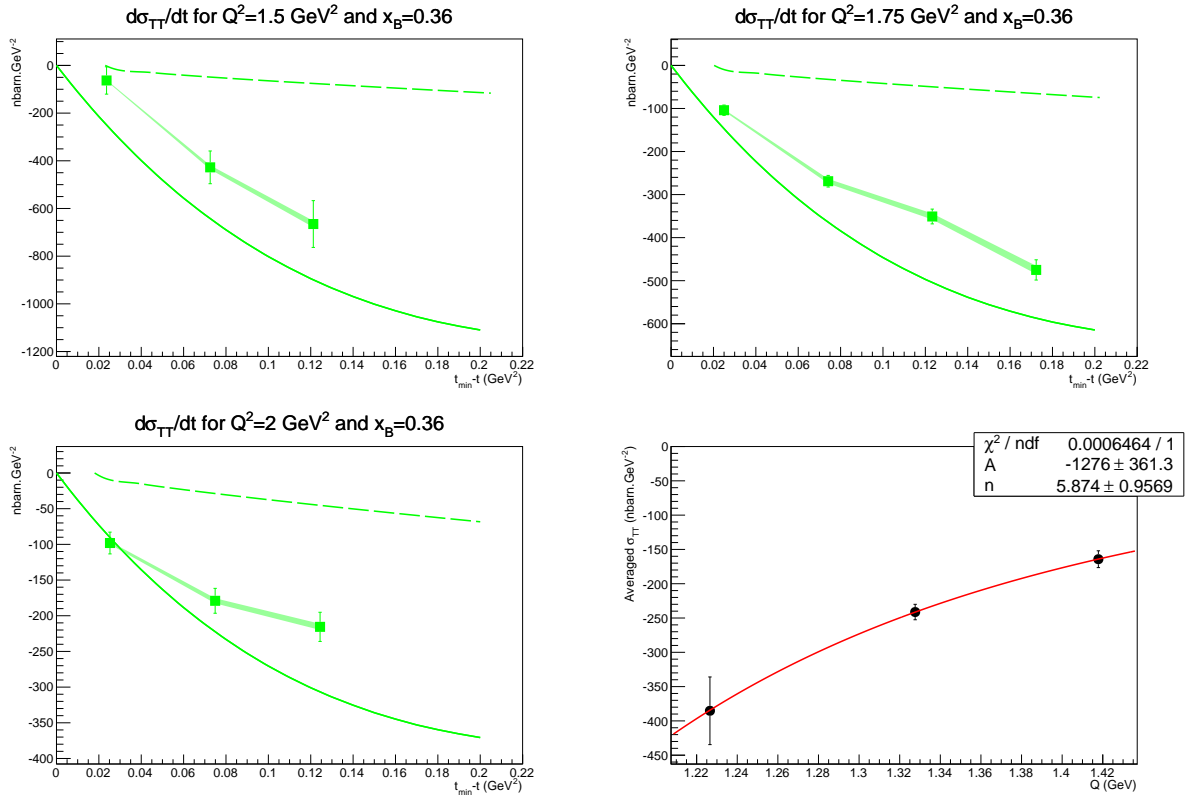
Figure 7.12: Transverse/transverse interference term σ_{TT} for π^0 electroproduction in nbarn.GeV^{-2} as a function of $t_{min} - t$ in GeV^2. The shaded area represents the systematic normalization uncertainty. The solid lines represent predictions by GK [20], the dashed lines represent predictions by LG [39]. Bottom right: Fit Q^2-dependence of σ_{TT} when averaged over t'.
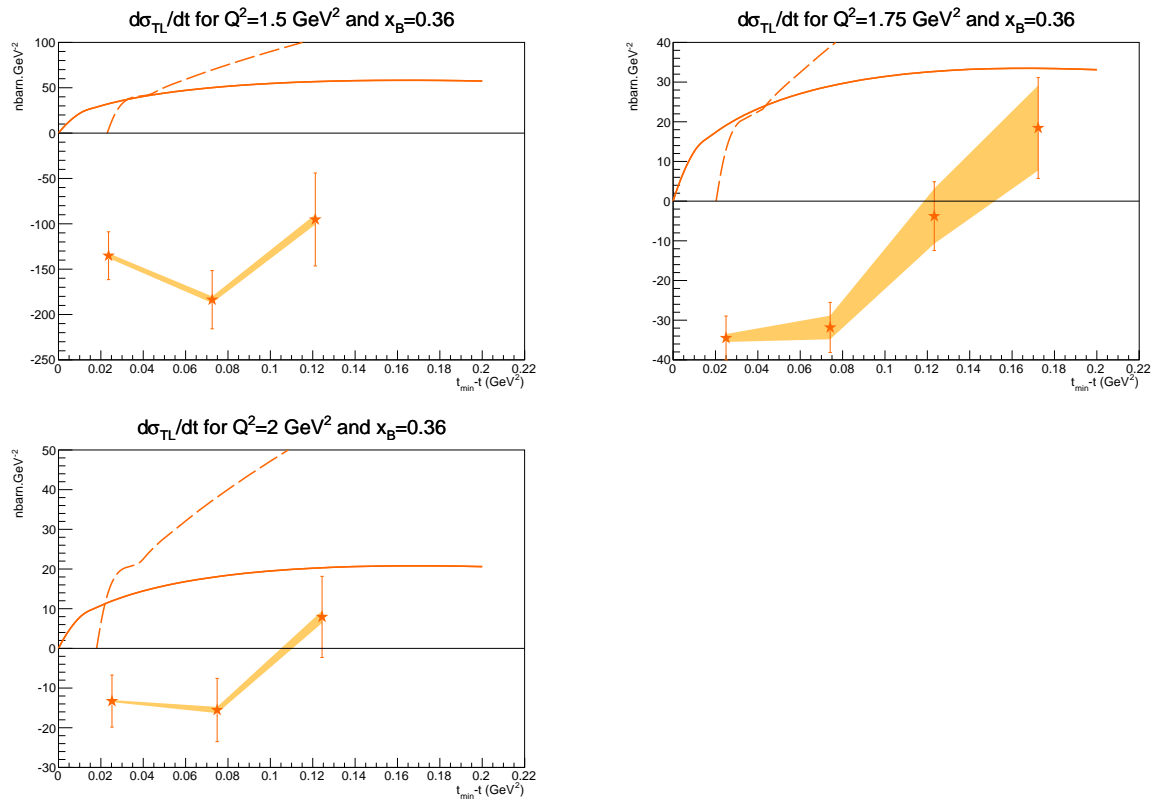
Figure 7.13: Transverse/longitudinal interference term σ_{TL} for π^0 electroproduction in nbarn.GeV^{-2} as a function of $t_{min} - t$ in GeV^2. The shaded area represents the systematic normalization uncertainty. The solid lines represent predictions by GK [20], the dashed lines represent predictions by LG [39].

Conclusion

In this thesis we have analyzed two different data sets and studied photon and π^0 electro-production cross sections. The high statistical accuracy of both data sets requires a careful study of the systematic errors: identification, cause(s) and evaluation. For instance we have identified the calibration and resolution of the calorimeter as the critical parameters that might induce the largest systematic error for both processes. Nevertheless this error can be reduced by reproducing as much as possible the calibration and resolution of the calorimeter in the Monte-Carlo simulation. To do so, we have developed a fitting/calibration/smearing procedure based on the comparison between the experimental and the Monte-Carlo missing-mass squared distributions (and the invariant mass of the two photons in the case of π^0 electroproduction). The systematic uncertaintes from the normalization and the HRS acceptance have been studied through the extraction of the deep inelastic scattering cross section for the 2010 run period. Because of the damaged BCMs in 2010, we estimate the normalization+HRS acceptance systematic uncertainty at 4.5% whereas it was only 2.5% for the 2004 run period.

Concerning the photon electroproduction, we have extended the kinematical domain of the previous Hall A measurements for both polarized and unpolarized cross sections. In addition we have extracted a set of effective CFFs following the formalism developed in [17]. For both the unpolarized and polarized cases, these effective CFFs show no Q^2-dependence. In other words the handbag diagram seems to be dominant despite the rather low Q^2 values. The E07-007 experiment ran in 2010 and performed DVCS cross section measurements at two beam energies in order to separate the contributions of the $|DVCS|^2$ and the interference terms. With such a clean separation, we will be able to further test the scaling property. We have also compared our results to existing GPD models. The model of reference, KM10a, is in good agreement with the polarized data points. Nevertheless it seems to underestimate the unpolarized signal around $\phi = 180°$. Recent work about target-mass and finite-t corrections have shown that such effects may change significantly the cross section behavior around $\phi = 180°$. We have applied the bulk of the TMC to the KM10a model and noticed that this modification improves very significantly the agreement with most of the unpolarized cross section results.

We have also performed the first Rosenbluth separation of the π^0 electroproduction cross section. We observe that most of the cross section is induced by transverse virtual photons. Although the factorization cannot be demonstrated with transversely polarized photons in the case of DVMP, the fair agreement with the Goloskokov-Kroll model might indicate that higher-twist contributions from the meson distribution amplitude couples to transversity GPDs. Indeed the large kinematical factor $\mu_\pi = \frac{m_\pi^2}{m_u + m_d}$ coming with the twist-3 DAs would compensate the twist-3 Q^2-suppression and induce a large transverse response at our moderate Q^2. If this hypothesis holds, neutral pion electroproduction becomes the golden channel to access these elusive transversity GPDs. The longitudinal π^0 cross section is found compatible with zero for most of our data. At the highest Q^2 and smallest $(t_{min} - t)$ values, a non-zero longitudinal signal appears where $R = \frac{\sigma_L}{\sigma_T}$ is supposed to be maximal. Note that

it should be possible to get information about GPDs $\tilde{H}$ and $\tilde{E}$ by studying σ_L at higher Q^2 where it becomes sizable. Moreover π^0's are particularly good candidates to study these GPDs as they do not involve a pion-pole contribution like π^+.

Additional data for both processes will be provided by 12 GeV data at Jefferson and by COMPASS at CERN in the near future. Indeed, the E12-06-114 experiment in Hall A is currently running and aims at high precision measurements in a larger kinematical domain compared to 6 GeV running. The CLAS12 DVCS program is also very ambitious, with unpolarized and polarized target running in a large kinematical domain. Finally, using the High Momentum Spectrometer in Hall C, Rosenbluth separations of photon and π^0 electroproduction will be carried out at higher Q^2 and x_B compared to data shown in this thesis. The COMPASS experiment at CERN will run its dedicated DVCS program starting in 2016. Besides DVCS and π^0 electroproduction, the GPD experimental program will also include the studies of Timelike Compton Scattering, Double-DVCS and electroproduction of other mesons. On a longer time scale, the Electron-Ion Collider will add the missing pieces of the GPD puzzle such as an unprecedented kinematical domain and statistical precision, as well as data related to GPDs which can only be accessed precisely with transverse protons, easy to achieve in such a collider. The next 15 years will be extremely exciting!

Nevertheless, the experimental progress will be such that an equally intense effort has to be carried out on the data analysis front, as well as in theory and phenomenology. For the data analysis, most collaborations still use sequential cuts to select events, which is crude and often inefficient: much cleverer tools such as neural networks or boosted decision trees could be investigated in order to optimize the selection of events and improve the accuracy of the measurement. Also, experimentalists and theorists need to work together in order to improve the calculation of radiative corrections, which are sizable and still in their infancy for the processes of interest. In this thesis, we have associated a systematic uncertainty of 2% to the QED radiative corrections and it is already a large uncertainty compared to the statistical precision of the data. For instance, CLAS12 expects a statistical accuracy of 2% or less in some experimental bins. Clearly, the present accuracy of radiative corrections is not sufficient for the future experiments which will be limited by systematic errors. As far as phenomenology is concerned, the statistical precision is already such that QCD corrections (Next-to-Leading Order corrections, Q^2-evolution,...) have to be included in order to reliably extract GPDs. Moreover, both the photon and the π^0 electroproduction results shown in this thesis strongly hint at the necessity to include some form of higher-twist effects for their interpretation. However, it is striking to observe that only a few phenomenology groups currently work on GPD extraction, which is a task immensely more complicated than the extraction of PDFs from DIS data. It is absolutely crucial to start focusing our efforts on GPD extraction. Once everything is in place, only then will we be able to cast our eyes on the first realistic three-dimensional pictures of the nucleon.

Appendix A

Preliminary DVCS results for the 2010 run period

Another goal of the 2010 run period was to perform a Rosenbluth separation of the photon electroproduction cross section. This separation allows to disentangle the contributions of the squared DVCS amplitude and the interference terms which have different beam energy dependences. We checked the normalization through the extraction of the DIS cross section when the trigger was an inclusive elctron trigger. But there is a significant part of the 2010-Kin2high which ran with the calorimeter in the trigger and for which there is no direct way to test the normalization. In the first section of this appendix, we compare the photon electroproduction cross sections with and without the calorimeter in the trigger. In the second one, we compare the results extracted from 2004-Kin2 to 2010-Kin3high which are kinematically close to each other.

The 2010 results presented in this appendix are preliminary results.

A.1 Inclusive electron trigger versus dedicated DVCS trigger

In Chapter 3, we mentioned that the 2010-Kin2high ran with two different triggers. Whereas it was possible to study the DIS cross section to check the normalization with the inclusive electron trigger, there is no such check with the dedicated DVCS trigger (Level-2 trigger requiring one cluster in the calorimeter above 200 MeV). Nevertheless we can compare the photon electroproduction cross section for both triggers.

Both results are statistically compatible as illustrated by Figure A.1 whereas the triggers were different.

A.2 Comparison with the 2004 run period

We have compared the 2010-Kin3high results (Q^2=2 GeV^2, E=5.55 GeV, x_B=0.36) to the 2004-Kin2 results (Q^2=1.9 GeV^2, E=5.7572 GeV, x_B=0.36) : indeed, using the effective CFFs extracted on 2004-Kin2, we can estimate the cross section at the kinematics of 2010-Kin3high with Eq. 5.19. We applied the same binning in t for this study as for the 2004 analysis. As seen on Figure A.2, the predictions with the 2004 results match the cross sections extracted for 2010-Kin3high within the statistical/systematic uncertainties.

In conclusion of this appendix, all the results (2004, 2010 with or without calorimeter in the trigger) are compatible with each other.
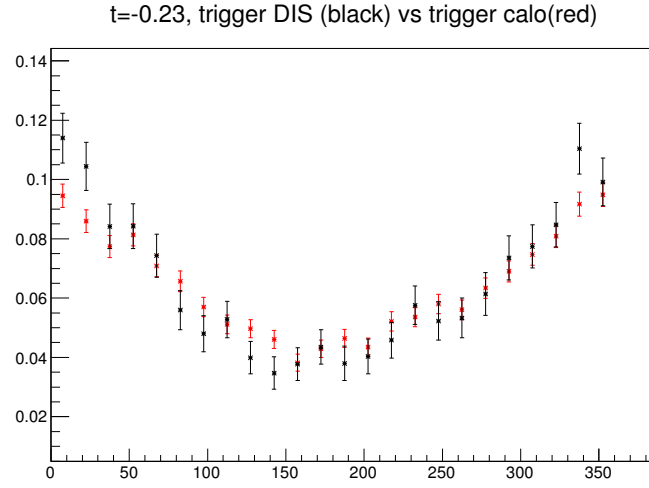
Figure A.1: Photon electroproduction cross section in nbarn.GeV^{-4} as a function of ϕ in degrees. The black points are extracted from the 2010-Kin2high data taken with the inclusive electron trigger (runs from 9257 to 9292, and from 9577 to 9615), the red points with the dedicated DVCS trigger (run 9705 to 9850).
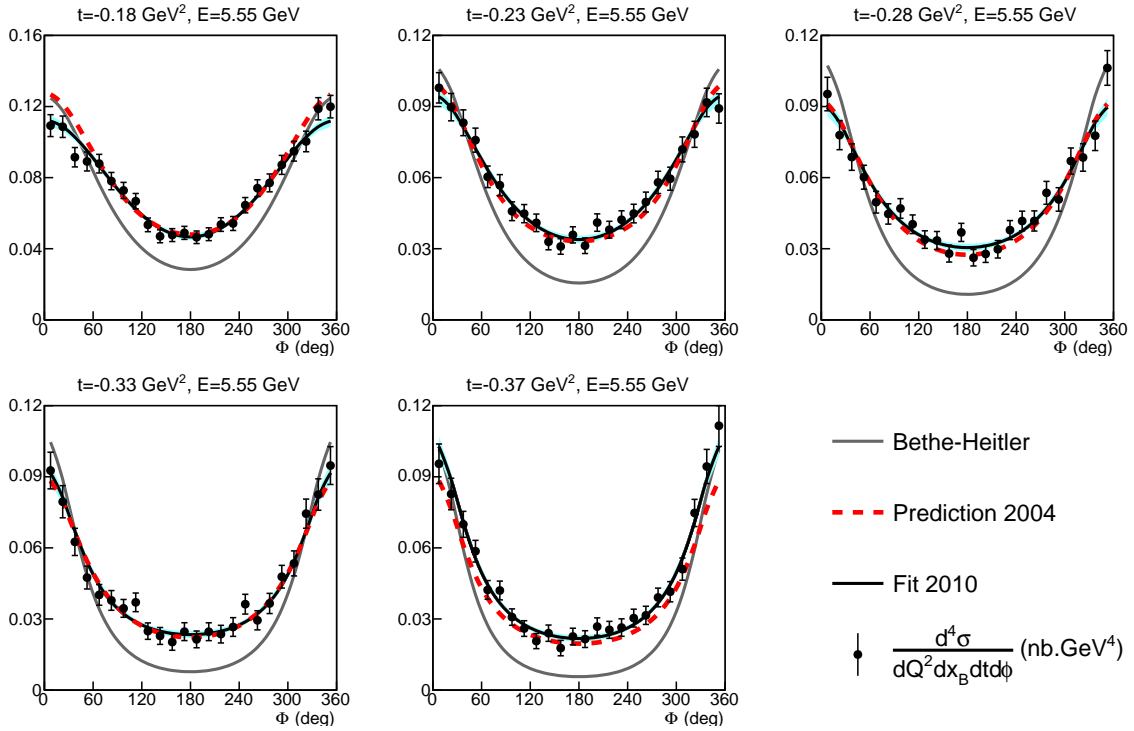
Figure A.2: Photon electroproduction cross sections in nbarn.GeV^{-4} as a function of ϕ in degrees for 2010-Kin3high. The grey solid line is the Bethe-Heitler contribution, The blue solid line $\mathcal{C}^{DVCS}(\mathcal{F}, \mathcal{F}^*)$ (Eq. 1.63), the red solid line $\Re e[\mathcal{C}^{\mathcal{I}}(\mathcal{F})]$ (Eq. 1.68) and the green solid line $\Re e[\mathcal{C}^{\mathcal{I}}(\mathcal{F}_{eff})]$ (Eq. 1.69). The black solid line represents the sum of all the contributions. The dashed pink line is the prediction using the results of 2004-Kin2.

Appendix B

Tables of unpolarized and polarized dvcs cross sections

B.1 Unpolarized cross sections
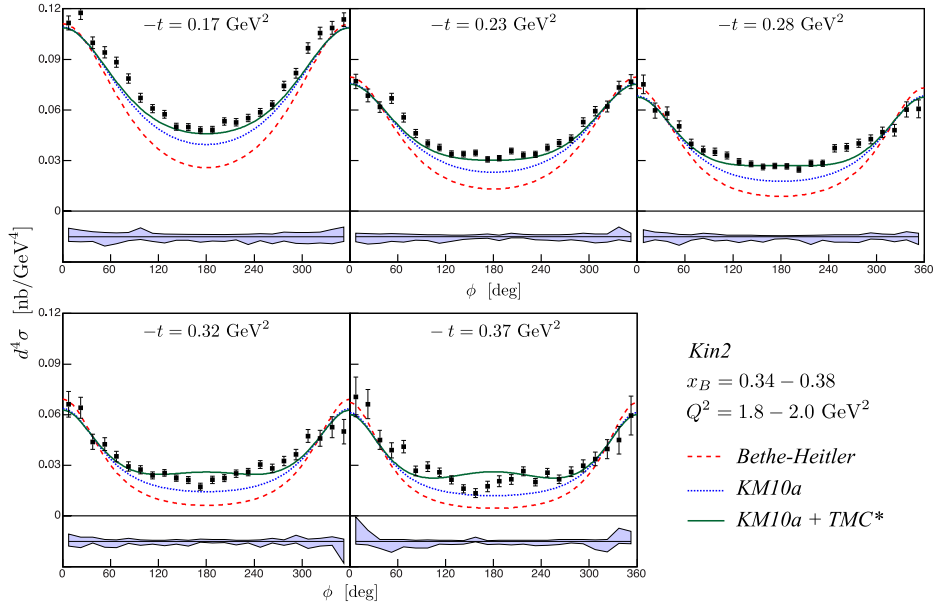
Figure B.1: (Color online) Unpolarized cross sections for Kin2. Error bars are statistical only. The light blue area represents the point-to-point systematic uncertainties added linearly to the normalization error. The KM10a model along with its modified version including TMC effects are shown as dotted blue and solid green curves respectively. The Bethe-Heitler contribution is represented as a dashed red line.
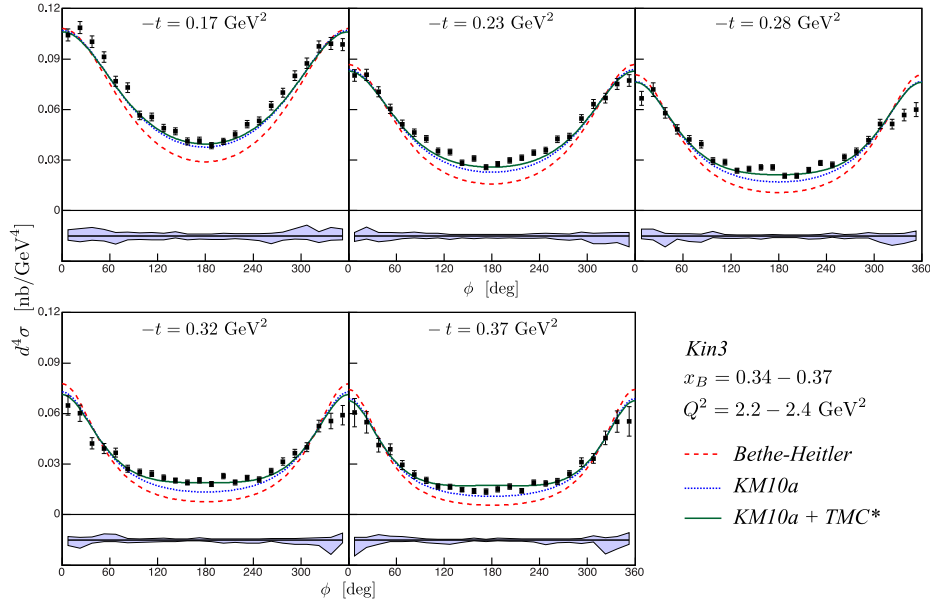
Figure B.2: (Color online) Unpolarized cross sections for Kin3. Error bars are statistical only. The light blue area represents the point-to-point systematic uncertainties added linearly to the normalization error. The KM10a model along with its modified version including TMC effects are shown as dotted blue and solid green curves respectively. The Bethe-Heitler contribution is represented as a dashed red line.
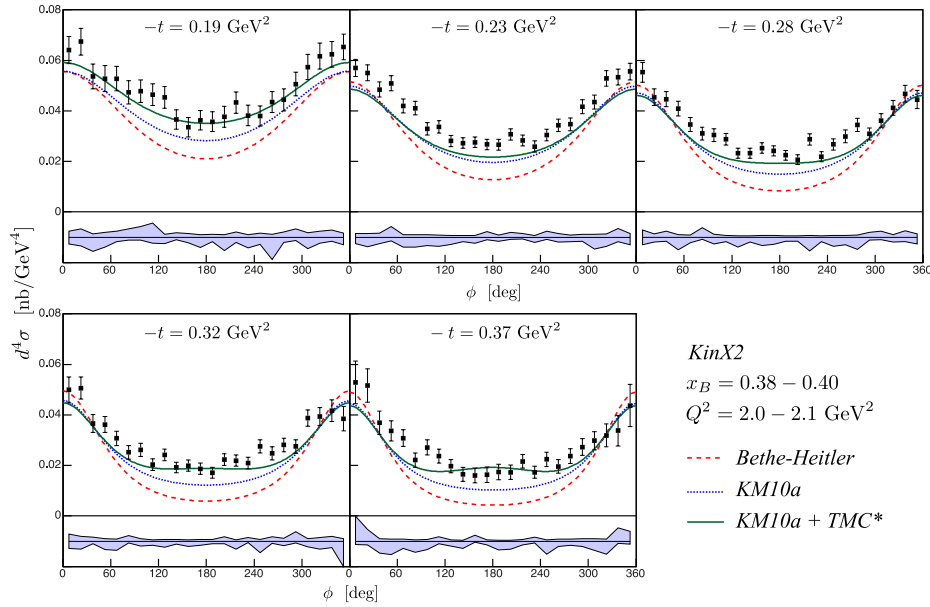
Figure B.3: (Color online) Unpolarized cross sections for KinX2. Error bars are statistical only. The light blue area represents the point-to-point systematic uncertainties added linearly to the normalization error. The KM10a model along with its modified version including TMC effects are shown as dotted blue and solid green curves respectively. The Bethe-Heitler contribution is represented as a dashed red line.

ϕ (deg)	$x_B = 0.343$ $Q^2 = 1.820$ GeV² $t = -0.172$ GeV²	$x_B = 0.368$ $Q^2 = 1.933$ GeV² $t = -0.232$ GeV²	$x_B = 0.375$ $Q^2 = 1.964$ GeV² $t = -0.278$ GeV²	$x_B = 0.379$ $Q^2 = 1.986$ GeV² $t = -0.323$ GeV²	$x_B = 0.381$ $Q^2 = 1.999$ GeV² $t = -0.371$ GeV²
7.5	$111.6 \pm 4.1\ ^{+2.3}_{-0.0}$	$76.9 \pm 4.2\ ^{+0.0}_{-1.1}$	$75.2 \pm 5.6\ ^{+2.2}_{-1.7}$	$66.2 \pm 7.7\ ^{+3.2}_{-0.9}$	$70.6 \pm 11.8\ ^{+13.1}_{-0.0}$
22.5	$117.6 \pm 3.9\ ^{+0.7}_{-0.3}$	$68.6 \pm 3.7\ ^{+0.0}_{-2.8}$	$59.7 \pm 4.5\ ^{+1.4}_{-0.6}$	$64.1 \pm 6.3\ ^{+0.9}_{-2.0}$	$66.3 \pm 8.7\ ^{+5.2}_{-0.4}$
37.5	$99.8 \pm 3.5\ ^{+0.3}_{-0.5}$	$61.7 \pm 3.2\ ^{+0.0}_{-2.6}$	$57.9 \pm 3.8\ ^{+0.9}_{-1.5}$	$43.9 \pm 4.5\ ^{+1.8}_{-0.0}$	$45.1 \pm 5.7\ ^{+0.0}_{-3.3}$
52.5	$94.1 \pm 3.3\ ^{+0.0}_{-3.4}$	$66.9 \pm 3.0\ ^{+0.0}_{-1.2}$	$50.4 \pm 3.2\ ^{+0.0}_{-4.2}$	$42.5 \pm 3.8\ ^{+0.0}_{-2.8}$	$39.0 \pm 4.5\ ^{+0.0}_{-5.8}$
67.5	$88.2 \pm 3.0\ ^{+0.0}_{-2.1}$	$55.5 \pm 2.7\ ^{+0.0}_{-2.0}$	$40.0 \pm 2.8\ ^{+0.2}_{-1.1}$	$35.3 \pm 3.1\ ^{+0.0}_{-2.9}$	$41.0 \pm 3.7\ ^{+0.0}_{-2.4}$
82.5	$78.7 \pm 2.8\ ^{+0.4}_{-0.4}$	$46.1 \pm 2.4\ ^{+0.1}_{-0.9}$	$36.1 \pm 2.5\ ^{+1.3}_{-0.0}$	$29.4 \pm 2.8\ ^{+1.2}_{-0.4}$	$26.7 \pm 2.9\ ^{+0.0}_{-3.3}$
97.5	$67.2 \pm 2.6\ ^{+3.6}_{-0.0}$	$40.1 \pm 2.1\ ^{+0.1}_{-1.4}$	$35.2 \pm 2.2\ ^{+0.6}_{-1.8}$	$27.4 \pm 2.4\ ^{+0.0}_{-2.0}$	$29.2 \pm 2.8\ ^{+0.0}_{-3.3}$
112.5	$60.8 \pm 2.4\ ^{+0.5}_{-1.3}$	$37.7 \pm 2.0\ ^{+0.0}_{-3.1}$	$33.0 \pm 2.1\ ^{+0.0}_{-1.4}$	$24.0 \pm 2.1\ ^{+0.0}_{-1.3}$	$25.9 \pm 2.6\ ^{+0.0}_{-1.0}$
127.5	$57.5 \pm 2.3\ ^{+0.0}_{-2.3}$	$34.0 \pm 1.8\ ^{+0.0}_{-2.2}$	$29.3 \pm 1.8\ ^{+0.1}_{-3.0}$	$25.5 \pm 2.0\ ^{+0.0}_{-2.2}$	$21.4 \pm 2.4\ ^{+0.1}_{-1.4}$
142.5	$50.1 \pm 2.1\ ^{+0.2}_{-0.8}$	$33.9 \pm 1.7\ ^{+0.0}_{-0.9}$	$28.0 \pm 1.7\ ^{+0.0}_{-1.4}$	$22.4 \pm 1.9\ ^{+0.5}_{-1.3}$	$16.1 \pm 2.4\ ^{+0.0}_{-1.4}$
157.5	$49.9 \pm 2.1\ ^{+0.0}_{-0.9}$	$34.6 \pm 1.7\ ^{+0.2}_{-0.5}$	$26.3 \pm 1.7\ ^{+0.0}_{-2.8}$	$21.3 \pm 2.1\ ^{+0.0}_{-2.6}$	$13.5 \pm 2.7\ ^{+2.7}_{-0.0}$
172.5	$48.1 \pm 2.0\ ^{+0.0}_{-2.0}$	$30.7 \pm 1.6\ ^{+0.9}_{-0.3}$	$26.8 \pm 1.7\ ^{+0.0}_{-0.7}$	$17.4 \pm 2.0\ ^{+1.3}_{-0.0}$	$17.5 \pm 3.2\ ^{+0.0}_{-1.7}$
187.5	$48.3 \pm 2.0\ ^{+0.0}_{-1.5}$	$31.5 \pm 1.6\ ^{+0.0}_{-1.6}$	$26.6 \pm 1.7\ ^{+0.2}_{-0.6}$	$21.4 \pm 2.1\ ^{+0.7}_{-0.3}$	$20.5 \pm 3.2\ ^{+0.0}_{-1.4}$
202.5	$53.2 \pm 2.1\ ^{+0.0}_{-1.6}$	$35.7 \pm 1.7\ ^{+1.2}_{-0.0}$	$24.7 \pm 1.6\ ^{+0.0}_{-1.5}$	$22.5 \pm 2.1\ ^{+0.6}_{-0.3}$	$21.7 \pm 2.9\ ^{+0.0}_{-1.8}$
217.5	$52.7 \pm 2.2\ ^{+0.0}_{-0.7}$	$33.3 \pm 1.7\ ^{+0.6}_{-0.0}$	$28.4 \pm 1.8\ ^{+0.0}_{-4.2}$	$25.1 \pm 2.1\ ^{+0.0}_{-1.7}$	$26.5 \pm 2.6\ ^{+0.0}_{-1.4}$
232.5	$55.2 \pm 2.2\ ^{+0.0}_{-3.4}$	$33.7 \pm 1.8\ ^{+0.2}_{-1.1}$	$28.4 \pm 1.9\ ^{+0.0}_{-1.5}$	$26.0 \pm 2.1\ ^{+0.0}_{-0.4}$	$20.1 \pm 2.2\ ^{+0.0}_{-2.4}$
247.5	$58.5 \pm 2.3\ ^{+0.2}_{-0.9}$	$37.7 \pm 2.0\ ^{+0.0}_{-1.3}$	$37.3 \pm 2.2\ ^{+0.0}_{-2.5}$	$30.5 \pm 2.4\ ^{+0.1}_{-3.1}$	$25.7 \pm 2.6\ ^{+0.0}_{-1.8}$
262.5	$63.1 \pm 2.4\ ^{+0.0}_{-2.8}$	$40.4 \pm 2.1\ ^{+0.0}_{-1.7}$	$37.8 \pm 2.3\ ^{+0.0}_{-2.5}$	$28.2 \pm 2.5\ ^{+1.3}_{-0.3}$	$21.7 \pm 2.6\ ^{+0.6}_{-1.6}$
277.5	$74.2 \pm 2.7\ ^{+0.8}_{-0.7}$	$42.9 \pm 2.3\ ^{+0.2}_{-0.7}$	$40.2 \pm 2.4\ ^{+0.0}_{-2.6}$	$32.6 \pm 2.7\ ^{+0.0}_{-1.7}$	$26.2 \pm 2.9\ ^{+0.5}_{-0.3}$
292.5	$81.8 \pm 2.9\ ^{+0.3}_{-2.1}$	$52.8 \pm 2.6\ ^{+0.6}_{-1.2}$	$42.6 \pm 2.7\ ^{+1.1}_{-0.1}$	$36.4 \pm 3.1\ ^{+3.0}_{-0.0}$	$29.7 \pm 3.5\ ^{+0.4}_{-0.7}$
307.5	$96.7 \pm 3.2\ ^{+0.0}_{-1.8}$	$59.3 \pm 2.8\ ^{+0.0}_{-2.6}$	$46.8 \pm 3.1\ ^{+0.4}_{-0.4}$	$47.4 \pm 3.8\ ^{+0.0}_{-3.2}$	$33.8 \pm 4.1\ ^{+0.0}_{-4.1}$
322.5	$105.6 \pm 3.5\ ^{+0.0}_{-1.2}$	$62.0 \pm 3.2\ ^{+0.0}_{-1.9}$	$48.0 \pm 3.5\ ^{+0.0}_{-2.0}$	$46.0 \pm 4.7\ ^{+0.7}_{-1.8}$	$39.6 \pm 5.7\ ^{+0.0}_{-5.5}$
337.5	$108.6 \pm 3.8\ ^{+1.5}_{-1.5}$	$73.3 \pm 3.8\ ^{+4.1}_{-0.0}$	$60.3 \pm 4.5\ ^{+1.6}_{-0.5}$	$52.6 \pm 6.3\ ^{+1.4}_{-0.8}$	$44.9 \pm 8.2\ ^{+6.9}_{-0.0}$
352.5	$113.6 \pm 4.0\ ^{+2.9}_{-0.0}$	$76.8 \pm 4.2\ ^{+0.0}_{-1.1}$	$60.7 \pm 5.3\ ^{+0.5}_{-3.5}$	$50.0 \pm 7.3\ ^{+0.0}_{-13.0}$	$59.5 \pm 11.6\ ^{+4.4}_{-0.0}$

ϕ (deg)	$x_B = 0.345$ $Q^2 = 2.218$ GeV^2 $t = -0.176$ GeV^2		$x_B = 0.363$ $Q^2 = 2.318$ GeV^2 $t = -0.232$ GeV^2		$x_B = 0.368$ $Q^2 = 2.348$ GeV^2 $t = -0.279$ GeV^2		$x_B = 0.371$ $Q^2 = 2.360$ GeV^2 $t = -0.325$ GeV^2		$x_B = 0.373$ $Q^2 = 2.375$ GeV^2 $t = -0.372$ GeV^2	
7.5	104.3 ± 3.6	$+ 1.1$ $- 0.2$	80.3 ± 3.5	$+ 0.0$ $- 1.1$	66.6 ± 4.2	$+ 3.1$ $- 0.0$	64.8 ± 5.8	$+ 0.5$ $- 1.9$	60.6 ± 8.4	$+ 0.0$ $- 8.2$
22.5	108.6 ± 3.6	$+ 1.6$ $- 0.9$	80.6 ± 3.3	$+ 3.6$ $- 0.0$	71.9 ± 4.0	$+ 2.6$ $- 0.6$	60.2 ± 4.9	$+ 0.0$ $- 3.9$	54.8 ± 6.3	$+ 0.0$ $- 3.3$
37.5	100.3 ± 3.4	$+ 2.6$ $- 0.0$	70.5 ± 3.0	$+ 0.1$ $- 1.8$	58.0 ± 3.2	$+ 0.0$ $- 5.8$	42.3 ± 3.4	$+ 0.9$ $- 0.6$	41.2 ± 4.1	$+ 2.2$ $- 1.4$
52.5	91.2 ± 3.2	$+ 1.5$ $- 1.0$	60.4 ± 2.7	$+ 0.5$ $- 1.3$	48.2 ± 2.8	$+ 0.2$ $- 0.7$	39.2 ± 3.0	$+ 3.1$ $- 0.0$	38.8 ± 3.3	$+ 1.4$ $- 0.0$
67.5	76.8 ± 2.9	$+ 0.0$ $- 3.1$	51.3 ± 2.4	$+ 0.6$ $- 0.4$	42.2 ± 2.4	$+ 0.2$ $- 2.5$	36.8 ± 2.6	$+ 3.0$ $- 0.0$	29.5 ± 2.6	$+ 1.4$ $- 0.1$
82.5	73.0 ± 2.8	$+ 0.4$ $- 0.6$	46.3 ± 2.2	$+ 1.1$ $- 0.1$	39.4 ± 2.2	$+ 0.0$ $- 3.0$	27.3 ± 2.1	$+ 0.0$ $- 1.0$	23.8 ± 2.2	$+ 0.6$ $- 0.2$
97.5	56.5 ± 2.5	$+ 0.4$ $- 0.7$	42.6 ± 2.0	$+ 0.5$ $- 0.7$	29.5 ± 1.9	$+ 2.1$ $- 0.2$	25.1 ± 1.9	$+ 0.0$ $- 0.8$	20.3 ± 1.9	$+ 0.0$ $- 1.1$
112.5	55.7 ± 2.3	$+ 0.6$ $- 1.2$	35.3 ± 1.8	$+ 0.8$ $- 0.3$	28.7 ± 1.7	$+ 0.0$ $- 0.8$	24.3 ± 1.7	$+ 0.4$ $- 0.7$	16.6 ± 1.6	$+ 0.0$ $- 1.8$
127.5	49.0 ± 2.2	$+ 0.4$ $- 1.1$	34.8 ± 1.7	$+ 0.0$ $- 1.5$	23.8 ± 1.5	$+ 0.0$ $- 0.9$	21.9 ± 1.6	$+ 0.5$ $- 0.4$	16.5 ± 1.5	$+ 0.0$ $- 2.6$
142.5	47.0 ± 2.1	$+ 1.4$ $- 0.0$	28.4 ± 1.6	$+ 0.1$ $- 0.5$	24.8 ± 1.5	$+ 0.0$ $- 0.6$	20.3 ± 1.5	$+ 0.0$ $- 0.6$	14.9 ± 1.4	$+ 0.0$ $- 1.3$
157.5	41.1 ± 2.0	$+ 0.1$ $- 1.4$	30.9 ± 1.6	$+ 0.1$ $- 0.9$	25.7 ± 1.6	$+ 0.0$ $- 1.4$	19.0 ± 1.5	$+ 0.2$ $- 0.2$	14.0 ± 1.5	$+ 0.9$ $- 0.0$
172.5	41.6 ± 2.0	$+ 0.0$ $- 0.9$	25.7 ± 1.5	$+ 0.1$ $- 0.6$	25.7 ± 1.6	$+ 0.1$ $- 0.5$	20.4 ± 1.6	$+ 0.9$ $- 0.0$	13.7 ± 1.7	$+ 0.0$ $- 0.7$
187.5	38.5 ± 1.9	$+ 0.0$ $- 1.1$	27.7 ± 1.5	$+ 0.0$ $- 0.9$	20.6 ± 1.5	$+ 0.0$ $- 0.6$	18.1 ± 1.5	$+ 0.3$ $- 0.6$	15.1 ± 1.7	$+ 1.1$ $- 0.2$
202.5	41.1 ± 1.9	$+ 0.4$ $- 1.1$	29.7 ± 1.6	$+ 0.1$ $- 0.6$	20.7 ± 1.5	$+ 0.1$ $- 0.4$	22.8 ± 1.6	$+ 0.0$ $- 1.7$	16.7 ± 1.6	$+ 0.5$ $- 0.3$
217.5	45.3 ± 2.1	$+ 0.3$ $- 0.6$	31.4 ± 1.6	$+ 0.1$ $- 0.6$	24.2 ± 1.5	$+ 0.0$ $- 1.5$	19.1 ± 1.5	$+ 0.0$ $- 1.0$	14.2 ± 1.4	$+ 0.3$ $- 0.5$
232.5	51.3 ± 2.2	$+ 0.0$ $- 0.9$	34.4 ± 1.7	$+ 0.3$ $- 0.6$	28.3 ± 1.6	$+ 0.0$ $- 1.0$	21.9 ± 1.5	$+ 0.0$ $- 1.5$	19.0 ± 1.5	$+ 0.0$ $- 0.7$
247.5	53.3 ± 2.3	$+ 0.0$ $- 1.6$	35.8 ± 1.8	$+ 0.5$ $- 0.3$	27.2 ± 1.7	$+ 1.3$ $- 0.1$	20.8 ± 1.6	$+ 0.0$ $- 1.5$	18.5 ± 1.7	$+ 0.1$ $- 2.4$
262.5	62.2 ± 2.5	$+ 0.0$ $- 3.2$	42.4 ± 2.0	$+ 0.1$ $- 1.1$	31.7 ± 1.8	$+ 0.1$ $- 1.0$	25.6 ± 1.9	$+ 0.3$ $- 0.1$	19.6 ± 1.8	$+ 0.0$ $- 1.3$
277.5	70.0 ± 2.7	$+ 0.4$ $- 1.0$	43.9 ± 2.1	$+ 0.0$ $- 1.6$	35.1 ± 2.0	$+ 0.1$ $- 0.3$	31.5 ± 2.1	$+ 0.0$ $- 1.2$	24.2 ± 2.0	$+ 0.0$ $- 0.9$
292.5	80.1 ± 2.9	$+ 2.3$ $- 0.0$	54.6 ± 2.3	$+ 1.0$ $- 0.6$	41.8 ± 2.2	$+ 1.2$ $- 0.1$	36.4 ± 2.4	$+ 0.0$ $- 1.9$	31.2 ± 2.5	$+ 0.0$ $- 1.4$
307.5	87.4 ± 3.1	$+ 4.3$ $- 0.0$	63.3 ± 2.6	$+ 0.0$ $- 3.3$	51.4 ± 2.7	$+ 0.0$ $- 2.6$	40.0 ± 2.7	$+ 0.0$ $- 1.8$	33.3 ± 2.9	$+ 1.6$ $- 0.2$
322.5	97.4 ± 3.3	$+ 0.0$ $- 1.8$	66.8 ± 2.9	$+ 0.0$ $- 3.3$	51.4 ± 2.9	$+ 0.0$ $- 4.9$	52.6 ± 3.4	$+ 0.0$ $- 2.1$	45.5 ± 4.0	$+ 0.0$ $- 7.6$
337.5	99.2 ± 3.5	$+ 2.7$ $- 0.0$	75.2 ± 3.3	$+ 0.0$ $- 2.2$	56.8 ± 3.5	$+ 0.0$ $- 3.2$	55.7 ± 4.6	$+ 0.0$ $- 8.2$	55.2 ± 6.4	$+ 0.7$ $- 4.0$
352.5	98.6 ± 3.6	$+ 1.7$ $- 0.0$	77.3 ± 3.5	$+ 0.0$ $- 4.7$	60.0 ± 4.1	$+ 2.0$ $- 1.1$	59.1 ± 5.7	$+ 3.2$ $- 0.0$	55.4 ± 8.7	$+ 3.1$ $- 1.3$

ϕ (deg)	$x_B = 0.378$ $Q^2 = 2.012$ GeV^2 $t = -0.192$ GeV^2		$x_B = 0.392$ $Q^2 = 2.054$ GeV^2 $t = -0.233$ GeV^2		$x_B = 0.398$ $Q^2 = 2.074$ GeV^2 $t = -0.279$ GeV^2		$x_B = 0.400$ $Q^2 = 2.084$ GeV^2 $t = -0.324$ GeV^2		$x_B = 0.401$ $Q^2 = 2.091$ GeV^2 $t = -0.371$ GeV^2	
7.5	64.0 ± 6.3	$+\,1.1$ $-\,0.9$	57.0 ± 3.8	$+\,0.1$ $-\,1.2$	56.3 ± 4.4	$+\,1.4$ $-\,1.7$	50.5 ± 5.9	$+\,2.1$ $-\,1.3$	53.3 ± 9.0	$+\,8.9$ $-\,0.0$
22.5	68.2 ± 6.2	$+\,1.8$ $-\,2.0$	55.1 ± 3.6	$+\,0.0$ $-\,2.5$	45.2 ± 3.8	$+\,0.1$ $-\,0.9$	51.7 ± 5.1	$+\,0.8$ $-\,1.7$	52.0 ± 6.9	$+\,3.4$ $-\,0.3$
37.5	52.8 ± 5.6	$+\,0.0$ $-\,4.6$	48.2 ± 3.3	$+\,0.5$ $-\,1.3$	44.9 ± 3.5	$+\,1.4$ $-\,0.5$	36.2 ± 4.0	$+\,1.0$ $-\,0.0$	36.9 ± 4.8	$+\,0.0$ $-\,3.8$
52.5	52.4 ± 5.8	$+\,0.6$ $-\,2.8$	51.4 ± 3.3	$+\,3.3$ $-\,0.1$	41.2 ± 3.4	$+\,0.0$ $-\,4.4$	36.4 ± 3.8	$+\,0.0$ $-\,2.7$	33.8 ± 4.1	$+\,0.0$ $-\,4.5$
67.5	53.0 ± 5.4	$+\,1.3$ $-\,0.5$	42.0 ± 3.0	$+\,0.0$ $-\,3.0$	34.6 ± 3.0	$+\,0.0$ $-\,1.5$	30.7 ± 3.2	$+\,0.0$ $-\,3.2$	31.0 ± 3.5	$+\,0.0$ $-\,2.0$
82.5	47.3 ± 5.1	$+\,2.3$ $-\,0.0$	41.4 ± 2.9	$+\,0.0$ $-\,3.0$	30.9 ± 2.9	$+\,3.3$ $-\,0.0$	24.9 ± 3.0	$+\,1.8$ $-\,0.0$	22.0 ± 3.0	$+\,0.0$ $-\,3.9$
97.5	48.2 ± 4.9	$+\,3.3$ $-\,0.0$	32.8 ± 2.7	$+\,0.3$ $-\,2.6$	30.5 ± 2.7	$+\,0.5$ $-\,2.0$	26.4 ± 2.9	$+\,0.4$ $-\,1.4$	27.4 ± 3.2	$+\,0.0$ $-\,2.7$
112.5	46.9 ± 4.7	$+\,4.8$ $-\,1.3$	33.9 ± 2.6	$+\,0.0$ $-\,2.9$	28.9 ± 2.5	$+\,0.0$ $-\,1.2$	20.0 ± 2.5	$+\,0.0$ $-\,1.2$	24.0 ± 3.1	$+\,1.3$ $-\,0.2$
127.5	45.8 ± 4.6	$+\,0.0$ $-\,1.5$	28.0 ± 2.3	$+\,0.0$ $-\,2.3$	23.1 ± 2.2	$+\,0.0$ $-\,3.4$	24.5 ± 2.6	$+\,0.0$ $-\,1.8$	19.7 ± 3.0	$+\,0.0$ $-\,1.5$
142.5	36.5 ± 4.2	$+\,1.0$ $-\,0.0$	27.3 ± 2.3	$+\,0.0$ $-\,1.0$	23.2 ± 2.2	$+\,0.0$ $-\,1.4$	18.9 ± 2.4	$+\,0.3$ $-\,0.7$	16.2 ± 3.2	$+\,0.0$ $-\,2.6$
157.5	33.2 ± 4.0	$+\,0.7$ $-\,1.3$	27.6 ± 2.2	$+\,0.0$ $-\,1.7$	25.4 ± 2.3	$+\,0.0$ $-\,2.8$	20.0 ± 2.7	$+\,0.0$ $-\,1.6$	15.5 ± 3.6	$+\,2.7$ $-\,0.0$
172.5	36.3 ± 4.1	$+\,0.0$ $-\,3.1$	26.7 ± 2.2	$+\,1.6$ $-\,0.3$	24.2 ± 2.2	$+\,0.0$ $-\,2.3$	18.5 ± 2.6	$+\,0.3$ $-\,1.2$	15.9 ± 3.9	$+\,0.1$ $-\,1.1$
187.5	35.6 ± 4.1	$+\,0.3$ $-\,0.8$	26.6 ± 2.2	$+\,0.2$ $-\,1.0$	22.4 ± 2.1	$+\,0.0$ $-\,0.9$	16.6 ± 2.6	$+\,0.5$ $-\,0.4$	17.4 ± 4.0	$+\,0.0$ $-\,3.5$
202.5	37.7 ± 4.3	$+\,0.0$ $-\,4.5$	30.9 ± 2.3	$+\,1.3$ $-\,0.0$	20.4 ± 2.0	$+\,0.0$ $-\,1.1$	22.8 ± 2.8	$+\,1.5$ $-\,0.3$	17.2 ± 3.4	$+\,0.0$ $-\,3.0$
217.5	43.6 ± 4.5	$+\,1.1$ $-\,1.0$	28.3 ± 2.3	$+\,0.8$ $-\,0.0$	29.1 ± 2.4	$+\,0.0$ $-\,5.0$	22.1 ± 2.6	$+\,0.0$ $-\,2.9$	22.2 ± 3.2	$+\,0.3$ $-\,0.9$
232.5	38.1 ± 4.4	$+\,0.0$ $-\,3.5$	25.6 ± 2.3	$+\,0.0$ $-\,1.5$	21.6 ± 2.2	$+\,0.0$ $-\,1.2$	20.8 ± 2.6	$+\,1.0$ $-\,0.0$	17.1 ± 2.7	$+\,1.5$ $-\,0.1$
247.5	37.7 ± 4.3	$+\,0.9$ $-\,1.8$	30.5 ± 2.5	$+\,1.7$ $-\,0.0$	26.7 ± 2.5	$+\,0.0$ $-\,3.1$	28.1 ± 2.9	$+\,0.0$ $-\,4.2$	22.6 ± 3.0	$+\,0.0$ $-\,4.7$
262.5	43.4 ± 4.6	$+\,0.0$ $-\,8.3$	34.3 ± 2.7	$+\,0.7$ $-\,1.1$	30.0 ± 2.7	$+\,0.0$ $-\,2.2$	24.8 ± 2.9	$+\,1.2$ $-\,0.2$	19.5 ± 2.9	$+\,0.4$ $-\,1.6$
277.5	44.1 ± 4.9	$+\,1.0$ $-\,0.8$	34.5 ± 2.8	$+\,0.0$ $-\,0.9$	34.9 ± 2.8	$+\,0.0$ $-\,4.2$	28.2 ± 3.1	$+\,0.4$ $-\,1.1$	23.7 ± 3.1	$+\,0.3$ $-\,1.0$
292.5	50.5 ± 5.3	$+\,2.3$ $-\,0.0$	41.8 ± 3.0	$+\,0.2$ $-\,0.6$	30.5 ± 2.7	$+\,1.4$ $-\,0.2$	27.0 ± 3.0	$+\,3.6$ $-\,0.0$	27.2 ± 3.5	$+\,0.4$ $-\,1.4$
307.5	57.7 ± 5.8	$+\,0.3$ $-\,3.4$	43.2 ± 3.2	$+\,0.0$ $-\,3.8$	35.9 ± 3.0	$+\,1.6$ $-\,0.0$	39.3 ± 3.6	$+\,0.0$ $-\,1.4$	29.7 ± 3.8	$+\,0.2$ $-\,2.8$
322.5	62.1 ± 5.9	$+\,0.9$ $-\,0.9$	53.2 ± 3.5	$+\,0.0$ $-\,2.5$	41.0 ± 3.3	$+\,0.0$ $-\,0.8$	39.5 ± 4.1	$+\,0.6$ $-\,2.2$	31.6 ± 4.8	$+\,0.0$ $-\,4.5$
337.5	62.3 ± 5.9	$+\,1.5$ $-\,0.0$	53.2 ± 3.5	$+\,2.3$ $-\,0.3$	46.9 ± 3.8	$+\,1.4$ $-\,0.7$	41.4 ± 5.0	$+\,0.9$ $-\,1.2$	33.4 ± 6.4	$+\,4.6$ $-\,0.0$
352.5	65.4 ± 6.0	$+\,0.0$ $-\,1.5$	55.5 ± 3.7	$+\,0.0$ $-\,1.5$	44.0 ± 4.1	$+\,0.3$ $-\,1.6$	37.4 ± 5.5	$+\,0.0$ $-\,9.8$	43.6 ± 8.8	$+\,2.9$ $-\,0.0$

ϕ (deg)	$x_B = 0.336$ $Q^2 = 2.161$ GeV^2 $t = -0.171$ GeV^2		$x_B = 0.342$ $Q^2 = 2.190$ GeV^2 $t = -0.231$ GeV^2		$x_B = 0.343$ $Q^2 = 2.194$ GeV^2 $t = -0.278$ GeV^2		$x_B = 0.342$ $Q^2 = 2.191$ GeV^2 $t = -0.324$ GeV^2		$x_B = 0.342$ $Q^2 = 2.193$ GeV^2 $t = -0.371$ GeV^2	
7.5	120.7 ± 4.7	$+ 0.9$ $- 0.4$	100.1 ± 7.6	$+ 2.1$ $- 2.5$	X		X		X	
22.5	132.5 ± 4.9	$+ 3.7$ $- 0.0$	106.9 ± 6.8	$+ 4.5$ $- 0.5$	X		X		X	
37.5	118.7 ± 4.5	$+ 2.8$ $- 0.0$	93.9 ± 6.1	$+ 0.2$ $- 1.6$	58.7 ± 7.0	$+ 1.1$ $- 4.3$	53.8 ± 10.1	$+ 0.7$ $- 9.3$	68.8 ± 21.3	$+ 0.9$ $- 14.6$
52.5	99.8 ± 4.1	$+ 1.3$ $- 1.9$	76.9 ± 5.0	$+ 0.1$ $- 2.7$	59.3 ± 5.8	$+ 1.5$ $- 1.1$	48.6 ± 7.3	$+ 8.3$ $- 0.3$	37.1 ± 10.4	$+ 1.6$ $- 9.7$
67.5	88.4 ± 3.8	$+ 0.0$ $- 5.5$	67.7 ± 4.5	$+ 2.2$ $- 1.3$	54.4 ± 5.1	$+ 0.9$ $- 0.9$	55.8 ± 6.2	$+ 6.5$ $- 0.0$	40.6 ± 7.0	$+ 6.2$ $- 0.0$
82.5	81.4 ± 3.6	$+ 0.5$ $- 0.7$	55.1 ± 3.9	$+ 3.6$ $- 0.0$	47.8 ± 4.2	$+ 0.0$ $- 2.6$	34.2 ± 4.4	$+ 0.7$ $- 1.8$	29.0 ± 5.0	$+ 2.1$ $- 1.0$
97.5	62.7 ± 3.1	$+ 1.5$ $- 0.8$	53.8 ± 3.7	$+ 1.2$ $- 0.7$	36.7 ± 3.6	$+ 1.8$ $- 0.0$	30.9 ± 3.8	$+ 0.0$ $- 1.1$	27.0 ± 4.3	$+ 0.2$ $- 2.9$
112.5	61.3 ± 3.0	$+ 0.6$ $- 1.5$	40.3 ± 3.1	$+ 0.7$ $- 0.7$	36.5 ± 3.3	$+ 0.0$ $- 1.4$	28.6 ± 3.4	$+ 0.0$ $- 1.2$	21.0 ± 3.5	$+ 0.0$ $- 3.1$
127.5	58.1 ± 3.0	$+ 0.5$ $- 1.9$	37.3 ± 2.8	$+ 0.0$ $- 3.7$	25.9 ± 2.6	$+ 0.0$ $- 1.2$	27.6 ± 3.1	$+ 0.8$ $- 0.6$	18.8 ± 2.9	$+ 0.1$ $- 3.4$
142.5	52.9 ± 2.7	$+ 2.8$ $- 0.0$	33.6 ± 2.7	$+ 0.0$ $- 1.7$	27.3 ± 2.7	$+ 1.0$ $- 0.5$	26.7 ± 3.0	$+ 0.0$ $- 2.0$	17.9 ± 2.8	$+ 0.5$ $- 0.9$
157.5	43.9 ± 2.6	$+ 0.2$ $- 0.8$	34.4 ± 2.8	$+ 0.7$ $- 0.6$	29.2 ± 2.8	$+ 0.0$ $- 2.8$	24.8 ± 2.8	$+ 1.0$ $- 0.0$	18.7 ± 3.0	$+ 1.6$ $- 0.0$
172.5	45.4 ± 2.5	$+ 0.0$ $- 1.2$	31.9 ± 2.6	$+ 0.2$ $- 0.6$	29.9 ± 2.8	$+ 0.3$ $- 0.2$	23.5 ± 2.8	$+ 1.7$ $- 0.0$	17.2 ± 3.2	$+ 1.1$ $- 0.3$
187.5	41.0 ± 2.4	$+ 0.9$ $- 0.1$	32.6 ± 2.7	$+ 0.5$ $- 0.3$	27.7 ± 2.8	$+ 0.1$ $- 2.1$	21.6 ± 2.8	$+ 1.4$ $- 0.0$	16.2 ± 2.9	$+ 2.2$ $- 0.0$
202.5	44.2 ± 2.5	$+ 0.9$ $- 0.9$	37.1 ± 2.8	$+ 0.0$ $- 1.6$	23.7 ± 2.6	$+ 0.1$ $- 0.5$	29.2 ± 3.0	$+ 0.0$ $- 3.1$	21.3 ± 3.0	$+ 2.1$ $- 0.5$
217.5	51.6 ± 2.7	$+ 0.8$ $- 0.8$	39.5 ± 2.9	$+ 0.1$ $- 2.0$	31.2 ± 2.8	$+ 1.1$ $- 0.7$	23.0 ± 2.7	$+ 0.0$ $- 2.1$	17.7 ± 2.8	$+ 0.1$ $- 0.8$
232.5	57.7 ± 2.9	$+ 0.6$ $- 0.8$	41.5 ± 3.0	$+ 1.1$ $- 0.0$	33.4 ± 2.9	$+ 0.0$ $- 1.9$	29.3 ± 3.0	$+ 0.0$ $- 0.9$	24.2 ± 3.0	$+ 0.0$ $- 1.3$
247.5	56.9 ± 2.9	$+ 0.1$ $- 2.3$	43.0 ± 3.1	$+ 1.4$ $- 0.0$	30.9 ± 3.0	$+ 1.5$ $- 0.4$	21.4 ± 3.1	$+ 0.5$ $- 0.7$	22.5 ± 3.4	$+ 0.4$ $- 3.9$
262.5	69.3 ± 3.2	$+ 0.0$ $- 3.7$	50.9 ± 3.5	$+ 0.0$ $- 0.8$	36.4 ± 3.4	$+ 0.7$ $- 1.2$	30.4 ± 3.9	$+ 0.6$ $- 0.3$	18.1 ± 3.6	$+ 0.0$ $- 2.6$
277.5	77.0 ± 3.5	$+ 0.7$ $- 0.4$	54.2 ± 3.7	$+ 0.5$ $- 2.0$	48.5 ± 3.9	$+ 0.4$ $- 1.8$	43.6 ± 4.4	$+ 0.1$ $- 3.2$	32.8 ± 4.5	$+ 0.0$ $- 2.5$
292.5	95.5 ± 3.9	$+ 2.5$ $- 0.0$	67.8 ± 4.2	$+ 0.0$ $- 1.4$	51.6 ± 4.3	$+ 3.3$ $- 0.2$	55.0 ± 5.6	$+ 0.9$ $- 1.2$	35.5 ± 6.3	$+ 2.0$ $- 1.9$
307.5	103.1 ± 4.0	$+ 4.8$ $- 0.0$	84.2 ± 4.8	$+ 0.0$ $- 6.6$	60.3 ± 5.4	$+ 0.2$ $- 3.9$	39.5 ± 6.2	$+ 0.5$ $- 2.9$	43.1 ± 8.7	$+ 4.1$ $- 0.3$
322.5	114.1 ± 4.4	$+ 0.4$ $- 1.7$	90.7 ± 5.5	$+ 0.0$ $- 6.5$	62.2 ± 6.4	$+ 0.0$ $- 8.6$	70.1 ± 9.9	$+ 0.0$ $- 7.6$	49.6 ± 15.5	$+ 3.6$ $- 10.8$
337.5	117.8 ± 4.6	$+ 2.0$ $- 0.6$	83.8 ± 6.6	$+ 0.0$ $- 5.6$	X		X		X	
352.5	120.3 ± 4.8	$+ 0.2$ $- 0.7$	87.9 ± 7.4	$+ 0.0$ $- 10.9$	X		X		X	
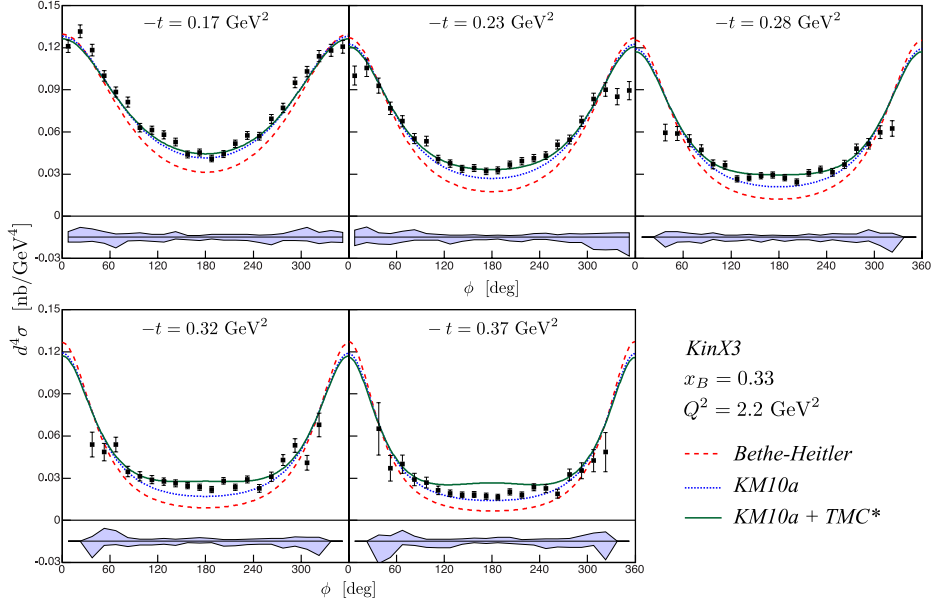
Figure B.4: (Color online) Unpolarized cross sections for KinX3. Error bars are statistical only. The light blue area represents the point-to-point systematic uncertainties added linearly to the normalization error. The KM10a model along with its modified version including TMC effects are shown as dotted blue and solid green curves respectively. The Bethe-Heitler contribution is represented as a dashed red line.

B.2 Polarized cross sections
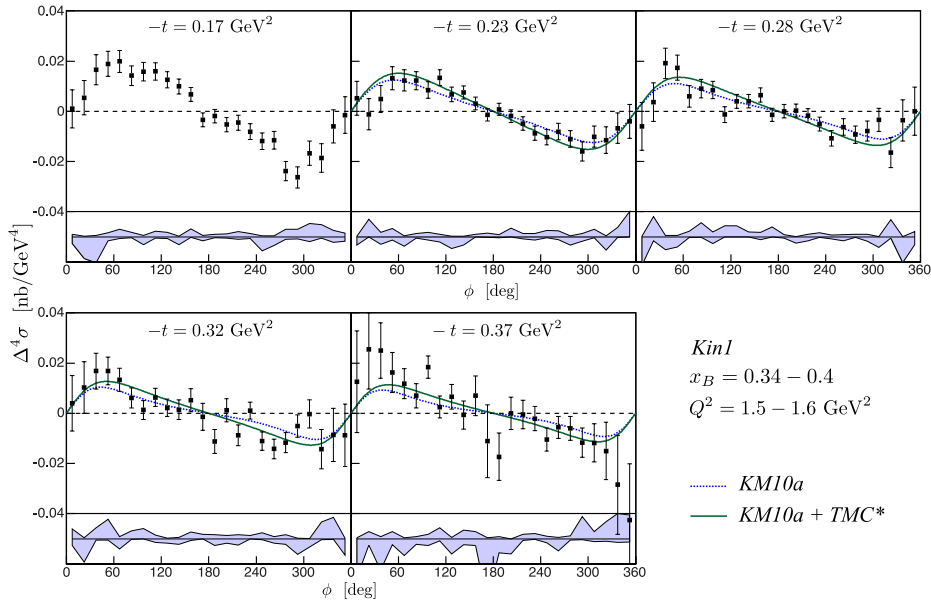
Figure B.5: (Color online) Cross section differences for opposite beam helicities for Kin1. Error bars are statistical only. The light blue area represents the point-to-point systematic uncertainties added linearly to the normalization error. The KM10a model along with its modified version including TMC effects are shown as dotted blue and solid green curves respectively, except for the first t-bin which is outside the prescribed range of this model.
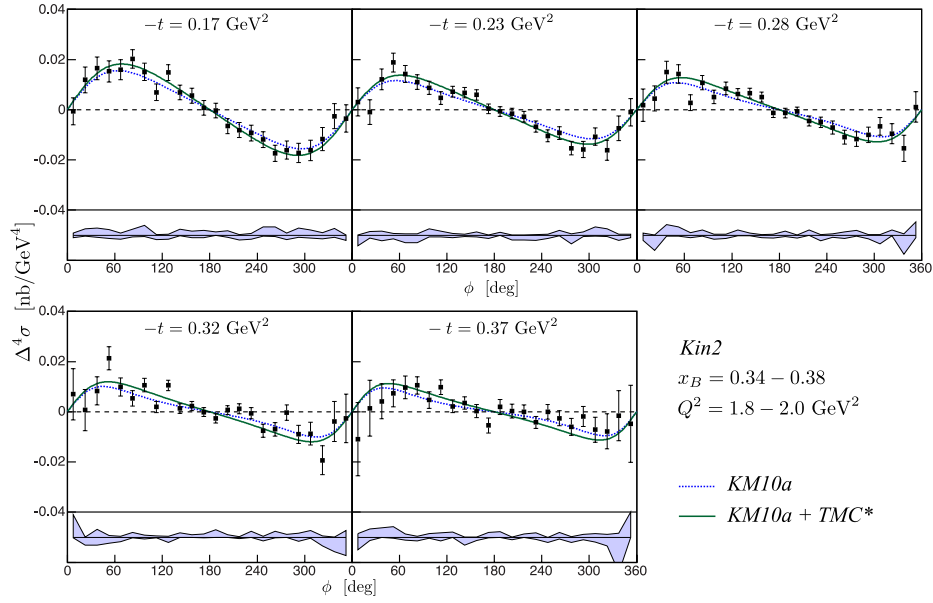
Figure B.6: (Color online) Cross section differences for opposite beam helicities for Kin2. Error bars are statistical only. The light blue area represents the point-to-point systematic uncertainties added linearly to the normalization error. The KM10a model along with its modified version including TMC effects are shown as dotted blue and solid green curves respectively.
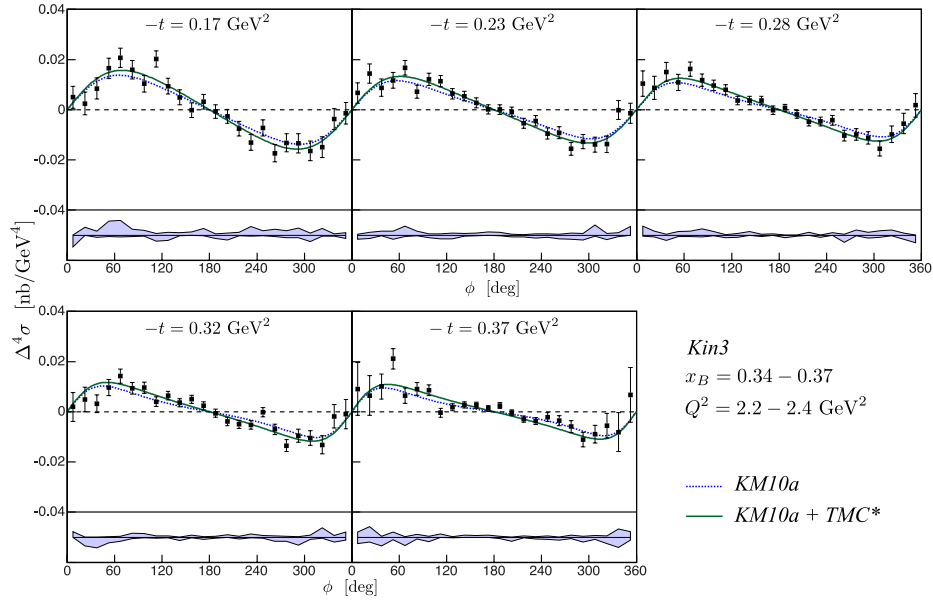
Figure B.7: (Color online) Cross section differences for opposite beam helicities for Kin3. Error bars are statistical only. The light blue area represents the point-to-point systematic uncertainties added linearly to the normalization error. The KM10a model along with its modified version including TMC effects are shown as dotted blue and solid green curves respectively.

ϕ (deg)	$x_B = 0.345$ $Q^2 = 1.453$ GeV^2 $t = -0.170$ GeV^2		$x_B = 0.374$ $Q^2 = 1.552$ GeV^2 $t = -0.232$ GeV^2		$x_B = 0.385$ $Q^2 = 1.589$ GeV^2 $t = -0.278$ GeV^2		$x_B = 0.391$ $Q^2 = 1.608$ GeV^2 $t = -0.323$ GeV^2		$x_B = 0.399$ $Q^2 = 1.633$ GeV^2 $t = -0.370$ GeV^2	
7.5	0.8 ± 7.9	$+1.0$ -3.0	5.7 ± 7.9	$+0.0$ -3.8	-7.2 ± 10.8	$+0.0$ -13.5	4.2 ± 13.8	$+4.5$ -3.2	12.7 ± 20.7	$+0.0$ -16.2
22.5	5.2 ± 7.1	$+0.0$ -9.4	-2.2 ± 7.1	$+8.4$ -0.0	3.1 ± 8.9	$+9.9$ -1.8	10.8 ± 13.1	$+0.0$ -11.6	25.7 ± 16.3	$+2.6$ -1.3
37.5	16.5 ± 6.3	$+0.0$ -10.7	4.3 ± 6.1	$+1.9$ -3.4	20.3 ± 6.9	$+0.0$ -5.1	18.0 ± 8.7	$+3.8$ -0.0	25.2 ± 11.2	$+0.0$ -12.1
52.5	18.8 ± 5.2	$+1.1$ -1.1	13.4 ± 5.1	$+3.2$ -1.2	18.3 ± 5.7	$+0.0$ -4.2	18.0 ± 6.6	$+7.8$ -0.0	16.3 ± 8.3	$+2.6$ -1.8
67.5	19.9 ± 4.5	$+2.6$ -0.0	12.4 ± 4.6	$+0.0$ -4.0	5.4 ± 4.8	$+2.4$ -0.0	13.9 ± 5.4	$+0.4$ -4.6	11.7 ± 6.2	$+0.0$ -6.8
82.5	14.0 ± 4.0	$+1.6$ -0.0	12.2 ± 3.8	$+1.0$ -0.0	9.0 ± 4.1	$+6.1$ -0.0	5.7 ± 4.6	$+3.6$ -0.0	6.9 ± 4.9	$+0.6$ -2.2
97.5	15.8 ± 3.8	$+0.0$ -2.8	8.3 ± 3.5	$+1.6$ -1.1	8.6 ± 3.9	$+1.8$ -2.9	0.6 ± 4.2	$+4.5$ -0.0	18.9 ± 4.7	$+1.4$ -2.3
112.5	15.9 ± 3.6	$+1.9$ -0.2	13.6 ± 3.3	$+0.7$ -1.7	-2.2 ± 3.5	$+5.1$ -0.0	6.3 ± 3.9	$+1.3$ -1.4	2.2 ± 4.7	$+4.8$ -0.8
127.5	12.7 ± 3.3	$+1.5$ -0.3	6.7 ± 3.1	$+0.0$ -4.9	4.0 ± 3.2	$+4.7$ -0.0	2.0 ± 3.9	$+0.1$ -2.1	7.1 ± 5.8	$+0.3$ -7.2
142.5	10.0 ± 3.1	$+0.0$ -3.0	7.7 ± 2.8	$+0.0$ -3.4	4.2 ± 3.3	$+1.8$ -0.0	1.2 ± 4.5	$+0.6$ -3.0	-1.5 ± 7.1	$+4.4$ -2.8
157.5	6.8 ± 2.9	$+3.0$ -0.0	3.0 ± 2.7	$+1.1$ -0.0	8.0 ± 3.7	$+0.9$ -1.8	5.9 ± 5.6	$+4.0$ -0.7	9.1 ± 10.9	$+3.5$ -4.0
172.5	-3.5 ± 2.8	$+0.4$ -1.6	-1.6 ± 2.7	$+1.5$ -0.3	-2.0 ± 3.6	$+5.0$ -0.0	-1.8 ± 6.6	$+2.3$ -0.0	-18.3 ± 23.5	$+0.0$ -34.1
187.5	-1.9 ± 2.8	$+1.1$ -0.3	1.0 ± 2.6	$+1.0$ -0.4	0.2 ± 3.6	$+1.2$ -0.8	-13.9 ± 6.1	$+0.0$ -4.2	-28.1 ± 15.5	$+5.6$ -7.0
202.5	-5.3 ± 2.9	$+1.1$ -0.3	-1.8 ± 2.8	$+4.0$ -0.0	0.9 ± 3.4	$+0.0$ -3.4	1.8 ± 5.5	$+2.0$ -2.1	0.6 ± 9.0	$+0.0$ -8.1
217.5	-4.4 ± 3.0	$+2.0$ -0.8	-4.9 ± 2.9	$+1.2$ -0.9	-1.5 ± 3.4	$+1.1$ -1.9	-9.8 ± 4.8	$+1.2$ -3.2	0.1 ± 7.4	$+2.3$ -0.8
232.5	-8.0 ± 3.2	$+1.1$ -0.4	-8.7 ± 2.9	$+1.1$ -1.2	-5.2 ± 3.2	$+1.9$ -0.0	1.8 ± 3.9	$+1.8$ -0.0	-1.9 ± 5.6	$+2.3$ -0.2
247.5	-11.8 ± 3.4	$+0.0$ -5.7	-10.4 ± 3.2	$+2.4$ -0.0	-11.5 ± 3.5	$+0.7$ -0.2	-11.7 ± 4.1	$+2.4$ -0.0	-10.9 ± 5.1	$+0.8$ -1.3
262.5	-11.3 ± 3.6	$+0.0$ -3.4	-7.9 ± 3.5	$+2.4$ -1.0	-6.2 ± 3.7	$+0.8$ -1.5	-15.0 ± 4.3	$+0.4$ -1.5	-5.5 ± 4.6	$+0.3$ -5.1
277.5	-24.0 ± 3.9	$+2.4$ -0.2	-11.0 ± 3.6	$+0.0$ -3.3	-9.3 ± 3.9	$+1.0$ -0.0	-12.1 ± 4.6	$+1.6$ -2.1	-5.8 ± 4.9	$+0.9$ -0.5
292.5	-26.5 ± 4.4	$+2.4$ -0.0	-16.4 ± 4.2	$+0.9$ -1.5	-7.5 ± 4.5	$+0.9$ -1.7	-4.2 ± 5.2	$+0.0$ -7.3	-11.7 ± 6.1	$+9.2$ -0.0
307.5	-16.6 ± 5.0	$+5.2$ -1.5	-10.0 ± 4.7	$+3.1$ -0.0	-2.5 ± 5.3	$+0.0$ -4.9	1.8 ± 6.7	$+0.0$ -4.2	-11.7 ± 7.8	$+2.6$ -0.9
322.5	-18.7 ± 6.0	$+4.7$ -0.0	-11.8 ± 6.0	$+0.0$ -5.5	-17.4 ± 6.9	$+7.5$ -0.0	-15.0 ± 9.4	$+7.9$ -0.0	-14.9 ± 11.7	$+6.7$ -0.5
337.5	-5.7 ± 6.9	$+2.7$ -2.3	-6.8 ± 7.0	$+4.3$ -0.0	-3.0 ± 9.4	$+0.0$ -12.4	-8.7 ± 12.8	$+9.5$ -0.0	-28.7 ± 20.1	$+16.1$ -0.6
352.5	-1.4 ± 7.6	$+1.6$ -1.9	-4.3 ± 7.8	$+15.1$ -0.0	0.5 ± 11.2	$+2.6$ -3.8	-10.2 ± 15.5	$+0.0$ -7.2	-43.5 ± 23.1	$+8.2$ -0.0

ϕ (deg)	$x_B = 0.343$ $Q^2 = 1.820$ GeV^2 $t = -0.172$ GeV^2	$x_B = 0.368$ $Q^2 = 1.933$ GeV^2 $t = -0.232$ GeV^2	$x_B = 0.375$ $Q^2 = 1.964$ GeV^2 $t = -0.278$ GeV^2	$x_B = 0.379$ $Q^2 = 1.986$ GeV^2 $t = -0.323$ GeV^2	$x_B = 0.381$ $Q^2 = 1.999$ GeV^2 $t = -0.371$ GeV^2
7.5	$-1.0 \pm 6.0\ ^{+1.0}_{-1.1}$	$3.1 \pm 6.1\ ^{+0.0}_{-4.8}$	$1.7 \pm 7.7\ ^{+0.9}_{-2.5}$	$7.3 \pm 11.1\ ^{+10.3}_{-0.0}$	$-12.1 \pm 16.0\ ^{+1.4}_{-5.2}$
22.5	$12.2 \pm 5.7\ ^{+2.3}_{-0.0}$	$-1.9 \pm 5.4\ ^{+1.9}_{-1.4}$	$4.1 \pm 6.2\ ^{+0.0}_{-7.5}$	$-0.1 \pm 9.0\ ^{+0.0}_{-3.7}$	$1.1 \pm 12.0\ ^{+3.6}_{-1.4}$
37.5	$16.8 \pm 4.9\ ^{+2.6}_{-0.5}$	$12.0 \pm 4.5\ ^{+1.6}_{-2.0}$	$16.1 \pm 5.2\ ^{+4.2}_{-0.0}$	$7.9 \pm 6.1\ ^{+3.2}_{-3.4}$	$4.1 \pm 7.5\ ^{+4.0}_{-0.0}$
52.5	$15.3 \pm 4.5\ ^{+1.9}_{-0.9}$	$19.3 \pm 4.2\ ^{+0.1}_{-0.9}$	$15.0 \pm 4.3\ ^{+3.2}_{-0.0}$	$22.4 \pm 5.1\ ^{+0.2}_{-1.9}$	$7.3 \pm 5.8\ ^{+4.4}_{-0.2}$
67.5	$15.8 \pm 4.3\ ^{+0.5}_{-1.2}$	$14.4 \pm 3.7\ ^{+0.1}_{-3.0}$	$1.8 \pm 3.6\ ^{+1.2}_{-1.1}$	$9.9 \pm 4.0\ ^{+0.1}_{-1.6}$	$9.9 \pm 4.9\ ^{+1.1}_{-1.1}$
82.5	$20.5 \pm 3.9\ ^{+2.0}_{-0.0}$	$10.8 \pm 3.2\ ^{+0.2}_{-3.1}$	$10.9 \pm 3.2\ ^{+2.0}_{-0.0}$	$5.1 \pm 3.5\ ^{+2.1}_{-0.0}$	$10.8 \pm 3.8\ ^{+0.0}_{-1.4}$
97.5	$15.1 \pm 3.6\ ^{+3.8}_{-0.0}$	$8.6 \pm 2.8\ ^{+2.6}_{-0.5}$	$4.8 \pm 2.9\ ^{+0.4}_{-1.7}$	$11.3 \pm 3.0\ ^{+0.6}_{-0.4}$	$4.7 \pm 3.5\ ^{+1.4}_{-0.3}$
112.5	$6.7 \pm 3.4\ ^{+0.0}_{-1.7}$	$4.3 \pm 2.7\ ^{+1.6}_{-0.7}$	$8.6 \pm 2.7\ ^{+0.2}_{-1.3}$	$1.5 \pm 2.7\ ^{+0.7}_{-0.1}$	$10.5 \pm 3.2\ ^{+1.5}_{-1.2}$
127.5	$14.9 \pm 3.2\ ^{+0.0}_{-1.1}$	$7.2 \pm 2.4\ ^{+0.4}_{-1.0}$	$6.4 \pm 2.3\ ^{+2.2}_{-0.0}$	$12.2 \pm 2.6\ ^{+0.0}_{-1.9}$	$2.1 \pm 2.9\ ^{+2.4}_{-0.0}$
142.5	$6.9 \pm 3.0\ ^{+2.4}_{-0.0}$	$7.0 \pm 2.3\ ^{+0.0}_{-0.5}$	$6.9 \pm 2.2\ ^{+0.8}_{-0.0}$	$1.0 \pm 2.5\ ^{+2.5}_{-0.0}$	$3.7 \pm 2.8\ ^{+0.0}_{-3.6}$
157.5	$5.7 \pm 3.0\ ^{+1.5}_{-0.9}$	$6.2 \pm 2.3\ ^{+1.3}_{-0.7}$	$5.4 \pm 2.2\ ^{+0.0}_{-1.1}$	$2.7 \pm 2.6\ ^{+1.4}_{-0.0}$	$0.1 \pm 3.1\ ^{+0.0}_{-1.6}$
172.5	$0.7 \pm 2.9\ ^{+2.0}_{-1.0}$	$0.4 \pm 2.2\ ^{+0.0}_{-1.5}$	$-1.5 \pm 2.2\ ^{+0.4}_{-1.4}$	$-0.3 \pm 2.5\ ^{+2.1}_{-0.4}$	$-7.0 \pm 3.8\ ^{+2.6}_{-0.0}$
187.5	$-0.3 \pm 2.9\ ^{+1.4}_{-0.0}$	$-0.7 \pm 2.2\ ^{+1.4}_{-0.0}$	$-1.4 \pm 2.1\ ^{+1.8}_{-0.5}$	$-3.6 \pm 2.7\ ^{+4.5}_{-0.0}$	$2.5 \pm 3.7\ ^{+2.7}_{-0.0}$
202.5	$-6.5 \pm 3.0\ ^{+1.6}_{-0.7}$	$-1.4 \pm 2.3\ ^{+0.0}_{-2.1}$	$-0.5 \pm 2.1\ ^{+0.0}_{-1.3}$	$1.5 \pm 2.6\ ^{+1.4}_{-0.0}$	$0.6 \pm 3.4\ ^{+0.0}_{-1.3}$
217.5	$-8.1 \pm 3.1\ ^{+0.0}_{-1.9}$	$-2.6 \pm 2.3\ ^{+0.0}_{-2.2}$	$-4.6 \pm 2.2\ ^{+2.4}_{-0.0}$	$2.3 \pm 2.6\ ^{+0.3}_{-0.8}$	$0.4 \pm 3.1\ ^{+1.6}_{-0.0}$
232.5	$-9.2 \pm 3.1\ ^{+0.4}_{-1.5}$	$-6.7 \pm 2.4\ ^{+0.0}_{-2.1}$	$-5.0 \pm 2.3\ ^{+0.0}_{-2.4}$	$0.0 \pm 2.7\ ^{+3.0}_{-0.0}$	$-4.4 \pm 2.7\ ^{+1.9}_{-0.9}$
247.5	$-11.8 \pm 3.2\ ^{+3.2}_{-0.0}$	$-10.6 \pm 2.6\ ^{+0.0}_{-1.1}$	$-7.0 \pm 2.8\ ^{+0.4}_{-0.8}$	$-8.1 \pm 3.0\ ^{+0.1}_{-1.6}$	$0.4 \pm 3.1\ ^{+0.0}_{-2.5}$
262.5	$-17.5 \pm 3.4\ ^{+3.0}_{-0.0}$	$-9.2 \pm 2.8\ ^{+1.9}_{-0.0}$	$-11.0 \pm 3.0\ ^{+1.1}_{-1.0}$	$-7.1 \pm 3.1\ ^{+2.7}_{-0.0}$	$-2.5 \pm 3.2\ ^{+2.2}_{-0.7}$
277.5	$-16.0 \pm 3.8\ ^{+0.5}_{-1.4}$	$-15.5 \pm 3.0\ ^{+0.0}_{-3.5}$	$-11.9 \pm 3.2\ ^{+1.8}_{-0.0}$	$0.6 \pm 3.5\ ^{+1.3}_{-0.0}$	$-6.1 \pm 3.6\ ^{+0.0}_{-2.1}$
292.5	$-17.2 \pm 4.0\ ^{+2.6}_{-0.4}$	$-16.0 \pm 3.5\ ^{+0.9}_{-0.0}$	$-9.9 \pm 3.5\ ^{+0.0}_{-1.3}$	$-8.9 \pm 4.0\ ^{+1.6}_{-1.5}$	$-1.6 \pm 4.4\ ^{+1.2}_{-1.1}$
307.5	$-16.3 \pm 4.5\ ^{+1.7}_{-0.6}$	$-10.3 \pm 3.9\ ^{+3.3}_{-0.0}$	$-6.0 \pm 4.1\ ^{+0.0}_{-3.9}$	$-8.4 \pm 5.1\ ^{+2.8}_{-0.0}$	$-7.1 \pm 5.4\ ^{+1.6}_{-1.9}$
322.5	$-11.6 \pm 4.9\ ^{+0.7}_{-1.3}$	$-16.5 \pm 4.5\ ^{+2.3}_{-0.0}$	$-9.6 \pm 4.8\ ^{+2.4}_{-0.0}$	$-20.1 \pm 6.3\ ^{+0.0}_{-3.6}$	$-7.9 \pm 7.6\ ^{+1.1}_{-3.5}$
337.5	$-1.9 \pm 5.5\ ^{+2.7}_{-1.0}$	$-7.2 \pm 5.5\ ^{+0.2}_{-2.3}$	$-17.2 \pm 6.2\ ^{+0.0}_{-8.0}$	$-3.3 \pm 8.8\ ^{+0.0}_{-6.7}$	$-1.2 \pm 10.9\ ^{+1.7}_{-15.4}$
352.5	$-3.6 \pm 5.9\ ^{+0.0}_{-2.2}$	$-0.7 \pm 6.1\ ^{+0.5}_{-1.1}$	$1.8 \pm 7.4\ ^{+6.3}_{-1.3}$	$-2.6 \pm 10.6\ ^{+3.0}_{-8.5}$	$-5.1 \pm 16.7\ ^{+13.3}_{-0.0}$

ϕ (deg)	$x_B = 0.345$ $Q^2 = 2.218$ GeV^2 $t = -0.176$ GeV^2		$x_B = 0.363$ $Q^2 = 2.318$ GeV^2 $t = -0.232$ GeV^2		$x_B = 0.368$ $Q^2 = 2.348$ GeV^2 $t = -0.279$ GeV^2		$x_B = 0.371$ $Q^2 = 2.360$ GeV^2 $t = -0.325$ GeV^2		$x_B = 0.373$ $Q^2 = 2.375$ GeV^2 $t = -0.372$ GeV^2	
7.5	5.2 ± 5.1	$+ 0.0$ $- 5.4$	7.4 ± 4.9	$+ 0.2$ $- 1.8$	11.5 ± 5.9	$+ 3.9$ $- 0.1$	1.7 ± 7.3	$+ 2.9$ $- 0.0$	9.4 ± 10.9	$+ 2.0$ $- 2.5$
22.5	1.8 ± 5.1	$+ 3.6$ $- 0.0$	15.4 ± 4.6	$+ 0.9$ $- 1.3$	8.6 ± 5.3	$+ 1.6$ $- 0.4$	4.4 ± 6.2	$+ 0.0$ $- 4.3$	6.4 ± 8.2	$+ 4.6$ $- 1.9$
37.5	8.0 ± 4.7	$+ 1.5$ $- 0.7$	8.3 ± 4.1	$+ 1.8$ $- 0.0$	15.4 ± 4.2	$+ 0.0$ $- 1.9$	1.9 ± 4.4	$+ 0.0$ $- 5.3$	10.0 ± 5.3	$+ 0.0$ $- 3.6$
52.5	16.7 ± 4.5	$+ 5.7$ $- 0.1$	11.5 ± 3.6	$+ 1.5$ $- 1.5$	10.5 ± 3.6	$+ 1.5$ $- 0.2$	9.6 ± 3.8	$+ 0.0$ $- 2.3$	21.8 ± 4.3	$+ 1.6$ $- 0.4$
67.5	21.1 ± 4.1	$+ 6.0$ $- 0.0$	17.1 ± 3.2	$+ 3.7$ $- 0.0$	16.7 ± 3.2	$+ 1.2$ $- 0.0$	15.0 ± 3.4	$+ 0.0$ $- 1.4$	6.2 ± 3.3	$+ 0.0$ $- 3.5$
82.5	16.0 ± 4.0	$+ 2.1$ $- 0.1$	6.6 ± 2.9	$+ 1.6$ $- 0.0$	11.9 ± 2.8	$+ 2.4$ $- 0.4$	9.3 ± 2.6	$+ 1.7$ $- 0.2$	9.3 ± 2.7	$+ 1.0$ $- 0.5$
97.5	10.1 ± 3.5	$+ 1.9$ $- 0.1$	12.3 ± 2.7	$+ 0.0$ $- 0.7$	9.8 ± 2.4	$+ 1.4$ $- 0.0$	9.9 ± 2.4	$+ 1.3$ $- 0.0$	9.0 ± 2.4	$+ 0.1$ $- 1.8$
112.5	20.7 ± 3.4	$+ 0.1$ $- 1.8$	11.6 ± 2.4	$+ 0.1$ $- 1.3$	8.0 ± 2.2	$+ 0.0$ $- 0.9$	3.7 ± 2.2	$+ 0.5$ $- 0.3$	-1.1 ± 2.0	$+ 1.6$ $- 0.0$
127.5	9.3 ± 3.2	$+ 0.9$ $- 1.9$	6.4 ± 2.3	$+ 0.7$ $- 1.4$	3.5 ± 1.9	$+ 0.7$ $- 1.0$	6.6 ± 2.0	$+ 0.4$ $- 0.4$	1.6 ± 1.8	$+ 0.1$ $- 0.4$
142.5	4.8 ± 3.1	$+ 1.0$ $- 0.1$	5.5 ± 2.1	$+ 0.6$ $- 0.2$	3.7 ± 2.0	$+ 1.6$ $- 0.0$	3.6 ± 1.9	$+ 0.0$ $- 1.5$	3.2 ± 1.8	$+ 0.9$ $- 0.0$
157.5	-0.4 ± 3.0	$+ 1.4$ $- 0.0$	2.7 ± 2.2	$+ 0.9$ $- 0.1$	4.0 ± 2.0	$+ 0.3$ $- 0.5$	5.5 ± 1.8	$+ 0.8$ $- 0.2$	3.6 ± 1.9	$+ 0.7$ $- 0.0$
172.5	3.3 ± 3.0	$+ 2.9$ $- 0.2$	0.0 ± 2.0	$+ 1.5$ $- 0.0$	-0.3 ± 2.0	$+ 0.7$ $- 0.1$	2.7 ± 1.9	$+ 0.1$ $- 0.9$	2.1 ± 2.0	$+ 1.1$ $- 0.2$
187.5	-0.6 ± 2.8	$+ 0.6$ $- 1.4$	0.2 ± 2.1	$+ 1.2$ $- 0.2$	1.0 ± 1.9	$+ 0.0$ $- 1.2$	-0.6 ± 1.9	$+ 0.4$ $- 0.5$	4.4 ± 2.0	$+ 0.0$ $- 1.0$
202.5	-2.6 ± 2.9	$+ 0.9$ $- 2.0$	-0.7 ± 2.1	$+ 0.4$ $- 0.7$	-1.8 ± 1.8	$+ 0.0$ $- 0.5$	-4.2 ± 2.0	$+ 1.1$ $- 0.0$	-0.1 ± 2.0	$+ 0.0$ $- 2.5$
217.5	-7.5 ± 3.0	$+ 1.1$ $- 0.0$	-5.4 ± 2.2	$+ 0.2$ $- 0.5$	-5.1 ± 2.0	$+ 1.3$ $- 0.0$	-5.2 ± 1.8	$+ 0.4$ $- 0.7$	-3.5 ± 1.8	$+ 0.8$ $- 0.1$
232.5	-13.1 ± 3.2	$+ 3.3$ $- 0.0$	-4.2 ± 2.3	$+ 0.5$ $- 1.2$	-4.7 ± 2.1	$+ 0.0$ $- 0.8$	-5.2 ± 1.9	$+ 1.4$ $- 0.0$	-4.0 ± 1.9	$+ 0.2$ $- 0.7$
247.5	-6.9 ± 3.3	$+ 1.7$ $- 0.0$	-9.5 ± 2.4	$+ 0.4$ $- 0.7$	-3.8 ± 2.1	$+ 0.9$ $- 0.0$	0.6 ± 2.1	$+ 0.9$ $- 0.4$	-1.8 ± 2.1	$+ 0.6$ $- 1.0$
262.5	-17.5 ± 3.6	$+ 2.1$ $- 0.0$	-9.0 ± 2.7	$+ 0.1$ $- 1.4$	-10.5 ± 2.4	$+ 0.0$ $- 3.0$	-6.8 ± 2.4	$+ 0.4$ $- 1.7$	-3.4 ± 2.3	$+ 0.0$ $- 1.1$
277.5	-13.0 ± 3.8	$+ 1.4$ $- 0.7$	-16.0 ± 2.8	$+ 0.5$ $- 1.2$	-9.8 ± 2.6	$+ 2.1$ $- 0.0$	-14.2 ± 2.7	$+ 0.0$ $- 1.5$	-5.8 ± 2.6	$+ 0.7$ $- 0.3$
292.5	-13.2 ± 4.2	$+ 2.9$ $- 0.6$	-12.6 ± 3.1	$+ 0.4$ $- 1.8$	-11.0 ± 2.9	$+ 1.0$ $- 0.9$	-9.6 ± 3.1	$+ 0.0$ $- 3.6$	-11.3 ± 3.1	$+ 0.0$ $- 1.8$
307.5	-16.6 ± 4.3	$+ 0.4$ $- 2.1$	-14.0 ± 3.5	$+ 4.4$ $- 0.0$	-15.8 ± 3.5	$+ 1.7$ $- 0.5$	-10.6 ± 3.6	$+ 0.7$ $- 0.6$	-8.8 ± 3.7	$+ 0.4$ $- 0.5$
322.5	-15.2 ± 4.6	$+ 2.8$ $- 0.0$	-14.0 ± 3.8	$+ 0.2$ $- 1.5$	-9.4 ± 3.8	$+ 2.1$ $- 0.0$	-14.2 ± 4.5	$+ 4.4$ $- 0.0$	-5.2 ± 5.1	$+ 0.4$ $- 2.6$
337.5	-3.1 ± 4.8	$+ 0.5$ $- 0.4$	1.4 ± 4.4	$+ 1.1$ $- 0.8$	-5.0 ± 4.7	$+ 0.8$ $- 1.7$	-0.5 ± 5.9	$+ 0.7$ $- 2.6$	-8.1 ± 8.1	$+ 3.4$ $- 4.3$
352.5	-1.2 ± 4.9	$+ 1.1$ $- 1.5$	-1.1 ± 4.8	$+ 4.3$ $- 0.0$	2.7 ± 5.5	$+ 0.0$ $- 3.8$	-0.5 ± 7.3	$+ 2.9$ $- 1.5$	7.3 ± 11.5	$+ 2.2$ $- 1.1$

ϕ (deg)	$x_B = 0.378$ $Q^2 = 2.012$ GeV^2 $t = -0.192$ GeV^2		$x_B = 0.392$ $Q^2 = 2.054$ GeV^2 $t = -0.233$ GeV^2		$x_B = 0.398$ $Q^2 = 2.074$ GeV^2 $t = -0.279$ GeV^2		$x_B = 0.400$ $Q^2 = 2.084$ GeV^2 $t = -0.324$ GeV^2		$x_B = 0.401$ $Q^2 = 2.091$ GeV^2 $t = -0.371$ GeV^2	
7.5	-2.8 ± 9.1	$+4.3$ -2.5	-2.4 ± 5.1	$+0.0$ -3.5	-0.2 ± 5.9	$+0.8$ -1.0	3.8 ± 7.7	$+6.9$ -0.0	-9.0 ± 11.9	$+1.1$ -3.2
22.5	2.7 ± 8.8	$+0.7$ -5.6	-0.6 ± 4.8	$+0.5$ -2.4	1.4 ± 5.0	$+0.0$ -4.0	-1.2 ± 6.8	$+0.0$ -3.5	0.9 ± 9.2	$+2.7$ -1.1
37.5	-6.0 ± 7.9	$+3.6$ -0.0	4.1 ± 4.4	$+1.6$ -1.1	13.3 ± 4.6	$+4.3$ -0.0	5.5 ± 5.2	$+2.0$ -3.0	0.4 ± 6.2	$+1.4$ -0.0
52.5	7.2 ± 8.1	$+2.6$ -2.5	13.7 ± 4.5	$+2.6$ -0.4	11.2 ± 4.4	$+2.3$ -0.0	12.3 ± 4.8	$+1.9$ -1.2	8.3 ± 5.3	$+2.0$ -0.4
67.5	-5.9 ± 7.7	$+2.2$ -0.7	5.0 ± 4.1	$+1.1$ -0.0	6.0 ± 3.9	$+0.6$ -1.4	8.4 ± 4.2	$+0.4$ -2.0	5.9 ± 4.5	$+0.6$ -1.0
82.5	18.2 ± 7.2	$+0.7$ -1.9	12.4 ± 4.0	$+0.1$ -3.3	10.6 ± 3.7	$+0.2$ -1.8	3.5 ± 3.7	$+0.0$ -1.4	7.9 ± 3.8	$+0.0$ -1.7
97.5	-0.8 ± 7.3	$+4.8$ -0.6	4.6 ± 3.6	$+3.2$ -0.0	4.2 ± 3.5	$+0.2$ -1.8	7.2 ± 3.7	$+1.8$ -0.0	3.3 ± 4.0	$+0.9$ -0.2
112.5	14.0 ± 6.7	$+2.8$ -0.0	-0.6 ± 3.6	$+0.0$ -2.5	7.2 ± 3.3	$+1.0$ -1.1	-1.1 ± 3.1	$+2.4$ -0.0	6.5 ± 3.9	$+1.8$ -0.5
127.5	-0.3 ± 6.7	$+2.9$ -0.7	3.0 ± 3.1	$+0.0$ -1.6	7.3 ± 2.8	$+3.5$ -0.0	11.1 ± 3.2	$+0.0$ -4.8	-1.5 ± 3.6	$+2.9$ -0.0
142.5	1.6 ± 6.0	$+0.0$ -4.0	4.8 ± 3.1	$+0.2$ -1.7	4.8 ± 2.8	$+2.9$ -0.0	3.3 ± 3.0	$+1.8$ -0.0	6.1 ± 3.8	$+0.0$ -3.8
157.5	-9.0 ± 5.9	$+2.5$ -2.4	4.9 ± 3.0	$+0.1$ -1.2	5.6 ± 2.9	$+2.1$ -0.8	5.3 ± 3.3	$+0.1$ -1.5	-2.7 ± 4.2	$+0.6$ -0.6
172.5	-4.9 ± 5.9	$+0.0$ -3.1	1.0 ± 3.0	$+0.8$ -1.5	0.6 ± 2.8	$+1.5$ -0.1	-0.7 ± 3.2	$+1.5$ -0.3	-8.4 ± 4.5	$+0.1$ -2.0
187.5	-2.7 ± 6.0	$+1.4$ -3.3	2.5 ± 3.0	$+0.6$ -1.1	1.4 ± 2.7	$+0.4$ -1.1	-0.5 ± 3.2	$+2.2$ -0.7	2.9 ± 4.7	$+4.7$ -0.0
202.5	6.7 ± 6.3	$+0.9$ -4.1	-1.0 ± 3.2	$+0.0$ -3.2	1.7 ± 2.6	$+0.0$ -1.4	1.0 ± 3.4	$+1.8$ -0.0	3.8 ± 4.1	$+0.0$ -1.4
217.5	-0.8 ± 6.6	$+0.5$ -10.0	1.3 ± 3.1	$+0.0$ -2.6	-5.0 ± 3.1	$+1.9$ -0.0	-1.2 ± 3.2	$+0.0$ -1.6	0.8 ± 3.9	$+2.6$ -0.0
232.5	-8.7 ± 6.3	$+2.6$ -0.0	-1.1 ± 3.1	$+0.0$ -4.4	-4.3 ± 2.8	$+0.3$ -1.0	0.3 ± 3.2	$+3.2$ -0.7	-6.6 ± 3.2	$+0.5$ -0.2
247.5	-12.9 ± 6.2	$+0.5$ -4.0	-10.3 ± 3.4	$+0.0$ -2.8	-6.8 ± 3.2	$+0.4$ -0.2	-6.6 ± 3.7	$+1.6$ -1.2	-3.0 ± 3.7	$+0.0$ -3.2
262.5	-4.0 ± 6.5	$+0.3$ -3.8	-2.4 ± 3.7	$+2.5$ -0.0	-8.4 ± 3.5	$+1.9$ -0.4	-7.9 ± 3.6	$+1.3$ -1.1	-0.1 ± 3.7	$+3.5$ -0.4
277.5	-1.2 ± 6.9	$+0.6$ -2.9	-12.5 ± 3.7	$+0.0$ -3.0	-9.4 ± 3.7	$+2.4$ -0.6	4.4 ± 3.8	$+3.4$ -0.0	-3.2 ± 3.9	$+0.4$ -1.0
292.5	-6.0 ± 7.4	$+0.6$ -1.6	-13.8 ± 4.1	$+2.6$ -0.0	-7.3 ± 3.5	$+1.5$ -0.3	-4.5 ± 3.9	$+0.6$ -0.7	-7.4 ± 4.4	$+2.4$ -0.6
307.5	0.6 ± 8.3	$+1.7$ -5.6	-5.3 ± 4.2	$+5.0$ -0.0	-6.2 ± 4.0	$+0.5$ -1.8	-4.1 ± 4.8	$+4.7$ -0.2	-7.2 ± 4.9	$+0.8$ -1.7
322.5	-2.6 ± 8.3	$+0.0$ -8.0	-15.7 ± 4.6	$+1.1$ -1.2	-10.4 ± 4.3	$+1.0$ -1.1	-14.6 ± 5.3	$+0.0$ -3.9	-5.8 ± 6.2	$+1.0$ -2.7
337.5	-14.3 ± 8.6	$+3.4$ -1.6	-1.8 ± 4.8	$+0.8$ -0.8	-14.9 ± 5.0	$+0.0$ -4.6	-0.2 ± 6.5	$+0.0$ -4.5	-1.0 ± 8.4	$+1.2$ -10.7
352.5	4.7 ± 8.7	$+7.7$ -0.0	-3.1 ± 5.0	$+0.9$ -0.8	1.0 ± 5.6	$+4.9$ -0.7	-1.7 ± 7.3	$+2.0$ -5.9	-3.8 ± 12.5	$+9.3$ -0.0

ϕ (deg)	$x_B = 0.336$ $Q^2 = 2.161$ GeV^2 $t = -0.171$ GeV^2		$x_B = 0.342$ $Q^2 = 2.190$ GeV^2 $t = -0.231$ GeV^2		$x_B = 0.343$ $Q^2 = 2.194$ GeV^2 $t = -0.278$ GeV^2		$x_B = 0.342$ $Q^2 = 2.191$ GeV^2 $t = -0.324$ GeV^2		$x_B = 0.342$ $Q^2 = 2.193$ GeV^2 $t = -0.371$ GeV^2	
7.5	7.3 ± 6.5	$+\,0.0$ $-\,8.0$	14.4 ± 10.1	$+\,0.3$ $-\,6.4$	X		X		X	
22.5	1.7 ± 6.7	$+\,2.8$ $-\,1.8$	32.4 ± 8.9	$+\,0.3$ $-\,3.2$	X		X		X	
37.5	7.6 ± 6.1	$+\,2.8$ $-\,0.4$	16.2 ± 7.9	$+\,8.5$ $-\,0.0$	16.8 ± 8.7	$+\,0.0$ $-\,7.4$	5.3 ± 11.9	$+\,2.6$ $-\,3.5$	-23.9 ± 23.3	$+\,5.6$ $-\,11.7$
52.5	22.5 ± 5.6	$+\,9.3$ $-\,0.0$	17.7 ± 6.4	$+\,3.3$ $-\,2.7$	11.7 ± 7.4	$+\,6.6$ $-\,1.6$	16.5 ± 9.0	$+\,0.0$ $-\,4.3$	7.7 ± 12.1	$+\,10.5$ $-\,0.0$
67.5	25.8 ± 5.3	$+\,5.7$ $-\,0.0$	20.2 ± 5.8	$+\,2.9$ $-\,1.6$	12.5 ± 6.5	$+\,0.0$ $-\,4.6$	17.9 ± 8.0	$+\,0.0$ $-\,5.4$	5.9 ± 8.6	$+\,0.2$ $-\,4.5$
82.5	14.9 ± 5.1	$+\,3.2$ $-\,0.4$	8.7 ± 5.0	$+\,0.7$ $-\,3.4$	17.9 ± 5.4	$+\,0.9$ $-\,0.9$	13.0 ± 5.5	$+\,4.5$ $-\,0.7$	0.2 ± 6.1	$+\,3.9$ $-\,1.3$
97.5	14.2 ± 4.5	$+\,3.3$ $-\,0.0$	21.1 ± 4.8	$+\,0.4$ $-\,0.8$	13.5 ± 4.6	$+\,2.4$ $-\,0.0$	12.5 ± 4.9	$+\,5.0$ $-\,0.2$	12.7 ± 5.3	$+\,0.9$ $-\,3.4$
112.5	23.3 ± 4.2	$+\,0.0$ $-\,2.6$	18.6 ± 4.0	$+\,1.4$ $-\,0.6$	11.3 ± 4.2	$+\,0.2$ $-\,2.0$	1.5 ± 4.2	$+\,3.8$ $-\,0.0$	-3.2 ± 4.3	$+\,1.0$ $-\,1.0$
127.5	11.3 ± 4.2	$+\,0.8$ $-\,3.8$	11.5 ± 3.6	$+\,0.1$ $-\,4.6$	2.3 ± 3.3	$+\,1.2$ $-\,0.8$	9.5 ± 3.9	$+\,0.1$ $-\,0.7$	5.1 ± 3.6	$+\,0.1$ $-\,2.0$
142.5	7.0 ± 3.9	$+\,1.2$ $-\,0.2$	10.7 ± 3.5	$+\,1.6$ $-\,0.7$	5.7 ± 3.4	$+\,1.7$ $-\,0.0$	7.8 ± 3.7	$+\,0.0$ $-\,1.1$	4.5 ± 3.5	$+\,0.6$ $-\,1.9$
157.5	-3.1 ± 3.7	$+\,1.2$ $-\,0.0$	6.4 ± 3.5	$+\,0.2$ $-\,0.9$	4.1 ± 3.5	$+\,0.2$ $-\,3.0$	7.2 ± 3.6	$+\,0.0$ $-\,1.0$	3.8 ± 3.7	$+\,0.5$ $-\,0.4$
172.5	4.5 ± 3.7	$+\,4.0$ $-\,0.3$	1.4 ± 3.4	$+\,3.6$ $-\,0.0$	0.8 ± 3.6	$+\,0.5$ $-\,0.9$	0.8 ± 3.4	$+\,0.4$ $-\,1.9$	-0.2 ± 3.9	$+\,3.4$ $-\,0.0$
187.5	-1.7 ± 3.5	$+\,0.1$ $-\,2.5$	-1.2 ± 3.4	$+\,2.2$ $-\,0.5$	2.5 ± 3.6	$+\,0.3$ $-\,1.9$	-0.2 ± 3.4	$+\,0.0$ $-\,1.0$	8.5 ± 3.6	$+\,1.3$ $-\,0.3$
202.5	-2.1 ± 3.6	$+\,1.8$ $-\,1.3$	1.4 ± 3.6	$+\,0.5$ $-\,1.1$	-3.3 ± 3.3	$+\,0.9$ $-\,0.1$	-9.4 ± 3.8	$+\,2.5$ $-\,0.0$	0.5 ± 3.8	$+\,0.0$ $-\,3.6$
217.5	-9.2 ± 3.9	$+\,0.6$ $-\,0.7$	-9.5 ± 3.7	$+\,0.0$ $-\,2.2$	-6.3 ± 3.6	$+\,1.4$ $-\,0.0$	-7.3 ± 3.4	$+\,1.2$ $-\,0.0$	-4.1 ± 3.4	$+\,2.6$ $-\,0.2$
232.5	-13.5 ± 4.1	$+\,2.6$ $-\,0.0$	-3.8 ± 3.8	$+\,0.0$ $-\,2.1$	-3.4 ± 3.7	$+\,0.6$ $-\,0.5$	-3.9 ± 3.8	$+\,0.9$ $-\,0.8$	-7.9 ± 3.8	$+\,1.3$ $-\,0.2$
247.5	-6.8 ± 4.1	$+\,2.4$ $-\,0.0$	-8.4 ± 4.0	$+\,0.0$ $-\,1.8$	-3.6 ± 3.8	$+\,0.2$ $-\,0.9$	-0.6 ± 3.8	$+\,1.8$ $-\,0.0$	-4.9 ± 4.2	$+\,2.1$ $-\,0.5$
262.5	-22.7 ± 4.5	$+\,2.2$ $-\,0.8$	-11.2 ± 4.5	$+\,0.9$ $-\,0.7$	-19.1 ± 4.3	$+\,0.0$ $-\,5.1$	-3.0 ± 4.8	$+\,0.7$ $-\,2.0$	-0.9 ± 4.4	$+\,2.0$ $-\,0.1$
277.5	-19.9 ± 4.8	$+\,0.4$ $-\,1.4$	-22.1 ± 4.8	$+\,2.2$ $-\,0.8$	-14.7 ± 5.0	$+\,5.1$ $-\,0.0$	-19.4 ± 5.6	$+\,0.0$ $-\,3.1$	-4.8 ± 5.7	$+\,0.0$ $-\,2.5$
292.5	-17.6 ± 5.4	$+\,2.3$ $-\,0.5$	-21.5 ± 5.4	$+\,0.8$ $-\,1.6$	-16.1 ± 5.5	$+\,0.5$ $-\,2.7$	-20.0 ± 7.1	$+\,1.5$ $-\,2.7$	-15.4 ± 7.7	$+\,0.0$ $-\,3.8$
307.5	-23.2 ± 5.5	$+\,0.0$ $-\,4.8$	-27.4 ± 6.3	$+\,7.9$ $-\,0.0$	-3.2 ± 6.9	$+\,1.1$ $-\,3.4$	-21.8 ± 7.8	$+\,2.2$ $-\,1.8$	-9.7 ± 10.6	$+\,2.2$ $-\,1.5$
322.5	-19.2 ± 5.9	$+\,3.5$ $-\,0.0$	-17.0 ± 7.2	$+\,0.0$ $-\,2.9$	-2.6 ± 8.1	$+\,3.4$ $-\,0.0$	-26.5 ± 12.3	$+\,13.9$ $-\,0.0$	-19.9 ± 17.6	$+\,0.0$ $-\,25.8$
337.5	-4.7 ± 6.2	$+\,0.4$ $-\,0.9$	5.9 ± 8.3	$+\,0.0$ $-\,5.4$	X		X		X	
352.5	-4.1 ± 6.5	$+\,1.8$ $-\,3.4$	6.6 ± 9.4	$+\,2.5$ $-\,2.0$	X		X		X	
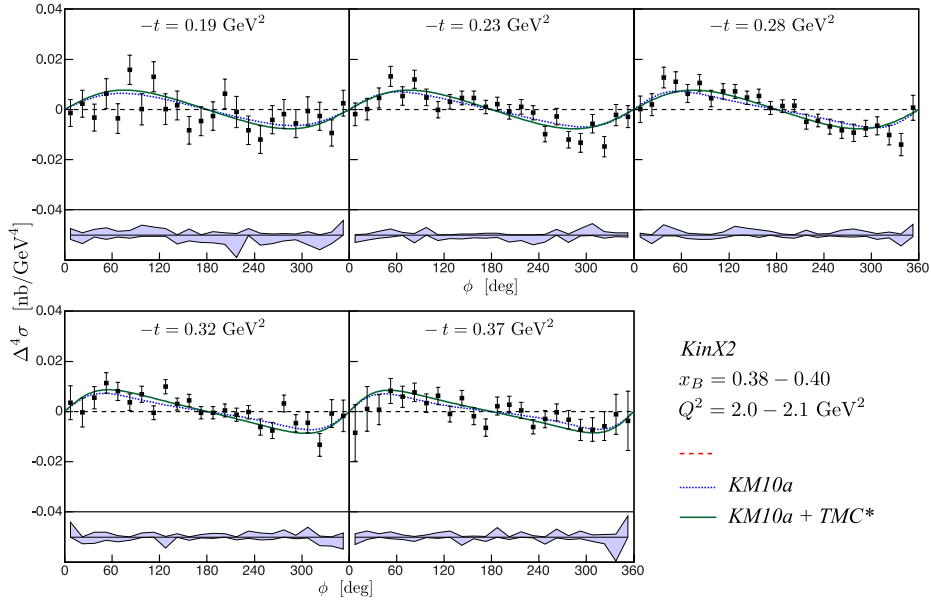
Figure B.8: (Color online) Cross section differences for opposite beam helicities for KinX2. Error bars are statistical only. The light blue area represents the point-to-point systematic uncertainties added linearly to the normalization error. The KM10a model along with its modified version including TMC effects are shown as dotted blue and solid green curves respectively.
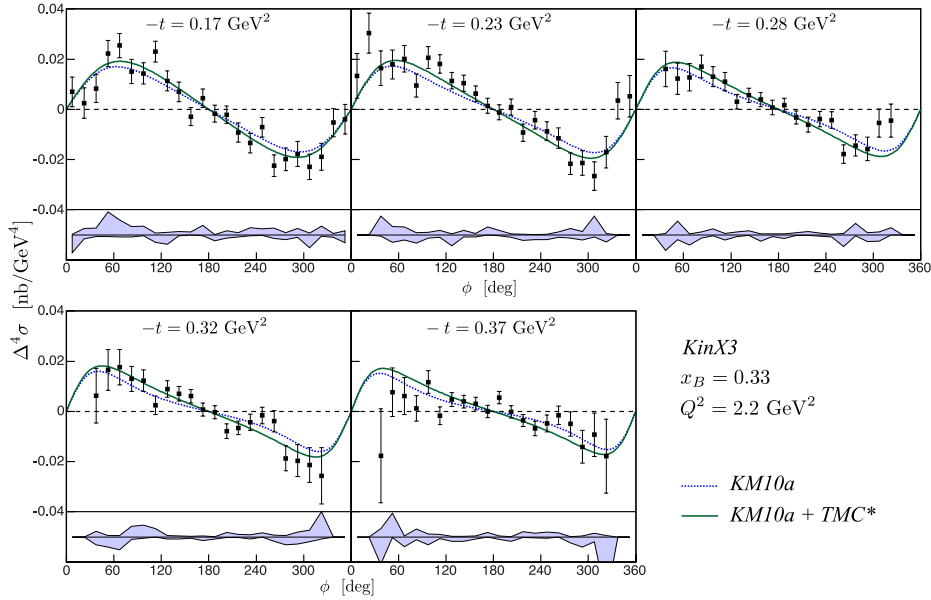
Figure B.9: (Color online) Cross section differences for opposite beam helicities for KinX3. Error bars are statistical only. The light blue area represents the point-to-point systematic uncertainties added linearly to the normalization error. The KM10a model along with its modified version including TMC effects are shown as dotted blue and solid green curves respectively.

Appendix C

Light cone coordinates

We are going to use the light cone coordinates, convenient to simplify the calculations and to understand the physics. We define the Sudakov vectors such as:

$$\tilde{p} = \frac{1}{\sqrt{2}} \begin{pmatrix} 1 \\ 0 \\ 0 \\ 1 \end{pmatrix} \text{ and } n = \frac{1}{\sqrt{2}} \begin{pmatrix} 1 \\ 0 \\ 0 \\ -1 \end{pmatrix}, \tag{C.1}$$

As a consequence we have $n \cdot \tilde{p} = 1$ and $n^2 = \tilde{p}^2 = 0$.

With $q^+ = q^0 + q^3$ and $q^- = q^0 - q^3$, we can write:

$$q = q^+ \tilde{p} + q^- n + \vec{q}_\perp, \tag{C.2}$$

where $\vec{q}_\perp$ are the remaining components orthogonal to $\tilde{p}$ and n.

Bibliography

[1] E. Rutherford. The scattering of alpha and beta particles by matter and the structure of the atom. *Phil.Mag.*, 21:669–688, 1911.

[2] M.N. Rosenbluth. High Energy Elastic Scattering of Electrons on Protons. *Phys.Rev.*, 79:615–619, 1950.

[3] J. C. Bernauer, P. Achenbach, C. Ayerbe Gayoso, R. Böhm, D. Bosnar, L. Debenjak, M. O. Distler, L. Doria, A. Esser, H. Fonvieille, J. M. Friedrich, J. Friedrich, M. Gómez Rodríguez de la Paz, M. Makek, H. Merkel, D. G. Middleton, U. Müller, L. Nungesser, J. Pochodzalla, M. Potokar, S. Sánchez Majos, B. S. Schlimme, S. Širca, Th. Walcher, and M. Weinriefer. High-precision determination of the electric and magnetic form factors of the proton. *Phys. Rev. Lett.*, 105:242001, Dec 2010.

[4] Peter J. Mohr, Barry N. Taylor, and David B. Newell. CODATA Recommended Values of the Fundamental Physical Constants: 2006. *Rev.Mod.Phys.*, 80:633–730, 2008.

[5] Randolf Pohl, Aldo Antognini, Francois Nez, Fernando D. Amaro, Francois Biraben, et al. The size of the proton. *Nature*, 466:213–216, 2010.

[6] Martin Breidenbach, Jerome I. Friedman, Henry W. Kendall, Elliott D. Bloom, D.H. Coward, et al. Observed Behavior of Highly Inelastic electron-Proton Scattering. *Phys.Rev.Lett.*, 23:935–939, 1969.

[7] Elliott D. Bloom, D.H. Coward, H.C. DeStaebler, J. Drees, Guthrie Miller, et al. High-Energy Inelastic e p Scattering at 6-Degrees and 10-Degrees. *Phys.Rev.Lett.*, 23:930–934, 1969.

[8] Murray Gell-Mann. A Schematic Model of Baryons and Mesons. *Phys.Lett.*, 8:214–215, 1964.

[9] G. Zweig. An SU(3) model for strong interaction symmetry and its breaking. Version 2. pages 22–101, 1964.

[10] Xiang-Dong Ji. Gauge-Invariant Decomposition of Nucleon Spin. *Phys.Rev.Lett.*, 78:610–613, 1997.

[11] Xiang-Dong Ji. Lorentz symmetry and the internal structure of the nucleon. *Phys.Rev.*, D58:056003, 1998.

[12] A.V. Radyushkin. Double distributions and evolution equations. *Phys.Rev.*, D59:014030, 1999.

[13] A.V. Radyushkin. Symmetries and structure of skewed and double distributions. *Phys.Lett.*, B449:81–88, 1999.

[14] Dieter Müller, D. Robaschik, B. Geyer, F.-M. Dittes, and J. Hořejši. Wave functions, evolution equations and evolution kernels from light ray operators of QCD. *Fortsch.Phys.*, 42:101–141, 1994.

[15] M. Diehl, Th. Feldmann, R. Jakob, and P. Kroll. Generalized parton distributions from nucleon form-factor data. *Eur.Phys.J.*, C39:1–39, 2005.

[16] Alessandro Bacchetta, Umberto D'Alesio, Markus Diehl, and C. Andy Miller. Single-spin asymmetries: The Trento conventions. *Phys.Rev.*, D70:117504, 2004.

[17] A.V. Belitsky and Dieter Mueller. Exclusive electroproduction revisited: treating kinematical effects. *Phys.Rev.*, D82:074010, 2010.

[18] Andrei V. Belitsky, Dieter Mueller, and A. Kirchner. Theory of deeply virtual Compton scattering on the nucleon. *Nucl.Phys.*, B629:323–392, 2002.

[19] S.V. Goloskokov and P. Kroll. An Attempt to understand exclusive pi+ electroproduction. *Eur.Phys.J.*, C65:137–151, 2010.

[20] S.V. Goloskokov and P. Kroll. Transversity in hard exclusive electroproduction of pseudoscalar mesons. *Eur.Phys.J.*, A47:112, 2011.

[21] A. Accardi, J.L. Albacete, M. Anselmino, N. Armesto, E.C. Aschenauer, et al. Electron Ion Collider: The Next QCD Frontier - Understanding the glue that binds us all. 2012.

[22] H.S. Jo et al. Cross sections for the exclusive photon electroproduction on the proton and Generalized Parton Distributions. 2015.

[23] M. Defurne et al. The E00-110 experiment in Jefferson Lab's Hall A: Deeply Virtual Compton Scattering off the Proton at 6 GeV. 2015.

[24] S. Chekanov et al. Measurement of deeply virtual Compton scattering at HERA. *PLB*, 573:46, 2003.

[25] A. Aktas et al. Measurement of deeply virtual compton scattering at HERA. *Eur.Phys.J.*, C44:1–11, 2005.

[26] S. Chekanov et al. A Measurement of the Q**2, W and t dependences of deeply virtual Compton scattering at HERA. *JHEP*, 0905:108, 2009.

[27] F.D. Aaron et al. Measurement of deeply virtual Compton scattering and its t-dependence at HERA. *Phys.Lett.*, B659:796–806, 2008.

[28] F.D. Aaron et al. Deeply Virtual Compton Scattering and its Beam Charge Asymmetry in e+- Collisions at HERA. *Phys.Lett.*, B681:391–399, 2009.

[29] A. Airapetian, E.C. Aschenauer, S. Belostotski, A. Borissov, A. Borisenko, et al. The HERMES Recoil Detector. *JINST*, 8:P05012, 2013.

[30] A. Airapetian et al. Separation of contributions from deeply virtual Compton scattering and its interference with the Bethe-Heitler process in measurements on a hydrogen target. *JHEP*, 0911:083, 2009.

[31] A. Airapetian et al. Measurement of double-spin asymmetries associated with deeply virtual Compton scattering on a transversely polarized hydrogen target. *Phys.Lett.*, B704:15–23, 2011.

[32] A. Airapetian et al. Beam-helicity asymmetry arising from deeply virtual Compton scattering measured with kinematically complete event reconstruction. *JHEP*, 1210:042, 2012.

[33] F.X. Girod et al. Measurement of Deeply virtual Compton scattering beam-spin asymmetries. *Phys.Rev.Lett.*, 100:162002, 2008.

[34] E. Seder, A. Biselli, S. Pisano, and S. Niccolai. Longitudinal target-spin asymmetries for deeply virtual Compton scattering. *Phys.Rev.Lett.*, 114(3):032001, 2015.

[35] S. Pisano et al. Single and double spin asymmetries for deeply virtual Compton scattering measured with CLAS and a longitudinally polarized proton target. 2015.

[36] Peter Kroll, Herve Moutarde, and Franck Sabatie. From hard exclusive meson electroproduction to deeply virtual Compton scattering. *Eur.Phys.J.*, C73:2278, 2013.

[37] E. Fuchey, A. Camsonne, C. Munoz Camacho, M. Mazouz, G. Gavalian, et al. Exclusive Neutral Pion Electroproduction in the Deeply Virtual Regime. *Phys.Rev.*, C83:025201, 2011.

[38] I. Bedlinskiy et al. Exclusive π^0 electroproduction at $W > 2$ GeV with CLAS. *Phys.Rev.*, C90(2):025205, 2014.

[39] G.R. Goldstein, J. Osvaldo Gonzalez Hernandez, and S. Liuti. Flexible Parametrization of Generalized Parton Distributions: The Chiral-Odd Sector. 2013.

[40] T. Horn, X. Qian, J. Arrington, R. Asaturyan, F. Benmokthar, et al. Scaling study of the pion electroproduction cross sections and the pion form factor. *Phys.Rev.*, C78:058201, 2008.

[41] V. Tadevosyan et al. Determination of the pion charge form-factor for Q**2 = 0.60-GeV**2 - 1.60-GeV**2. *Phys.Rev.*, C75:055205, 2007.

[42] P. Bertin, C. E. Hyde, R. Ransome, F. Sabatié, et al. E00-110. JLab Experiment E00-110, Deeply Virtual Compton Scattering at 6 GeV, 2000.

[43] P. Bertin, C. E. Hyde, C. Muñoz Camacho, J. Roche, et al. E07-007. JLab Experiment E07-007, Separation of Deeply Virtual Photon and pi-0 Electroproduction Observables of Unpolarized Protons, 2007.

[44] C. Muñoz Camacho et al. Scaling tests of the cross-section for deeply virtual compton scattering. *Phys.Rev.Lett.*, 97:262002, 2006.

[45] J.M. Laget. Unitarity constraints on neutral pion electroproduction. *Phys.Lett.*, B695:199–204, 2011.

[46] D.T. Pierce, F. Meier, and P. Zürcher. Direct observation of spin dependent electronic structure of gaas using spin polarized photoemission. *Physics Letters A*, 51(8):465 – 466, 1975.

[47] J. Alcorn, B.D. Anderson, K.A. Aniol, J.R.M. Annand, L. Auerbach, et al. Basic Instrumentation for Hall A at Jefferson Lab. *Nucl.Instrum.Meth.*, A522:294–346, 2004.

[48] F. Feinstein. The analogue ring sampler: A front-end chip for ANTARES. *Nucl.Instrum.Meth.*, A504:258–261, 2003.

[49] F. Druillole et al. The analog ring sampler: An ASIC for the front-end electronics of the ANTARES neutrino telescope. *IEEE Trans.Nucl.Sci.*, 49:1122–1129, 2002.

[50] M. Rvachev. Effective use of hall a hrs acceptance with r-functions. Technical Report Jlab-TN-01-055, Jefferson Laboratory, 2001.

[51] L. Morand. *Mesure de l'électroproduction de mésons oméga à grand transfer d'énergie impulsion.* PhD thesis, Université Paris VII - Diderot, 2003.

[52] V. Laine. *Polarimetry of the polarized hydrogen deuteride HDice target under an electron beam.* PhD thesis, Université Blaise Pascal, 2013.

[53] L. W. MO and Y. S. TSAI. Radiative corrections to elastic and inelastic ep and up scattering. *Rev. Mod. Phys.*, 41:205–235, Jan 1969.

[54] M. Vanderhaeghen, J.M. Friedrich, D. Lhuillier, D. Marchand, L. Van Hoorebeke, et al. QED radiative corrections to virtual Compton scattering. *Phys.Rev.*, C62:025501, 2000.

[55] M. Arneodo et al. Measurement of the proton and the deuteron structure functions, F2(p) and F2(d). *Phys.Lett.*, B364:107–115, 1995.

[56] Ingo Schienbein, Voica A. Radescu, G.P. Zeller, M. Eric Christy, C.E. Keppel, et al. A Review of Target Mass Corrections. *J.Phys.*, G35:053101, 2008.

[57] M. Mazouz and E. Voutier. *JLab Technical Note*, JLAB-05-033, 2005.

[58] V. Breton, et al. *Nucl. Inst. and Meth.*, A362:478, 1995.

[59] R. De Masi et al. Measurement of e p –¿ e p pi0 beam spin asymmetries above the resonance region. *Phys.Rev.*, C77:042201, 2008.

[60] M. Vanderhaeghen, Pierre A.M. Guichon, and M. Guidal. Deeply virtual electroproduction of photons and mesons on the nucleon: Leading order amplitudes and power corrections. *Phys.Rev.*, D60:094017, 1999.

[61] K. Goeke, Maxim V. Polyakov, and M. Vanderhaeghen. Hard exclusive reactions and the structure of hadrons. *Prog. Part. Nucl. Phys.*, 47:401–515, 2001.

[62] Kresimir Kumericki and Dieter Mueller. Deeply virtual Compton scattering at small x(B) and the access to the GPD H. *Nucl.Phys.*, B841:1–58, 2010.

[63] V.M. Braun, A.N. Manashov, and B. Pirnay. Finite-t and target mass corrections to deeply virtual Compton scattering. *Phys.Rev.Lett.*, 109:242001, 2012.

[64] Vladimir M. Braun, Alexander N. Manashov, Dieter Müller, and Bjoern M. Pirnay. Deeply Virtual Compton Scattering to the twist-four accuracy: Impact of finite-t and target mass corrections. *Phys.Rev.*, D89(7):074022, 2014.

[65] V. M. Braun, A. N. Manashov, D. Mueller, and B. Pirnay. Resolving kinematic ambiguities in QCD predictions for Deeply Virtual Compton Scattering. *PoS*, DIS2014:225, 2014.

[66] V. Braun. Target Mass Corrections, Private communication, 2015.

[67] H. Moutarde, B. Pire, F. Sabatie, L. Szymanowski, and J. Wagner. Timelike and spacelike deeply virtual Compton scattering at next-to-leading order. *Phys.Rev.*, D87(5):054029, 2013.

[68] M. Mazouz. Calorimeter calibration with π^0. Technical Report DVCS Collaboration note, 109, Faculté des sciences de Monastir, 2011.

[69] E. Fuchey. *Electroproduction de pions neutres dans le Hall A au Jefferson Laboratory.* PhD thesis, Université Blaise Pascal, 2010.